creative commons
COMMONS DEED

저작자표시-비영리-변경금지 2.0 대한민국

이용자는 아래의 조건을 따르는 경우에 한하여 자유롭게

- 이 저작물을 복제, 배포, 전송, 전시, 공연 및 방송할 수 있습니다.

다음과 같은 조건을 따라야 합니다:

저작자표시. 귀하는 원저작자를 표시하여야 합니다.

비영리. 귀하는 이 저작물을 영리 목적으로 이용할 수 없습니다.

변경금지. 귀하는 이 저작물을 개작, 변형 또는 가공할 수 없습니다.

- 귀하는, 이 저작물의 재이용이나 배포의 경우, 이 저작물에 적용된 이용허락조건을 명확하게 나타내어야 합니다.
- 저작권자로부터 별도의 허가를 받으면 이러한 조건들은 적용되지 않습니다.

저작권법에 따른 이용자의 권리는 위의 내용에 의하여 영향을 받지 않습니다.

이것은 이용허락규약(Legal Code)을 이해하기 쉽게 요약한 것입니다.

Disclaimer

dCollection

공학박사학위논문

Analytical and Experimental Evaluation of an Active Trailing-edge Flap (ATF) for Vibratory Loads Reduction in Rotorcraft

회전익기 진동 저감을 위한 능동 뒷전 플랩 블레이드의 해석 및 실험 평가

2017 년 12 월

서울대학교 대학원

기계항공공학부

은 원 종

Abstract

Analytical and Experimental Evaluation of an Active Trailing-edge Flap (ATF) for Vibratory Loads Reduction in Rotorcraft

WonJong Eun

Department of Mechanical and Aerospace Engineering

The Graduate School

Seoul National University

This dissertation focuses on improving a Mach-scaled helicopter rotor blade prototype with a flap-driving mechanism termed as Seoul National University Flap (SNUF). The flap-driving mechanism is further improved by considering performance of the piezoelectric actuator and aerodynamic loads acting on the flap. In order to improve its vibratory load reduction capability, blade design optimization is conduced. First, multibody dynamic analysis is performed to determine the influence of the flap dimension and location within the rotor

blade upon the hub vibratory load reduction. Second, numerical optimization technique is applied to improve the blade sectional design. The cross sectional optimization framework using the genetic algorithm is established and extracts improved design, such as the decreased first torsional frequency and the reduced blade weight. The structural integrity of the present blade is evaluated in various ways. The strain recovery analysis is conducted and the in-plane stress near the blade root is estimated. Furthermore, the three-dimensional static structural analysis including the hub, blade and detailed flap-driving component is performed by considering the external aerodynamic/centrifugal loading and the practical contact condition among those components. The present flap-driving mechanism is fabricated and its flap deflection is measured by a static bench experiment, however excluding aerodynamic and centrifugal loads. In addition, a virtual centrifugal load is applied on the flap, and the flap deflection under such condition is monitored during the required operation duration. Finally, system identification of the present SNUF rotor system is conducted and a continuous-time higher harmonic control compensator is designed. Stability and the vibratory load reduction capability of the controller are demonstrated analytically.

Keywords: Hub Vibratory Load Reduction, Active Trailing-edge Flap, Blade Design Optimization, Endurance Experiment, Closed-Loop Control

Student Number: 2012-20868

Contents

Page

Abstract.....i

Contents..... iii

List of Tables..... viii

List of Figures.....x

Chpater 1 Introduction.....1

1.1 Background 1

1.1.1 Introduction to Vibration in Helicopters.....2

1.1.2 Methodology for Vibration Reduction.....5

1.1.2.1 Passive Method 6

1.1.2.2 Active Method.....8

1.2 Literature Survey Relevant to the Dissertation.....17

1.2.1 University of Maryland.....18

1.2.1.1 Piezoelectric Bimorph Actuator 18

1.2.1.2 Piezoelectric Stack Actuator 21

1.2.2 Massachusetts Institute of Technology 22

1.2.3 McDonnell-Douglas and Boeing companies 24

1.2.4 US Army Aviation RD&E Center.....27

1.2.5 University of Michigan.....28

1.2.6 Advanced Technology Institute of Commuter-helicopter, Ltd. (ATIC)

.....29
1.2.7 Eurocopter 30
1.2.8 The Pennsylvania State University 32
1.2.9 Office National d'Études et de Recherches Aérospatiales (ONERA) 34
1.2.10 Japan Aerospace Exploration Agency (JAXA).....34
1.2.11 US Army Research, Development, and Engineering Command (AMRDEC) 36
1.2.12 Korea Aerospace Research Institute (KARI).....36
1.3 Aims and Scope 37
1.4 Outline of Dissertation 40
Chpater 2 Further Improvement in the SNUF Blade Design 42
2.1 Previous SNUF Design and Experimental Results.....42
2.1.1 SNUF Development History.....42
2.1.2 Flap-Driving Mechanism Improvements.....44
2.1.2.1 Evolution of the Flap-Driving Design.....44
2.1.2.2 Previous Bench Test Results 46
2.1.3 SNUF Blade Configuration Revision 47
2.1.3.1 Blade Planform Modification.....47
2.1.3.2 Detailed Root Design 48
2.2 Multidisplinary Design for Flap Driving Mechanism 51
2.2.1 Hinge Moment Estimation.....51

2.2.1.1 Analytic method for hinge moment prediction 51
2.2.1.2 Computational Fluid Dynamics (CFD) estimation 54
2.2.1.3 Numerical Estimation of the Hinge Moment 57
2.2.2 Flap Driving Mechanism Design 60
2.3 Design Optimization Strategy 66
2.3.1 Blade Planform Parametric Study.....67
2.3.1.1 Theoretical Background of Multibody Dynamics.....67
2.3.1.2 Multibody Dynamic Modeling for SNUF blade 71
2.3.1.3 Parametric Study for the Shape of the Trailing-edge Flap 76
2.3.2 Optimization for the Blade Cross Section 77
2.3.2.1 Optimization Method by the Genetic Algorithm.....78
2.3.2.2 Cross Sectional Analysis of Composite Rotor Blade 79
2.3.2.3 Framework Development for the Cross Sectional Design 82
2.4 Numerical Investigation on Design Optimization 89
2.4.1 Vibratory Loads Reduction Preliminary Analysis 89
2.4.2 Forward Flight Baseline Condition Selection.....95
2.4.3 Effect of the Flap Shape Parameters.....98
2.4.3.1 Case 1: Flap Center location Change 99
2.4.3.2 Case 2: Flap Length Change 102
2.4.3.3 Case 3: Flap Chord Length Change 106
2.4.4 Blade Cross Sectional Design Results.....109
2.4.5 Vibratory Load Reduction Capability.....116

Chpater 3 Evaluation on the Structural Integrity of the Composite Blade.....126

3.1 Strain Recovery Analysis within the Cross Section 126

3.2 Two Dimensional In-plane Stress Estimation.....133

3.3 Three-dimensional Static Structural Analysis 136

3.3.1 Three-dimensional Modeling of the SNUF Blade 138

3.3.2 Loading Condition for the Three-dimensional Analysis.....143

3.3.3 Stress/Strain Distribution in the Composite Blade 145

Chpater 4 Static Bench and Endurance Experiments on the Present Flap-driving Components.....163

4.1 Fabrication of the Flap-driving Components.....164

4.1.1 Guide Component for the Stoke Conservation 164

4.1.2 Thrust Bearing for the Flap Deflection.....168

4.1.3 Prototype Flap-driving Components Fabrication 170

4.2 Static Bench Experiment 172

4.2.1 Experimental Setup for Bench Test 172

4.2.1.1 Drive System.....174

4.2.1.2 Measurement System 175

4.2.2 Static Bench Experiment Results.....177

4.3 Endurance Experiment 178

4.3.1 Endurance Experiment Set-up including Centrifugal Loading.....179

4.3.2 Flap Deflection Measurement Results.....182

Chpater 5 Active Flap Closed-loop Controller for Vibration Reduction in Forward Flight 185

5.1 System Identification of the SNUF rotor system in Forward Flight ... 185

5.1.1 Linear time periodic system [168] 186

5.1.2 Input Data Requirements 189

5.1.3 System Identification Result of the SNUF Rotor System 194

5.2 Closed-loop Controller Design 198

5.2.1 Discrete-time HHC Algorithm 199

5.2.2 HHC Algorithm Implementation for Vibration Reduction 201

5.2.3 Continuous-time HHC algorithm 202

5.3 Implementation of the Closed-loop Controller 205

5.3.1 Stability Evaluation of the Closed-loop System 205

5.3.2 Numerical Simulation of the Closed-loop Controller 210

5.4 Flap-driving Mechanism Representation 212

Chpater 6 Conclusion 217

6.1 Summary 217

6.2 Contribution of the Present Work 219

6.3 Future Works 222

Reference 224

국문초록 251

List of Tables

Page

Table 2.1 Flap deflection results of the previous flap-driving mechanism 46

Table 2.2 Revised SNUF blade specification.....48

Table 2.3 CFD analysis condition 58

Table 2.4 Properties of various APA actuators 65

Table 2.5 Degree of freedom by SNUF multibody modeling 73

Table 2.6 Setting for the flap shape parametric study 76

Table 2.7 Spanwise regions for cross-sectional analysis.....80

Table 2.8 Design Variables Used in the Present Optimization.....86

Table 2.9 Material Properties Used in the Present Design 87

Table 2.10 Forward flight conditions for the baseline study 96

Table 2.11 Trim target for the forward flight 96

Table 2.12 Constraints and optimized values.....109

Table 2.13 Design optimization results 113

Table 3.1 Locations and types of sections used in the strain recovery analysis 128

Table 3.2 SNUF components used in the contact analysis.....139

Table 3.3 Contact table at the flexure-blade root connection.....141

Table 4.1 SNUF components used in the guide analysis 165

Table 4.2 Contact table in Case A 166

Table 4.3 Contact table in Case B 166

Table 4.4 Properties of the various thrust bearings 170

Table 4.5 Comparison of the amplifiers possibly used 175

Table 4.6 Flap deflection results of the present static bench experiment.....178

Table 4.7 Flap deflection results of the present static bench experiment.....180

List of Figures

Page

Fig. 1.1 Trend of the helicopter vibration level....3

Fig. 1.2 Complex aerodynamic environment of a helicopter....4

Fig. 1.3 Methods used for helicopter vibration reduction....6

Fig. 1.4 Schematics of dynamic vibration absorber....7

Fig. 1.5 Application of ACSR to EH-101 9

Fig. 1.6 Schematic diagram for ASCR....10

Fig. 1.7 Schematics of the higher harmonic control 10

Fig. 1.8 Schematics of the individual blade control....12

Fig. 1.9 Schematics of the active twist rotor....15

Fig. 1.10 Schematics of the active trailing-edge flap rotor 16

Fig. 1.11 Types of the trailing-edge flap 18

Fig. 1.12 Tapered piezoelectric bimorph actuated trailing-edge flap [83] 20

Fig. 1.13 Integrated mechanical amplifier for a stack actuator [87] 22

Fig. 1.14 X-frame actuation system [98] 24

Fig. 1.15 The SMART rotor system in the NASA wind tunnel [106].....27

Fig. 1.16 PZT bimorph bender and elevon mechanism [108].....28

Fig. 1.17 Serial C-block actuator [111].....29

Fig. 1.18 Piezoelectric actuated trailing-edge flap by Eurocopter [114].....31

Fig. 1.19 Penn State's induced-shear piezoelectric actuator [117].....33

Fig. 1.20 Blade with the flap-driving components [118] 35
Fig. 1.21 The piezoelectric based active elevon [124].....36
Fig. 2.1 SNUF research flow diagram 43
Fig. 2.2 Previous flap-driving mechanisms for SNUF.....45
Fig. 2.3 CAD drawing of the hingeless hub.....49
Fig. 2.4 SNUF blade planform.....49
Fig. 2.5 Blade root reinforcement layup pattern 50
Fig. 2.6 Sign convections of a hinged airfoil 52
Fig. 2.7 Analytical hinge moment characteristics of a plain trailing-edge flap [143].....53
Fig. 2.8 CFD analysis grid for airfoil with the trailing-edge flap 55
Fig. 2.9 y^+ value on the wall.....58
Fig. 2.10 Hinge moment coefficient by the flap actuation at 65 Hz, ±4°.....59
Fig. 2.11 Hinge moment coefficients of the analytic formulation and the unsteady CFD analysis.....60
Fig. 2.12 Actuator operation under specific situations.....61
Fig. 2.13 Flap-driving mechanism schematic diagram 61
Fig. 2.14 Flap deflection under specific situation 63
Fig. 2.15 Required input voltage according to the length of the moment arm65
Fig. 2.16 Revised flap-driving mechanism design.....66
Fig. 2.17 Six lower pairs of joint in DYMORE [146] 67
Fig. 2.18 Reference and deformed configuration [146].....69

Fig. 2.19 Multibody modeling of the SNUF blade 72
Fig. 2.20 Maximum flap azimuthal location for an IBC mode with 3/rev actuation frequency 74
Fig. 2.21 Pitch link and pitch horn.....75
Fig. 2.22 Root retention geometry 81
Fig. 2.23 Flexure geometry.....82
Fig. 2.24 Blade geometry.....83
Fig. 2.25 Flowchart of the SNUF blade design optimization [140].....84
Fig. 2.26 Design variables used in the present optimization.....85
Fig. 2.27 Flowchart of the three-dimensional strain recovery analysis module 88
Fig. 2.28 Preliminary trim analysis results 91
Fig. 2.29 Hub vertical shear load of preliminary trim analysis.....92
Fig. 2.30 4P hub vibratory loads of the preliminary analysis.....93
Fig. 2.31 Fluctuation of 4/rev hub vibratory loads of the preliminary analysis 94
Fig. 2.32 Variation of 4/rev hub shear vibratory moments of the preliminary analysis.....95
Fig. 2.33 4/rev hub vibratory load results for the forward flight conditions...97
Fig. 2.34 Vibration quality criterion for the forward flight conditions 98
Fig. 2.35 4/rev hub vibratory loads according to flap center location 100
Fig. 2.36 4/rev hub vibratory moment according to flap center location.....101

Fig. 2.37 Vibration index according to flap center location.....102
Fig. 2.38 4/rev hub vibratory loads according to flap length.....103
Fig. 2.39 4/rev hub vibratory moment according to flap length 104
Fig. 2.40 Vibration index according to flap length 105
Fig. 2.41 4/rev hub vibratory loads according to flap chord length.....107
Fig. 2.42 4/rev hub vibratory moment according to flap chord length 108
Fig. 2.43 Vibration index according to flap chord length 109
Fig. 2.44 Comparison of the natural frequencies between the previous SNUF blade and the present.....110
Fig. 2.45 Final cross-sectional design configuration of the SNUF blade 112
Fig. 2.46 Blade internal load distributions.....115
Fig. 2.47 Strain recovery analysis results.....116
Fig. 2.48 4/rev hub forward vibratory shear loads.....120
Fig. 2.49 4/rev hub sideward vibratory shear loads 121
Fig. 2.50 4/rev hub vertical vibratory shear loads.....122
Fig. 2.51 4/rev hub vibratory chord bending moments.....123
Fig. 2.52 4/rev hub vibratory flap bending moments.....124
Fig. 2.53 Vibration index for 4P hub vibratory loads.....125
Fig. 3.1 Stiffness properties of optimized SNUF blade 127
Fig. 3.2 Blade root cross section (Section B1).....129
Fig. 3.3 Blade standard section (Section B5).....129
Fig. 3.4 Blade special section (Section B7) 130

Fig. 3.5 Strain margin of safety at the blade root section.....131
Fig. 3.6 Strain margin of safety at the 33%*R* section.....132
Fig. 3.7 Strain margin of safety at the 75%*R* section.....133
Fig. 3.8 Flexure – blade root connection 134
Fig. 3.9 Three basic in-plane failure modes of the pin-loaded joints.....134
Fig. 3.10 Illustration of the cosine radial stresses near the circular pin 135
Fig. 3.11 Loading condition at the blade root 136
Fig. 3.12 Radial stress distribution around a pin hole.....137
Fig. 3.13 Three-dimensional configuration of the SNUF blade.....138
Fig. 3.14 Contact and glue condition at the flexure-root connection.....141
Fig. 3.15 Contact locations within the flap-driving components 142
Fig. 3.16 Blade root boundary condition 142
Fig. 3.17 Guide and hinge mount attachment condition 143
Fig. 3.18 Aerodynamic load distribution for the present SNUF blade.....144
Fig. 3.19 Sectional aerodynamic load distribution within the SNUF finite element analysis 145
Fig. 3.20 Stress margin distribution on the root retention.....146
Fig. 3.21 Stress margin distribution on the roving.....146
Fig. 3.22 Stress margin distribution on the root plate 146
Fig. 3.23 Stress margin distribution on the flap-driving components.....147
Fig. 3.24 Longitudinal strain margin distribution on the blade root 149
Fig. 3.25 Transverse strain margin distribution on the blade root.....150

Fig. 3.26 Shear strain margin distribution on the blade root.....151

Fig. 3.27 Longitudinal strain margin distribution on the blade transition.....152

Fig. 3.28 Transverse strain margin distribution on the blade transition.....153

Fig. 3.29 Shear strain margin distribution on the blade transition 154

Fig. 3.30 Longitudinal strain margin distribution on the upper blade skin...157

Fig. 3.31 Transverse strain margin distribution on the upper blade skin 158

Fig. 3.32 Shear strain margin distribution on the upper blade skin 159

Fig. 3.33 Longitudinal strain margin distribution on the lower blade skin...160

Fig. 3.34 Transverse strain margin distribution on the lower blade skin 161

Fig. 3.35 Shear strain margin distribution on the lower blade skin 162

Fig. 4.1 Exertion of the centrifugal loads on the actuator.....165

Fig. 4.2 Deflection result for Case A 167

Fig. 4.3 Deflection result for Case B 167

Fig. 4.4 Detailed drawing of the linear bushing.....168

Fig. 4.5 Fabricated flap-driving components 170

Fig. 4.6 Thrust bearing mounted between the hinge and flap 171

Fig. 4.7 Flap horn component for adjustment of the moment arm 171

Fig. 4.8 Experimental set-up for SNUF flap-driving components.....172

Fig. 4.9 Block diagram of the experimental set-up.....173

Fig. 4.10 Flap deflection measurement.....176

Fig. 4.11 Deflection angle measurement with dynamic voltage input, 150 $V_{peak\text{-}peak}$.....178

Fig. 4.12 Schematic of the centrifugal loading condition 180
Fig. 4.13 Test bed with the ball screw type electric cylinder and the servo motor 181
Fig. 4.14 Endurance experiment set-up.....181
Fig. 4.15 Flap deflection measurement.....183
Fig. 4.16 FFT results of the flap deflection.....183
Fig. 4.17 Flap drift measurement.....184
Fig. 4.18 FFT results of the flap drift.....184
Fig. 5.1 Flap deflection chirp signals for each trailing-edge flap 193
Fig. 5.2 Time history of hub vertical shear loads from which the baseline loads are subtracted 194
Fig. 5.3 Five harmonic transfer functions estimated for hub vertical shear load 196
Fig. 5.4 Component remaining from the original response after subtracting the one represented by G_0 197
Fig. 5.5 Schematic of the higher harmonic control architecture implemented on a helicopter.....199
Fig. 5.6 Continuous-time higher harmonic control architecture [169] 203
Fig. 5.7 Block diagram of the classical disturbance rejection representation 203
Fig. 5.8 Block diagram of the standard cascade compensation and unity feedback system 205

Fig. 5.9 Bode plot of the closed-loop transfer function and sensitivity 207

Fig. 5.10 Nichols plot of the loop transfer functions according to the control gain k=0.5, 1.0 and 2.0.....208

Fig. 5.11 Nichols plot of the loop transfer functions with the control gain k=1.0 and 18.0.....210

Fig. 5.12 Hub vertical shear loads for μ = 0.3, α_s = -6° and C_T/σ = 0.060 without and with the closed-loop controller.....215

Fig. 5.13 Input and output responses of the flap-driving mechanism at 65.0 Hz (3/rev).....216

Chpater 1

Introduction

1.1 Background

Rotorcraft is one of vertical take-off and landing (VTOL) aircrafts. Owing to its VTOL capability, rotorcraft is capable of performing unique missions such as high altitude rescue, firefighting, and police patrols in the city. However, rotorcraft has several shortcomings such as poor ride quality due to high vibration levels, short lives of structural components due to fatigue, high levels of noise, limited flight envelopes, and high operating costs. Those shortcomings of rotorcraft originate from its lift generation mechanism. The lift generation mechanism of the rotorcraft is different from that of the conventional fixed wing airplane. Helicopter rotor generates lift by rotating blades, while fixed wing airplanes does it by the propulsive force from jet engines. Due to the rotation of blades, each radial station of a rotor blade experiences different incoming freestream speed. Thus, aerodynamic forces acting on the blade are proportional to the cube of blade radial distance. Furthermore, when it is related with the forward flight speed, incoming free stream speed distribution around the rotor disk will become further complicated. As a result, the aerodynamic environment of rotorcraft becomes quite complex, especially for forward flight

condition.

The current chapter describes the main sources of vibration in rotorcraft and various techniques currently being used to reduce vibration. Different methods available for vibration reduction are classified depending upon their nature (active/passive) and implementation (components of the helicopter that it influences). Based on the literature survey, key areas where further improvement can be made in the vibration reduction techniques are identified and those provides motivation for the present dissertation. Finally, an outline of the dissertation is presented.

1.1.1 Introduction to Vibration in Helicopters

Vibration in helicopters leads to passenger/pilot discomfort and fatigue and it affects the reliability and fatigue life of the airframe and its components. Other effects of vibration are reduced weapon effectiveness, difficulty in reading instruments, etc. A study conducted by Sikorsky Aircraft in 1973 [1] showed that reduction in vibration could significantly improve the reliability and reduce the costs associated with maintenance and life cycle. The current requirement for the overall vibration in helicopters (approximately 0.05g to 0.1g) [2] is specified to be significantly larger than those for a fixed-wing aircraft (0.01g) [3]. Such high vibration level does not satisfy the ‘jet smooth ride condition’ shown in Fig. 1.1 [4] and it causes discomfort of the occupants.

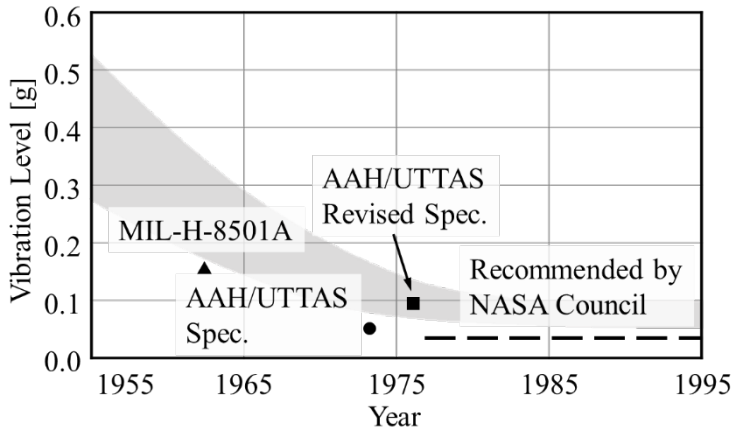

Fig. 1.1 Trend of the helicopter vibration level

In reality the rotorcraft vibration is a major cause of increased operating and maintenance costs by shortening the mean time between failures (MTBF) of the rotor components.

The main sources of vibration in a helicopter are the main rotor, tail rotor, engine, gearbox and fuselage. Among those, the most dominant source of vibration is the main rotor. The vibratory loads are produced by the main rotor in the rotating frame. However, when the loads are transferred to the hub or the fuselage in the fixed system, only the loads corresponding to the N_b/rev frequency are observed, where N_b is the number of rotor blades. Thus, the rotor acts as a filter for the vibratory loads. The tail rotor, engine and gearbox also generate a certain amount of vibration. The tail rotor blade is a source of vibration in the tail boom. The dynamic components such as engine and gearbox rotate at a high speed within a predetermined number of revolution during flight operation, resulting in high frequency vibratory loads.

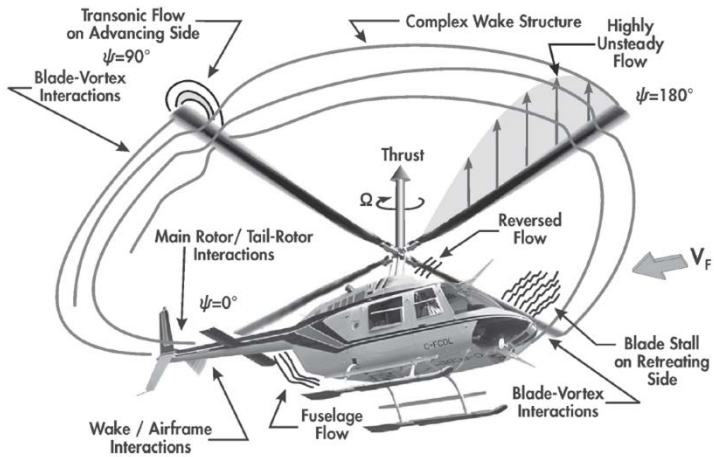

Fig. 1.2 Complex aerodynamic environment of a helicopter

The main rotor blade in a helicopter experiences highly unsteady aerodynamic loads [5] as shown in the Fig. 1.2, in addition to the time varying pitch angles. For a rotor in forward flight, the advancing side of the blade experiences different aerodynamic conditions as compared to the retreating side. On the advancing side, highly unsteady aerodynamic loads are produced due to the blade-vortex interactions. That occurs when the rotating blades encounter tip vortices shed by the preceding blades. The effects of blade-vortex interaction are more pronounced at low forward flight speeds (μ = 0.15). At higher advance ratios (μ = 0.35), quite high Mach numbers are observed at the blade tip on the advancing side, and the flow will reach transonic conditions (supercritical flow). On the retreating side, the dynamic stall condition is observed which is characterized by flow separation. Also, near the root section on the retreating side, reverse flow occurs in the region where the rotational speed at a radial

location is smaller than the forward flight speed. In that region, the flow over the airfoil section is from the trailing edge to the leading edge. In addition to those, the finite length of the rotor blade results in tip vortices, as in a fixed wing aircraft. In the case of an articulated rotor, the structural deflection in the flap, torsion and lag directions increases due to the combination of unsteady aerodynamics and blade rigid body rotation. And, in the hingeless or bearingless rotors, flexible blade root induces the similar level of elastic deflection, and geometric nonlinearity will be significant by such deflection. Those behaviors of the rotor blades lead to the generation of significant oscillatory loads. In this dissertation, the main focus will be on main rotor hub vibratory reduction.

1.1.2 Methodology for Vibration Reduction

From the earliest days of rotorcraft development, the problem of vibration has been a serious concern. In the quite early study [6], researchers identified three different approaches to obtain vibration reduction, namely: a) by minimizing the source of vibration, b) by reducing the response of the structure to the vibration, and c) by isolating the structure from the source of vibration. Based on those approaches, the vibration reduction can be implemented by both passive and active techniques. Different methods for vibration reduction that have been discussed in the literature are summarized in Fig. 1.3.

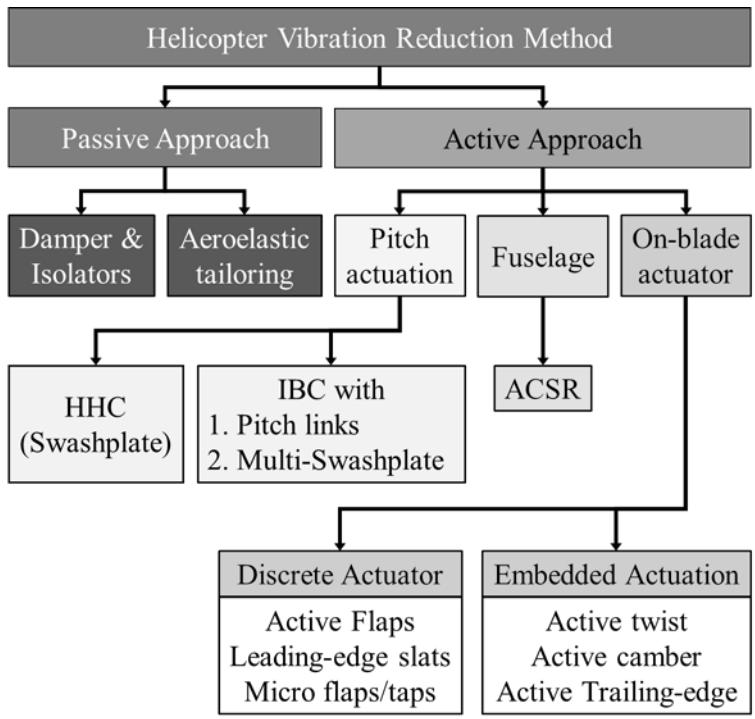

Fig. 1.3 Methods used for helicopter vibration reduction

1.1.2.1 Passive Method

Variety of passive control devices were tested and used in helicopter mainly for vibration reduction. Those passive devices can be grouped into major categories: dynamic vibration absorber and the vibration isolation mounts. The dynamic vibration absorber consists of a single degree of freedom system with a relatively small mass attached to a spring. Schematic of the dynamic vibration absorber is shown at Fig. 1.4. If the natural frequency of the absorber is adjusted to excitation frequency, an opposing oscillatory force will be generated which

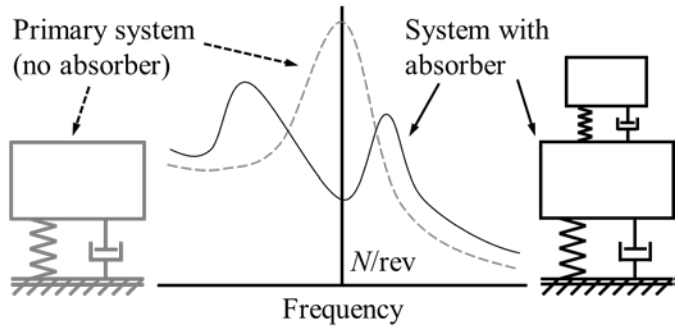

Fig. 1.4 Schematics of dynamic vibration absorber

is in resonance with excitation frequency. Dynamic hub absorbers such as simple [7] or bifilar pendulums [8] has been studied, in particular the bifilar pendulum has been applied with success to S-76 aircraft. However, actual flight tests were required to determine the final design of those devices, which were very expensive, and therefore not pursued.

Vibration isolation device is another example of widely used passive control system. Pads of rubber or springs are installed between the vibrating systems in order to reduce the transmission of vibrating forces to the support structure. Furthermore, anti-resonant principles were adopted for vibration reduction, and were proven to be successful [9-11]. However, in modern helicopters, elastomeric supports are used in place of conventional transmission mounting.

Passive control also includes passive devices designed by optimization techniques [12-16]. Structural and aerodynamic tailoring of rotor blade is a good example. In addition, composite tailoring has also been conducted because composite material provides elastic couplings for potential optimal

designs, as well as providing excellent opportunities for developing light weight/high stiffness structures [17-21].

The major benefit of passive control approach is that additional control power is not required for the passive control system. However, passive devices may result in a large increase of weight (up to 1% of gross weight) due to the additional masses that may be used. Furthermore, complex mechanical parts are usually attached to the rotating system or hub, which inevitably increase rotorcraft drag. The major disadvantage of passive system is the lack of adaptability. Passive system is tuned to or optimized for specific operating conditions, therefore, if there is a change in flight conditions, rotational frequency, or system dynamics (for example, cargo, fuel, and passenger), passive systems are likely to show limited performance.

1.1.2.2 Active Method

When comparing the principles between the passive / active control devices, one can find a big difference. Passive control device operates after the vibration is generated, whereas active control generates force to counteract the vibration at the source. Thus, the active control researches primarily aim at the direct change of the excitation force. Active vibration methods may be categorized into the following two groups; 1) to attenuate the vibration in the fuselage; 2) to alleviate the vibration on the rotor before it reaches to the fuselage.

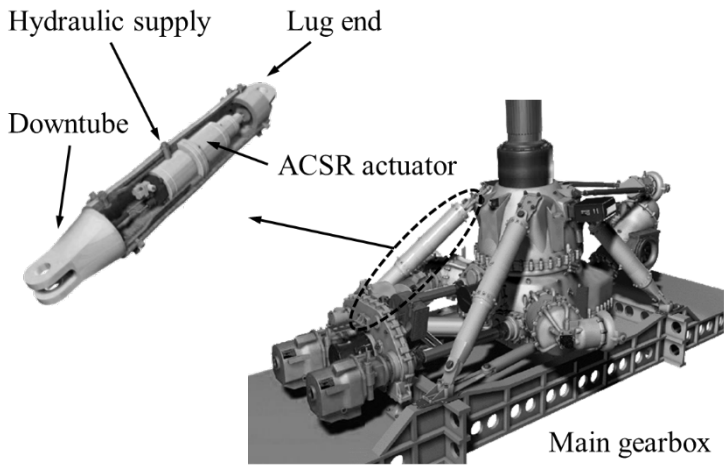

Fig. 1.5 Application of ACSR to EH-101

First, the active control of structural response (ACSR) aims to attenuate the vibration in the fuselage directly. ACSR method is based on the idea that in a linear system one superimposes two independent response quantities so that the total response may become zero [22]. Such method also shows satisfactory results of vibration reduction, and it has been incorporated in modern production helicopters such as EC-255, S-76 and EH-101 as shown in Fig. 1.5. The schematic diagram about how the ASCR operates is illustrated in Fig. 1.6.

The second category of active control approach aims to alleviate the vibratory loads induced in the rotor system directly by modifying the unsteady aerodynamic forces acting on it. Among various methods suggested, higher harmonic control (HHC) seems to be the most feasible solution. In HHC, servo-actuators are used to excite conventional swash plate in all cyclic modes at the frequency of N_b/rev (Fig. 1.7).

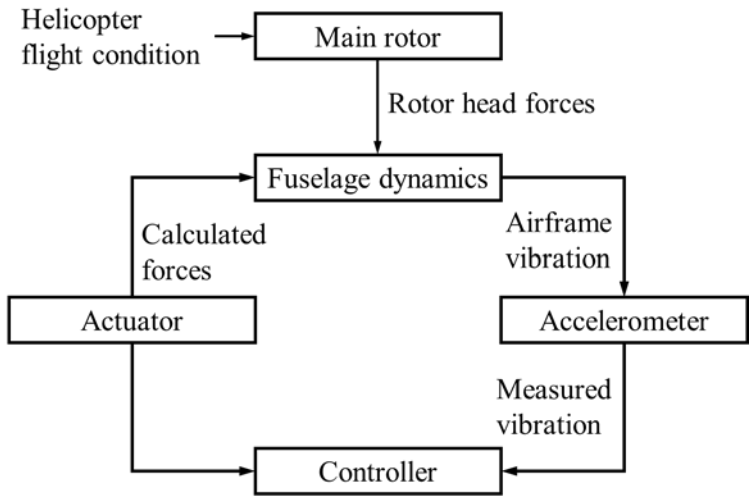

Fig. 1.6 Schematic diagram for ASCR

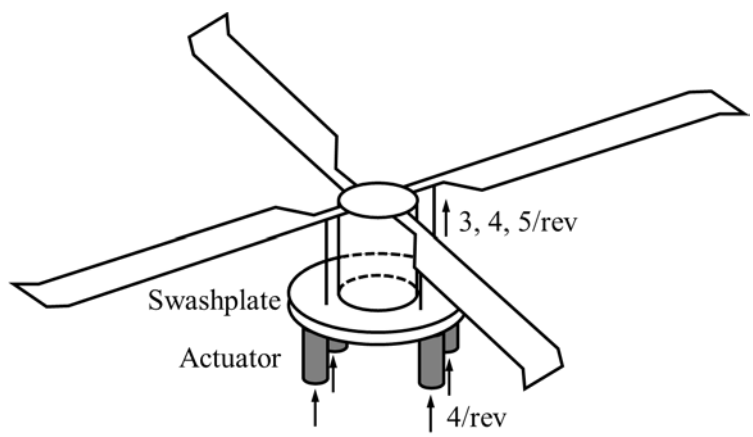

Fig. 1.7 Schematics of the higher harmonic control

Due to the excitation on the entire cyclic mode, pitching oscillation at the three frequencies, (N_b−1)/rev, N_b /rev, (N_b+1)/rev, will be generated in the rotating frame. As a result of HHC blade pitch motions, additional unsteady aerodynamic and oscillatory inertial loads will be generated, which are used to alleviate hub vibration. Therefore, the vibration propagating to the fuselage can

be reduced at its source. Throughout many research attempts, for example, numerical simulations [23-27], full scale wind tunnel tests [28-34], and full-scale flight tests [35-37], remarkable vibration reduction has been demonstrated with HHC. The pitch input magnitude required for HHC was less than 3°, in general. Even though noticeable reduction in vibration could be achieved using HHC, two major disadvantages still remain:

- High actuation power required to excite the entire rotor blades at N_b/rev

Significant weight penalty associated with the hydraulic actuators to provide higher control authority

Moreover, an additional drawback comes from the fact that only single excitation frequency (N_b/rev) of the swash plate is available for reduction of the N_b/rev vibration in the fixed frame. However, if HHC control needs to be used for other purposes such as stall alleviation or blade loads reduction, the excitation of entire blades at the other harmonics may be necessary. That is not possible using HHC, because non−N_b/rev swashplate excitation would result in blade response close to that of dissimilar blades, which would create a large 1/rev in the fixed frame.

Individual blade control (IBC) concept was proposed as an extension of HHC concept to overcome the limitation to single frequency (N_b/rev) swash plate excitation. By that method each blade is excited with actuator in the rotating frame, as compared to the HHC concept where the entire swash plate is actuated in the fixed frame. Therefore, an IBC has the advantage of varying the blade

excitation frequency, which enables those types of systems to be used for various applications such as noise reduction, lag damping augmentation, and stall flutter suppression. One important thing to note is that not only the actuation mechanism for each individual blade but also feedback control system of each blade is considered as an integral part of that concept. A conventional IBC concept, referred to as individual blade pitch actuation, has been extensively studied to date. In that concept, hydraulic actuators are installed between pitch link and swashplate (Fig. 1.8). The power to drive hydraulic actuator is provided with by slip ring unit.

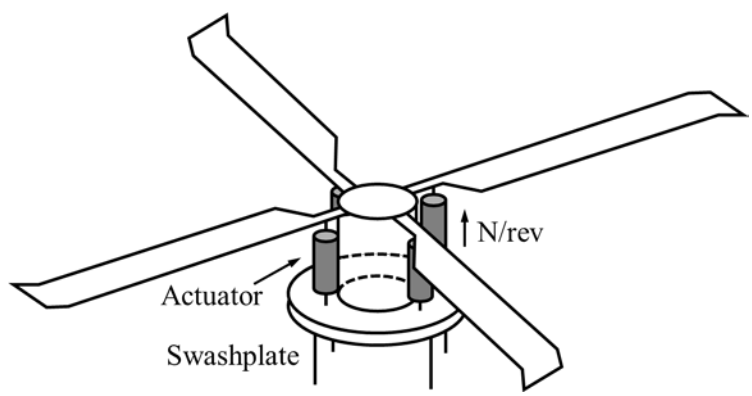

Fig. 1.8 Schematics of the individual blade control

Initially, the conventional IBC concept was developed for other purposes rather than vibration reduction [38]. An early study by Guinn [39] addressed a practical design consideration of conventional IBC concept to helicopter blade. Significant research progress on conventional IBC concept was also made by Ham [40, 41]. In that system, hydraulic actuators were mounted on the pitch

links to independently control each blade and the control system for the actuators was designed with the feedback signal from on-blade measurements to control the response of the blade first elastic flapwise mode of blade dynamics. Considerable effort has been made towards the practical implementation of IBC by the helicopter industry. The three major bodies of work in that area are:

- An IBC composed of hydraulic actuators was developed and extensively tested both in wind tunnel and in flight on a BO-105 helicopter [42-46]. Such 4-bladed hingeless rotor test was conducted for a single frequency, in an open loop configuration. Using a 2/rev blade pitch actuation, significant reduction of vibration and noise levels was achieved significant weight penalty associated with the hydraulic actuators to provide higher control authority
- Similar blade root actuation system was also installed on the Sikorsky UH-60 [47]. That system was developed under a joint research program by ZF Luftfahrttechnik (ZFL) in Germany, NASA Ames Research Center, and Sikorsky Aircraft Co.
- An experimental IBC system on CH-53G was developed, extensively tested, and certified by ZFL [48-51]. For the 6-bladed articulated rotor, more than 60% of vibration reduction was achieved with an open loop configuration using a 5/rev IBC input. The reduction in required rotor power as well as noise level was also demonstrated using 2/rev IBC inputs.

The IBC technique exhibits the possibilities for multiple objectives like vibration reduction, noise reduction and rotor performance enhancement. However, the conventional IBC using blade pitch actuation requires a heavy and complex hydraulic slip ring, which makes it impractical to implement on production helicopter. Besides, large actuation power is needed to pitch the entire blade with desired high frequencies. Moreover, conventional IBC concept was implemented on the top of the conventional swashplate, the airworthiness of the helicopter needed to be re-evaluated. In order to overcome such drawbacks, recent research effort was made to implement swashplateless IBC using an electro-mechanical actuator [52].

In addition to the limitations of conventional IBC concept mentioned before, conventional IBC changes only blade root pitch, thus tailoring of unsteady airloads is only possible along with the change in azimuth. Thus, on-blade actuation concepts were studied in conjunction with the use of smart materials as an actuator. Several methods were proposed and studied for on-blade actuation, for example, active trailing edge flaps, active twist, active tips and active tabs. Among those methods, active twist rotor (ATR) have been explored for vibration reduction (Fig. 1.9).

The key component of that concept is smart materials, for example, Active Fiber Composite (AFC), Macro-Fiber Composite (MFC) and piezoelectric materials. Chen and Chopra [53, 54] implemented ATR concept with piezoelectric materials by embedding piezoelectric monolithic elements at +45°

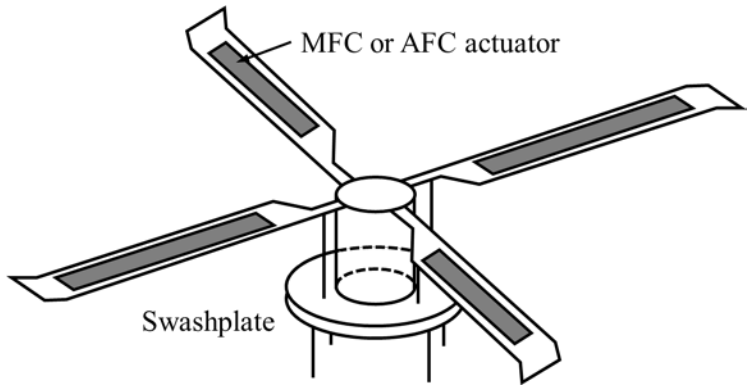

Fig. 1.9 Schematics of the active twist rotor

under the upper skin and -45° under the lower skin of the rotor blade. Blade tip twist amplitudes of 0.25° were achieved, and significant changes in the hub loads were also measured. Another way to induce blade twist is to use Active Fiber Composite (AFC) [55]. With the composite ply cured in a +45°/-45° orientation on the blade, actuation imposes a linear twist along the blade. Several research teams have tested the active blade twist concept using AFC on model scale rotors [56-60], demonstrated to achieve tip blade twists of up to ±1°. One of the advantages of ATR concept is the simplicity of actuation mechanism compared to Active Trailing-edge Flap (ATF). ATR concept also has a benefit in that it does not increase profile drag compared to active trailing-edge flap deflection, which usually produce significant drag increment as a device cost. Even though ATR concept showed promising result for vibration reduction, the power requirement for the on-blade actuators is known to be far greater than that of ATF.

Under the same IBC framework, trailing-edge flaps are deflected to generate

additional unsteady aerodynamic loads which result in blade response changes. In general, trailing-edge flap is applied to the small portion of the blade, usually at the outer board region (Fig. 1.10). Therefore much smaller power is required to deflect small trailing edge flap rather than to change root pitch of entire blade (IBC) or to actuate swashplate (HHC). Furthermore, the active flap is separated from the primary control; thus it has little interference to airworthiness of the helicopter.

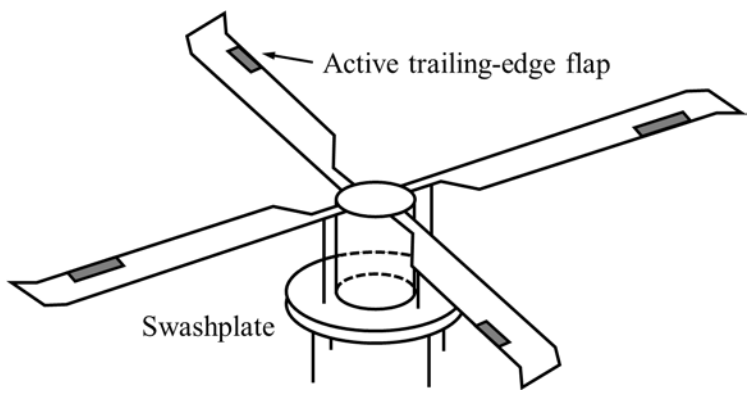

Fig. 1.10 Schematics of the active trailing-edge flap rotor

Servo flaps (moment flap) have been used for primary flight control. For example, use on-blade servo-flaps were adopted for blade pitch control in Kaman helicopters [61, 62]. The effect of servo-flaps on for vibration reduction was also investigated [63]. In their study, the flap deflection under steady and 1/rev frequency were actuated by way of swashplate, while 4/rev control was given in the rotating frame by electro-hydraulic actuators. An amplitude of 6◦ deflection at 4/rev exhibited significant vibration reduction.

For plain flaps (lift flaps; hereafter active flaps) extensive analytical studies [64-73] have been conducted. Analytic studies showed a comparable vibration reduction with respect to conventional IBC using moderate flap deflection. The experiments of active flaps for vibration were conducted on model-scale, four-bladed rotors. For the experiments at McDonnell Douglas [74-77], the flaps were actuated by mechanical devices (cam and cable linkage), while hydraulic actuators in rotating frame was used in the experiment at Sikorsky [78]. However, the weight and complexity of the actuation system still remains a major technical barrier hindering the implementation of those systems on production helicopters.

1.2 Literature Survey Relevant to the Dissertation

The use of a flap on the rotor blade was pioneered by Charles Kaman. Those flaps are still used in Kaman Helicopters. That type of flap, which the company called a servo-flap was external to the blade as shown in Fig. 1.11(a). Most active flaps use a plain flap; it forms a portion of the airfoil and is flush with the surrounding trailing edge when in the neutral position (Fig. 1.11(b)). Both of those flaps are being considered trailing edge flaps.

(a) External Flap

(b) Plain Flap

Fig. 1.11 Types of the trailing-edge flap

1.2.1 University of Maryland

The researchers in the University of Maryland has been studying helicopter blade vibration reduction using a trailing-edge flap for a long period of time, and those researches can be roughly classified into the following two types:

a) Active flap actuated by piezoelectric bimorph actuator

b) Active flap actuated by piezoelectric stack actuator

1.2.1.1 Piezoelectric Bimorph Actuator

Samak and Chopra [79, 80] developed and tested a piezoelectric bimorph actuated trailing-edge flap. The flap was powered by 3 bimorphs. A fixed wing model with trailing-edge flap was fabricated and tested in an open-jet at speeds up to 33 m/s and flap actuation frequencies of 5 Hz, 10 Hz, and 15 Hz. The flap deflection was ±7°, and it was not change appreciably with the excitation

frequency and the blade angle of attack. The system was also tested on a hover test stand, with rotational speeds of 300, 600 and 900 RPM (operating speed) and the flap actuation frequency 1 to 4/rev. At the highest RPM, the amplitude of flap deflection decreased to less than ±2° for all actuation frequencies.

Ben-Zeev and Chopra [81] expanded upon the previous bimorph [79]. The authors considered both a two-layer and four-layer bimorph. Both systems were tested in the rotating environment, via a vacuum whirl tower. The addition of a thrust bearing at the hinge point greatly reduced friction and improved performance at the rotational speed of less than 900 RPM, However, At 900 RPM the responses with both a two-layer and four-layer bimorph actuators were comparable at 0.5°.

Walz and Chopra [82] discussed the design of the four-layer bimorph used by Ben-Zeev and Chopra [81]. To analyze the various bimorph configurations, the aerodynamic hinge moments were predicted using a quasi-steady, incompressible aerodynamic model. The result of the aerodynamic analysis was that a four-layer bimorph should provide sufficient authority (10% change in lift), whereas the two-layer bimorph was unable to do so. The authors also improved upon the original mechanical design. A centered bimorph using a cusp was developed. At 4/rev actuation frequency, flap deflection increased from ±10.5° to ±17° by using the revised flap-driving mechanism.

The design of the bimorph actuator with the cusp was further refined by Koratkar and Chopra [83, 84]. The piezoelectric bimorph was tampered

amongst the various layers, as in Fig. 1.12. The 4-layered actuator used in the Froude scaled designed was replaced with an 8-layered, tapered bender. The flap deflection of over ±8° were recorded at 2000 RPM in vacuum chamber. It was predicted that the flap deflection of ±5° to ±10° could be achieved in the 1-5/rev frequency range, in hover at the Mach scaled operating speed to 2000 RPM.

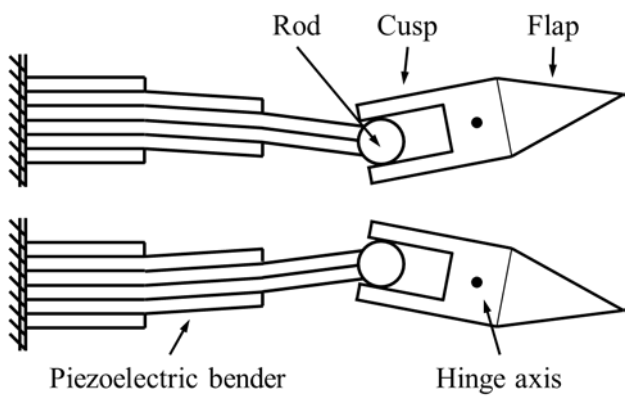

Fig. 1.12 Tapered piezoelectric bimorph actuated trailing-edge flap [83]

Koratkar and Chopra [85] also conducted a wind tunnel test of the above actuator. The operating RPM was 1800 giving a tip Mach number of 0.45. The wind tunnel itself had a top speed of 98 m/s. The blades were mounted to a 1/7th scale Bell 412 hingeless rotor hub. First open-loop testing was conducted, testing flap deflection at 3, 4 and 5/rev. At an advance ratio of 0.3, deflections ranging from ±4.1° to ±4.4° were achieved. The authors also encountered an uncommanded 1/rev flap response of ±1.5° due to blade flapping. The authority

of the actuator on the bending moment due to flapping was improved significantly for a 3/rev flap frequency. That was because the first torsional frequency of the blade was 3.13/rev. Using the neural network based controller, initial closed-loop testing indicated 39% reduction in the baseline vibration level.

1.2.1.2 Piezoelectric Stack Actuator

Spencer and Chopra [86] devised the flap-driving mechanism using a piezoelectric stack. The stack configurations have larger block forces at the expense of smaller displacements compared to the bimorphs previously considered. To drive the flap, two stacks were arranged in series. The stacks drove an L-shaped hinge, converting spanwise motion to chordwise one. Using a basic aerodynamic model, based on thin-airfoil theory, flap deflection versus air velocity was estimated. A static test showed experimental results were about 20% lower than analytical results.

Chandra and Chopra [87] improved the mechanical amplification of the stack actuator. An integrated mechanical amplifier was developed and is shown in Fig.1.13. The amplifier was a compliant mechanism with the L-arm attached via an elastic hinge. The L-arm was then attached to a pushrod, similar to Spencer and Chopra [86]. The wing model was tested in an open-jet wind tunnel. The actuator was actuated both with and without aerodynamic forces, with the

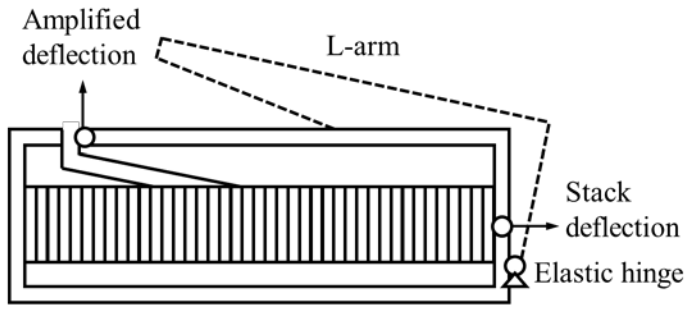

Fig. 1.13 Integrated mechanical amplifier for a stack actuator [87]

experimental values 12% and 30% lower than predicted, respectively. Without aerodynamic forces, flap deflections were about ±8° with the actuation frequency of 5 Hz.

Lee and Chopra [88-91] considered using piezoelectric stacks to drive a double lever amplification system. Stacks in series and parallel configuration were considered. The goal was to obtain a flap deflection of ±5° for a trailing-edge flap on an MD Explorer helicopter. While the actuator was not connected to any flap, it was tested both statically and in a rotating frame. The rotating frame results indicated the actuator would perform properly at full-scale centrifugal loading.

1.2.2 Massachusetts Institute of Technology

Spangler and Hall proposed trailing-edge servo-flap actuation using a piezoelectric bender actuator [92-95]. The bender was used because it was an expedient method to amplify the active material stroke. Spangler and Hall

demonstrated the feasibility of such actuation method through wind tunnel testing of an airfoil typical section. While they obtained appreciable flap deflections and force authority (±6° at 18.7 m/s test speed), they found that their design did not work entirely as expected due to hinge friction and backlash.

Hall and Prechtl [96] developed a trailing-edge flap driven by a tapered piezoelectric bender. That design had the bender beam fixed to the spar and running aft to the flap. The junction of the flap and bender was a connection of flexures. An analytical model was developed and benchtop tests conducted. The benchtop testing achieved a half-peak deflection of 11.5° at 10 Hz. The authors expected deflection (half-peak) for a full scale helicopter to be greater than 5°. Prechtl and Hall reported several results regarding an X-frame actuator [97, 98]. The actuator consisted of dual piezoelectric stacks on top of each other. The pivot end served as the hinge for the two frames. Actuating the stacks caused the two frames on the output end to move with respect to each other. For implementation in a rotor blade, the output end connected to a control rod to drive the flap as in Fig. 1.14. The actuator was tested for sensitivity to blade accelerations and only under the highest acceleration cases were there any effects noticed. Whirl tower tests showed that spinning the actuator caused no major degradation of the actuator performance [99]. Results of a hover test [97], at the maximum voltage, peak-to-peak 1200 V, the actuator produced between 5-7° (peak-to-peak) flap deflections well past 6/rev (133.6 Hz) actuation.

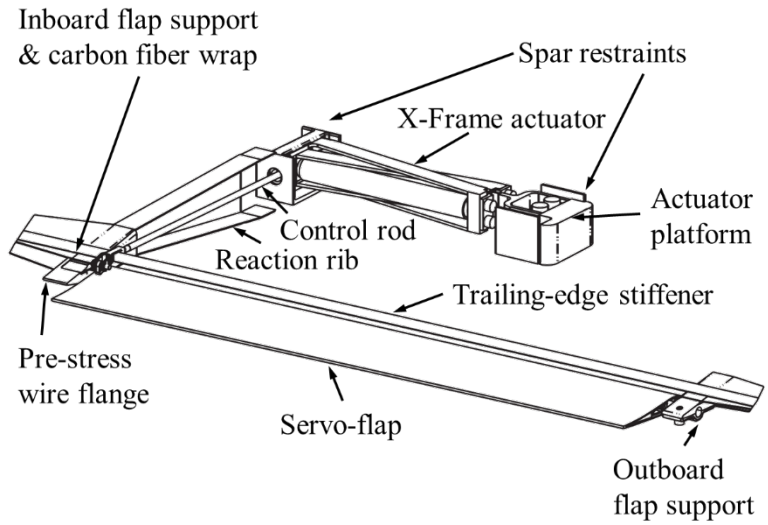

Fig. 1.14 X-frame actuation system [98]

1.2.3 McDonnell-Douglas and Boeing companies

Dawnson and Straub [100] looked at how a flap can be used to reduce rotor loads and noise. Their study considered both predicted results and compares them with tests. The test flap used a cam follower actuation system. The authors found good correlation between their predictions and the test results.

Straub reported several results regarding the use of trailing edge flaps using smart materials, a few for McDonnell-Douglas and the others for Boeing. He [101] first considered the various smart materials available as well as different actuation methods. The goal was to drive a flap that can replace the swashplate control system of the standard helicopter. The various methods considered included: pitch control, twist control, camber control, and control surfaces. The

servo-flap was considered the most feasible. Straub also considered the different smart materials available: piezoelectric materials, electrostrictive materials, magnetostrictive materials, shape memory alloys, and electrorheological fluids. Lastly, various actuator designs were considered including: bender elements, stack actuators, actuation tubes, and ultrasonic motors.

Straub and Merkley [102] considered a servo-flap (one where the flap extends beyond the airfoil) for an AH-64 helicopter. The actuation was two-part. First a piezoelectric or magnetostrictive actuator was used for cyclic and active control. A composite tube connected the actuator to a hydraulic amplification system. The composite tub had shape memory alloys for collective control. Each blade has 4 servo-flaps, located between 62% and 82% radius. Estimated flap deflection required to control the helicopter were ±7.3° collective, ±3.8° cyclic, and ±0.4° for active vibration reduction, based on flap and rotor design.

Straub and Merkley presented a paper discussing a magnetostrictive based hybrid actuator [103]. In trying to design a magnetostrictive actuator to provide cyclic and active control authority, it was found that the best the materials could manage was limited maneuvering. An initial study looked at SMAs for collective controls showed capability.

Straub et al. [104-107] participated in DARPA SMART (Smart Material Actuated Rotor Technology) program. The goal was to use smart materials to augment the traditional swashplate control system. In particular the hope was

to reduce vibration and noise. A piezoelectric actuator was chosen to drive a flap to reduce noise and vibration. A SMA actuator was chosen for blade tracking. The MD900 helicopter was chosen and testing in the NASA Ames 40 × 80 ft. wind tunnel. Goals for the program included an 80% reduction in vibrations and a 10 dB reduction in blade vortex interaction (BVI) noise. The SMA actuator would provide in-flight blade tracking, reducing vibrations.

The first actuator considered was a biaxial piezoelectric driven actuator [104, 106]. The design consisted of four stack actuators rotating an outer housing. The initial design had a second amplification stage, whereas the final design did not. The final design was expected to meet design requirements. In Phase II of the program, the actuator was switched to M.I.T.'s X-frame actuator, where both of them were used [105]. The actuator was successfully tested for 66 million cycles (560 hours at 5/rev). A whirl tower test was conducted with both static and dynamic deflections (up to 6/rev). Static flap deflection of 3° peak-to-peak was observed. Similar deflections were achieved with dynamic deflection of the flap. That level of deflection resulted in a 10% variation in thrust compared to steady state. Results from a wind tunnel test of the rotor showed BVI noise reductions on the order of 3-6 dB, with increased hub vibratory loads. Using the flaps for vibration reduction, the 1-5/rev normal hub vibrations were reduced by 95% for level and descending flight. The rotor system used for those tests is depicted in Fig. 1.15.

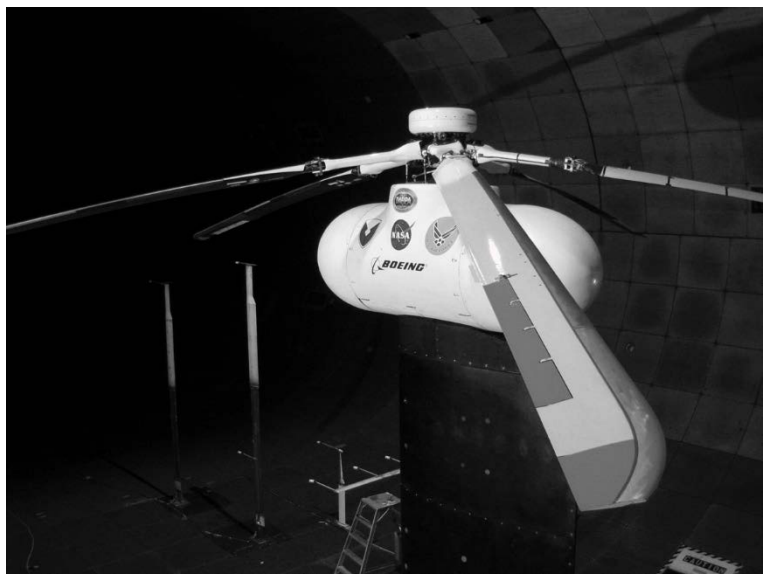

Fig. 1.15 The SMART rotor system in the NASA wind tunnel [106]

1.2.4 US Army Aviation RD&E Center

Fulton and Ormiston [108, 109] considered trailing edge flaps powered by piezoelectric bimorphs. The authors called the flap an elevon and used a piezoelectric bimorph driving a flap (Fig. 1.16) via a cusp similar to the University of Maryland [82]. Flap deflections of ±5° at 4/rev in hover were observed. Forward flight tests under various conditions were tested in wind tunnel and the 4/rev flap bending moment was reduced by 88% at the advance ratio of 0.2 and 760 RPM.

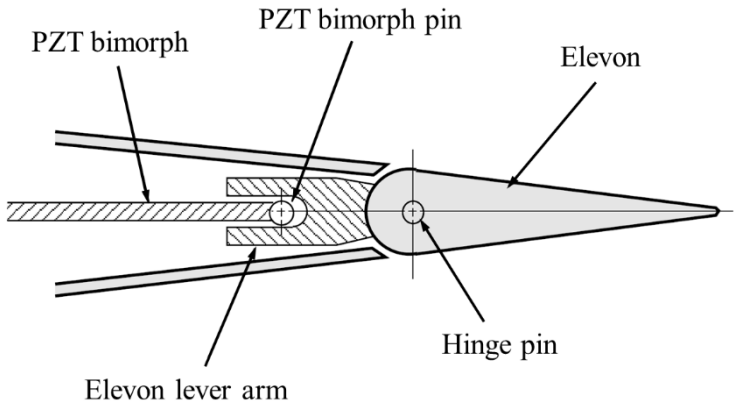

Fig. 1.16 PZT bimorph bender and elevon mechanism [108]

1.2.5 University of Michigan

Clement et al. [110, 111] considered the trailing-edge flap using what they called a C-block, a piezoelectric based actuator shown in Fig. 1.17. By coupling the C-blocks such that an undulating actuator results, the actuator provided axial motion. Static benchtop tests revealed maximum peak-to-peak deflections of 8°. Dynamic tests up to 40 Hz showed similar performance. With the tunnel running at 30.5 m/s, static peak-to-peak deflections of 9° were achieved driving the flap that was mass and aerodynamically balanced. Again, dynamic tests showed similar results. The system was not tested in the rotating frame.

Liu et al. [73] looked at rotor performance and vibration reduction achievable with trailing-edge flaps. The helicopter rotor was modeled as a hingeless blade with flapping, lead-lag, and torsion degrees all accounted for and coupled. The

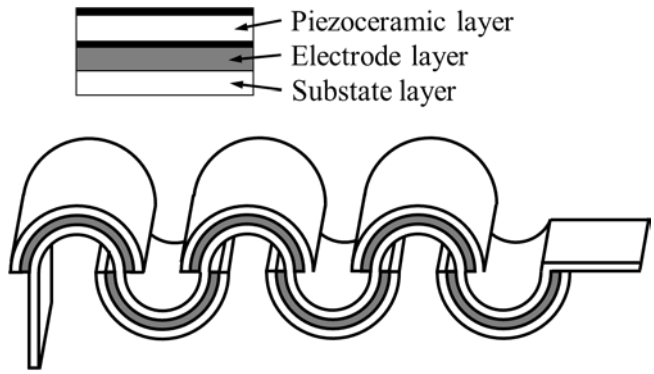

Fig. 1.17 Serial C-block actuator [111]

two-dimensional unsteady time-domain theory with compressible flow was used for aerodynamic estimation. The blade aerodynamics were coupled with the free wake model. With a separated flow, ONERA's dynamic stall model was used. Two controllers were used, the first was the HHC algorithm, which sought to reduce both vibration and noise. Flap inputs were 2/rev to 5/rev. A nonlinear least-squares optimizer found in MATLAB was also used. The rotor was based on the BO-105. At advance ratios of 0.35 and 0.40, the power reductions were 4% and 6.37%, respectively. However, those power reductions result in an increase of vibrations. Targeting both power reduction and vibration reduction, rotor power was reduce by 1% through 4% and vibration was reduced by 47% through 70%.

1.2.6 Advanced Technology Institute of Commuter-helicopter, Ltd. (ATIC)

Hongu et al. [112] considered several actuators to drive a flap. The first

concept involved twisting an aluminum plate by inducing shear with piezoelectric elements. The last concept used magnetostrictive materials with either a mechanical or hydraulic amplification. In the static condition, the aluminum and composite plate achieved flap deflections of ±7.6° and ±7.1°, respectively. Also, the hydraulic and mechanical stroke amplifications of the magnetostrictive material achieved ±3.4° and ±4.6°, respectively. A piezoelectric stack with mechanical amplification was imbedded on a wing configuration and tested in a wind tunnel. The flap deflection was ±2.3° at Mach 0.3 and deflections were only ±1.1° at Mach 0.74.

Hasegawa et al. [113] of Kawasaki Heavy Industries and in partnership with Advanced Technology Institute of Commuter-helicopter conducted a whirl test considering a trailing-edge flap. Dual piezoelectric stacks were used to drive a stoke amplification system. The actuators drove 3 different flaps, each 10% of the blade radius. Three different flap chords were considered: 10%*c*, 15%*c*, and 20%*c*. During a whirl tower test, the flap with 10%c chord had measured deflections of ±2.8° to ±3.9° for 1/rev and 5/rev actuation frequency respectively. The 20%c chord flap achieved deflections around ±1°, changing little with frequency.

1.2.7 Eurocopter

Enenkl et al. [114] described the piezoelectric actuators used in a series of

Eurocopter whirl tower and flight tests. Being located inside a whirling rotor blade placed stringent requirements on the actuation, including accepting high loading and fitting in a constrained space. Both piezoelectric and electromechanical actuators were considered, but piezoelectric was selected based on the centripetal acceleration experienced by the actuator and the zero-power stiffness. Important flap design characteristics included a frequency range of 0-40 Hz, no mechanical play, and an aerodynamically sealed flap. A monolithic co-fired multilayer stack actuator was used and amplification was required. Compliant hinges were used to provide a stroke amplification of around 10. The flap can be seen in Fig. 1.18.

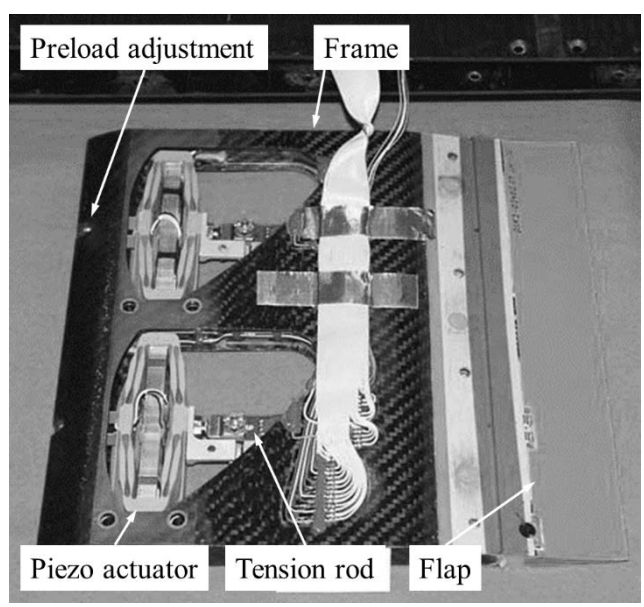

Fig. 1.18 Piezoelectric actuated trailing-edge flap by Eurocopter [114]

In 2005, Dieterich et al. [115], successfully flew a BK117 (EC145) with piezoelectric actuated trailing-edge flaps. The span locations of the units was 71.8%R to 82.7%R. A whirl tower test was conducted in 2002 and 2004. The goal was to measure blade characteristics with both static and dynamic flap actuation. The latter test was used to ensure that the rotor was ready for the flight test. The flight test showed reduction of vibration for level flight at 31 and 51 m/s, with flap deflecting ±3°.

Roth et al. [116] described the same test. The flap unit deflection angle limits were ±10°. The authors detailed the control system used in actuating the flaps as well as data acquisition. The control system targeted the 4/rev hub force and moments. In particular the roll moment, pitch moment, and vertical force were targeted. Dynamic feedback compensators were implemented to achieve that. In level flight vibration reduction between 50% and 90% were observed, the system was also effective in climb and decent at 33 m/s.

1.2.8 The Pennsylvania State University

Centolanza et al. [117] used the shear present in piezoelectric materials to create twist. The torsion of the actuator was connected to an arm that connects to the flap via a cusp, as in Fig. 1.19. A benchtop test was conducted and flap deflections from ±2.75° with no hinge moment to 1.5° for a 400 RPM equivalent hinge moment (based on the MD900) were observed. The authors

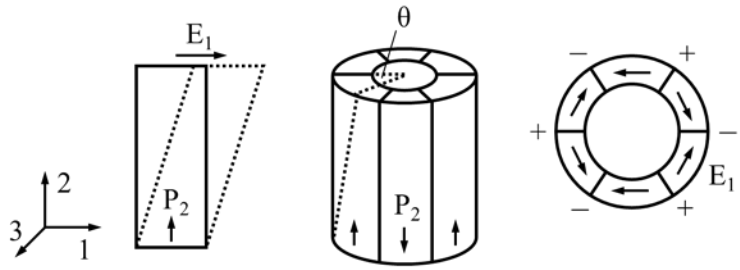

(a) Shearing piezoelectric elements resulting in torsion

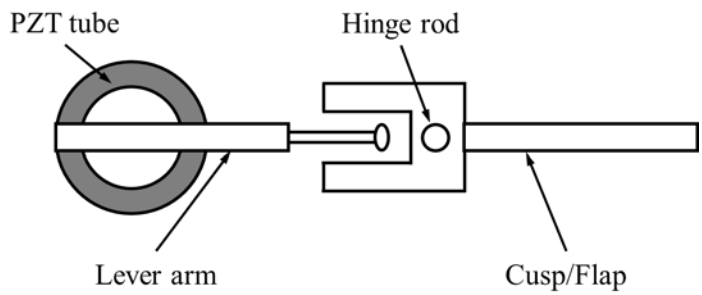

(b) Implementation of PZT tube to drive a flap

Fig. 1.19 Penn State's induced-shear piezoelectric actuator [117]

expected a future improved induced shear tube to provide similar performance to the double X-frame actuator of M.I.T., with less than half the weight.

In 2006, research by Penn State and local company Invercon considered a piezoelectric driven actuator utilizing a buckling beam [118]. Szefi et al. envisioned using a piezoelectric stack to buckle a pinned-pinned beam, with the beam's tip rotation driving the flap. Benchtop testing using both with and without aerodynamic loading resulted in deflections of 8.4° and 4°, respectively.

1.2.9 Office National d'Études et de Recherches Aérospatiales (ONERA)

ONERA conducted a study involving an Active Blade Concept (ABC) in cooperation with Eurocopter and the Deutsches Zentrum für Luft- und Raumfahrt (DLR). Leconte and Des Rochettes [119] considered the design and initial testing of the actuation system. The goal actuation was a minimum of ±5° at 5/rev. After looking at several designs, a piezoelectric stack circumscribed by an ellipse, seen in Fig. 1.20, was selected. That amplification was achieved via a compliant mechanism, providing a 2.6 amplification factor. The flap itself was connected via a compliant hinge. The actuator was tested at rest and under a 2000 g acceleration with flap peak-to-peak deflections of 6° and 5°, respectively. Low-speed wind tunnel tests showed good flap deflection values. At higher Mach numbers, it was found that the flap lacked sufficient stiffness. Using an updated actuator, wind tunnel tests were conducted [120]. The results showed the flap behaving as both a direct-lift flap and servo-flap, which was changing the local loft coefficient as well as twisting the blade.

1.2.10 Japan Aerospace Exploration Agency (JAXA)

Noboru et al. [121] used an active flap for reduction in BVI noise. The authors first worked on sizing the flap to achieve the objectives while not exceeding limitations of the actuator. The requirements for the actuator were an

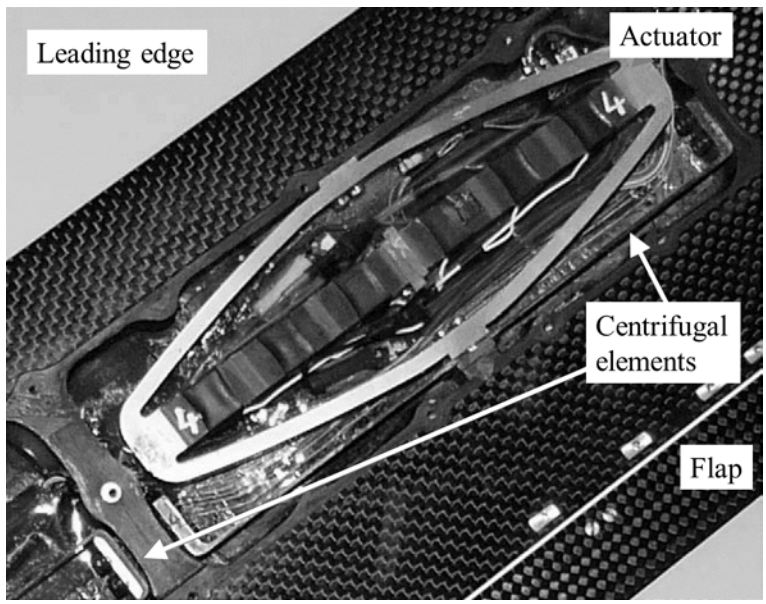

Fig. 1.20 Blade with the flap-driving components [118]

operating frequency of 2/rev and an amplitude of ±6°. Two stack actuators were used in a push-pull arrangement, thus rotating an arm. The arm drove a linkage connected to the flap's control horn. Static deflection tests indicated sufficient flap deflection. Dynamic tests revealed deflections of ±6°. Noboru and Saito [122] performed wind tunnel tests (nonrotating) of the flap. At Mach numbers of 0.47, 0.55, and 0.7, flap displaced of ±6°, ±6°, and ±3.8° were recorded at a 2/rev actuation frequency. Saito et al. [123] reported on a joint project between JAXA and NASA. The active rotor of JAXA was to be tested in the 40 by 80 ft. wind tunnel at NASA Ames.

1.2.11 US Army Research, Development, and Engineering Command (AMRDEC)

Fulton et al. [124] developed and hover tested an active elevon rotor. The deflection target of the active elevon was ±5°. The elevons were located on a 27% scaled AH-64 Apache blade, with two flaps per blade, centered at 0.64R and 0.9R, each with having a span 5%R. Figure 1.21 shows the piezoelectric material forming the lower surface of the blade, the conformal actuators were PZT based actuators, utilizing the d_{13} coupling. The actuation system consisted of an upper and lower actuators, operating in opposite directions. The elevon deflection of ±2° was measured experimentally at an RPM of 1025 at 0.41/rev.

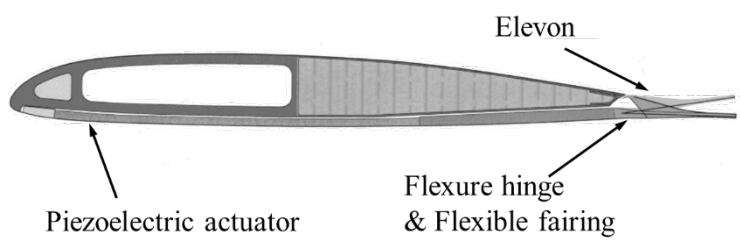

Fig. 1.21 The piezoelectric based active elevon [124]

1.2.12 Korea Aerospace Research Institute (KARI)

Jung et al. [125] carried out the ground operation and rotating performance test by mounting the active trailing-edge flap, which was driven by the

piezoelectric ceramic laminated actuator, on the NRSB-II blade [126]. The deflection of the flap actuated at 4/rev under rotation test at 830 RPM was measured to be 1.75° and the active flap control resulted in a 31% reduction in vibration level compared to the situation without the flap actuation.

1.3 Aims and Scope

The previous researches have attempted to generate the deflection of the trailing-edge flap using actuators of various materials, types, and mechanisms. And active flap systems have been implemented on the several particular rotor blades. Those earlier studies focused on reducing vibration and noise by producing the sufficient flap deflection, which was actuated certain frequencies, under desired operating conditions. In most cases, existing rotor blades were used without modification, or simple shape blades were adopted. Since the purpose of the previous studies was to reduce the vibrations of existing blade, further blade design improvement or optimization were not required. In several of the previous studies, wind tunnel experiments were carried out by changing the location of the flap, using the blade fabricated to mount the trailing-edge flap at multiple designated locations [127]. Also, Kumar developed the mixed variable optimization framework to design the blade section for three specified flap locations [128]. However, in those studies [127, 128], the effectiveness of the flap dimension was not evaluated. In addition, the stacking sequence of the

blade section was not considered as a design variable in the previous study [128], and the maximization of the dynamic twist angle at the blade tip was assigned as the objective function. As a result, vibratory vertical shear forces were increased and it was found that the control authority was expanded. However, vibration reduction results according to the various flap actuation frequencies and control phases were not presented.

From the results and restriction of those previous studies, the objective of this dissertation is derived. In this dissertation, the flap-driving mechanism that achieves the desired flap deflection angle under significant aerodynamic loads condition, will be proposed. Also, a new rotor blade design, which has improved vibration reduction capability by the active flap, will be presented. In this procedure, the blade configuration with decreased hub vibratory loads will be created considering both location and dimension of the flap. Also, a number of design variables will be considered in the blade cross sectional design optimization process, including the type of material and the stacking sequence. In it, the first torsional frequency will be restricted to be smaller than 3/rev. The SNUF (Seoul National University Flap) is an active trailing-edge flap system that has been evolved over the last decade [130-139]. However, flap deflections of those mechanisms were not sufficient even under a static bench condition, and comprehensive studies were not conducted. Therefore, further improvement of the SNUF and the detailed design of an optimum blade will be investigated in this dissertation.

First, the flap-driving mechanism of the previous design [130-135] will be revised through considering the flap aerodynamic circumstance. The computational fluid dynamics with moving grid will be adopted and flap hinge moment will be estimated. After that, vibratory load reduction analysis will be performed to investigate the influence of the dimensions and location of the trailing-edge flap within the rotor blade. In this procedure, a multibody dynamic analysis will be implemented for the modeling of the hingeless rotor blade with a flap. This will be followed by the introduction and performance of the design optimization procedure for blade sections to improve the cross-sectional design. The structural integrity will be evaluated with the optimized blade design. A three-dimensional static structural analysis will be conducted to predict the realistic stress distribution including detailed components such as the actuator, guide and push rod. The flap-driving components will be fabricated and tested. In order to ascertain the flap deflection under the centrifugal loading condition, the endurance experiment will be devised and conducted. Finally, closed-loop controller will be designed to reduce the hub vibratory load under the forward flight condition, and its performance will be evaluated numerically. All of these procedures are intended for future tensile experiments and ground rotation tests.

1.4 Outline of Dissertation

To provide an outline of this dissertation, the contents of the chapters are presented in the following

In Chapter 2, flap-driving mechanism of the previous SNUF blade and its measured flap deflection will be reported. The drawback of the previous design will be identified, and a revised blade design including the detailed root geometry will be presented.

In addition, the blade design improvement approaches will be discussed. The governing equation of the flap-driving mechanism is derived in consideration of the flap hinge moment and the characteristics of the piezoelectric actuator. And to predict more accurately the hinge moment, CFD analysis using moving grid is performed.

In the following section, design optimization strategy will be developed. The design optimization will be performed in two stage. First, the hub vibratory load reduction capability depending on the dimension and location of the trailing-edge flap will be predicted. After that, cross sectional design optimization framework using the genetic algorithm will be introduced. In addition, numerical investigation of the design optimization will be conducted.

In Chapter 3, the structural integrity of the present blade will be evaluated in

various aspects. The two dimensional in-plain and cross section stress will be obtained. Furthermore, three dimensional static structural analysis considering detailed contact conditions will be conducted including flap-driving components.

In Chapter 4, the present flap-driving mechanism will be fabricated and the flap deflection will be measured. First, in the absence of any load on the flap, the flap deflection will be measured when the piezoelectric actuator is operated. Also, to presume the rotation, a virtual centrifugal load will be applied to the flap using a weight. Under these condition, the flap deflection will be measured during the expected operating period.

In Chapter 5, the system identification of the SNUF blade will be conducted. Based on this results, the continuous-time higher harmonic control compensator will be introduced. The vibratory load reduction capability of the controller will be verified numerically.

In Chapter 6, conclusions and future works of this dissertation are included.

Chpater 2

Further Improvement in the SNUF Blade Design

2.1 Previous SNUF Design and Experimental Results

2.1.1 SNUF Development History

Figure 2.1 shows the process of designing and fabricating the SNUF blade for the whirl tower experiment, and this process is divided into three stages. The first stage is to design the flap-driving mechanism. From the initial blade shape, the hinge moment on the flap is predicted by going through the flow analysis. Considering the flap hinge moment, the flap-driving mechanism is designed and a suitable actuator is selected. The flap-driving components is fabricated and the bench experiment is performed to measure the flap deflection. If the flap deflection is sufficient, the next stage will be proceeded. Otherwise, the flap mechanism design will is revised.

In the second stage, numerical analysis is performed. The vibration reduction capability of the blade equipped with the present flap-driving mechanism is estimated. In this process, the influence of the location and dimension of the flap is evaluated, and the optimization process including the cross sectional analysis is performed. The structural integrity of the present blade and flap-

driving components is verified by the three-dimensional static structural analysis.

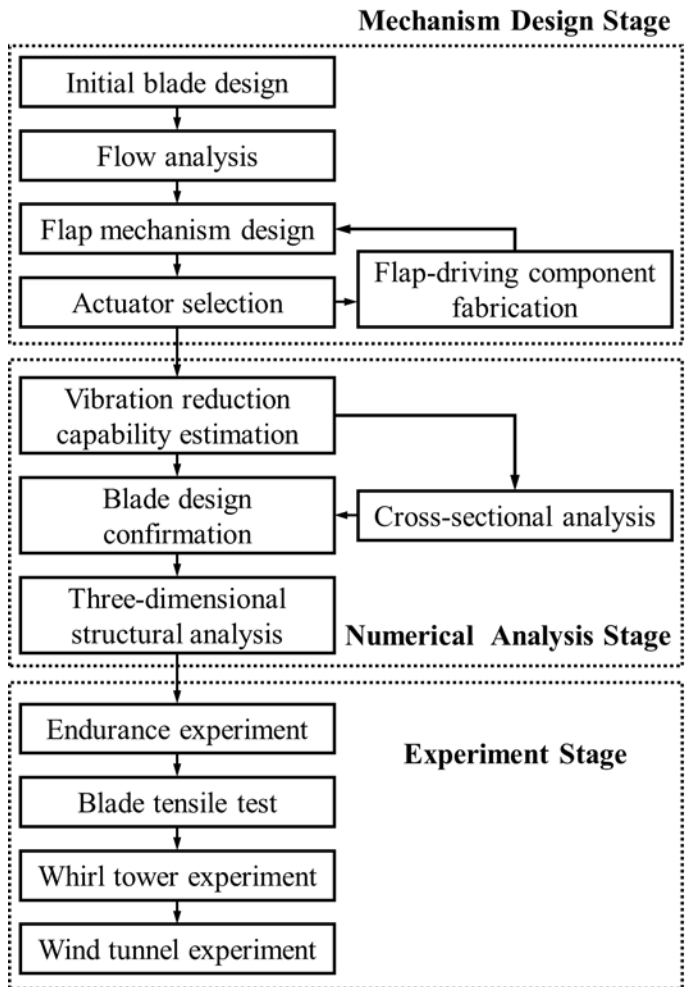

Fig. 2.1 SNUF research flow diagram

The third stage is to perform the specific experiments. In the endurance experiment, the centrifugal loading is imposed on the fabricated flap-driving components and actuated for operating period to determent whether sufficient

flap deflection is obtained. Thereafter, the ground rotation test will be prepared after the tensile test of the blade is completed. The final goal of this dissertation is to verify the capability of the trailing-edge flap to reduce the hub vibratory load by carrying out forward flight experiments.

Previous SNUF studies [130-139] have iterated upon the first stage. In spite of various flap-driving mechanisms, there were no mechanisms that produced the desired flap deflection of ±4°. However, finally in this dissertation, a flap-driving mechanism that achieves the desired flap deflection will be designed. In addition, the numerical analysis of the second stage will be conducted, and the endurance experiment results of the third stage will be presented.

2.1.2 Flap-Driving Mechanism Improvements

In this section, the flap-driving mechanisms designed though the previous studies [130-134] and their flap deflection measurement results are presented.

2.1.2.1 Evolution of the Flap-Driving Design

Figure 2.2 shows the various flap-driving mechanisms that have been designed. The design of all the flap-driving mechanisms employ piezoelectric actuators named APA200M and attempts were made to arrange the piezoelectric actuators in various ways to ensure sufficient flap deflection and

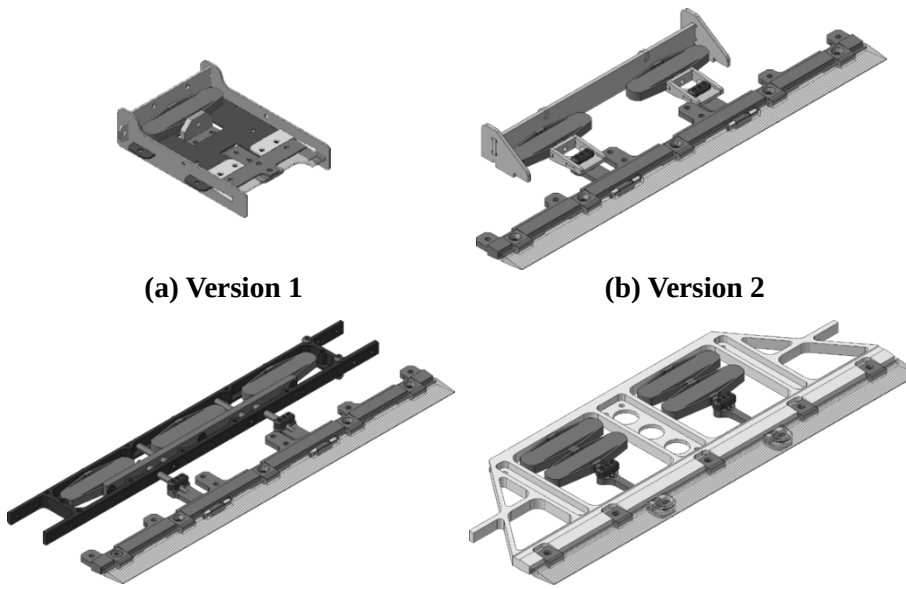

(a) Version 1 **(b) Version 2**

(c) Version 3 **(d) Version 4**

Fig. 2.2 Previous flap-driving mechanisms for SNUF

blocked force. In the first version, only one piezoelectric actuator was used to move the flap connected to the skin hinge. From the second version of the flap-driving mechanism, pin hinges have been applied and such type is also used in the current flap-driving mechanism design. In the second and third version, the actuators were arranged in parallel, and the number of the actuators was increased for the flap-driving mechanism design. By the fourth version, two pairs of actuators connected in series were used to overcome the small stroke of the APA200M actuator.

2.1.2.2 Previous Bench Test Results

Static bench test is an initial process for validating the flap-driving mechanism before testing with the practical loading condition such as aerodynamic and centrifugal loads. However, the previous prototypes of SNUF could not achieve the target flap deflection (±4°) even during the bench test. Table 2.1 indicates the results of the bench test. It is mainly assumed that the unexpected friction force arose more than it was anticipated to occur. It also turned out that the method of connecting multiple actuators was not effective for attaining the target performance. The fourth version (Fig. 2.2(d)) could not convert the rectilinear motion into curvilinear one without loss of the stroke and force. In addition, those results were static bench tests except for the aerodynamic forces to apply in the flap yet. When the aerodynamic forces are applied to the flap, it is obvious that the flap deflection will be reduced. Thus none of the previous flap-driving mechanism could operate with the required performance.

Table 2.1 Flap deflection results of the previous flap-driving mechanism

Version	Actuator	Hinge type	Flap deflection
1	Single	Skin hinge	±2.0°
2	Two in parallel		±1.5°
3	Three in parallel	Pin hinge	±2.5°
4	Four in parallel and series		±3.7°

2.1.3 SNUF Blade Configuration Revision

2.1.3.1 Blade Planform Modification

The previous results reveal that increasing merely the number of the actuators used did not provide an effective way to attain the satisfactory results. Since the inner space for the actuators is restricted, there is a limit upon the number of the actuators that can be added. Furthermore, there are also concerns about weight penalty when increasing the number of the actuators.

As those problems were discovered, an extensive revision on the design of the SNUF blades was conducted. First, modification on the dimensions of the blade were required. The SNUF blade is a Mach-scaled blade with the tip speed of Mach 0.6. The length of the existing SNUF blade was 1.28 m and the rotation speed was over than 1,500 RPM. Since the whirl tower test of the SNUF blade is to be conducted in the atmospheric environment, such high RPM could induce excessive centrifugal force on the flap and flap-driving mechanism. In addition, the flap-driving mechanism using the APA200M actuator did not reach the ±4° flap deflection even in static bench. It required an alternate piezoelectric actuator with increased blocked force and stroke. The SNUF blade properties were revised as summarized in Table 2.2. For airfoil, NACA 0015 was adopted instead of NACA 0012 because it was necessary to accommodate the APA 1000L actuator into the inner space of the blade.

Table 2.2 Revised SNUF blade specification

Property	Previous	Present
Hub type	Articulated	Hingeless
Rotor radius, mm	1,280	1,500
Blade chord, mm	102.4	135.0
Rotating speed, RPM	1,528	1,300
Airfoil type	NACA 0012	NACA 0015
Solidity ratio	0.1019	0.1146
Tip Mach number	0.6	
Pretwist, °	-10	
Number of blades	4	

2.1.3.2 Detailed Root Design

As summarized in Table 2.2, a hingeless hub is installed and used on the revised SNUF blade. Previous SNUF blade properties were selected based on the ATR blade design [56-58, 60, 140]. However, there was no question about which type of the hub would be suitable for the SNUF blade. Therefore, while revising the SNUF blade planform, practical whirl tower is considered together. As a results, it was decided to use the whirl tower [140] and hingeless hub [141] in Korea Aerospace Research Institute (KARI). And then all the design and analysis are based on the relevant hingeless hub, as shown in Fig. 2.3.

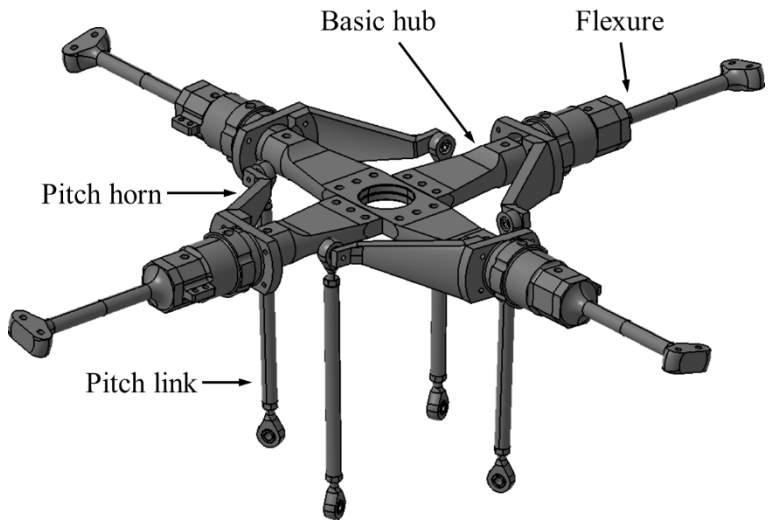

Fig. 2.3 CAD drawing of the hingeless hub

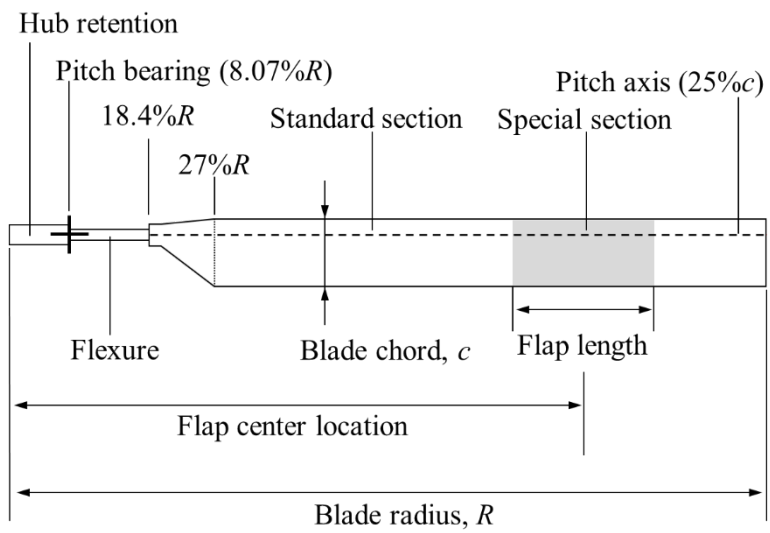

Fig. 2.4 SNUF blade planform

Figure 2.4 shows the overall planform of the SNUF blade. Considering the length of the KARI hingeless hub, the blade root begins at the 18.4%R (0.276 m). The full-length chord of the blade starts at 27%R (0.405 m). The location

and dimension of the trailing-edge flap are determined by going through a parametric study. The cross-sectional design of the blade is not established yet. However, the lamination pattern for the blade root is selected as shown in Fig. 2.5. The root reinforcement pattern is selected by referring to the layup information of the 1/6th Mach-scaled Chinook CH-47D blade [128]. The reinforcement lamination is placed from 33%R (0.495 m) and a total of 10 layers are added at the blade root.

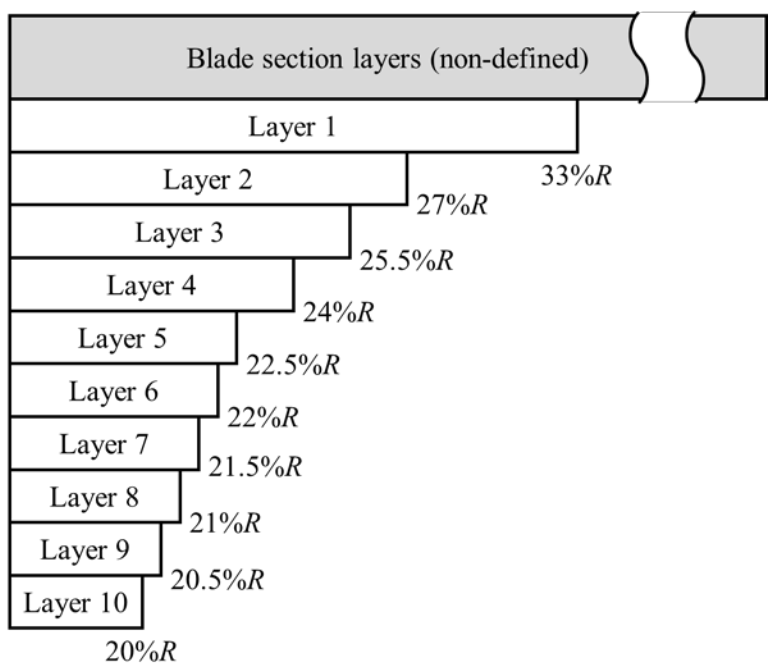

Fig. 2.5 Blade root reinforcement layup pattern

2.2 Multidisplinary Design for Flap Driving Mechanism

Since the various previous flap-driving components did not achieve the desired flap deflection, the blade planform was to be modified. Therefore, the flap-driving mechanism needs to be revised as well. In this subsection, the flap-driving mechanism design revision is conducted by considering the effects of external aerodynamic loadings and the performance of a piezoelectric actuator. In addition, a suitable piezoelectric actuator is selected by estimating the flap deflection.

2.2.1 Hinge Moment Estimation

2.2.1.1 Analytic method for hinge moment prediction

In order to design a flap-driving mechanism capable of driving the flap up to ±4° even under the aerodynamic loads, the aerodynamic hinge moment generated in the flap is predicted. Figure 2.6 shows the sign conventions for a hinged airfoil used in this dissertation. The formula suggested by Walz and Chopra [82] is not directly applicable here, since it was designed for a three-dimensional blade. Instead, a simpler prediction based on a two-dimensional blade is used for comparison with CFD results. The sectional hinge moment (h) is defined as follows:

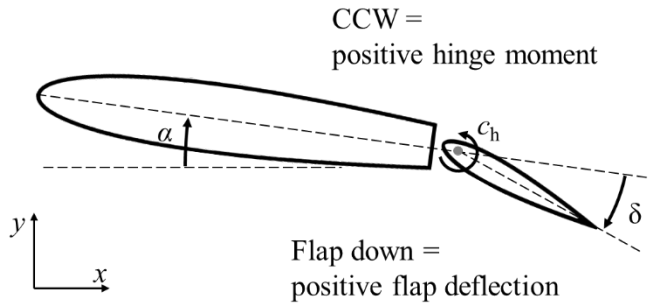

Fig. 2.6 Sign convections of a hinged airfoil

$$h = \frac{1}{2}\rho\left(\Omega r\right)^2 c_f^2 C_h \tag{2.1}$$

where ρ is the air density, Ω is the rotor rotational speed, r is the flap section location, c_f is the flap chord length and C_h is the hinge moment coefficient. Integrating Eq. (2.1) in the spanwise direction, the results will be

$$\begin{aligned} H &= \int_{R_1}^{R_2} h\,dr = \int_{R_1}^{R_2} \frac{1}{2}\rho\left(\Omega r\right)^2 c_f^2 C_h\left(\alpha, \mathrm{M}, \delta\right) \\ &= \frac{1}{2}\rho\Omega^2 c_f^2 C_h\left(\alpha, \mathrm{M}, \delta\right)\frac{1}{3}\left(R_2^3 - R_1^3\right) \end{aligned} \tag{2.2}$$

where R_1 and R_2 are the inboard and outboard flap location, respectively. α is the airfoil angle of attack (AOA), M is the Mach number of the flow and δ is the flap deflection. While all the parameters appearing in Eq. (2.2) originate from the geometric features of the flap or from environmental conditions, the hinge moment coefficient need to be provided. Glauert [143] estimated the effect of plain flaps while changing the flap hinge moment. In Fig. 2.7,

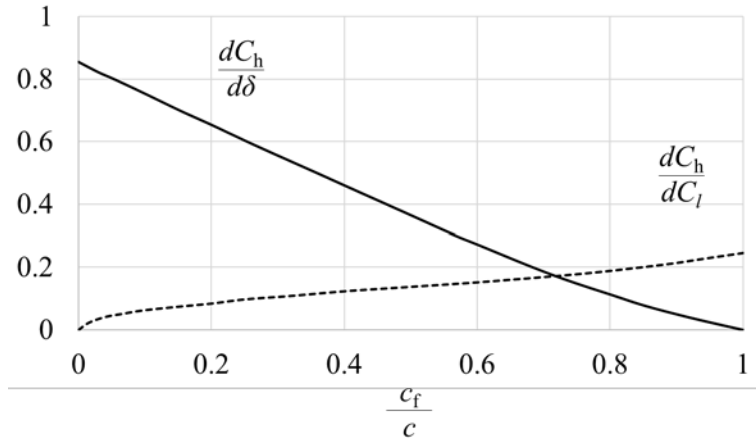

Fig. 2.7 Analytical hinge moment characteristics of a plain trailing-edge flap [143]

estimated values of the rate of change of the hinge moment with respect to the lift coefficient (dC_h/dC_l) is shown. In it, the rate of change of the hinge moment with respect to the flap deflection ($dC_h/d\delta$) is also included. For a symmetric wing section, the analytical expression for the sectional hinge moment coefficient is:

$$C_h = (\alpha, M, \delta) = C_l(\alpha, M)\frac{dC_h}{dC_l} + \delta\frac{dC_h}{d\delta} = C_{l_\alpha}(M)\alpha\frac{dC_h}{dC_l} + \delta\frac{dC_h}{d\delta} \qquad (2.3)$$

The variation of the hinge moment coefficient with respect to the lift coefficient and the deflection angle can be extracted as a function of the ratio between the airfoil chord and the flap chord, by using the curve fitting as follows.

$$\frac{dC_h}{dC_l} = 0.28\left(\frac{c_f}{c}\right)^4 - 0.24\left(\frac{c_f}{c}\right)^3 + 0.13\left(\frac{c_f}{c}\right)^2 - 1.02\left(\frac{c_f}{c}\right) + 0.85 \qquad (2.4)$$

$$\frac{dC_h}{d\delta} = -0.46\left(\frac{c_f}{c}\right)^4 + 1.32\left(\frac{c_f}{c}\right)^3 - 1.20\left(\frac{c_f}{c}\right)^2 + 0.58\left(\frac{c_f}{c}\right) \qquad (2.5)$$

2.2.1.2 Computational Fluid Dynamics (CFD) estimation

For more accurate estimation on the aerodynamic hinge moment, a computational fluid dynamics (CFD) analysis using ANSYS Fluent [144] has been tried. The first attempt was made by Kang [135]. In that analysis, a prediction derived from a mono-block airfoil gave only a rough estimate of the pressure distribution, as there was no separation between the front and the flap. For the second, in order to capture the more realistic flow phenomena of the SNUF, a flow analysis including a gap between the main airfoil and the flap was attempted by Visconti [136]. However, since sufficiently fine grids were not employed, those results turned out to be inaccurate. According to ANSYS requirements [144], a few layers of prismatic mesh had to be added along the physical wall of the airfoil. However, the number of layers chosen amounts to just four, which led to numerical inaccuracies, and those grids are too coarse to capture the sophisticated phenomenon on the unsteady flow analysis. On the other hand, the presently improved grid construction shown in Fig. 2.8 provides detachment between the main block and the flap. Thus further refined grid geometry leads to more precise computations and more reliable results.

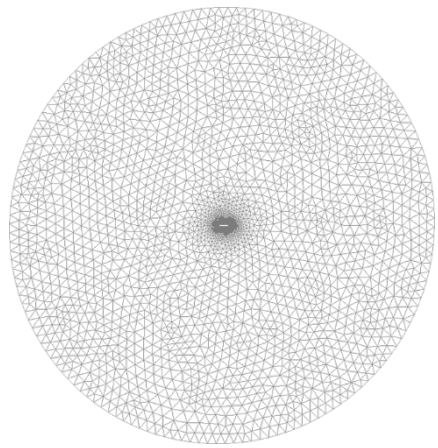

(a) CFD analysis grid for hinged airfoil

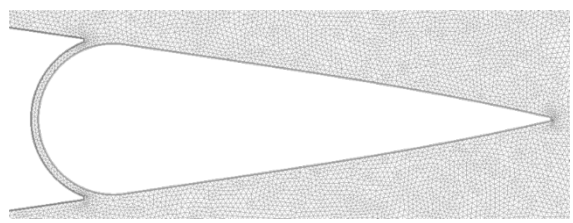

(b) Grids near the trailing-edge flap

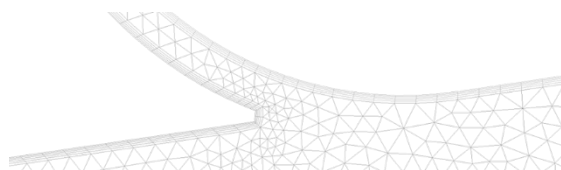

(c) Details of the grids near the gap

Fig. 2.8 CFD analysis grid for airfoil with the trailing-edge flap

An unsteady CFD analysis is implemented. The selected methodology consists of the dynamic grids encompassing the motion of the flap prescribed according to the sinusoidal movement and the consequent deformation of the fluid elements surrounding the flap. As it is customary in the unsteady flow analysis, a triangular unstructured grid is chosen over a hexahedral design. It is capable of modifying its layout in a smoother manner without noticeably

altering the overall quality. According to CFD requirements, a few layers of prismatic grids need to be added along both the physical walls of the airfoil and the external boundaries of the domain. This procedure is selected due to the incapability of the grids to deform when in contact with the walls and by the likeliness of a negative volume being created at the inlet and outlet boundaries. The number of layers chosen amounts to five, built according to an exponential trend. A further expansion of the prismatic zone completely fills the gap between the flap and the main block, leading to numerical inaccuracies.

In order to implement the unsteady flow analysis, appropriate movement must be imposed on the airfoil. Such requirement is accomplished in ANSYS Fluent with a C function which describes the flap deflection in terms of the frequency and amplitude. The specifications of the present device include oscillations up to 65 Hz and a deflection range of ± 4°. Aiming at optimizing the performance between the computational time and accuracy of the solution, a generally coarse grids are constructed to ensure accuracy in regions where instability is likely to surge, such as the gap between the airfoil and the flap. In such areas, greater refinement is introduced so as to consider anomaly which may arise due to the discontinuity of the wall.

2.2.1.3 Numerical Estimation of the Hinge Moment

First, the analytical hinge moment formulation of the plain trailing-edge flap (Eq. (2.2)) is exploited using the flap deflection angle and airfoil angle of attack as parameters. The results shown in Fig. 2.9 indicate a clearly increasing trend in the hinge moment values as the angle of attack increases due to the pressure on the lower surface of the flap, which is then forced to rotate in the counter-clockwise direction. Moreover, negative deflection of the flap (*i.e.*, counter-clockwise) will instead create additional hinge moment, forcing the flap to rotate downwards.

In addition, unsteady CFD analysis is conducted, in order to predict the hinge moment precisely. Table 2.3 summarizes the analysis conditions which are used in the present CFD analysis. First, in order to validate the quality of the presently generated grids, y^+ value on the wall surface is evaluated. y^+ is a non-dimensional coefficient indicating the relationship between the shear stress on the wall and the density of the grid, and it can be expressed as:

$$y^+ = \frac{y \times \sqrt{\tau_w / \rho}}{\nu} \tag{2.6}$$

where y is the distance from the wall to the center of the first cell, τ_w is the shear stress on the wall, and ν is the dynamic viscosity. As can be seen in Fig. 2.10, y^+ value is smaller than five on the entire wall zone. Thus the density of the grid

Table 2.3 CFD analysis condition

Property	Present
ANSYS Fluent version	17.0
Mach number	0.45
Altitude	Sea level
Viscosity model	k-ω SST
Turbulent intensity	1%
Turbulent viscosity ratio	1
Wall roughness constant	0.5
Number of cells	367,892
Number of nodes	188,503

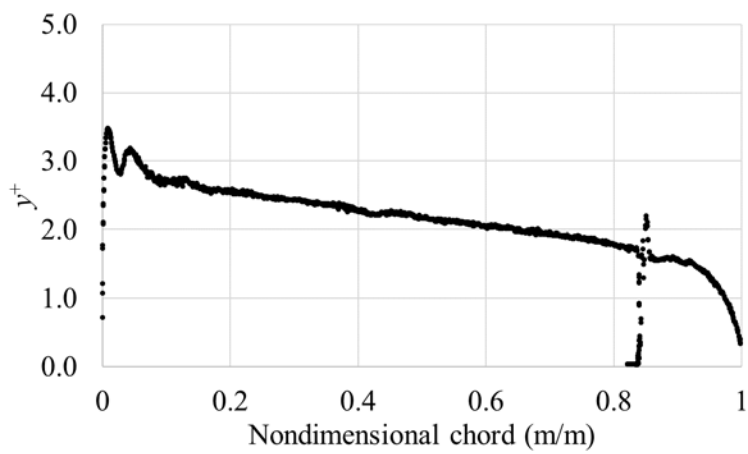

Fig. 2.9 y^+ value on the wall

is considered sufficient in the current analysis using the k-ω SST model, which is the one of the popular Reynolds-averaged Navier-Stokes (RANS) turbulent models.

In the present CFD analysis, the angle of attack is varied and the relevant

hinge moment is extracted from ANSYS Fluent as the hinge moment coefficient associated with the flap wall zone. An the unsteady flow analysis is conducted for a chosen frequency, 65 Hz, and for each value the airfoil angle of attack is varied from -10° to 10°. These results are shown in Fig. 2.11. In order to compare with analytical results, CFD analysis results are expressed as the flap displacement versus the hinge moment coefficient. This result is illustrated in Fig. 2.12. In the comparison between the hinge moment coefficient by the analytical formulation and that by the present unsteady flow analysis, it is clearly observed that greater values in the former prediction is due to the deflection of the flap. In light of the hinge moment acting on the flap during the unsteady flow analysis, the highest value occurring in the computation is extracted, in order to select the proper actuator and ensure sufficient performance.

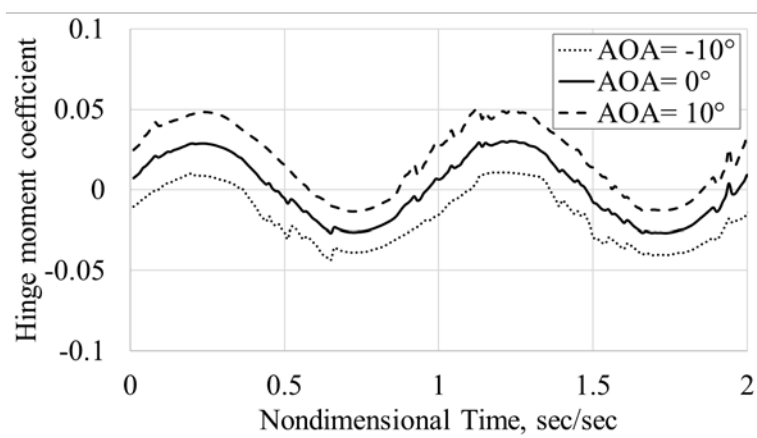

Fig. 2.10 Hinge moment coefficient by the flap actuation at 65 Hz, ±4°

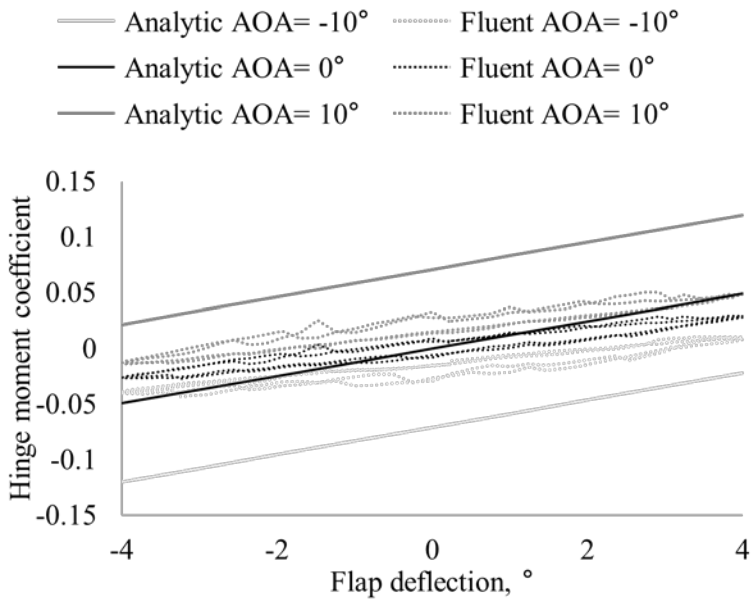

Fig. 2.11 Hinge moment coefficients of the analytic formulation and the unsteady CFD analysis

2.2.2 Flap Driving Mechanism Design

Flap driving mechanism is designed in order to achieve the target flap deflection of ±4° when considering the aerodynamic loads acting on the flap. First, considering the operation of the actuator as shown in Fig. 2.13, the characteristics of a piezoelectric actuator can be expressed analytically. The characteristics of the piezoelectric actuator are represented by the input voltage, stroke, and blocked force, and the relationship as shown in Eq. (2.7) is obtained.

$$\frac{F}{F_{\max}} + \frac{x}{x_{\max}} = \frac{V}{V_{\max}} \tag{2.7}$$

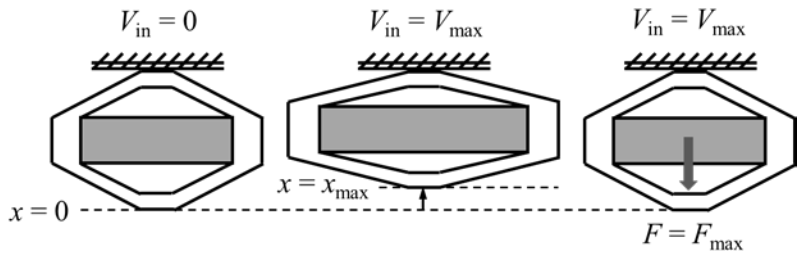

Fig. 2.12 Actuator operation under specific situations

where F is the blocked force, x is the stroke and V is the input voltage of the piezoelectric actuator. For example, if the maximum voltage is applied to the actuator and there exists no external loads, the actuator stoke will be located at its maximum. On the contrary, when the maximum voltage is applied and the stroke of the actuator is zero, the external loads will be applied to the actuator, which have the same amount of the maximum blocked force.

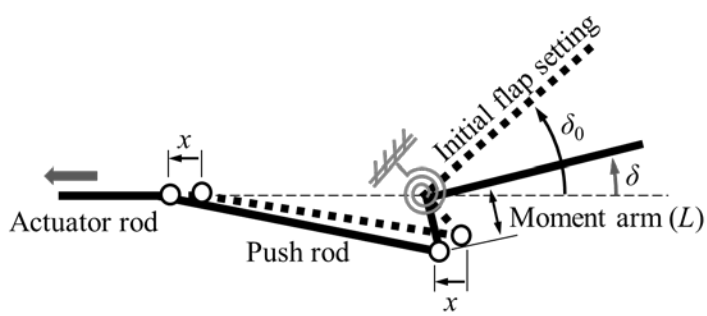

Fig. 2.13 Flap-driving mechanism schematic diagram

Figure 2.14 shows the flap driving mechanism including the actuator movement and flap hinge moment, which is implemented as a torsional spring. Also, a kinematic equation is formulated in order to describe the flap motion during its actuation.

$$H = -k\delta \tag{2.8}$$

$$\frac{H}{L} = F = -\frac{k}{L}\delta \tag{2.9}$$

$$x = L(\delta_0 - \delta) \tag{2.10}$$

In the above equations, H and F are respectively the hinge moment and force applied at the flap hinge, δ is the flap deflection, L is the moment arm, and k the torsional spring stiffness extracted by CFD results. Assuming that the relationship between the flap deflection and the hinge moment is linear, it can be expressed as Eq. (2.8), where the slope has the same unit as the coefficient of the torsional spring. With all the parameters defined, the final formulation which connects the input voltage, blocked force and stroke results from the combination of Eqs. (2.7), (2.9), and (2.10). The governing equation of the flap-driving mechanism can be expressed as Eq. (2.11).

$$V = -V_{\max}\left(\frac{k}{LF_{\max}} + \frac{L}{x_{\max}}\right)\delta + \frac{LV_{\max}}{x_{\max}}\delta_0 \tag{2.11}$$

Since the flap hinge moment is included in Eq. (2.11), a flap initial setting (δ_0) greater than the target flap deflection is required. Excluding the external aerodynamic load, Eq. (2.11) is improved as follows.

$$V = \frac{LV_{\max}}{x_{\max}}(\delta_0 - \delta) \tag{2.12}$$

According to Eq. (2.12), when the input voltage (V) is zero, the flap deflection becomes equal to the initial flap setting. However, in the presence of the external aerodynamic loads, the flap deflection is always smaller than the initial flap setting. As shown in Fig. 2.15, the input voltage should be zero when the positive flap deflection becomes maximum. This situation can be expressed by Eq. (2.13) and the initial flap setting value is derived from this equation.

$$0 = -V_{\max}\left(\frac{k}{LF_{\max}} + \frac{L}{x_{\max}}\right)\delta_{\max} + \frac{LV_{\max}}{x_{\max}}\delta_0 \tag{2.13}$$

$$\therefore \delta_0 = \left(\frac{kx_{\max}}{L^2F_{\max}} + 1\right)\delta_{\max} \tag{2.14}$$

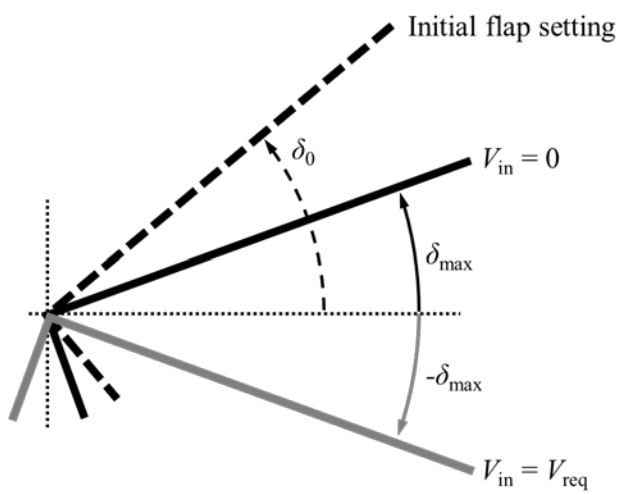

Fig. 2.14 Flap deflection under specific situation

Figure 2.15 shows that the greatest actuator input voltage is required when the negative flap deflection becomes maximum. This can be expressed as follows.

$$V_{\text{req}} = -V_{\max}\left(\frac{k}{LF_{\max}} + \frac{L}{x_{\max}}\right)\left(-\delta_{\max}\right) + \frac{LV_{\max}}{x_{\max}}\delta_0 \tag{2.15}$$

Substituting Eq. (2.14) into Eq. (2.15) yields the formula for the required voltage as in Eq. (2.16).

$$V_{\text{req}} = -V_{\max}\left(\frac{k}{LF_{\max}} + \frac{L}{x_{\max}}\right)\left(-\delta_{\max}\right) + \frac{LV_{\max}}{x_{\max}}\delta_0 \tag{2.16}$$

In order to achieve the desired flap deflection, the present flap-driving mechanism should select a piezoelectric actuator with a $V_{\text{req}}/V_{\max}$ value smaller than unity. The preferences of the various piezoelectric actuators are summarized in Table 2.4. Figure 2.16 shows the relationship between the hinge moment arm (L) and the required input voltage (V_{req}) depending on the various actuators. In the case of APA 200M actuator, the required input voltage is always larger than the maximum voltage, regardless of the length of the moment arm. On the other hand, APA 500L and 1000L have a ratio of the required voltage to the maximum voltage lower than unity even with a short moment arm of 0.5 mm. Considering the inner space of blade and the weight penalty, the smaller and lighter APA 1000L actuator is finally selected to drive

trailing-edge flap of SNUF. The flap-driving mechanism with APA 1000L actuator is shown in Fig. 2.17.

Table 2.4 Properties of various APA actuators

Property	APA 200M	APA 500L	APA 1000L
Maximum stroke, μm	230	500	900
Blocked force, N	73	570	373
Force limit (0-peak), N	27	285	93
Height, mm	17	55	35
Length, mm	55	145	145
Width, mm	9	16	16
Mass, g	15.7	200	190

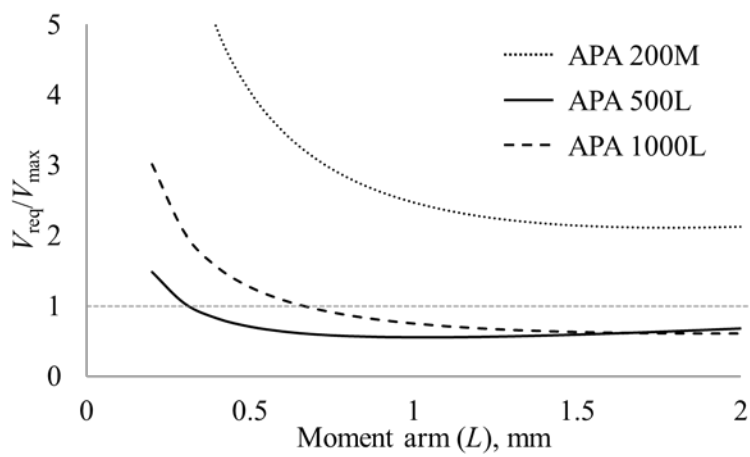

Fig. 2.15 Required input voltage according to the length of the moment arm

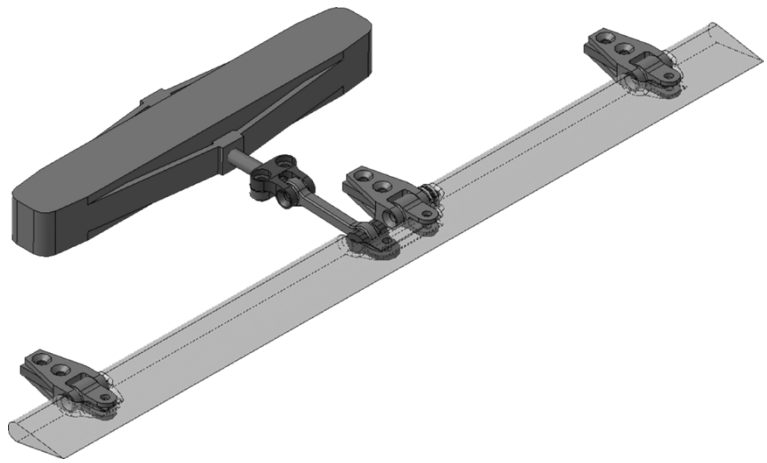

Fig. 2.16 Revised flap-driving mechanism design

2.3 Design Optimization Strategy

This section describes the techniques for the design optimization of a rotorcraft blade with a trailing-edge flap. First, the hub vibratory loads are predicted by conducting the multibody dynamics modeling of the active flap rotor. By such multibody dynamic analysis, the location and dimension of the trailing-edge flap will be optimized. Once the optimization of blade geometry is achieved, additional optimization on the blade sectional design will be conducted. For this process, the blade section design optimization framework by the genetic algorithm (GA) is established.

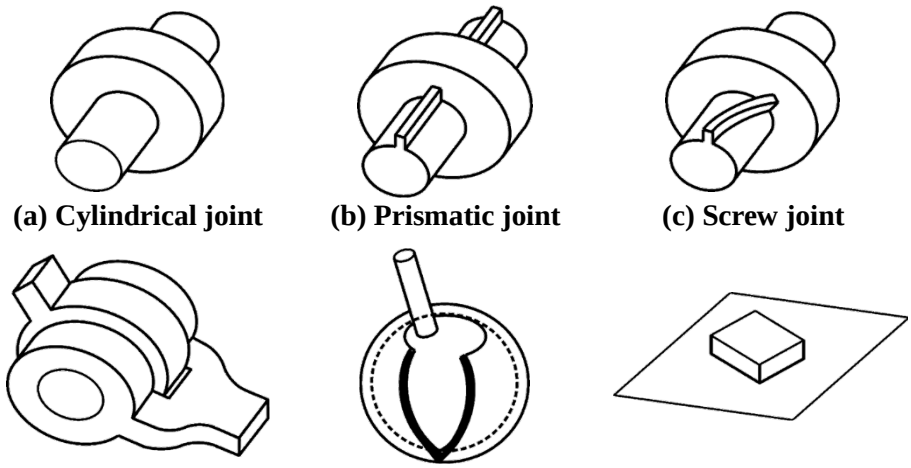

(a) Cylindrical joint **(b) Prismatic joint** **(c) Screw joint**

(d) Revolute joint **(e) Spherical joint** **(f) Planar joint**

Fig. 2.17 Six lower pairs of joint in DYMORE [146]

2.3.1 Blade Planform Parametric Study

2.3.1.1 Theoretical Background of Multibody Dynamics

Multibody dynamics modeling for the SNUF blade is conducted to estimate the hub vibratory loads. DYMORE [145] is a finite-element-based analysis for nonlinear, elastic multibody structures that is used in the present multibody dynamics analysis. It allows modeling of arbitrarily complex configurations by the assembly of deformable bodies with numerous joint elements [146]. Figure 2.18 depicts six lower pairs of joints that are provided by DYMORE. In this dissertation, deformable bodies are modeled by the finite element method, without resorting to modal approximations, and the active rotor blade

components are modeled as beam elements. In DYMORE, formulation of its beams is on the basis of geometrically exact beam element that considers arbitrarily large displacements, finite rotations, and small strains.

Consider the elastic body shown in Fig. 2.19. The overall rigid body motion of the elastic body is described by a floating frame whose orientation is defined by the orthonormal bases $B^{0F} \coloneqq (\bar{e}_{01}^F, \bar{e}_{02}^F, \bar{e}_{03}^F)$ and $B^F \coloneqq (\bar{e}_1^F, \bar{e}_2^F, \bar{e}_3^F)$ in the reference and deformed configurations, respectively. Similarly, two additional orthonormal bases define the orientation of a frame rigidly attached to the body at an arbitrary point P, $B^{0P} \coloneqq (\bar{e}_{01}^P, \bar{e}_{02}^P, \bar{e}_{03}^P)$ and $B^P \coloneqq (\bar{e}_1^P, \bar{e}_2^P, \bar{e}_3^P)$ in the reference and deformed configurations, respectively. R_0^F and R^F are the components of the rotation tensors from the inertial frame *I* to B^{0F} and B^{0F} to B^F, respectively, both measured in *I*. Similarly, R_0^P and R^P are the components of the rotation tensors from frame *I* to B^{0P} and B^{0P} to B^P, respectively, both measured in *I*. In the reference configuration, the origin of the floating and body-attached frames are denoted by $\underline{x}_0^P$ and $\underline{x}_0^F$ respectively. The position vector $\underline{s}^P$ of Point *P* with respect to the floating frame vector is $\underline{s}^P = \underline{x}_0^P - \underline{x}_0^F$. The orientations of the floating and body-attached frames are identical in the reference configuration, *i.e.* $R_0^F = R_0^P = R_0$. The displacement vectors of the floating and body-attached frames are denoted $\underline{x}^F$ and $\underline{x}^P$, respectively.

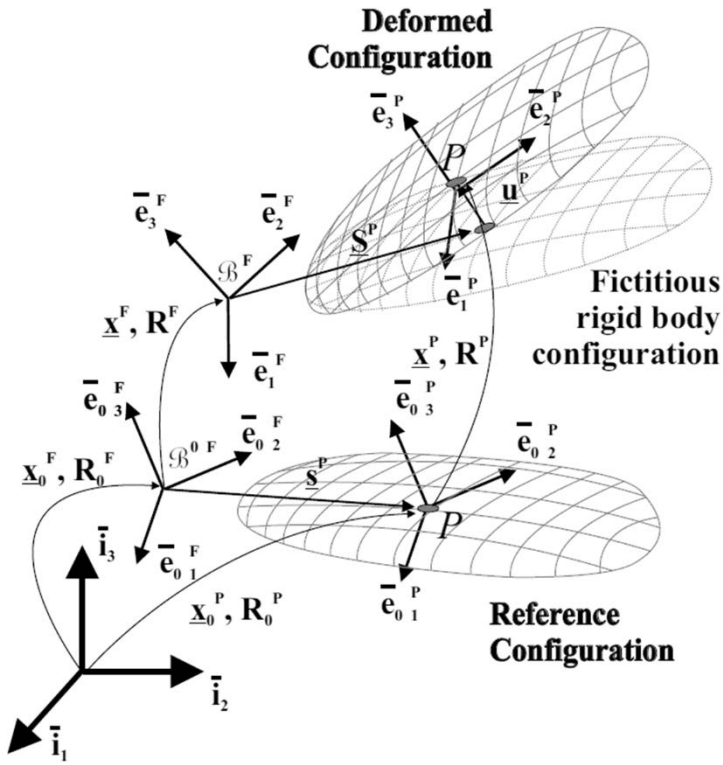

Fig. 2.18 Reference and deformed configuration [146]

The complete motion of the elastic body consists of the superposition of a rigid body motion and an elastic motion. The rigid body motion, defined by the motion of the floating frame, brings the elastic body to the fictitious rigid body configuration shown in Fig. 2.19. Since this motion is rigid, the position vector of point *P* with respect to the floating frame, measured in this frame, remains unchanged, *i.e.* $\underline{s}^{P*} = \underline{S}^{P*}$, where $\underline{s}^{P*} = R_0^T \underline{s}^P$, $\underline{S}^{P*} = (R^F R_0)^T \underline{S}^P$, and $\underline{S}^P$ denotes the position vector of point *P* in the fictitious rigid body configuration. The position of the point *P* is now written as:

$$\underline{x}_0^P + \underline{x}^P = \underline{x}_0^F + \underline{x}^F + \underline{S}^P + \underline{u}^P = \underline{x}_0^F + \underline{x}^F + \left(R^F R_0\right)\left(\underline{s}^{P*} + \underline{u}^{P*}\right) \qquad (2.17)$$

where $\underline{u}^P$ is the elastic displacement of the body, and $\underline{u}^{P*} = (R^F R_0)^T \underline{u}^P$ the components of this displacement vector measured in frame B^F solving Eq. (2.17) then yields

$$\underline{u}^{P*} = \left(R^F R_0\right)^T \left(\underline{x}_0^P + \underline{x}^P - \underline{x}_0^F - \underline{x}^F\right) - \underline{s}^{P*} \qquad (2.18)$$

In general, the elastic body also undergoes elastic rotations that will be defined in the following manner.

$$\theta^{P*} = \frac{1}{2}\begin{bmatrix} g_{32} - g_{23} \\ g_{13} - g_{31} \\ g_{21} - g_{12} \end{bmatrix} = \frac{1}{2}\begin{bmatrix} R_{32}^* - R_{23}^* \\ R_{13}^* - R_{31}^* \\ R_{21}^* - R_{12}^* \end{bmatrix} = \bar{n}^* \sin\phi \qquad (2.19)$$

where R_{ij}^* are the components of the relative rotation tensor $R^* = (R^F R_0)^T R^P R_0$, ϕ is the magnitude of this relative rotation, $\bar{n}^*$ is the unit vector about which it takes place, and $\mathrm{g}_{\alpha\beta} = (\bar{e}_\alpha^F)^T \bar{e}_\beta^P$. If the elastic displacements remain small, $\underline{\theta}^{P*} \approx \bar{n}^* \phi$ represents the infinitesimal rotation vector, although both R^P and R^F are finite rotations.

Since Eqs. (2.18) and (2.19) are valid for any point on the elastic body, they also hold for the boundary points, hence

$$\underline{u}^{B^*} = \left(R^F R_0\right)^T \left(\underline{x}_0^B + \underline{x}^B - \underline{x}_0^F - \underline{x}^F\right) - \underline{s}^{B^*} \tag{2.20}$$

and

$$\theta^{B^*} = \frac{1}{2}\begin{bmatrix} g_{32} - g_{23} \\ g_{13} - g_{31} \\ g_{21} - g_{12} \end{bmatrix} \tag{2.21}$$

Additionally, DYMORE incorporates the finite-state dynamic inflow unsteady aerodynamics to estimate unsteady aerodynamic loads [147]. This aerodynamic model corresponds to an intermediate level of wake representation between the simplest momentum and highly complicated free-wake methodologies.

2.3.1.2 Multibody Dynamic Modeling for SNUF blade

Figure 2.20 represents the multibody dynamics modeling of the SNUF four-bladed hingeless rotor used in the present dissertation, including the trailing-edge flap. The hub is connected to a revolute joint that is subjected to a prescribed rotational speed. The root retention involves an elastic beam attached rigidly to the hub, and the structural loads at the connection point are obtained and added over four of the loads to predict the hub vibratory loads. A single revolute joint that is located between the root retention and the flexure is

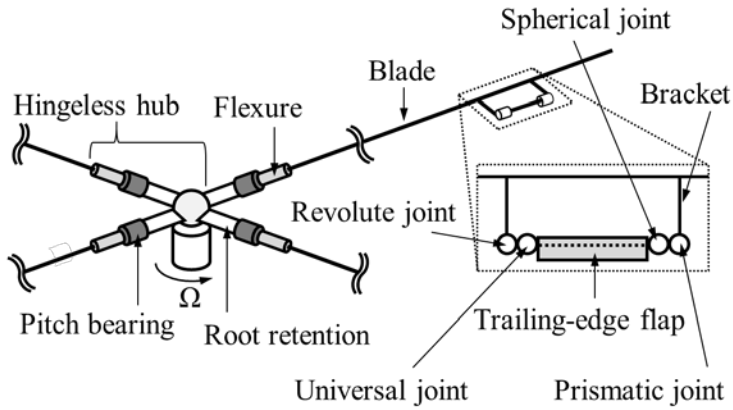

Fig. 2.19 Multibody modeling of the SNUF blade

implemented to apply the pitch bearing. This is followed by attaching geometrically exact nonlinear beams to embody the SNUF blades that contain the trailing-edge flap components. The inside of the flap is connected to the inner bracket by a revolute joint and a universal joint. The outside of the flap is connected to the outer bracket by a prismatic joint and a spherical joint to prevent buckling. The SNUF blades are discretized during the forward flight analysis as 28 elements per blade, each with 2nd-order interpolation polynomials. Thus, there will exist 3,000 degrees of freedom as summarized in Table 2.5 to be solved at each time step, including the finite-state dynamic inflow variables for aerodynamics.

Individual blade control (IBC) refers to a system in which control inputs are implemented in the rotor system, and each trailing-edge flap is controlled independently at any specific frequency. With respect to an IBC mode, the actuation on each flap behaves in the same phase at a specific azimuthal

Table 2.5 Degree of freedom by SNUF multibody modeling

Modeling part	DOF	Total
Blade	720 per blade	
Joint and motion	96 per blade	
Hub and clamp	40	3,000
Blade-joint sharing	48 per blade	
Blade-hub sharing	12 per blade	

location. The time input function of the flap motion is established by the following equation:

$$d_j(t) = d_{\max} \int \; g_j(t) = \frac{1}{2} d_{\max} \left\{ 1 - \cos\left(N_{\text{act}} \Psi_j - \phi_{\text{ctrl}} \right) \right\} \tag{2.22}$$

$$\begin{aligned} g_j(t) &= g_{\max} \sin\left[N_{\text{act}} \left\{ 2\pi f_{\text{rot}} t + \frac{1}{2}\pi (j-1) \right\} - \phi_{\text{ctrl}} \right] \\ &= g_{\max} \sin 2\pi \left[N_{\text{act}} f_{\text{rot}} t + \left\{ \frac{1}{4} N_{\text{act}} (j-1) - \frac{1}{2\pi} \phi_{\text{ctrl}} \right\} \right] \end{aligned} \tag{2.23}$$

where d_k, g_j = deflection, time input function of the j-th blade, respectively; N_{act} = 3, 4 or 5; Ψ_k = azimuthal position of the j-th blade (expressed in radian); ϕ_{ctrl} = 0°, 30°, … 360° (12 divisions around 360°); and $g_{\max}$ = amplitude of the time input function (varies with respect to the actuation frequency).

Figure 2.21 exemplifies the maximum flap amplitude location for an IBC mode corresponding to a 3/rev frequency for different phase angles. The maximum flap amplitude location between the first and second actuation

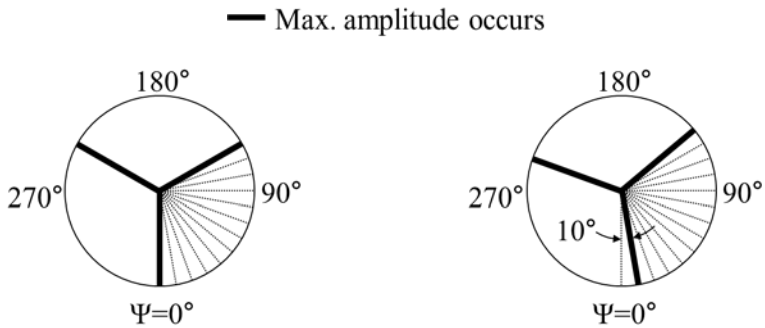

(a) ϕctrl = 0° **(b) ϕctrl = 30°**

Fig. 2.20 Maximum flap azimuthal location for an IBC mode with 3/rev actuation frequency

periods corresponds to an azimuthal difference of 10° in accordance with 120°/12 divisions even if it is specified as a phase difference of 30° in accordance with 360°/12 divisions from the aspect of the control phase.

In the present multibody dynamic modeling, a pitch horn and a pitch link are modeled using a torsional spring coefficient of the pitch bearing. Since the torsional spring coefficient of the pitch bearing has a great influence on the 1st torsional frequency of the rotor blade, it is important to use a practical value. Figure 2.22 illustrates the pitch horn and the pitch link implemented in the rotor blade. Therefore, the equivalent torsional spring coefficient can be obtained by the following equation.

$$d_{\mathrm{pl}} = L_{\mathrm{ph}} \sin\theta \approx L_{\mathrm{ph}}\theta \tag{2.24}$$

$$F = K_{\mathrm{pl}} d_{\mathrm{pl}} = \frac{E_{\mathrm{pl}} A_{\mathrm{pl}}}{L_{\mathrm{pl}}} d_{\mathrm{pl}} = \frac{E_{\mathrm{pl}} A_{\mathrm{pl}}}{L_{\mathrm{pl}}} L_{\mathrm{ph}} \theta \tag{2.25}$$

$$\begin{aligned} M &= F L_{\mathrm{ph}} = \frac{E_{\mathrm{pl}} A_{\mathrm{pl}}}{L_{\mathrm{pl}}} L_{\mathrm{ph}}^2 \theta \\ &= k_\theta \theta \end{aligned} \tag{2.26}$$

$$\therefore k_\theta = \frac{E_{\mathrm{pl}} A_{\mathrm{pl}}}{L_{\mathrm{pl}}} L_{\mathrm{ph}}^2 \tag{2.27}$$

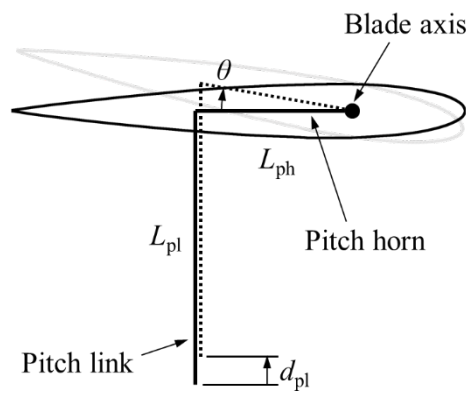

Fig. 2.21 Pitch link and pitch horn

where K_{pl} is the stiffness of the pitch link, E_{pl} is the young's modulus of the pitch link, A_{pl} is the section area of the pitch link and k_θ is the equivalent spring coefficient of the pitch bearing. In this dissertation, the equivalent torsional spring coefficient is obtained by using the geometries of the pitch link and pitch horn mounted on the hingeless hub in KARI as shown in Fig. 2.3.

2.3.1.3 Parametric Study for the Shape of the Trailing-edge Flap

The configuration of the revised SNUF blade summarized in Table 2.2, is shown in Fig. 2.4. However, parametric studies were not systematically performed according to the location within the rotor blade and dimension of the trailing-edge flap in the previous design process of the SNUF blade. Therefore, in this dissertation, the hub vibratory loads reduction capability is examined with respect to various flap design parameters. The flap center location, flap length, and flap chord length are used to determine the dimension and location of the flap. To understand the influence of these three shape parameters, three types of vibration reduction analyses are performed. In this procedure, a single parameter is varied and the remaining parameters are fixed, as summarized in Table 2.6.

Table 2.6 Setting for the flap shape parametric study

	Changed parameter	Range
Case 1	Flap center location	65~85%R
Case 2	Flap length	16~24%R
Case 3	Flap chord length	10~20%c

For example, in Case 1, the flap length and flap chord length are fixed at 20%R and 15%c, respectively. At this time, the flap center location is changed from 65 to 85%R and the analysis is performed. In this way, understanding of

the influence of the three flap parameters is attempted. Vibration reduction analyses are conducted by DYMORE. The cross-sectional properties applied in this procedure are obtained from the previous SNUF design [135] and the flap is allowed to move with a maximum deflection angle of ±4°.

2.3.2 Optimization for the Blade Cross Section

Optimization for the blade planform is conducted by the parametric analysis of the location and dimension of the trailing-edge flap. However the previous cross section design [135] is used in the blade planform optimization process. That cross-section, which was applied in the previous studies [135-137] was not designed as an analytical approach and is considered to be excessively reinforced due to concerns about the centrifugal loads on the flap-driving components. The highly stiffened sectional design brings the weight penalty of the blade, and the increased torsional frequency degrades the vibration reduction capability [129]. Therefore, it is required to design a blade section that has a smaller weight, the decreased first torsional frequency, and sufficient structural integrity. In this dissertation, the cross-sectional design framework using the genetic algorithm is developed to design a blade section that satisfies these requirements.

2.3.2.1 Optimization Method by the Genetic Algorithm

In the present optimization framework, an external optimization routine was developed on the basis of GA. MATLAB Global Optimization Toolbox [148] is adopted to perform the optimization. GA constitutes a metaheuristic approach motivated by a natural selection process [149]. Genetic algorithms are on the basis of natural genetics, and Darwin's theory of survival of the fittest forms the basic concept. In this procedure, possible solutions to problems are listed, and then genes are changed to produce increasingly accurate and improved solutions. In this dissertation, each solution is termed as the gene, and the evolutionary process involves transforming these genes to obtain an aimed result. It is a search algorithm that mimics evolution to find a better answer [150].

The overall process of GA can be divided into the following six stages: (1) initialization, (2) selection, (3) crossover, (4) mutation, (5) replacement, and (6) iteration. Various solutions are created randomly at the initialization. At this time, the fidelities of the objective function for the generated solutions are measured. The selected solutions are delivered to the next generation on the basis of the fitness. At the crossover stage, new genes are generated from the selected genes in a variety of ways. The gene thereby generated is replaced by a succeeding gene. At the crossover stage, new genes are produced in a variety of ways within the selected genes, and the mutation then occurs with a lower

probability. The new genes generated become the next genes. The selection, crossover, mutation, and replace are repeated to derive the desired solution until most of the genes are identical [151].

2.3.2.2 Cross Sectional Analysis of Composite Rotor Blade

The complete three-dimensional analysis of the rotor blade is broken into two steps. In the first step, a linear cross-sectional analysis of the composite rotor blade is performed to determine the cross-sectional properties of the blade at difference spanwise locations. And in the second step, aeroelastic analysis of the rotor blade is performed on the one-dimensional beam model using DYMORE[146]. This breakdown of the analysis is valid for slender structures like rotor blades. Depending upon the complexity in rotor blade geometry and variation in the layup, the blade is divided into several spanwise sections. Blade properties are assumed to be constant in each section. In the current analysis, the SNUF blade is divided into eighteen spanwise sections as described in Table 2.7. Since the blade geometry and layup, both vary significantly in the root region, the number of sections is more in the root region.

Cross-sectional shapes of different sections are determined based on the detailed geometries of KARI hingeless hub (Fig. 2.3) and revised blade configuration (Fig. 2.4). Once the layup information and the cross section profile is available, an ANSYS based mesh generator [152] is used to generate

Table 2.7 Spanwise regions for cross-sectional analysis

Section	Span	Chord, m	Material
Section R1	0.0%R	0.0400	Titanium alloy
Section R2	2.4%R	0.0394	Titanium alloy
Section R3	4.5%R	0.0297	Titanium alloy
Section R4	5.3%R~6.5%R	0.0260	Titanium alloy
Section R5	6.6%R~8.1%R	0.0200	Titanium alloy
Section F1	8.1%R~8.4%R	0.0390	Titanium alloy
Section F2	8.5%R~9.7%R	0.0340	Titanium alloy
Section F3	9.9%R~11.5%R	0.0280	Titanium alloy
Section F4	12.1%R~17.0%R	0.0095	Titanium alloy
Section F5	17.6%R	0.0244	Titanium alloy
Section F6	18.0%R	0.0330	Titanium alloy
Section F5	18.4%R	0.0244	Titanium alloy
Section B1	18.4%R~20.0%R	0.0559	Standard section + 10ply
Section B2	20.0%R	0.0559	Standard section + 9ply
Section B3	27.0%R	0.1350	Standard section + 2ply
Section B4	27.0%R~33.0%R	0.1350	Standard section + 1ply
Section B5	33.0%R~65.0%R	0.1350	Standard section
Section B6	65.0%R~73.5%R	0.1350	Special section with roving
Section B7	73.5%R~76.5%R	0.1350	Special section with titanium block
Section B6	76.5%R~85.0%R	0.1350	Special section with roving
Section B5	85.0%R~	0.1350	Standard section

the finite element mesh for GT/VABS [153]. Variational Asymptotic Beam Sectional Analysis (VABS) is a computer program implementing the various beam theories [154-157] based on the variational asymptotic method [157]

using the finite element method.

The geometries for different root sections are shown in Figs. 2.23-2.25. The root retention and flexure are connected through a pitch bearing at 8.1%R. From the 27% of the radial station, the blade has a full chord length of 0.135 m. The blade after 27%R can be divided into the standard section (Section B3 to B5) and the special section (Section B6, B7), as shown in Fig. 2.4. The inside of the nose of the standard section is filled with carbon roving from the front to 10%c. The special sections include the trailing-edge flap and the flap-driving components. The first special section (Section B6) also has roving at the inside of the nose. And the second special section (Section B7), does not have spar, and instead of carbon roving, there is a titanium block to hold the piezoelectric actuator.

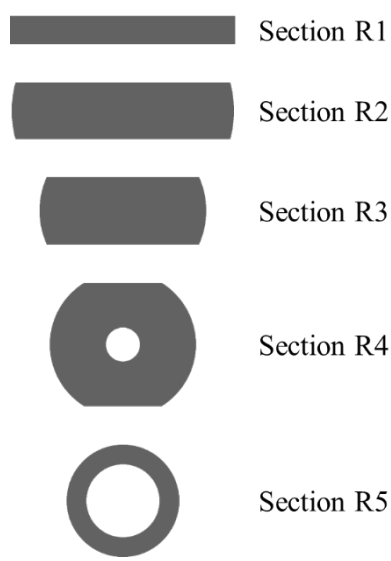

Fig. 2.22 Root retention geometry

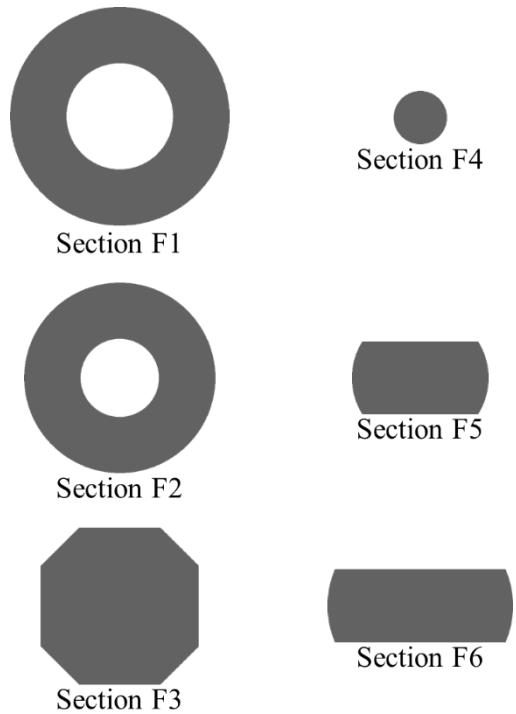

Fig. 2.23 Flexure geometry

2.3.2.3 Framework Development for the Cross Sectional Design

In the present cross-sectional design optimization procedure, the sectional optimization process is only attempted for the standard section. The special section and the section near the root are adjusted based on the optimized standard section results. The constraints of this design optimization are as follows:

- It is necessary to place the shear center such that it is located in the 1/4 chord and to adjust the center of gravity to the 1/4 chord point by

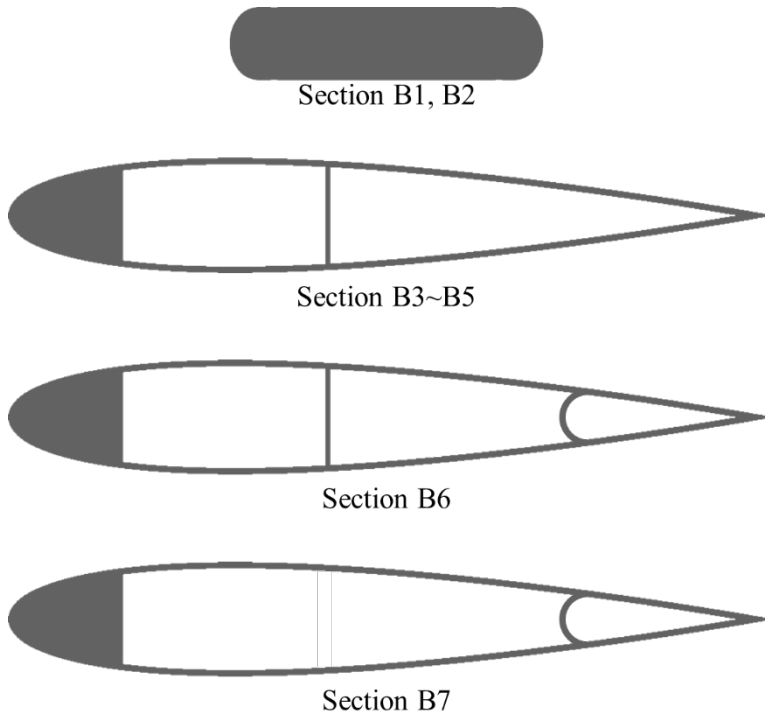

Fig. 2.24 Blade geometry

considering the lock number and ballast weight.

- The first torsional frequency should be smaller than 3/rev to increase the vibration reduction capability of the active trailing-edge flap.
- The stain existing on the cross section should be within the permissible range even in the safety factor corresponding to 1.5 is applied to the expected forward flight condition under a high blade loading.

In this dissertation, an improvement for the design of the SNUF blade is proposed by developing a cross-sectional design optimization framework. Figure 2.26 shows a flow chart of the present optimization framework. This optimization framework for the SNUF sectional design was established on the

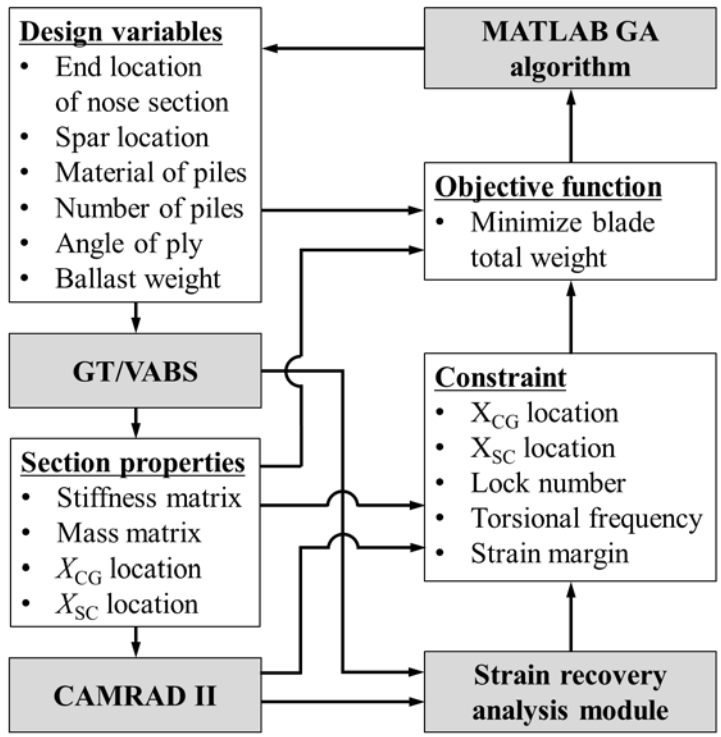

Fig. 2.25 Flowchart of the SNUF blade design optimization [140]

basis of the ATR optimization frame work as suggested in a previous study [140]. The objective function used in the current optimization framework is expressed in Eq. (2.28). The SNUF blade is equipped with the piezoelectric actuator and flap-driving components; thus, an objective function is established to minimize the weight of the blade in the range that satisfies Lock number of the blade.

$$J = \min\left[m_{\text{hub}} + m_{\text{composite blade}} + m_{\text{flap-driving components}} \right] \tag{2.28}$$

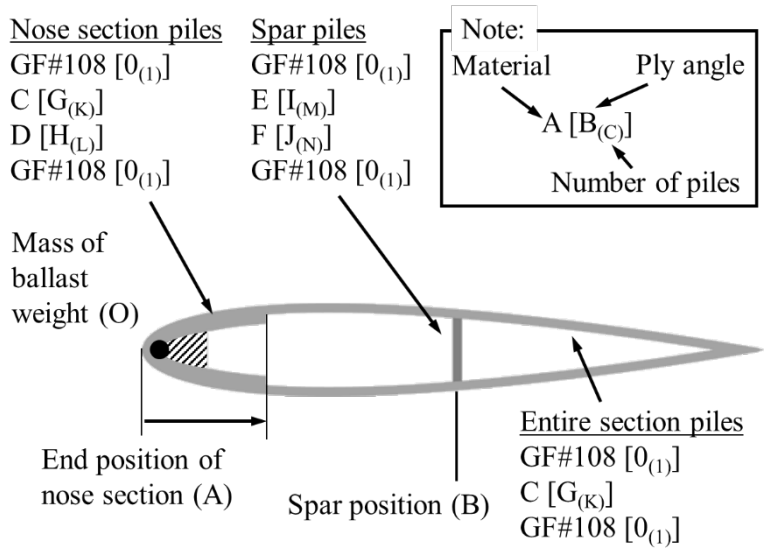

Fig. 2.26 Design variables used in the present optimization

In the present design framework, a cross sectional analysis is performed using GT/VABS [153]. As shown in Fig. 2.27, fifteen design variables are considered in the optimization procedure: a variable corresponding to the nose section end position, a variable corresponding to the spar position, four variables corresponding to material types, four variables corresponding to the ply angles, four variables corresponding to the ply sheets, and a variable corresponding to the mass of the ballast weight. Particularly, the mass of the ballast weight is determined by considering the mass per unit span of the present cross section and the allowable Lock number range. The outermost and innermost plies are fixed as a single 0° ply of glass fiber #108. Table 2.8 summarizes the design variables used in the present optimization framework.

Table 2.8 Design Variables Used in the Present Optimization

Symbol in Fig. 2.27	Design variable	Lower boundary	Upper boundary
A	End position of nose section	10%*c*	30%*c*
B	Spar position	20%*c*	60%*c*
C	Material for entire section	CF#3327, UD#730	
D	Material for nose section	CF#3327, UD#730	
E	Material for spar – inner	CF#3327, UD#730	
F	Material for spar – outer	CF#3327, UD#730	
G	Ply angle for entire section	0°, 45°, 90°	
H	Ply angle for nose section	0°, 45°, 90°	
I	Ply angle for spar – inner	0°, 45°, 90°	
J	Ply angle for spar – outer	0°, 45°, 90°	
K	Number of piles for entre section	1	3
L	Number of piles for nose section	1	3
M	Number of piles for spar – inner	1	3
N	Number of piles for spar – outer	1	3
O	Mass of ballast weight	0.0 kg/m	0.5 kg/m

Several restrictions are considered in the present optimization framework to improve the accuracy and reliability. First, the ply orientation angles are assigned to use only 0°, 45°, and 90°. Second, only three different materials, namely glass fiber #108, carbon fiber #3327, and carbon unidirectional (UD) #730, are used for the material selection in the present optimization framework. Therefore, when GA is executed, variables that correspond to the material and ply angle are allocated to several specified values as summarized in Table 2.8. The material properties of these composites are summarized in Table 2.9.

Table 2.9 Material Properties Used in the Present Design

Property	Glass fiber #108	Carbon fiber #3327	Carbon UD #730
Thickness, mm	0.08	0.27	0.30
Density, kg/m^3	950	759	1,067
E_L, MPa	21,271	47,423	100,131
E_T, MPa	20,236	52,027	4,206
G_{LT}, MPa	3,725	5,025	5,855
ε_L	0.017	0.007	0.012
ε_T	0.003	0.006	0.011
ε_{LT}	0.004	0.011	0.010
ν_{LT}	0.312	0.055	0.147
ν_{TL}	0.013	0.083	0.129

As shown in Fig. 2.26, to place the first torsional frequency within the desired range, a frequency analysis was performed using the sectional properties obtained, including the center of gravity and shear center. The frequency analysis was performed using CAMRAD II [159], which corresponds to a comprehensive rotorcraft analysis program. CAMRAD II incorporates a combination of multibody dynamics and rotorcraft nonlinear aerodynamics.

In this procedure, the three-dimensional strain recovery analysis is also conducted to confirm the structural integrity of present section. This process is illustrated in Fig. 2.28.

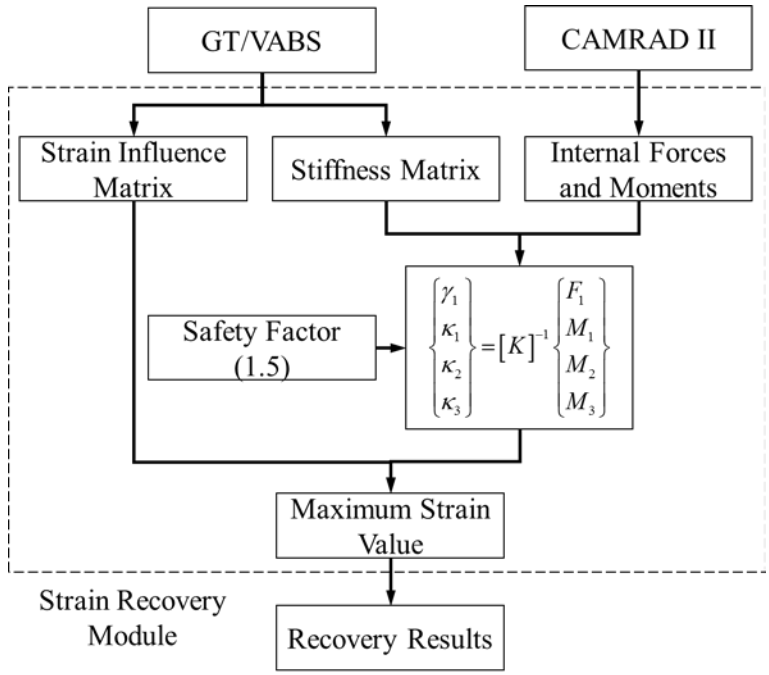

Fig. 2.27 Flowchart of the three-dimensional strain recovery analysis module

$$\begin{Bmatrix}\gamma_1\\ \kappa_1\\ \kappa_2\\ \kappa_3\end{Bmatrix}=[K]^{-1}\begin{Bmatrix}F_1\\ M_1\\ M_2\\ M_3\end{Bmatrix} \tag{2.29}$$

In Eq. (2.29), [*K*] denotes the stiffness matrix obtained from GT/VABS, and γ_1 denotes the axial strain, κ_1 denotes the elastic twist, κ_2 and κ_3 denote the two flexural curvatures. The internal loads and moments at each blade section are predicted by CAMRAD II trim analysis under the forward flight condition that will be determined through the baseline study in Section 3.3. In the trim analysis, the piezoelectric actuator and flap-driving components are each considered as

a point mass. A safety factor of 1.5 is considered in the present structural integrity analysis.

2.4 Numerical Investigation on Design Optimization

In this section, the design optimization results of SNUF composite blade will be presented. The numerical design optimization process is performed in the following order.

i. Vibratory load estimation without flap actuation under various flight condition to select baseline
ii. Comparison of the vibratory loads according to location and dimension of the trailing-edge flap
iii. Design of the blade section using developed optimization framework
iv. Vibratory load reduction capability prediction

2.4.1 Vibratory Loads Reduction Preliminary Analysis

The preliminary analysis is performed with the multibody structural dynamic modeling presented in Section 2.3.1 to confirm that the present multibody model is capable to capture the hub vibratory load of the rotor blade. In addition, it should be observed that the hub vibratory load is fluctuated due to the actuation of the trailing-edge flap. Hub vibration reduction analysis consists of

the following three steps. First, a static structure analysis for multibody modeling is performed. This static analysis is conducted without external aerodynamic loads, and the natural frequencies of the rotor system can be predicted. Second, the rotor trim analysis including aerodynamic loads is performed using the static analysis results as initial values. DYMORE [146] provides a module called 'Autopilot' witch can be implemented to conduct a moment trim of rotorcraft. Finally, a multibody dynamic analysis is performed with the trim angle obtained by the trim analysis. In this procedure, the baseline value of the hub vibratory load is estimated without the movement of the flap, and the vibration reduction capability can be calculated by applying the flap actuation of various phase.

The forward flight condition for preliminary analysis is considered as the advance ratio μ = 0.3, the rotor shaft angel of attack α_s = -6° and the non-dimensional thrust coefficient C_T/σ = 0.06. For the trim under this forward flight condition, target thrust is chosen as 2500 N, and target rolling/pitching moments are selected as both 0 N-m. Figure 2.29 gives the results of preliminary trim analysis for SNUF. As one can see, all three values of thrust, rolling and pitching moments are converged well to the target values. In addition, the trimmed pitch control angles for collective and two cyclic controls are obtained.

After the trim analysis is completed, first the hub vibratory load baseline is predicted. The hub loads of the rotor system can be obtained from summation

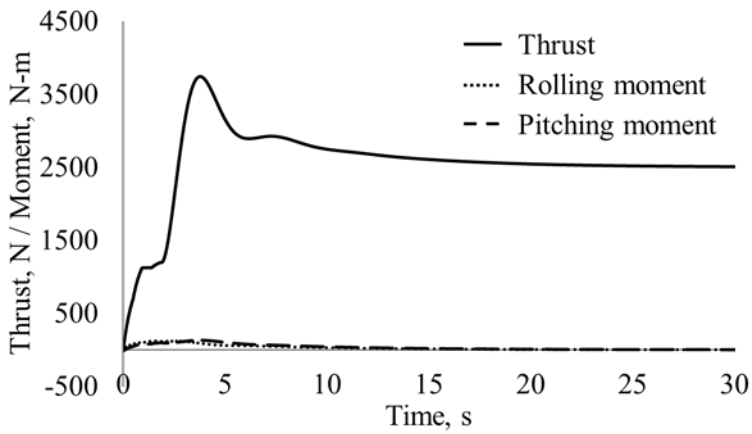

(a) Trimmed thrust and rolling/pitching moments

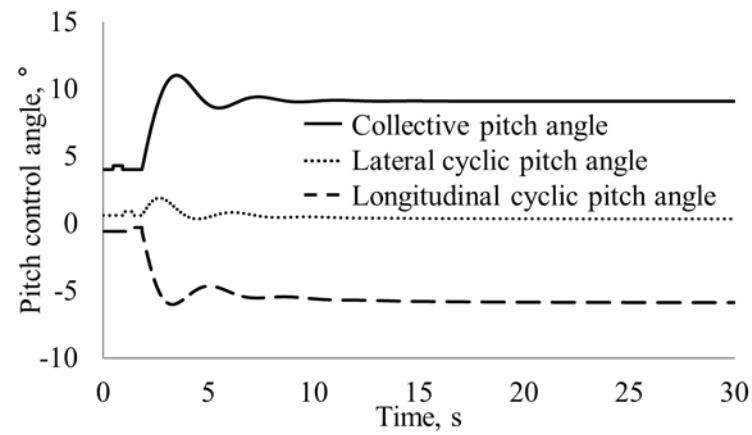

(a) Trimmed pitch control angles

Fig. 2.28 Preliminary trim analysis results

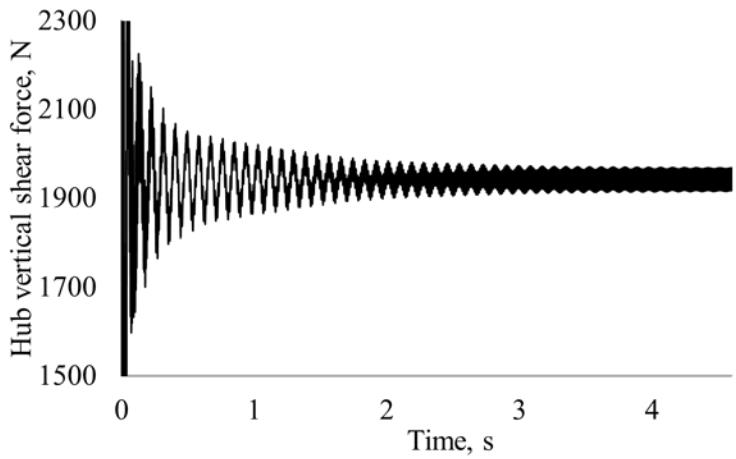

(a) Time history of hub vertical shear load

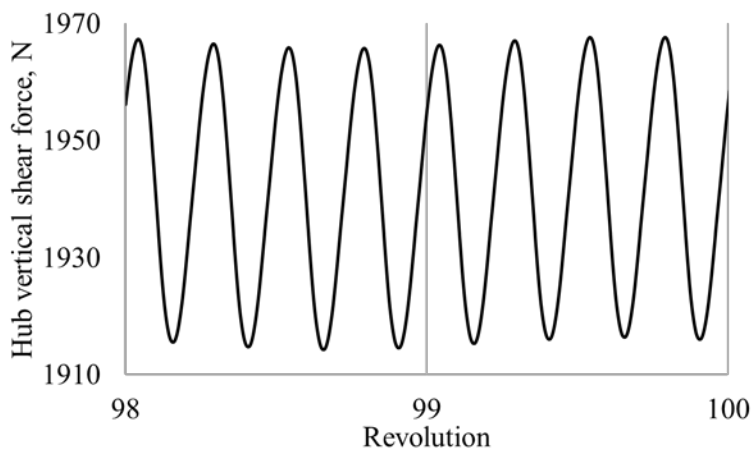

(b) Hub vertical shear load of last two revolution

Fig. 2.29 Hub vertical shear load of preliminary trim analysis

of all the loads in the four root retention elements at the roots. This analysis will be conducted while the rotor system rotates 100 revolutions. Figure 2.30(a) shows the time history of hub vertical shear loads without flap actuation. The final two revolution results are shown in Fig. 2.30(b). As can be seen, 4/rev vibratory loads are observed. Figure 2.31 shows the amplitude of the 4/rev vibratory load in each direction. Figures 2.32 and 2.33 give the variation of the 4/rev hub shear vibratory loads when the 3, 4 and 5/rev actuation frequencies are applied with the flap control phase. The fluctuation of the 4P hub vibratory loads are predicted with respect to the variation of the flap control phase angle. From these results, it is considered that the present multibody dynamic model simulates the phenomenon of vibratory load reduction by trailing-edge flap.

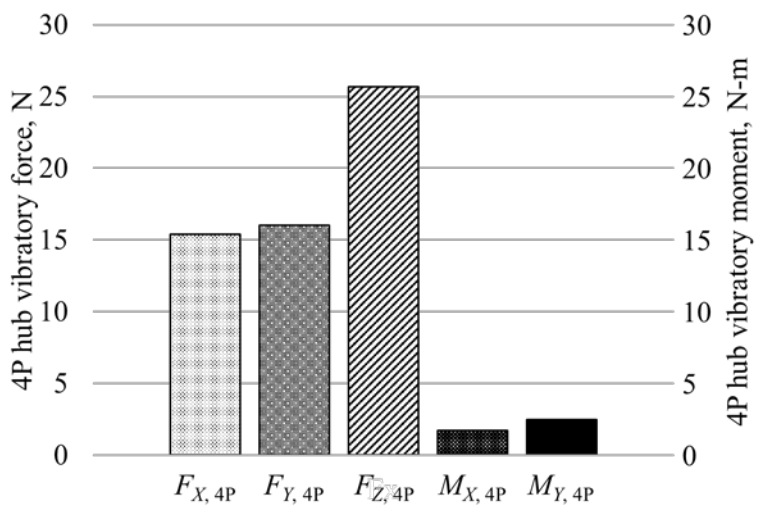

Fig. 2.30 4P hub vibratory loads of the preliminary analysis

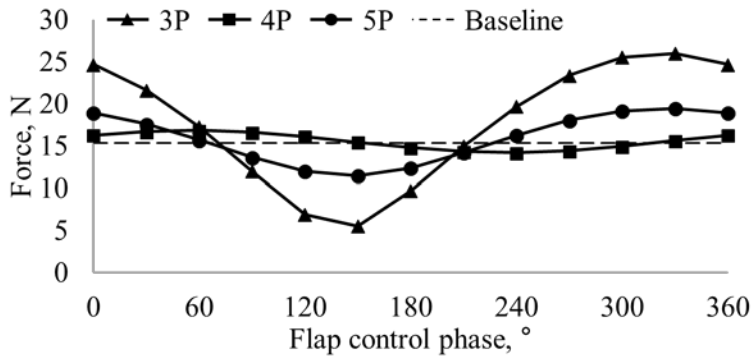

(a) Forward vibratory shear loads

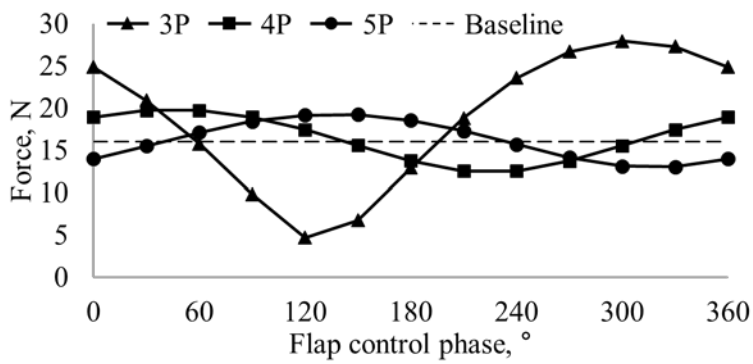

(b) Sideward vibratory shear loads

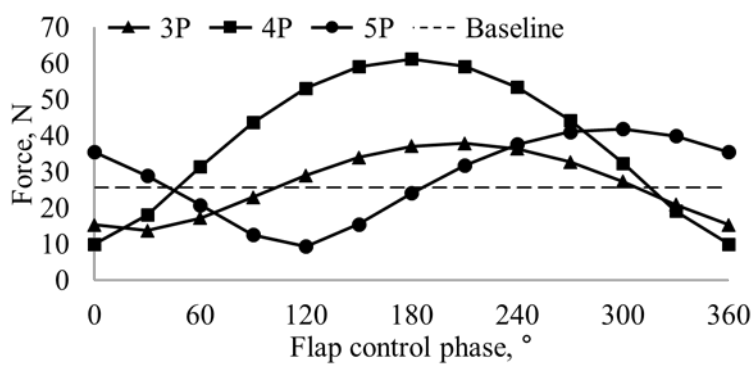

(c) Vertical vibratory shear loads

Fig. 2.31 Fluctuation of 4/rev hub vibratory loads of the preliminary analysis

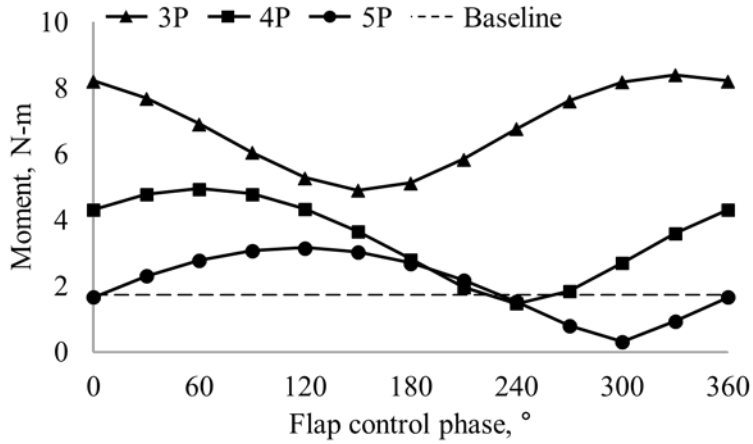

(a) Vibratory chord bending moments

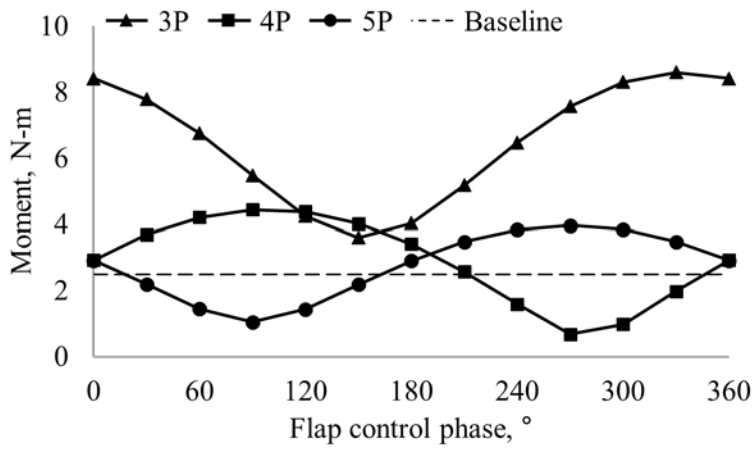

(b) Vibratory flap bending moments

Fig. 2.32 Variation of 4/rev hub shear vibratory moments of the preliminary analysis

2.4.2 Forward Flight Baseline Condition Selection

To investigate the effectiveness of the active flap to modify the aerodynamic loads and reduce vibratory hub loads, a specific flight condition for the research

baseline is required. Yet since the SNUF blade is not tested in a whirl tower or a wind tunnel, the vibratory loads of the present multibody model will be investigated under several forward flight condition, as summarized in Table 2.10. A total of six forward flight conditions considering of different advance ratio (μ) and shaft tilt angle (α_s) are established, and the common trim targets are summarized in Table 2.11. The forward flight trim analyses are conducted to obtain vibratory characteristics of the various rotor blade configuration with the previous cross-sectional properties [1.5]. Figure 2.34 shows the 4/rev hub vibratory loads, and the vibration index which was calculated from Eq. (2.30), is displayed in Fig. 2.35.

Table 2.10 Forward flight conditions for the baseline study

Advance ratio	Shaft tilt angle		
	α_s = -2°	α_s = -4°	α_s = -6°
μ = 0.1	Condition 1	Condition 2	Condition 3
μ = 0.2		Condition 4	Condition 5
μ = 0.3			Condition 6

Table 2.11 Trim target for the forward flight

Description	Property	Value
Thrust coefficient	C_T/σ	0.060
Thrust, N	T	2,500
Rolling moment, N-m	M_{Roll}	0.0
Pitching moment, N-m	M_{Pitch}	0.0

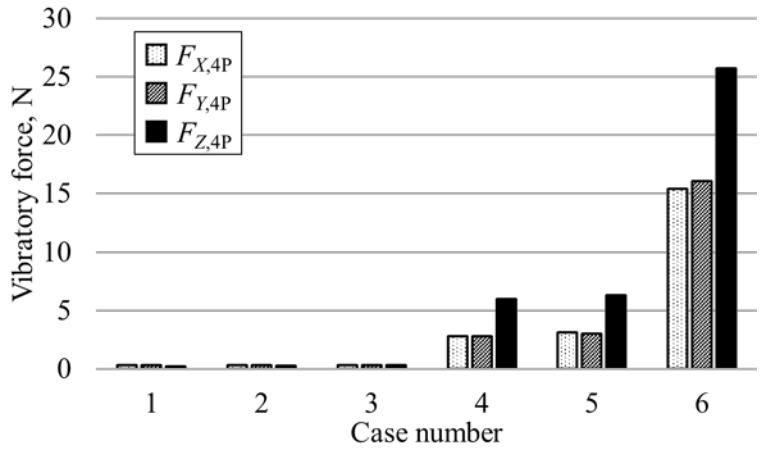

(a) 4/rev hub vibratory loads

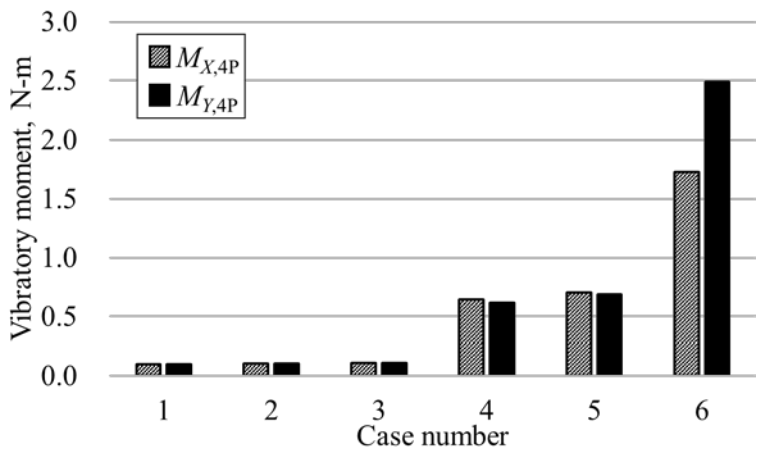

(b) 4/rev hub vibratory moments

Fig. 2.33 4/rev hub vibratory load results for the forward flight conditions

$$V_{\text{index}} = \frac{\sqrt{F_{X,4P}^2 + F_{Y,4P}^2 + F_{Z,4P}^2}}{T} + \frac{\sqrt{M_{X,4P}^2 + M_{Y,4P}^2}}{Q} \tag{2.30}$$

where T is the thrust, and Q is the torque at the hub.

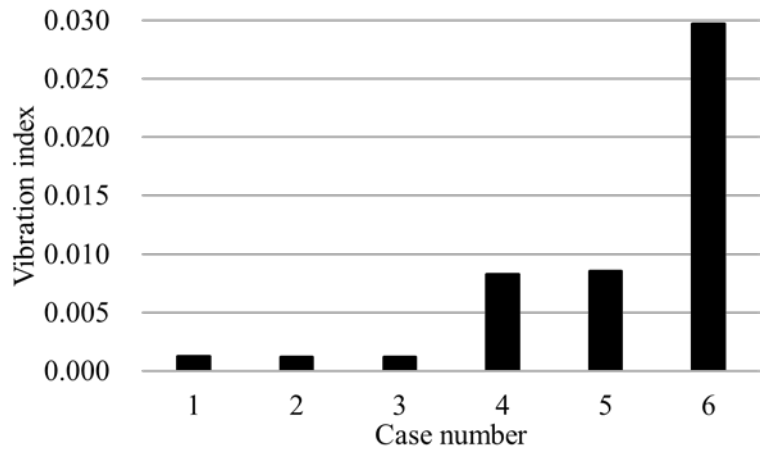

Fig. 2.34 Vibration quality criterion for the forward flight conditions

In the advance ratio conditions of 0.1 (Conditions 1-3) and 0.2 (Conditions 4, 5), the 4P hub vibratory loads are too minuscule to investigate the effectiveness of the vibratory load reduction capability. The sixth forward flight condition with advance ratio of 0.3 and rotor shaft angle-of-attack of -6° has the highest vibration index value. Therefore, this condition is selected as research baseline and will be applied in the vibration control simulation for this dissertation.

2.4.3 Effect of the Flap Shape Parameters

By studying the effect of the flap location and dimension on the hub vibratory load reduction, the planform of the SNUF blade is determined. This process involves parametric studies of the following three flap parameters: flap center location, flap length, flap chord length. The two flap parameters are fixed and

the dynamic analyses of the multibody model of SNUF rotor system are performed while changing another flap parameter. At this time, the trailing-edge flap is actuated at 3, 4 and 5 times the number of revolutions of the blade, and twelve different flap control phases are considered in these analyses.

Single specific flap control phase does not minimize the vibratory loads in all direction. For example, as shown in Figs. 2.32 and 2.33, when the trailing-edge flap is actuated with a frequency of 3/rev and the control phase of 150°, the forward vibratory shear load is minimized, but the same flap actuation cannot reduce the vertical shear loads. Therefore, in order to evaluate the hub vibratory load reduction according to the flap shape parameter, the vibratory loads in a particular flap control phase should not be compared. Instead, the minimized vibratory load of each direction according to the flap control phase is extracted and compared with the variations of the flap shape parameters.

2.4.3.1 Case 1: Flap Center location Change

In order to investigate the effect of the flap center location on the vibration reduction capability of the trailing-edge flap, multibody dynamic analyses were performed while changing the flap center location to 65~85%R. In this analyses, the flap length and flap chord length are 20%R and 15%c, respectively. The vibratory loads of the rotor hub and the vibration index values are shown in Figs. 2.36-2.38 when the flap is actuated at 3, 4, and 5/rev.

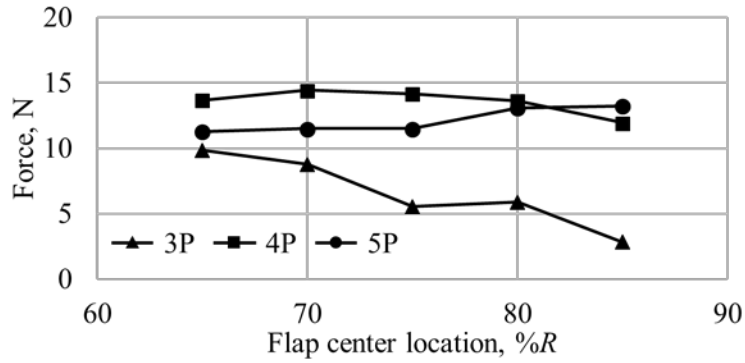

(a) Forward vibratory shear loads

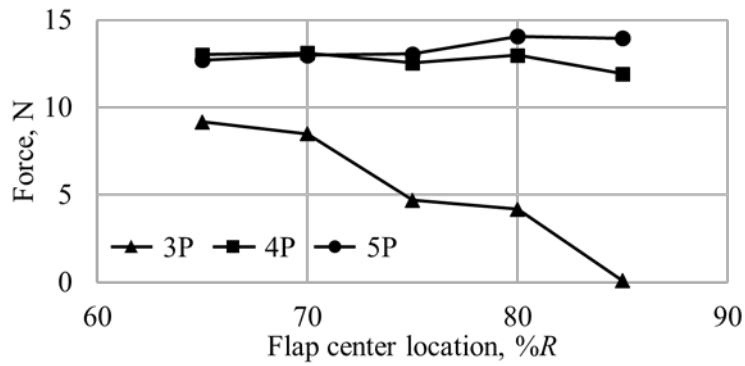

(b) Sideward vibratory shear loads

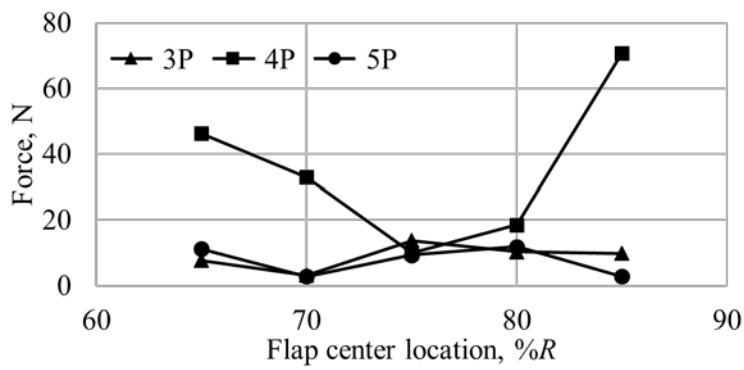

(c) Vertical vibratory shear loads

Fig. 2.35 4/rev hub vibratory loads according to flap center location

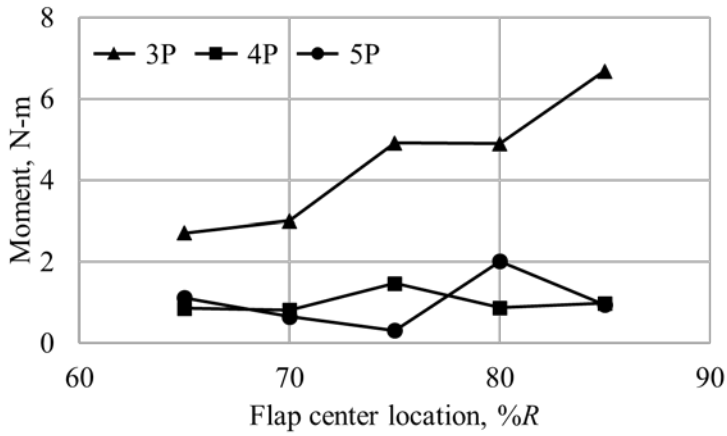

(a) Vibratory chord bending moments

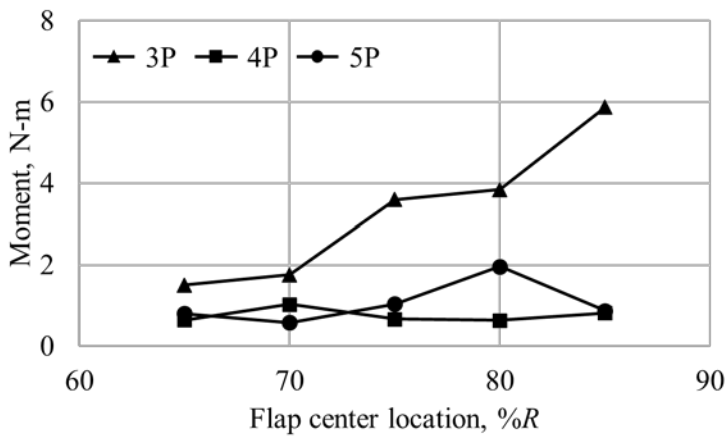

(b) Vibratory flap bending moments

Fig. 2.36 4/rev hub vibratory moment according to flap center location

As shown in the forward loads (Fig. 2.36(a)) and sideward loads (Fig. 2.36(b)), there is no significant difference in the 4 and 5/rev condition depending on the flap center location. However, in the 3/rev condition, the vibratory load decreases as the flap center location increases. Also, it is observed that the vibratory moment (Fig. 2.37) increased as the location of the

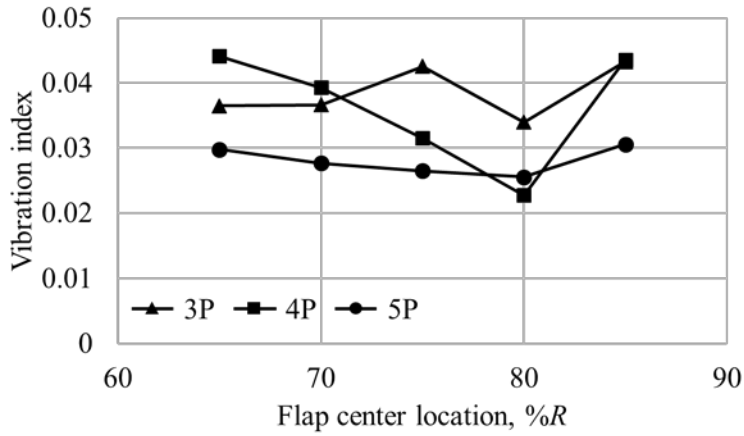

Fig. 2.37 Vibration index according to flap center location

flap was closer to the blade tip. In the vertical direction where the highest vibratory load occurs, vibratory loads are similar level under the 3 and 5/rev condition, but in the 4/rev actuation, the lower vibratory load is found at the 75%*R*.

As can be seen from these results, when the flap center location is smaller than 75%*R*, the vibratory moment decreases, and vice versa, the vibratory load in the forward and sideward directions increase. Based on these findings, the flap center location of the SNUF blade is determined to be 75%*R*.

2.4.3.2 Case 2: Flap Length Change

The results of hub vibratory loads of SNUF according to the flap length are shown in Figs. 2.39-2.41. While performing the multibody dynamic analysis with various flap length, the flap center location and the flap chord length are

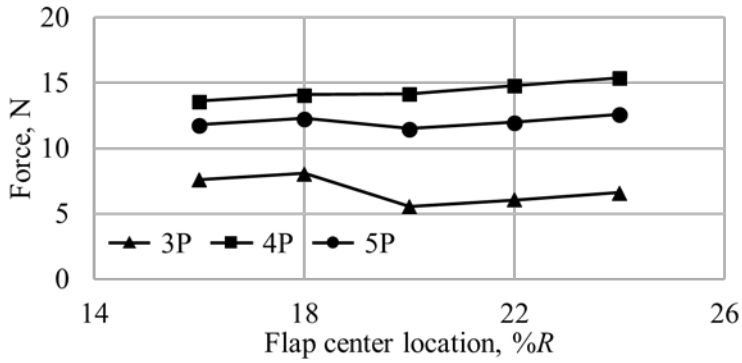

(a) Forward vibratory shear loads

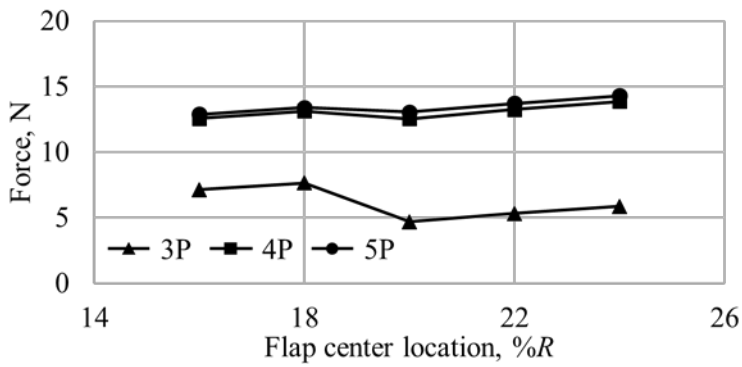

(b) Sideward vibratory shear loads

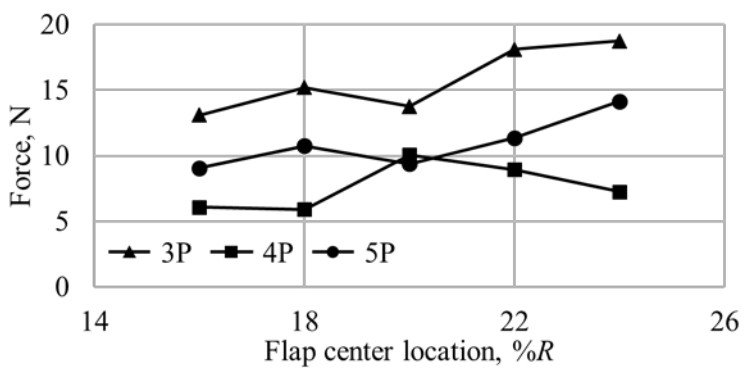

(c) Vertical vibratory shear loads

Fig. 2.38 4/rev hub vibratory loads according to flap length

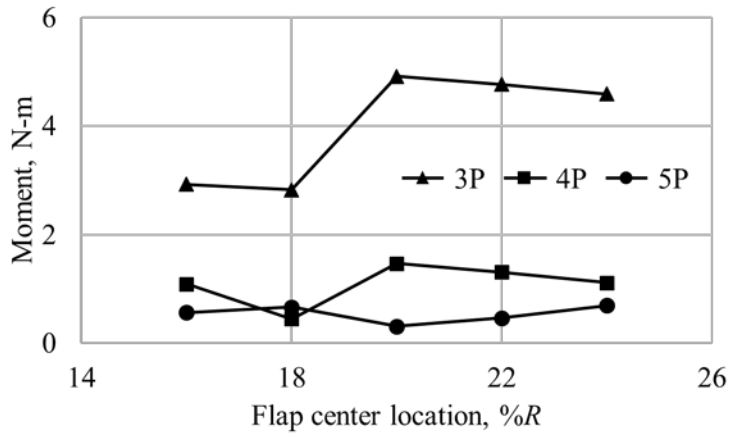

(a) Vibratory chord bending moments

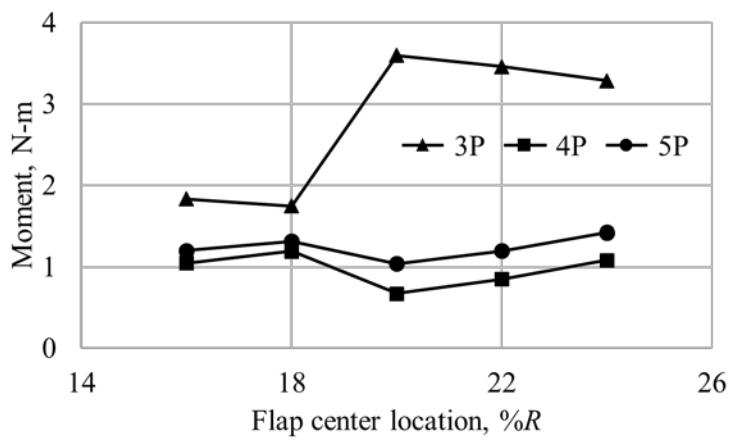

(b) Vibratory flap bending moments

Fig. 2.39 4/rev hub vibratory moment according to flap length

fixed at 75%*R* and 15%*c*, respectively. First, vibratory shear loads (Fig. 2.39) have the lowest values for flap length of 20%*R* in all actuation condition. The only 4/rev flap actuation induces a higher vertical vibratory load with the flap length of 20%*R*. In the case of the vibratory moments (Fig. 2.40), different tendencies are shown depending on the actuation frequency of the trailing-edge

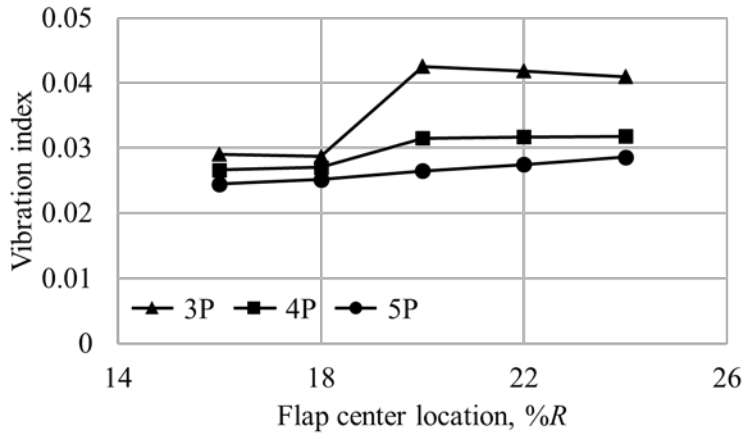

Fig. 2.40 Vibration index according to flap length

flap. In the chord bending moments, 3 and 4/rev actuation cause that the vibratory load of the 20%*R* flap is the highest value when compared with those of the other flap lengths. On the other hand, the vibratory load of 20%*R* flap which is actuated with 5/rev, is the lowest value among the chord bending moment results with 5/rev actuation. In case of the flap bending moments, the vibratory moment of 20%*R* flap is the highest value at 3/rev actuation, while the lowest vibratory moment is observed at 20%*R* when flap is actuated at 4 and 5/rev. Since the vibration index (Fig. 2.41) is considerably affected by vibratory moments, it has a similar tendency to that of the vibratory moments. It can be seen that even if the flap length is become longer than 20%*R*, there are not significant change in the vibration index value.

These results are summarized as follows: In the case of the hub shear load, the vibratory loads decrease when the flap is 20%*R* in length. Otherwise the hub moments have low values when flap is shorter than 20%*R*, and there are

not meaningful difference in the vibratory moment value when the flap length is 20%*R* or more. Considering the absolute amplitude, however, 20%*R* flap length is chosen to effectively reduce the vibratory shear loads, since the higher vibrations occur at the hub shear loads than hub moments.

2.4.3.3 Case 3: Flap Chord Length Change

Finally, in order to predict the influence of the flap chord length on the hub vibratory loads of the blade, the flap center location and flap length are restrained to 75%*R* and 20%*R* respectively, and the flap chord length is varied from 10%*c* to 20%*c* when the multibody dynamic analyses are conducted. The results are shown in Figs. 2.42-2.44.

The 4/rev vibration components of forward shear loads (Fig. 2.42(a)) and sideward shear loads (Fig. 2.42(b)) tend to decrease as the chord length of the flap increases. If the flap chord length are increased by more than 17.5%*c*, the vibratory loads are increased rather. Similar trend are found for vertical shear loads (Fig. 2.42(c)) in the 3 and 5/rev actuation condition, but opposite result is observed when the flap is actuated in 4/rev frequency. As the chord length of the flap becomes longer, the vibratory loads with 4/rev flap actuation are increased and the maximum vibratory vertical load occurs at 17.5%*c*. The vibratory hub moments (Fig. 2.43) have a similar tendency to the vertical shear loads of 4/rev flap actuation. The highest 4/rev vibratory moments occur at

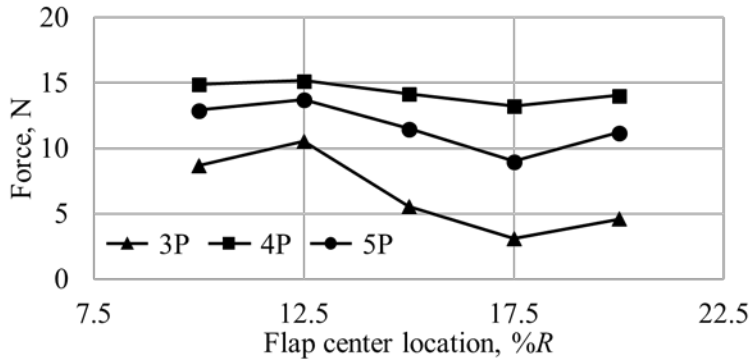

(a) Forward vibratory shear loads

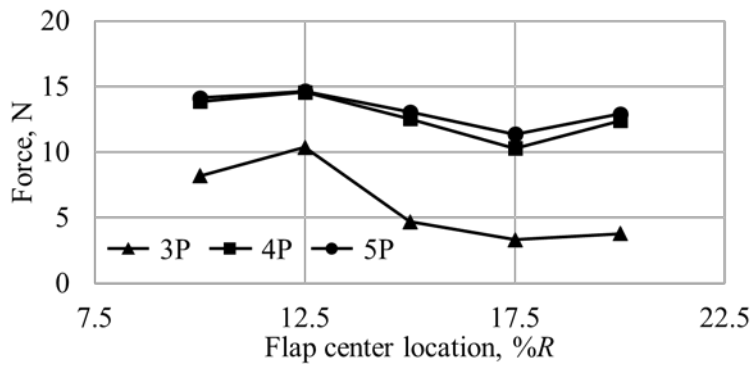

(b) Sideward vibratory shear loads

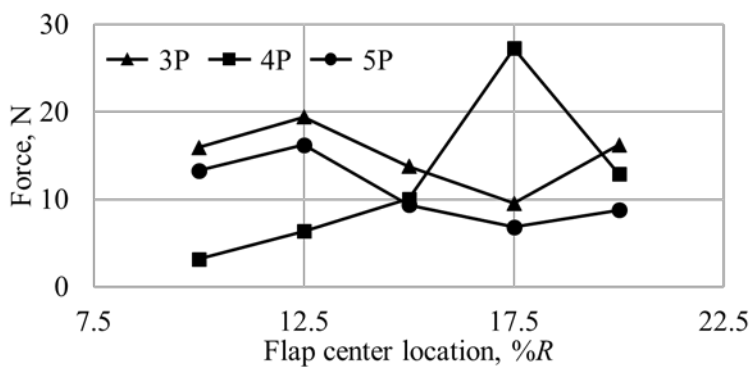

(c) Vertical vibratory shear loads

Fig. 2.41 4/rev hub vibratory loads according to flap chord length

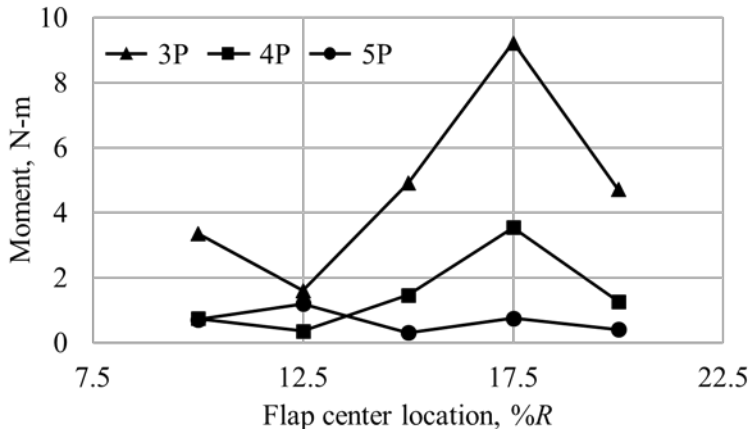

(a) Vibratory chord bending moments

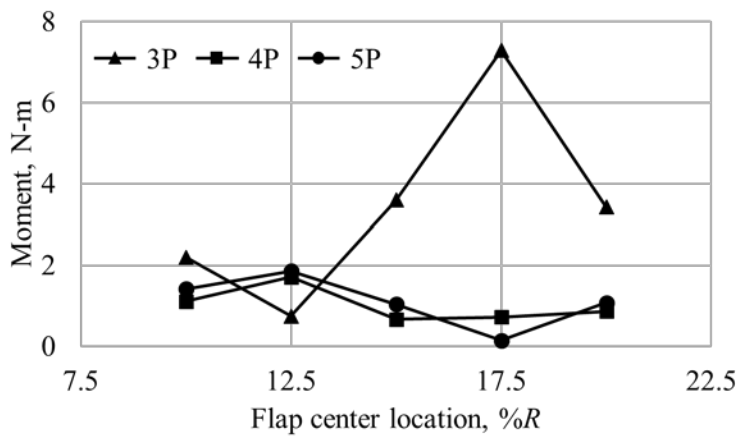

(b) Vibratory flap bending moments

Fig. 2.42 4/rev hub vibratory moment according to flap chord length

17.5%*c*. This tendency is also observed in the vibration index results (Fig. 2.44).

Based on these results, the flap chord length is determined to be 15%c. The trailing-edge flap shorter than 15%*c* does not successfully reduce the 4P vibration amplitude of the hub shear loads. Conversely, the flap longer than 15%*c* causes a higher hub vibratory moments, and the 17.5%*c* flap raises the vibratory loads in the vertical shear load and moments.

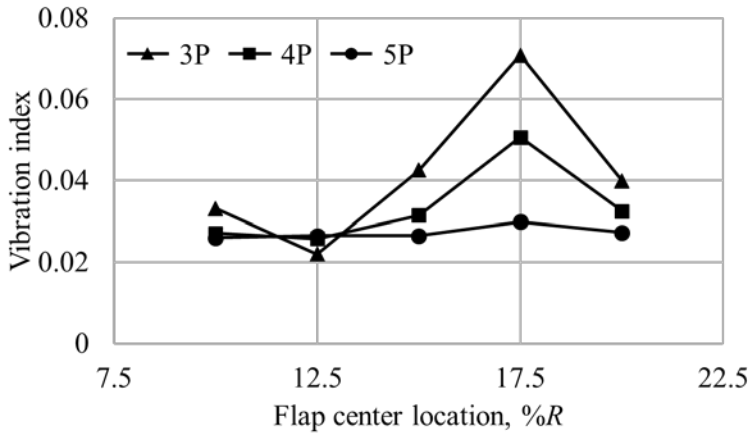

Fig. 2.43 Vibration index according to flap chord length

2.4.4 Blade Cross Sectional Design Results

In the present optimization process, optimized cross sectional configurations are obtained by the genetic algorithm with population size corresponding to thirty and an elite count corresponding to two. The parameters, constraints, and optimized values are summarized in Table 2.12. Violations of constraints are

Table 2.12 Constraints and optimized values

Parameter	Lower bound	Upper bound	Optimized
X_{CG}	24.0%c	26.0%c	24.9%c
X_{SC}	24.0%c	26.0%c	25.3%c
Lock number	8.5	10.5	9.3
1st Tors. Freq.	N/A	3.00/rev	2.53/rev
Strain margin	N/A	50%	35%

not observed. The shear center and the center of gravity are located at the 25% chord. The optimized SNUF blade correspond to the Lock number of 9.35. The 1st torsional frequency correspond to 2.53 /rev, which represents a significant decrease of 22% when compared to those of the previous SNUF blade.

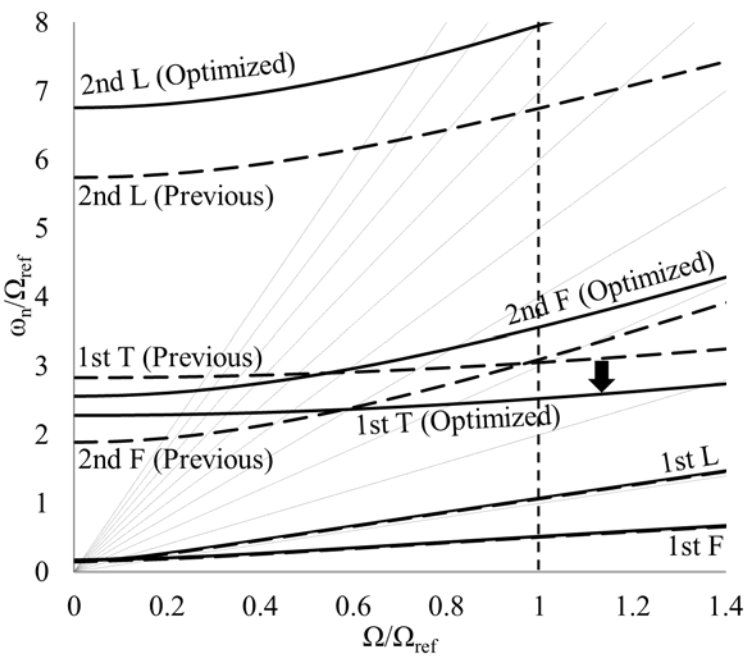

Fig. 2.44 Comparison of the natural frequencies between the previous SNUF blade and the present

Figure 2.45 shows the fan diagram that compares the frequency characteristics between the previous SNUF blade design and the present optimized SNUF blade design. As shown in Fig. 2.45, in the previous design, the 1st torsional and 2nd flap frequencies intersect near the nominal rotation speed and its value is quite close to $k \times N_b$/rev where k is an integer. These may

lead to flap-torsional coupled resonance under nominal rotating condition during practical operation. On the other hand, for the blades with the optimized section, the first torsional frequencies are lowered and the 2nd flap frequencies become higher. Therefore, natural frequencies that are integral multiples of the blade rotating frequency are not found near the nominal rotating condition. Since the first torsional frequencies are lowered, it is expected that the control authority of the hub vibratory loads by the trailing-edge flap will increased.

The optimized cross-sectional design configurations are illustrated in Fig. 2.46. With respect to the present optimization, the end position of the front section and the spar position is determined as 15%*c* and 42%*c*, respectively. Additionally, the mass of the ballast weight to adjust the center of gravity of the standard section and the special section to the quarter chord position are calculated as 0.0746 kg/m and 0.2536 kg/m, respectively. The total weight of the optimized SNUF blade corresponds to 0.907 kg, which was 15.2% less than the weight of the previous SNUF blade (1.069 kg). The detailed optimized and designed values are summarized in Table 2.13.

As shown, in Fig. 2.47, the internal loads and moments are predicted at each blade station by CAMRAD II. A non-uniform inflow using free-wake geometry is used in the analysis. As given in Table 2.11, three trim variables and quantities are used for the forward flight condition with an advance ratio of 0.3. The blade internal loads are used to evaluate the structural integrity of the present cross section with a safety factor corresponding to 1.5. The results of the structural

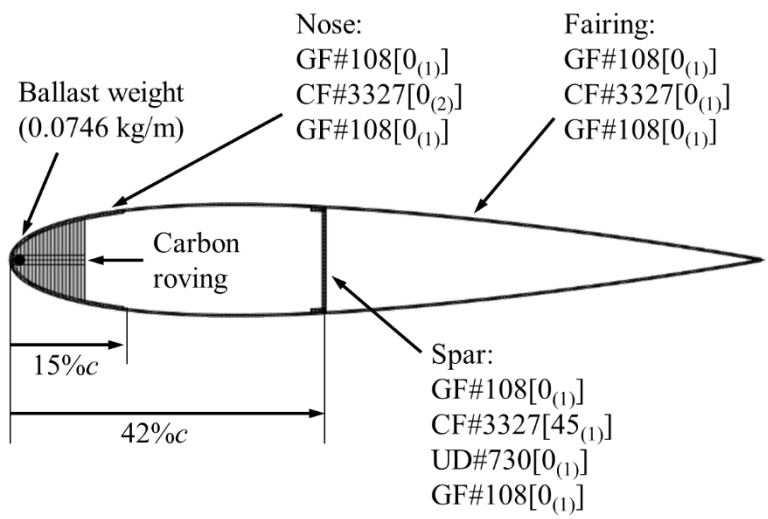

(a) Standard section optimization result (Section B5)

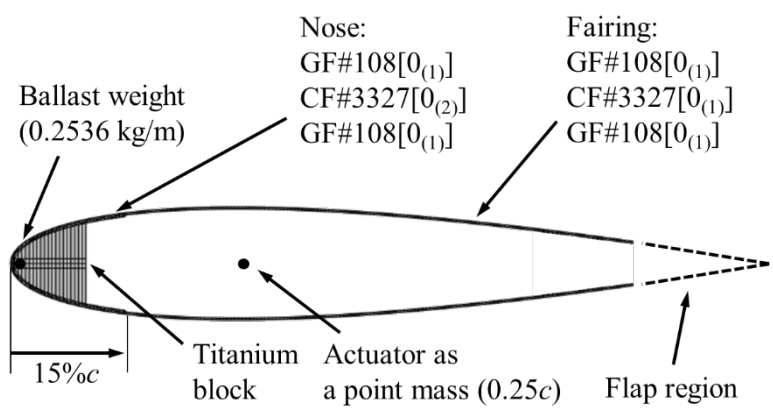

(b) Special section modification result (Section B7)

Fig. 2.45 Final cross-sectional design configuration of the SNUF blade

Table 2.13 Design optimization results

Symbol in Fig. 2.27	Design variable	Standard section	Special section
A	End position of nose section	15%*c*	
B	Spar position	42%*c*	N/A
C	Material for entire section	Carbon fiber #3327	
D	Material for nose section	Carbon fiber #3327	
E	Material for spar – inner	CF #3327	N/A
F	Material for spar – outer	UD #730	N/A
G	Ply angle for entire section	0°	
H	Ply angle for nose section	0°	
I	Ply angle for spar – inner	45°	N/A
J	Ply angle for spar – outer	0°	N/A
K	Number of piles for entre section	1	
L	Number of piles for nose section	1	
M	Number of piles for spar – inner	1	N/A
N	Number of piles for spar – outer	1	N/A
O	Mass of ballast weight, kg/m	0.0746	0.2536

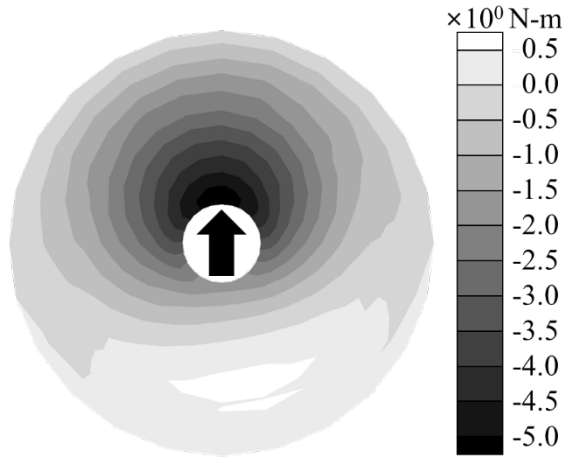

(a) Torsional moments

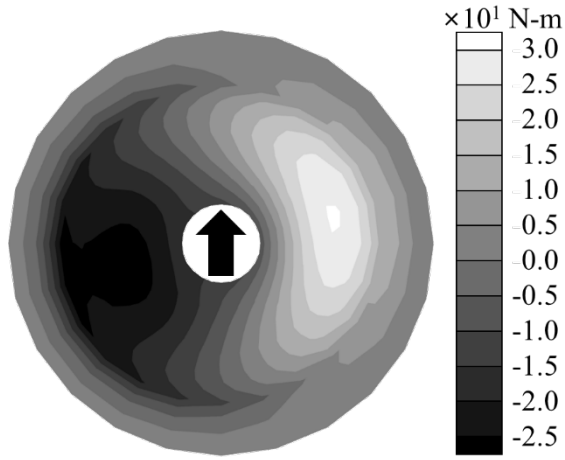

(b) Flapwise bending moments

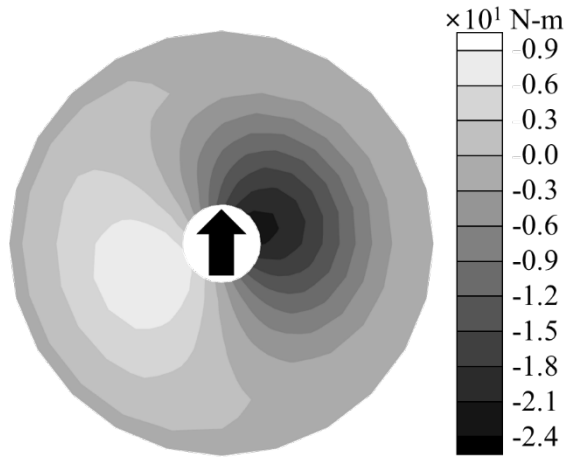

(c) Lagwise bending moments

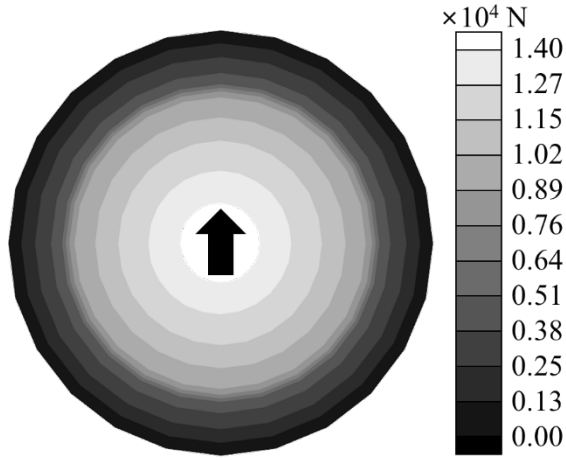

(b) Axial loads

Fig. 2.46 Blade internal load distributions

integrity along the blade span are shown in Fig. 2.48. Ply failures were not observed, and maximum strain in the optimized cross section corresponded to 35% of the allowable strain.

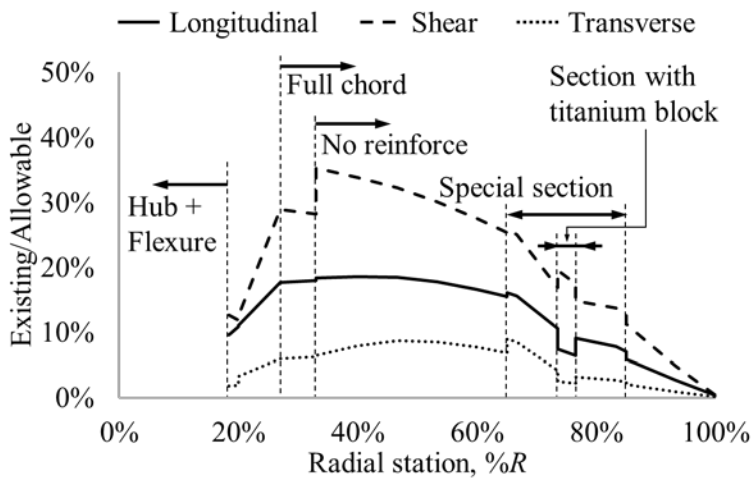

Fig. 2.47 Strain recovery analysis results

2.4.5 Vibratory Load Reduction Capability

The present optimization framework is used to design the cross sectional configuration of the SNUF blade that satisfied all the constraints. The optimized blade design does not feature ply failure, and the first torsional frequency is lower than that of the previous SNUF blade. Therefore, it is expected that the present optimized SNUF blade is more capable of handling the vibration reduction performance.

A multibody dynamic model for the SNUF blade with optimized section is generated and implemented to the hub vibratory load reduction analyses under the designated forward flight condition (μ = 0.3, α_s = -6°). Since the cross-sectional properties are newly obtained, the 4P hub vibratory load baseline of optimized SNUF blade differs from those of previous blade. Therefore, the baseline analysis for the optimized SNUF blade is performed first, and the vibratory load reduction analyses by the trailing-edge flap are conducted by applying the estimated trim angles. The vibratory load reduction results are shown in Figs. 2.49-2.54. In order to compare the vibration reduction capability of active flap blades with different baselines, the rate of changes with respect to the baseline for each vibratory load are shown instead of the absolute values.

For forward vibratory shear loads (Fig. 2.49), the maximum vibration reduction rates of previous and optimized blade are similar for 3 and 4/rev actuation. However, it can be seen that the optimized blade has better vibration reduction capability in all control phases, including 5/rev actuation condition. On average, the optimized blade further reduces the 4P hub forward vibratory shear load by 9% more than the previous blade. The similar tendency is also found in the results of vibratory loads in the sideward direction (Fig. 2.50). It is observed that the optimized blade decreases the vibratory load by 8% more than the previous blade on average. The fact that optimized blade have better vibration reduction capability is evident from the results of vertical vibratory shear loads (Fig. 2.51). In 3/rev actuation condition, optimized blade diminishes

the vibratory loads by 20% more than previous one. When the flap is actuated with 4/rev, the optimized blade can reduce vibratory loads by up to 67%, while vibration reduction of 59% occurs for previous one. For 5/rev flap actuation, the previous blade decreases vibration more than the optimized blade in some control phases, but in most of other control phase range the optimized blade reduces the vibratory load by an average of 17% more than the previous one.

The difference in vibration reduction capability is more obvious when the vibratory moment results are compared. When the trailing-edge flap is actuated with 3/rev, the vibratory chord bending moments (Fig. 2.52) are increased in both the previous and optimized blades. However, on previous blade, vibratory loads are increased by up to four times, while the optimized blade increase the vibration by only 2.5 times. In the 4/rev condition, the previous blade can only decrease the vibratory loads by as large as 15%, whereas the optimized blade can reduce the vibratory loads by up to 63%. For 5/rev actuation, the previous blade has a higher maximum vibration reduction rate than the optimized blade, but the average reduction rate of the optimized blade is 11% greater than that of the previous one. For the flap bending moments (Fig. 2.53), the optimized blade reduces vibratory loads by 54%, 27% and 14% on average for 3, 4 and 5/rev actuation condition, respectively, more than previous blade. Specifically, in 3/rev actuation, the optimized blade decreases vibratory loads up to 7%, while the previous blade does not reduce the vibratory load with all control phase. In the vibration index, vibratory loads in five directions are considered

together according to Eq. (2.30). The vibration index results (Fig. 2.54) show that the vibration reduction capability of the optimized blade is superior to that of the previous one. In all the flap actuation conditions, higher vibration reduction rate are observed than for the previous blade. Based on these results, it can be concluded that the optimized blade which is designed through the developed optimization framework have better vibration reduction capability than the blade with the previous sectional design.

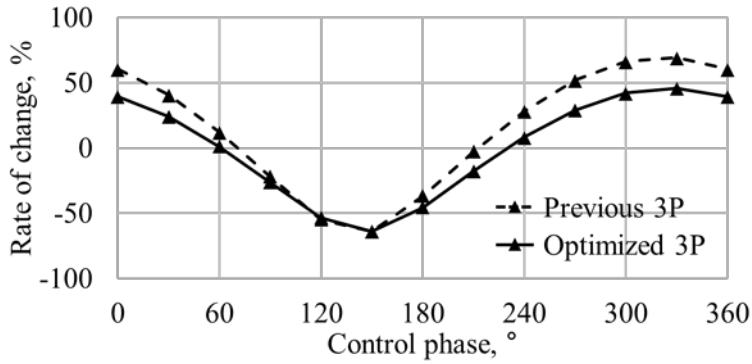

(a) 3P actuation

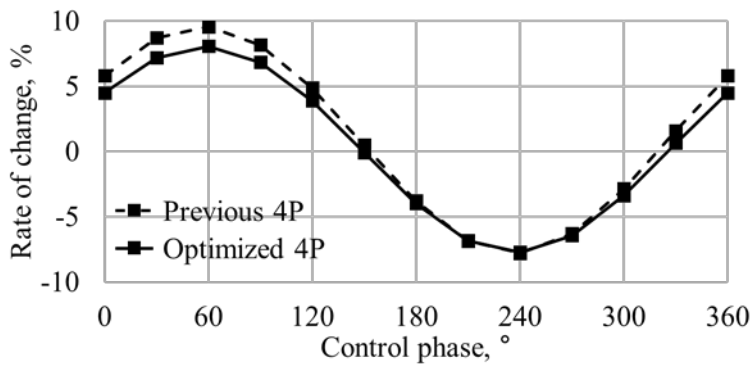

(b) 4P actuation

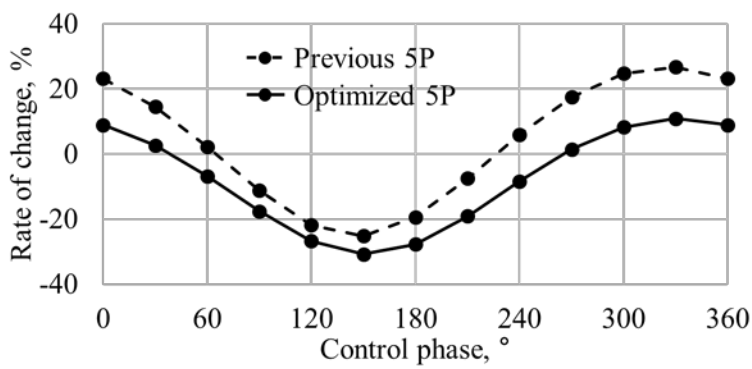

(c) 5P actuation

Fig. 2.48 4/rev hub forward vibratory shear loads

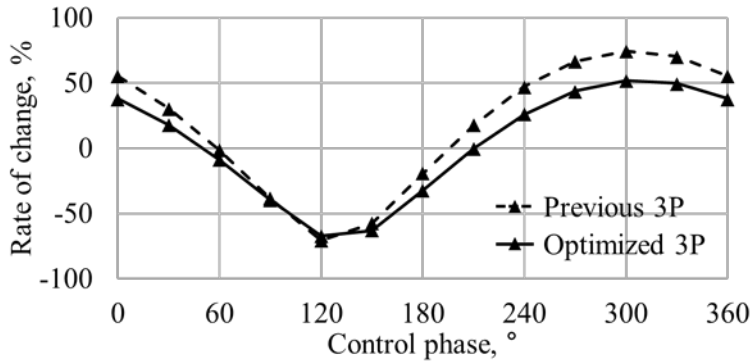

(a) 3P actuation

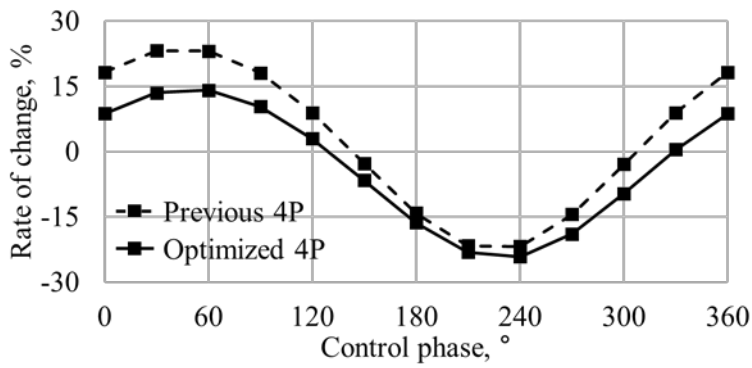

(b) 4P actuation

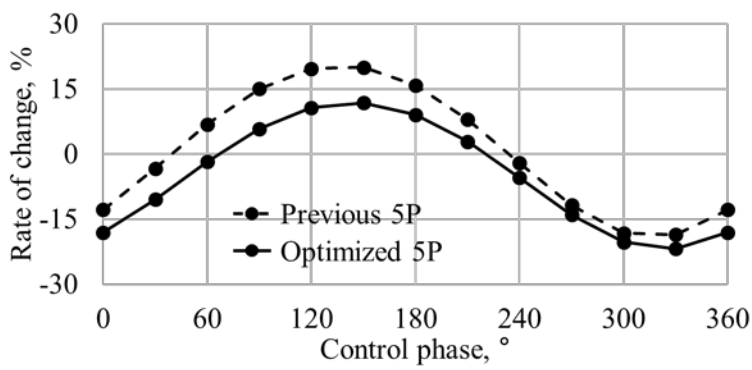

(c) 5P actuation

Fig. 2.49 4/rev hub sideward vibratory shear loads

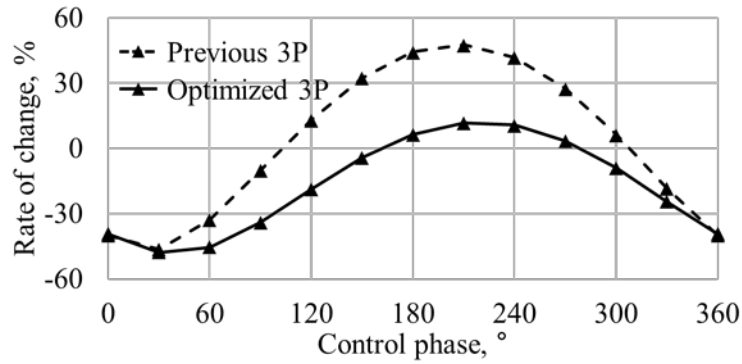

(a) 3P actuation

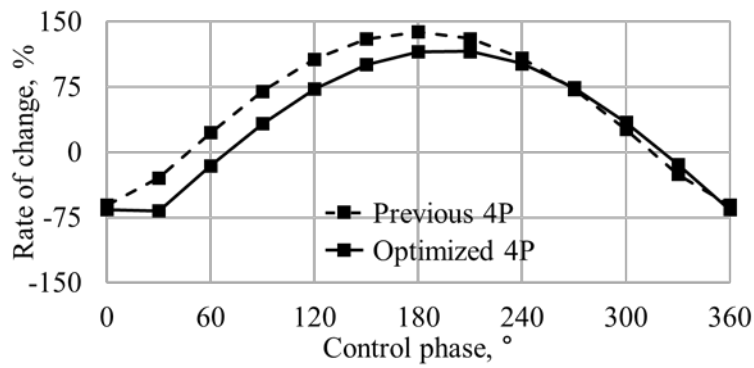

(b) 4P actuation

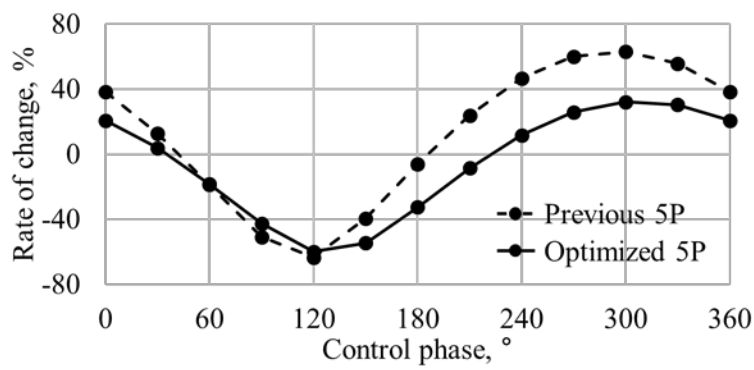

(c) 5P actuation

Fig. 2.50 4/rev hub vertical vibratory shear loads

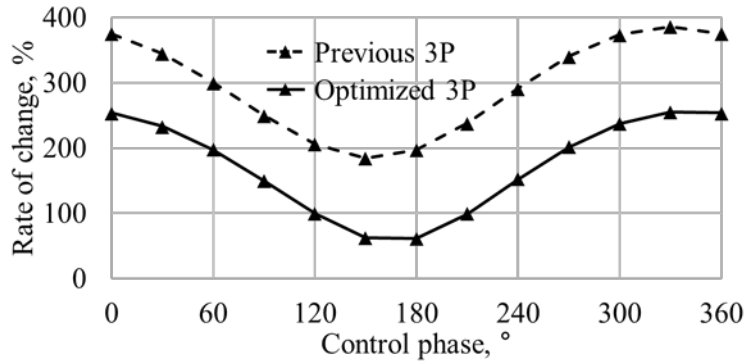

(a) 3P actuation

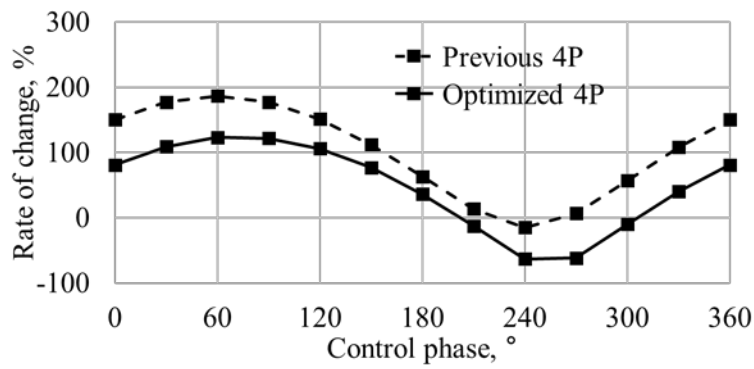

(b) 4P actuation

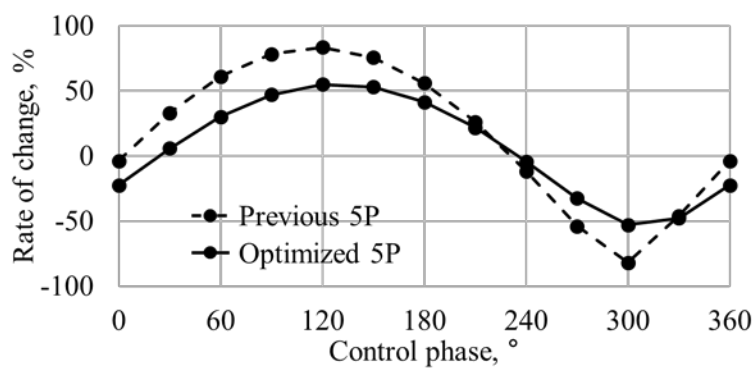

(c) 5P actuation

Fig. 2.51 4/rev hub vibratory chord bending moments

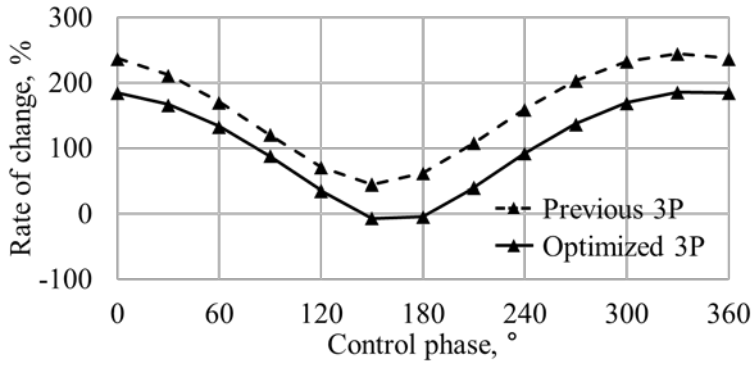

(a) 3P actuation

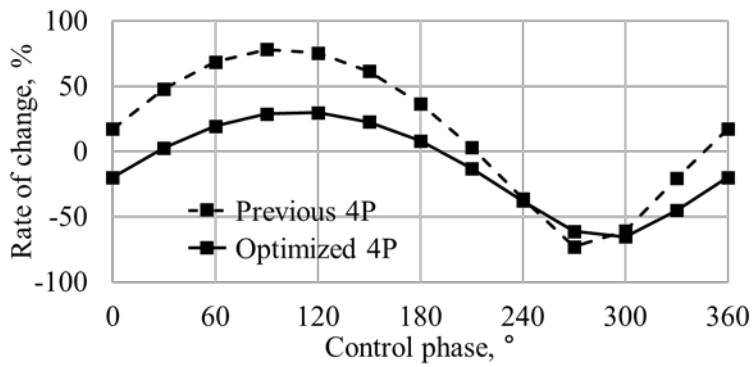

(b) 4P actuation

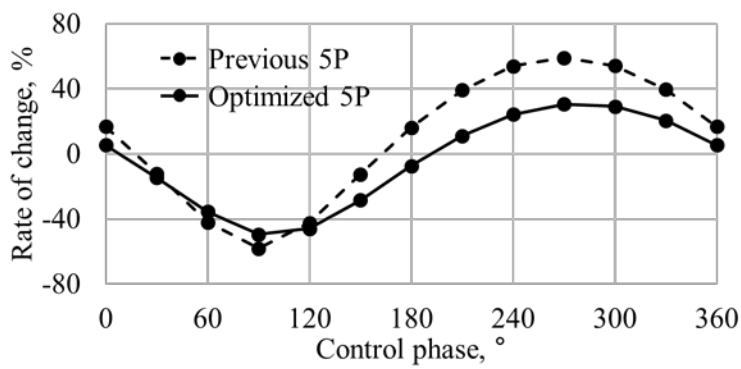

(c) 5P actuation

Fig. 2.52 4/rev hub vibratory flap bending moments

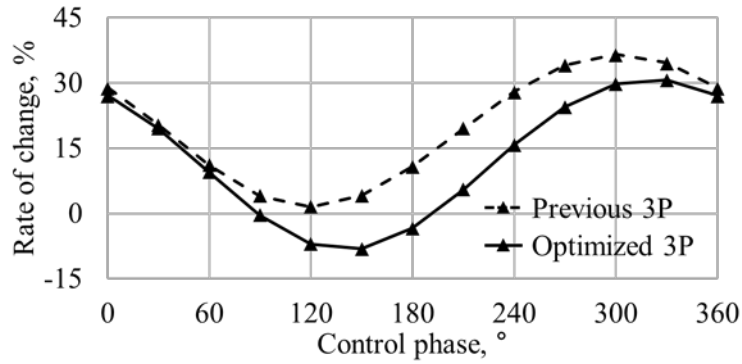

(a) 3P actuation

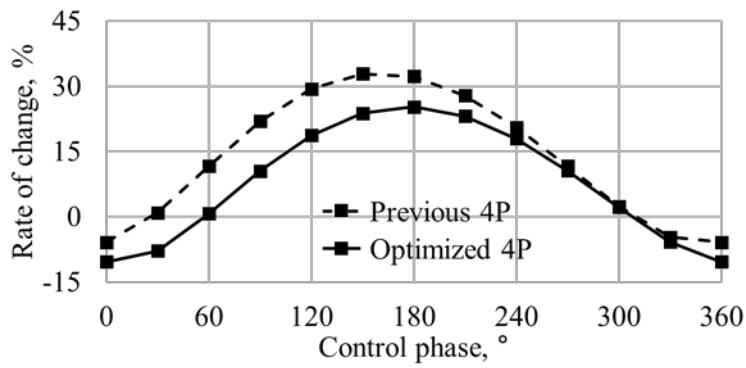

(b) 4P actuation

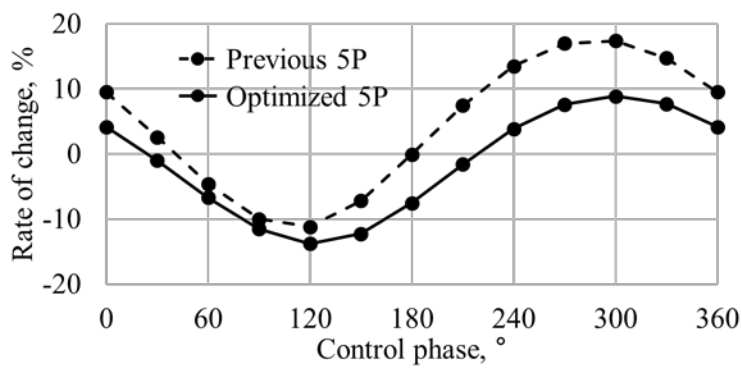

(c) 5P actuation

Fig. 2.53 Vibration index for 4P hub vibratory loads

Chpater 3

Evaluation on the Structural Integrity of the Composite Blade

This chapter will discuss the structural integrity of the present SNUF blade in various methods. First, detailed results and discussions on the strain recovery analysis used in the sectional design optimization framework introduced in Chapter 2 will be presented. Second, in-plane stresses occurring at the blade root – hub connection region will be considered. Finally, evaluation on the structural safety of the present rotor blade will be completed by performing three-dimensional static structural analysis including all the specific components, such as the flap-driving components.

3.1 Strain Recovery Analysis within the Cross Section

As presented in Chapter 2, the optimization framework provides for the blade section design and strain recovery analysis. In order to perform strain recovery analysis, the cross-sectional properties and blade internal load information at the designated locations are required. Sectional properties are obtained by GT/VABS [153], and internal loads are estimated by CAMRAD II [159]. The

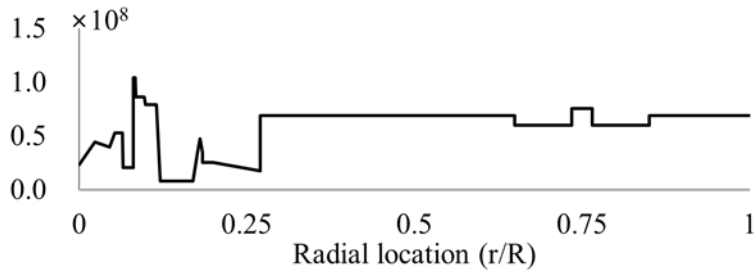

(a) Axial stiffness, N

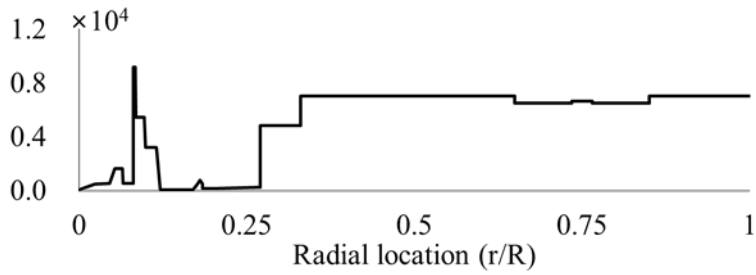

(b) Torsion stiffness, N-m^2

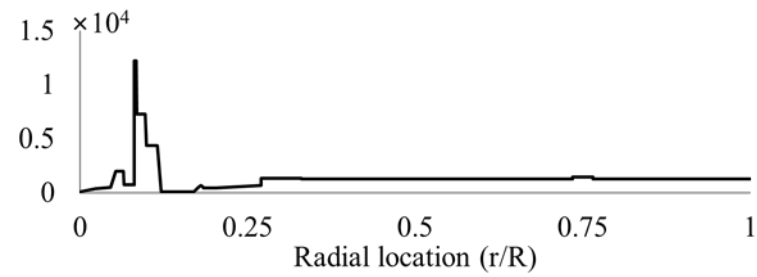

(c) Flap bending stiffness, N-m^2

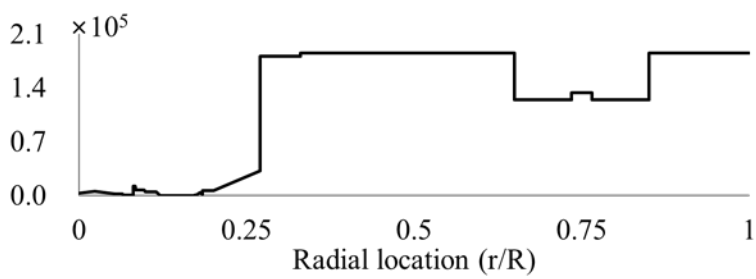

(d) Lag bending stiffness, N-m^2

Fig. 3.1 Stiffness properties of optimized SNUF blade

cross-sectional properties of the optimized SNUF blade are shown in Fig. 3.1.

The location of the sections where the strain recovery analysis is performed are summarized in Table 3.1 and the results are shown in Fig. 2.48. Regarding these results, the results for the following three locations are discussed in further detail: 1) the blade root region; 2) the section where the maximum strain occurs; 3) the section containing the titanium block. Figures 3.2-3.4 show the design results of the three specified locations.

Table 3.1 Locations and types of sections used in the strain recovery analysis

Location	Section number used in Table 2.7	Description
0.276 m	Section B1	Blade root (+10ply)
0.300 m	Section B1	Blade root (+10ply)
0.300 m	Section B2	Transition (+9ply)
0.405 m	Section B3	Full chord blade (+2ply)
0.405 m	Section B4	Full chord blade (+1ply)
0.495 m	Section B4	Full chord blade (+1ply)
0.495 m	Section B5	Standard section
0.975 m	Section B5	Standard section
0.975 m	Section B6	Special section with a roving
1.102 m	Section B6	Special section with a roving
1.102 m	Section B7	Special section with titanium block
1.148 m	Section B7	Special section with titanium block
1.148 m	Section B6	Special section with a roving
1.275 m	Section B6	Special section with a roving
1.275 m	Section B5	Standard section
1.500 m	Section B5	Standard section

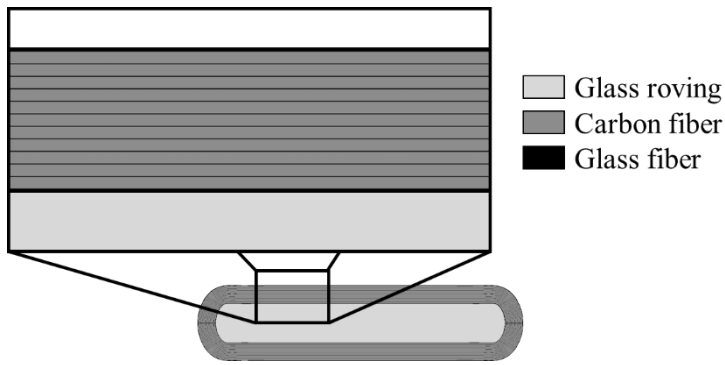

Fig. 3.2 Blade root cross section (Section B1)

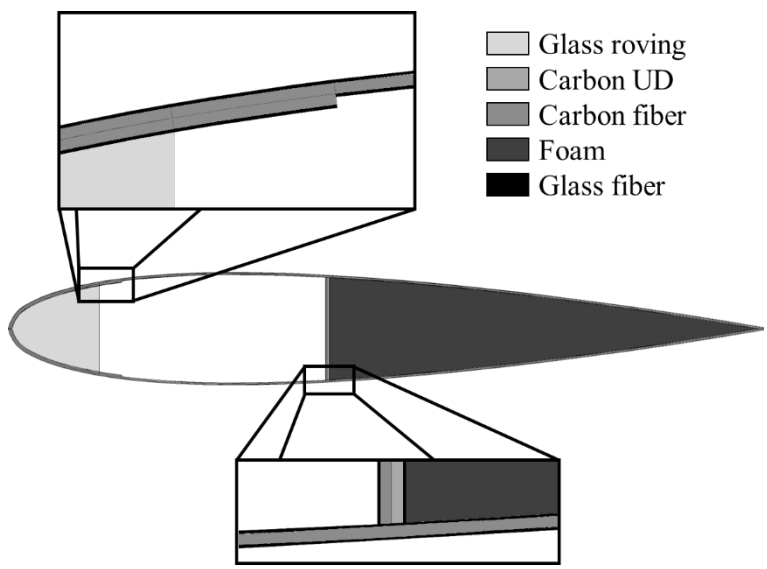

Fig. 3.3 Blade standard section (Section B5)

The first one is the section of the blade root region (Fig. 3.2). It is the location where the greatest axial load occurs on the blade due to the centrifugal loading. At the blade root section, 10 plies of carbon fiber are added to the baseline lay-up of the standard section. The innermost is filled with the glass fiber roving in order to grab the root pins. The largest strain is observed at the 33%*R* location

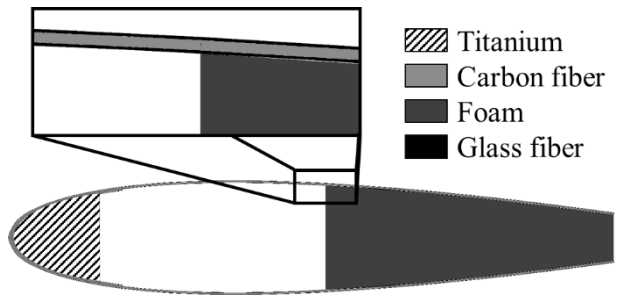

Fig. 3.4 Blade special section (Section B7)

(Fig. 3.3) where there is standard section with no additional plies for the blade reinforcement. This location has a cross-section of the standard section obtained by the design optimization process. The inside of the nose of the standard section is filled with the glass fiber roving and the rear side of the spar is filled with a foam core. Foam core is required in the fabrication process to provide sufficient back pressure for the prepreg plies during the curing process inside the mold. The presence of a foam core has little influence on the stiffness properties for the cross section. However, it is influential on the inertial properties. In the cross-sectional analysis performed in the present optimization framework, the existence of foam is considered for all the blade cross sections along the span. The last one is the special section filled with titanium instead of the glass fiber roving in front of the nose (Fig. 3.4). This section does not have the spar, and trailing-edge behind 80%*c* is eliminated considering trailing-edge flap mounting.

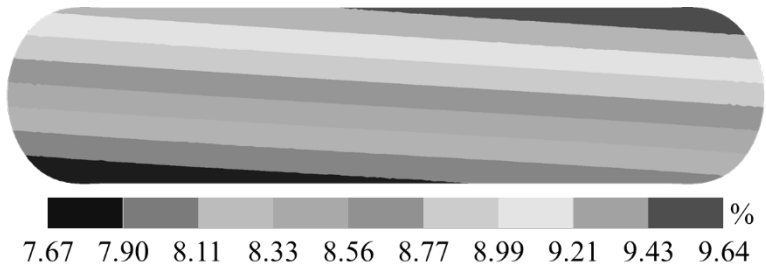

(a) Longitudinal strain

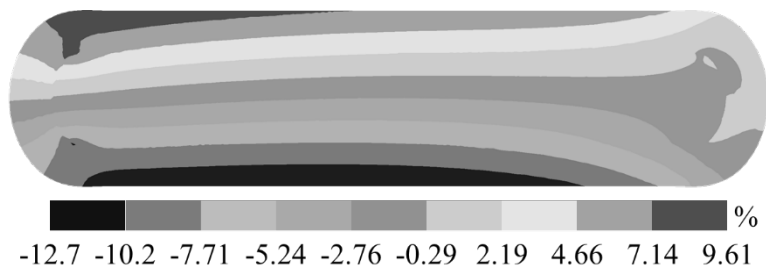

(b) Shear strain

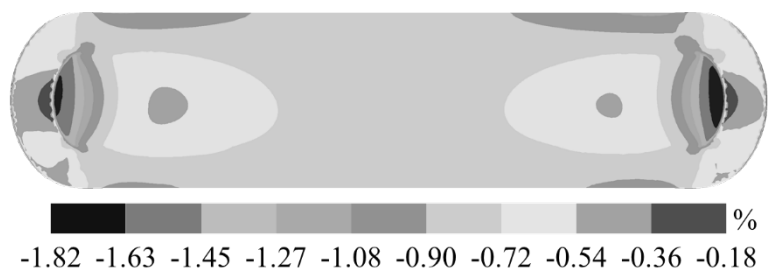

(c) Transverse strain

Fig. 3.5 Strain margin of safety at the blade root section

Figures 3.5-3.7 show the strain recovery analysis results at the following three locations: blade root, 33%*R* section, and 75%*R* section. The negative values shown in these figures indicate the compression strains. At the blade root (Fig. 3.5), the maximum strain occurs in the shear direction and is 12.7% out of the relevant allowable strain. The location where the maximum strain is observed is the 33%*R* of the blade, which amounts to 35% out of the allowable

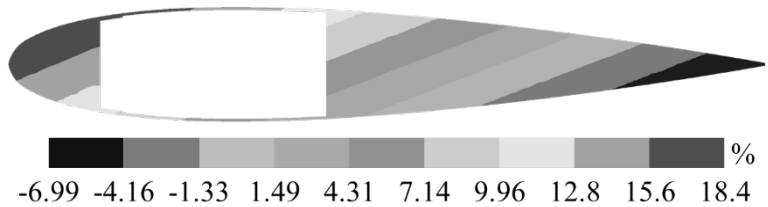

(a) Longitudinal strain

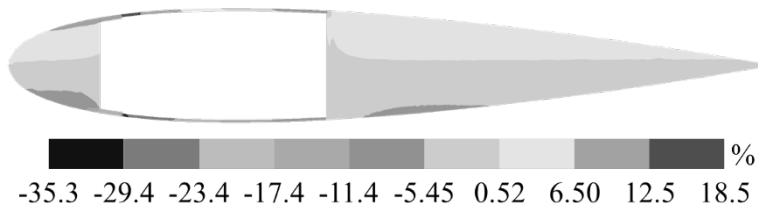

(b) Shear strain

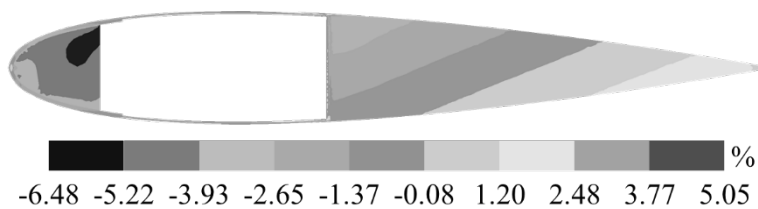

(c) Transverse strain

Fig. 3.6 Strain margin of safety at the 33%*R* section

shear strain (Fig. 3.6). At the 75%*R* location with the titanium block, ratio between the maximum strain and allowable strain is found in shear direction to be approximately 20%. Therefore, it is considered that the strain margin on the optimized cross section is sufficient, and no failure will occur under the loading condition occurring in the optimized SNUF blade.

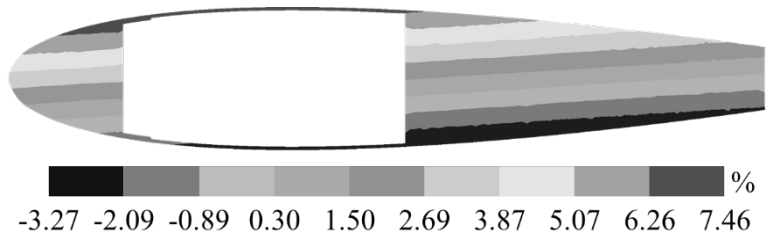

(a) Longitudinal strain

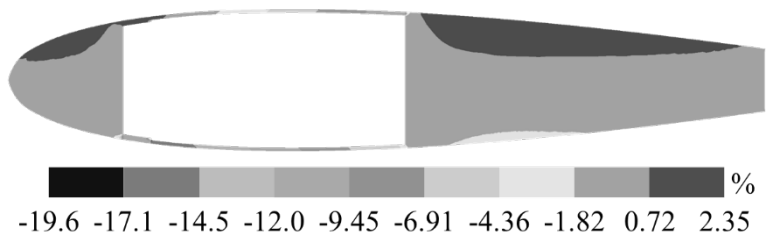

(b) Shear strain

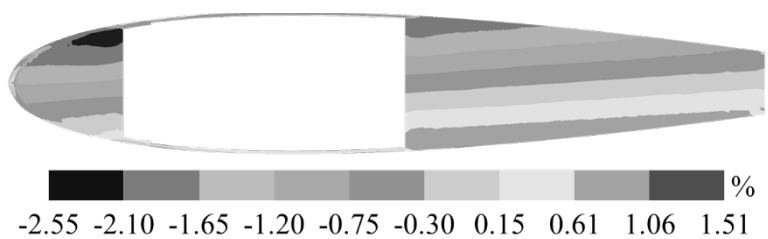

(c) Transverse strain

Fig. 3.7 Strain margin of safety at the 75%*R* section

3.2 Two Dimensional In-plane Stress Estimation

As shown in Fig. 3.8, the blade root is connected to the flexure using four pins and two plates. Therefore, the stress concentration occurs at the location where the pins and the holes are connected [160]. The stress distribution is significantly affected by the geometry of the holes and the pins. Investigations

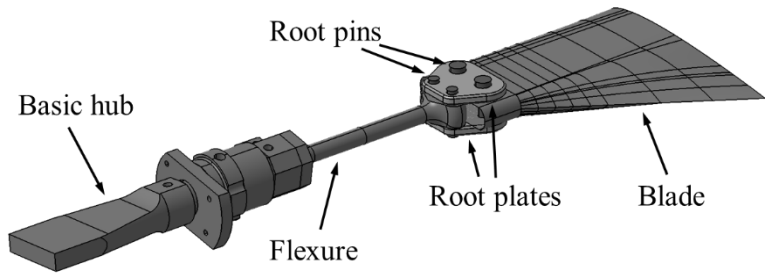

Fig. 3.8 Flexure – blade root connection

have revealed the three basic in-plane failure modes for the pin-loaded specimens: net-tension, shear-out and bearing [160]. Also, combinations of the two among the three modes may occur simultaneously under certain circumstances. Among those, the net-section failure is abrupt whereas the bearing failure is more ductile, which implies that the bearing failure is the preferred failure mode in many cases [161]. The typical three in-plane failure modes and the failure plane are illustrated in Fig. 3.9.

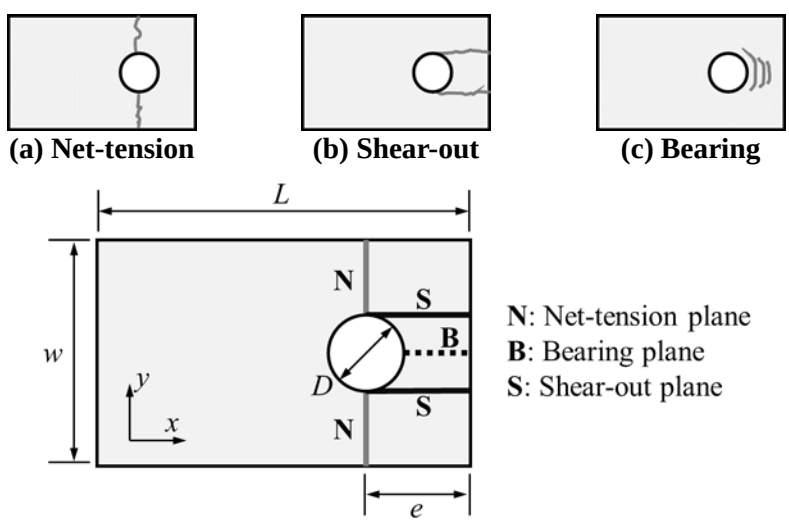

Fig. 3.9 Three basic in-plane failure modes of the pin-loaded joints

The bearing failure is primarily dominated by the matrix and fiber compression damage [162]. The bearing strength depends mainly on the maximum contact pressure applied. For the fixed-pin model, the contact pressure around the pin can be assumed to be co-sinusoidal [163], as illustrated in Fig. 3.10. When the friction coefficient is assumed to be zero, Ataş et al. [164] demonstrated that the cosine radial stress distribution could give a good approximation of the pin/laminate contact stresses around the hole boundary (the angle $\theta \in \left[-\frac{\pi}{2}, \frac{\pi}{2}\right]$ is measured in anti-clockwise direction from the *x* axis) and is expressed as

$$\sigma_{rr}(\theta) = \frac{4P}{\pi Dt}\cos\theta \tag{3.1}$$

where $\sigma_{rr}(\theta)$ is the radial bearing stress, P is the applied load, D is the hole diameter, and t is the thickness of the blade root.

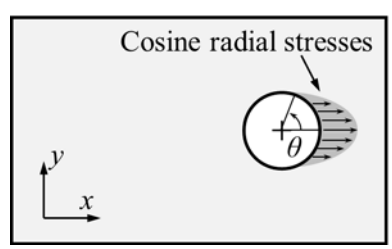

Fig. 3.10 Illustration of the cosine radial stresses near the circular pin

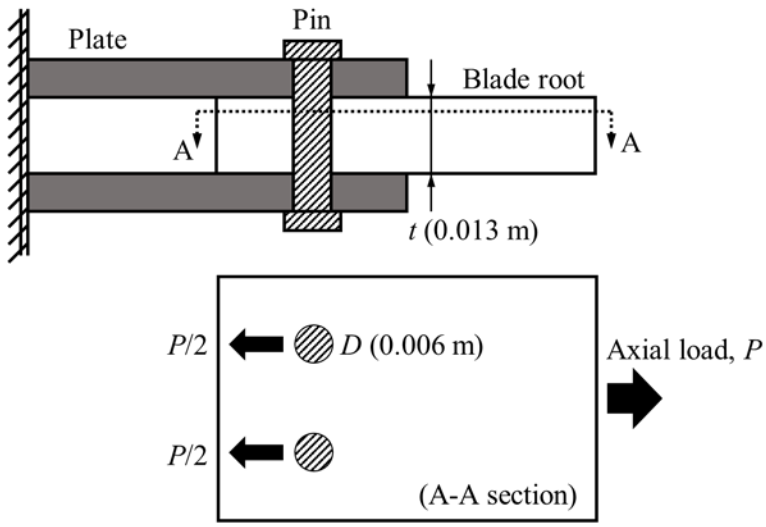

Fig. 3.11 Loading condition at the blade root

At the root region of the SNUF blade, there are two holes with 6 mm diameter steel pins. The axial load at that location is already derived from the CAMRAD II analysis and multiplied by a safety factor of 1.5. The loading situation at the blade root is simplified as shown in Fig. 3.11. Figure 3.12 shows the results of bearing stress prediction around the blade root pin. It can be seen that the maximum bearing stress is 49% out of the ultimate strength of the carbon fiber specified in Table 2.9. Therefore, it is concluded that bearing stress does not cause failure near the SNUF blade root pin.

3.3 Three-dimensional Static Structural Analysis

The strain recovery analysis that is implemented in the optimization framework can estimate only the structural integrity of the blade cross section.

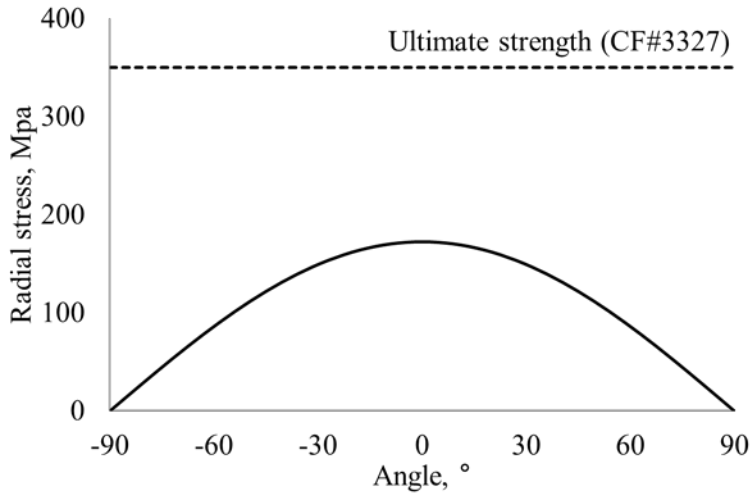

Fig. 3.12 Radial stress distribution around a pin hole

However, the piezoelectric actuator and flap-driving components are modeled as a single point mass. It is difficult to precisely predict the structural influence of the flap actuation components using the GT/VABS and CAMRAD II analysis. Thus, a detailed three-dimensional analysis that consider the contact situation is required for a better understanding of the structural behavior because of the additional components. It is possible to use the three-dimensional static structural analysis to estimate the stress distribution on the blade and observe the stress concentration. The strain recovery analysis, in-plane stress estimation, and three-dimensional structural analysis can be implemented to evaluate the structural integrity from the following three aspects:

- Strain recovery analysis: margin of safety for the strain along the blade span
- In-plane stress estimation: conservative predictions of bearing stress

around the root pin hole at the blade root region with the maximum axial load

- Three-dimensional static structural analysis: margin of safety for stress, stress distribution on the blade skin, the hub flexure, and the detailed components

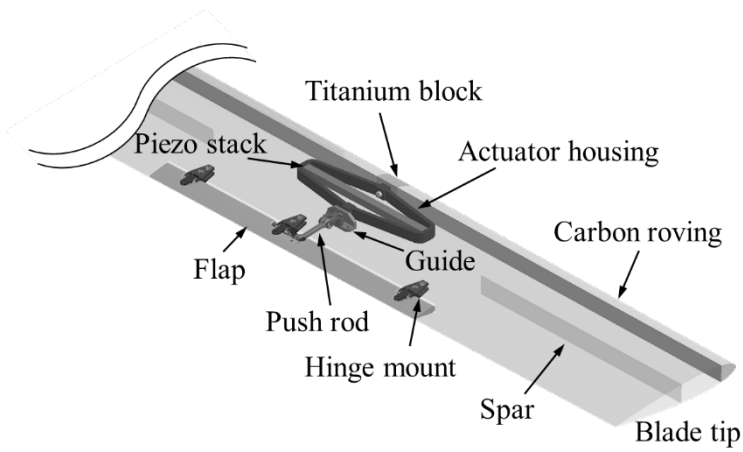

Fig. 3.13 Three-dimensional configuration of the SNUF blade

3.3.1 Three-dimensional Modeling of the SNUF Blade

The three-dimensional CATIA drawing of the optimized SNUF blade configuration is shown in Fig. 3.13. The three-dimensional finite element model with the contact condition is investigated by MSC.NASTRAN [165]. To account for the contact conditions among the components included in the analysis, each component is accounted. The list of the components and their

material types are summarized in Table 3.2. These detailed flap-driving components, and composite blade skin and spars, are incorporated into the three-dimensional finite element analysis.

Table 3.2 SNUF components used in the contact analysis

Number	Component	Material
1	Basic Hub	Ti6Al4V
2	Flexure	Ti6Al4V
3	4 mm root pin 1	SUS304
4	4 mm root pin 2	SUS304
5	6 mm root pin 1	SUS304
6	6 mm root pin 2	SUS304
7	Upper plate	Stainless steel
8	Lower plate	Stainless steel
9	Roving (root)	Carbon roving
10	Roving (tip)	Carbon roving
11	Titanium holder	Ti6Al4V
12	Actuator housing	Stainless steel
13	Piezo stack	PZT-5A
14	Actuator rod	SUJ2
15	Guide	Stainless steel
16	Bracket	SCM440C
17	Push rod bearing 1	SUJ2
18	Push rod	SCM440C
19	Push rod bearing 2	SUJ2
20	Horn	SCM440C
21	Hinge backlimb 1	Stainless steel
22	Hinge bearing 1	SUJ2

23	Hinge forelimb 1	Stainless steel
24	Hinge backlimb 2	Stainless steel
25	Hinge bearing 2	SUJ2
26	Hinge forelimb 2	Stainless steel
27	Hinge backlimb 3	Stainless steel
28	Hinge bearing 3	SUJ2
29	Hinge forelimb 3	Stainless steel
30	Thrust bearing	SUJ2
31	Flap	Carbon fiber reinforced plastics
32	Blade (root)	Composite lamination
33	Blade (transition)	Composite lamination
34	Blade (full chord)	Composite lamination

The sell elements (QUAD4) are used to model the blade skin and spar, and the solid elements (TET10) are used to model the flap-driving component and glass fiber roving. In addition, various contact and glue conditions are considered to derive a more accurate stress distribution. Figure 3.14 shows the contact and glue relationship among the components at the flexure-blade root connecting location. Also, this relationship can be described into the contact table as summarized in Table 3.3. In order to observe the stress concentration at the pin loaded region, contact conditions among the root pin, blade root, flexure, roving and root plates are implemented. A glue condition between the roving and blade root is also applied. The contact conditions also embody among the flap-driving components as shown in Fig. 3.15. A contact condition is applied between the guide and actuator rod, and another contact condition is

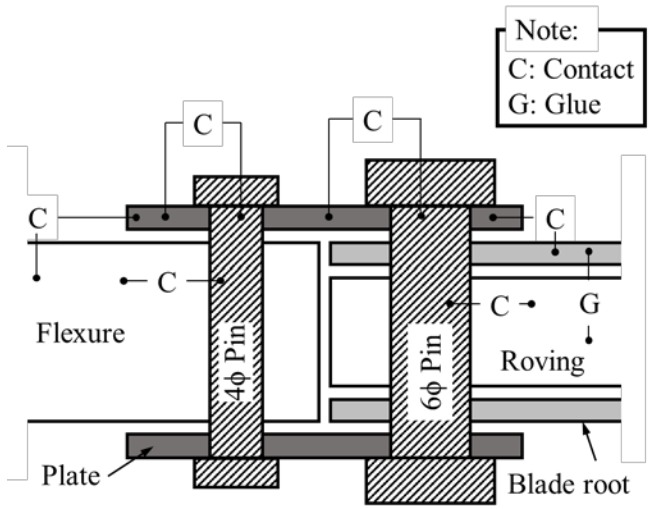

Fig. 3.14 Contact and glue condition at the flexure-root connection

Table 3.3 Contact table at the flexure-blade root connection

No. in Table 3.2	2	3	4	5	6	7	8	9	32
2		C	C						
3	C					C	C		
4	C					C	C		
5						C	C	C	
6						C	C	C	
7		C	C	C	C				
8		C	C	C	C				
9				C	C				G
32								G	

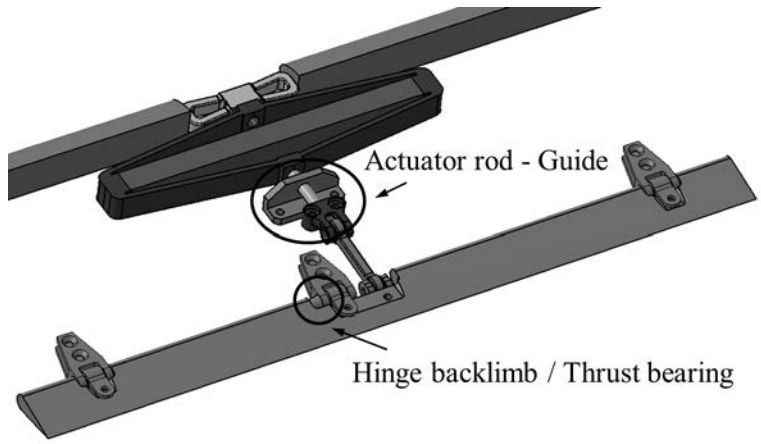

Fig. 3.15 Contact locations within the flap-driving components

designated at a surface between the thrust bearing and center hinge back limb. Among the other components, a glue condition is implemented to fix the relative location of the components. Figure 3.16 shows a fixed boundary condition which is applied to the basic hub component. The guide and hinge mount components are attached to the blade skin using RBE2 element as shown in Fig. 3.17.

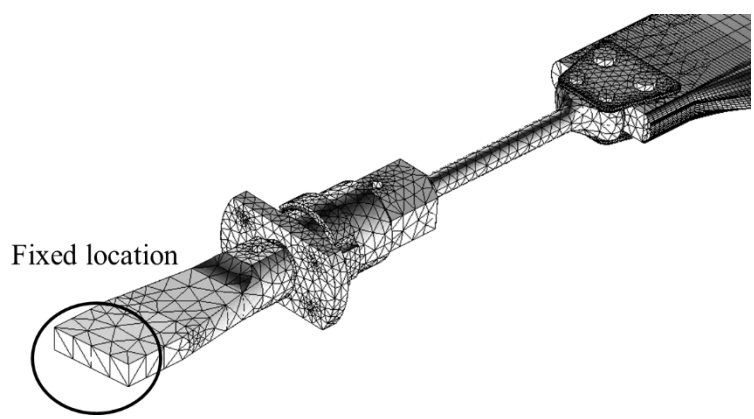

Fig. 3.16 Blade root boundary condition

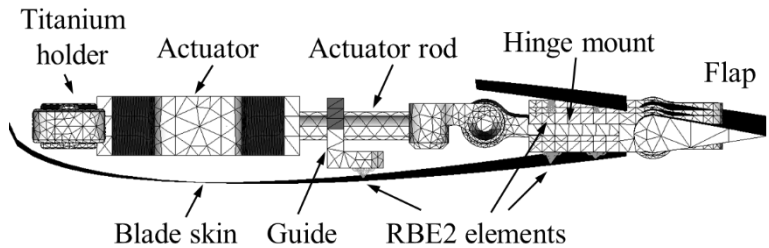

Fig. 3.17 Guide and hinge mount attachment condition

3.3.2 Loading Condition for the Three-dimensional Analysis

The external aerodynamic load obtained from the CAMRAD II trim analysis is imposed on the three-dimensional finite element analysis. Figure 3.18 shows the lift, drag, and moment distributions, which are obtained from the trim analysis for the present SNUF blade. Aerodynamic loads are selected at locations at which excessive lift and drag occur to perform the SNUF blade static structural analysis. As shown in Fig. 3.19, these aerodynamic loads are discretized according to each section and applied to the finite element model of the blade using an RBE2 element. Additionally, centrifugal loads and gravity also are included to confirm the effectiveness of the stress within the contact surfaces and attachment points.

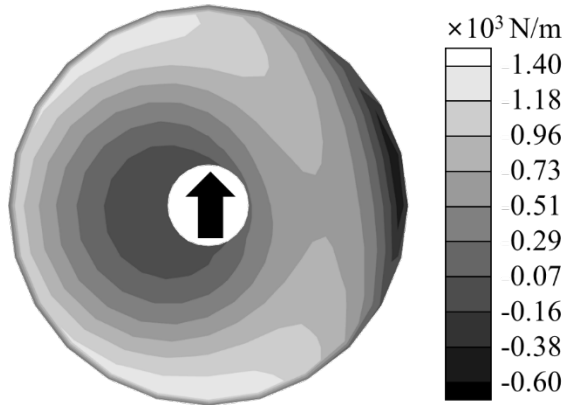

(a) Sectional lift distribution

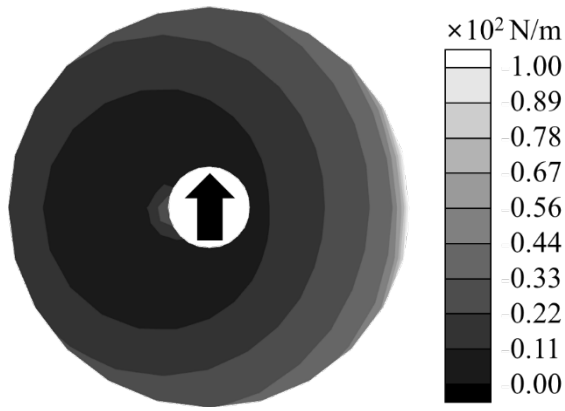

(b) Sectional drag distribution

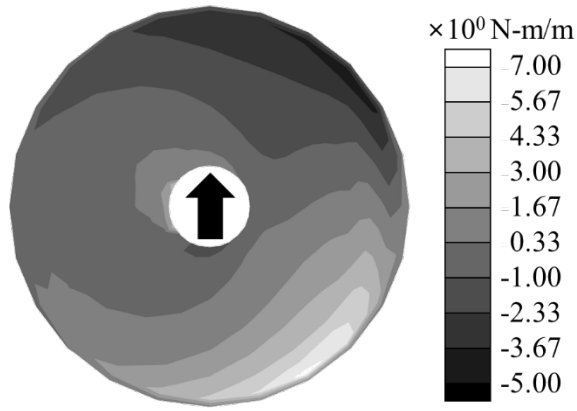

(c) Sectional moment distribution

Fig. 3.18 Aerodynamic load distribution for the present SNUF blade

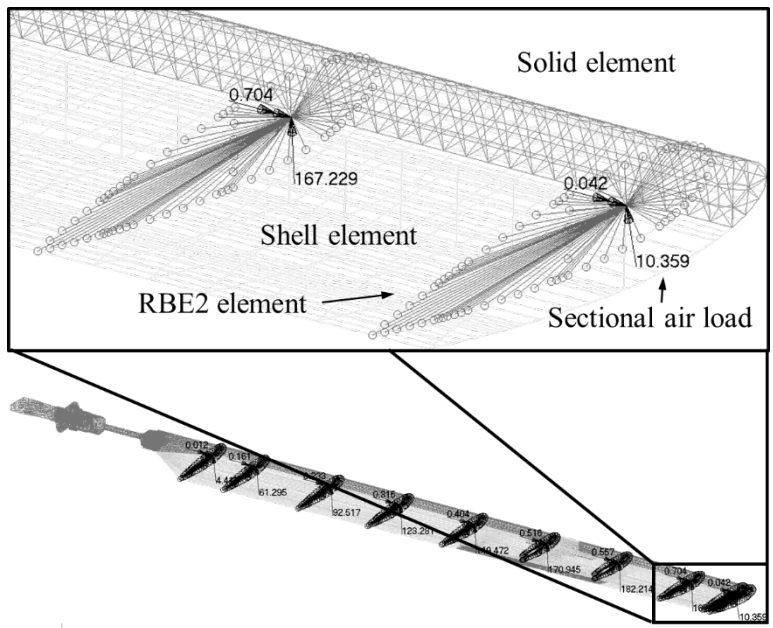

Fig. 3.19 Sectional aerodynamic load distribution within the SNUF finite element analysis

3.3.3 Stress/Strain Distribution in the Composite Blade

Three-dimensional finite element analysis is finally conducted using MSC.NASTRAN [165] with respect to the worst loading condition. The results from this analysis can be divided into the following two aspects: 1) the stress distributions in three-dimensional elements, such as flexure, root pin, glass fiber roving, actuator and guide; 2) the strain distributions in two-dimensional shell elements, such as blade skin.

The components of the present SNUF are made from different materials. Thus stress margin is used to evaluate the structural integrity on the three-

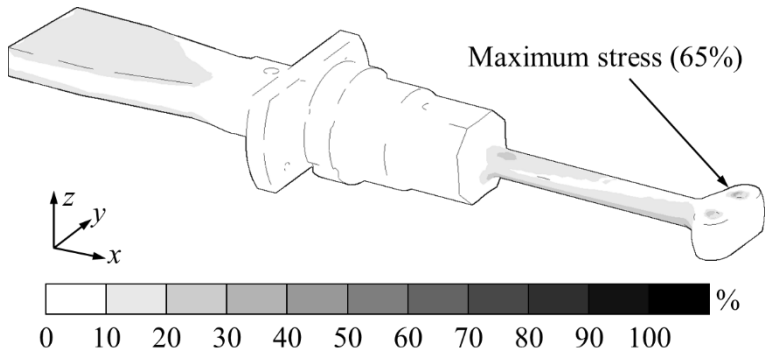

Fig. 3.20 Stress margin distribution on the root retention

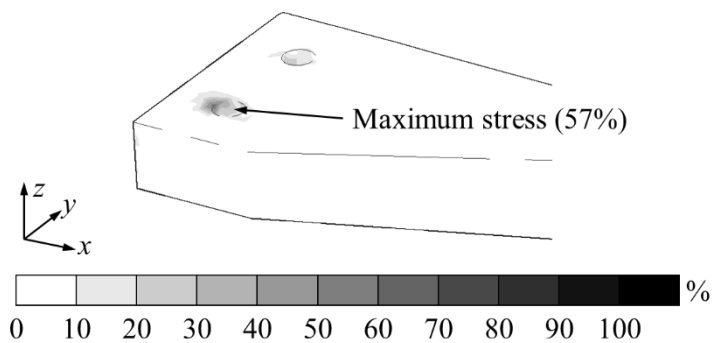

Fig. 3.21 Stress margin distribution on the roving

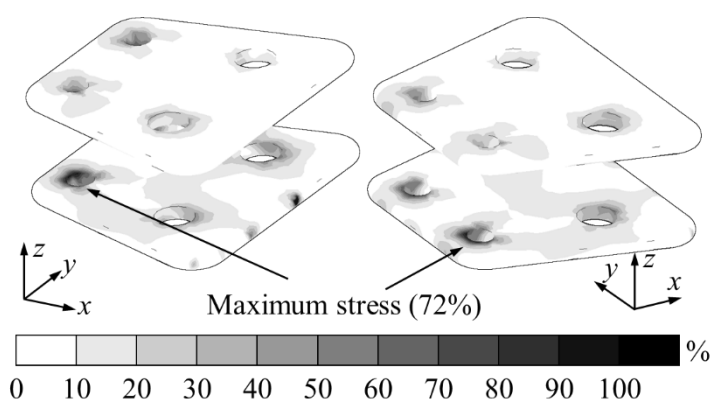

Fig. 3.22 Stress margin distribution on the root plate

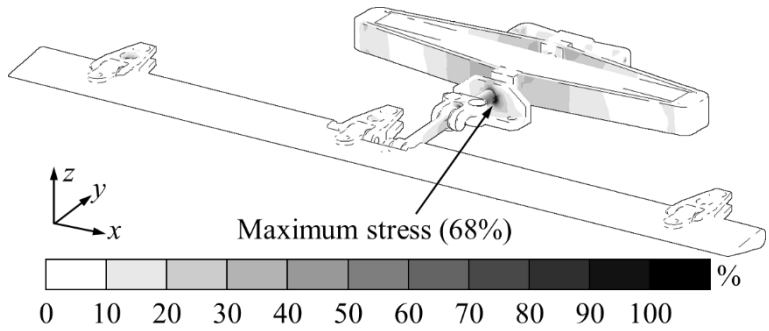

(a) Complete flap-driving components

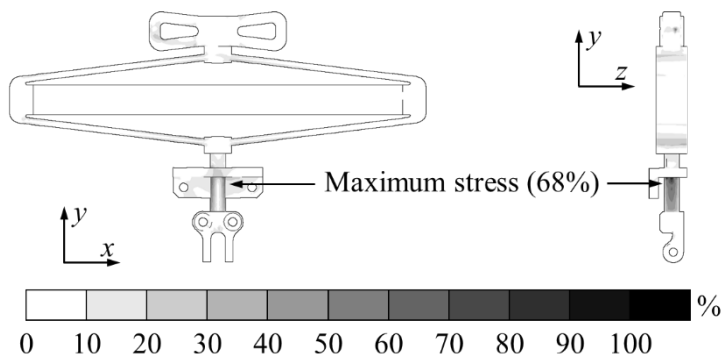

(b) Actuator rod and guide

Fig. 3.23 Stress margin distribution on the flap-driving components

dimensional elements. Since the three-dimensional elements are isotropic material, the stress margin represents the existing von Mises stress versus the allowable stress. Such stress margin distribution on the various components is depicted in Figs. 3.20-3.23. Figure 3.20 shows the stress margin on the baseline hub and flexure, which are made from titanium alloy. The maximum stress is found near the pin hole on the flexure, and it represents 65% out of the allowable stress. As shown in Fig. 3.21, the maximum stress at 53% out of the allowable stress occurs in the roving, which is located near the root pin hole.

The stress margin of the root plate is shown in Fig. 3.22. As can be seen in Fig. 3.22, 72% out of the allowable stress is observed at the location where the 4 mm diameter root pin is applied. This value is the largest one among the stress margins of the three-dimensional element in the present SNUF finite element analysis. Figure 3.23 presents the stress margin distribution on the flap-driving components. The maximum stress value is observed between the actuator rod and the guide, which corresponds to the contact point, and represents 53% out of the allowable stress.

In the strain recovery analysis using GT/VABS, it is not straightforward to examine the strain margin distribution corresponding to the blade skin. However, it is still possible to monitor these results by the present static structural analysis. Figures 3.24-3.26 show the strain margin results at the blade root region. The blade root consists of 13 plies as shown in Fig. 3.2. The largest strain margin is the longitudinal strain component that occurs in the second ply of the carbon fiber as shown in Fig. 3.24(b). In addition, it is observed that longitudinal compression strains occur due to the centrifugal loading near the root pin. By this, it is found that the present static structural analysis predicts the physical phenomenon in an accurate fashion. The maximum transverse strain margin is 40% out of the allowable strain in the second ply, as shown in Fig. 3.25. Figure 3.26 depicts the shear strain margin, its maximum value occurs in the first ply which is 26% out of the allowable shear strain.

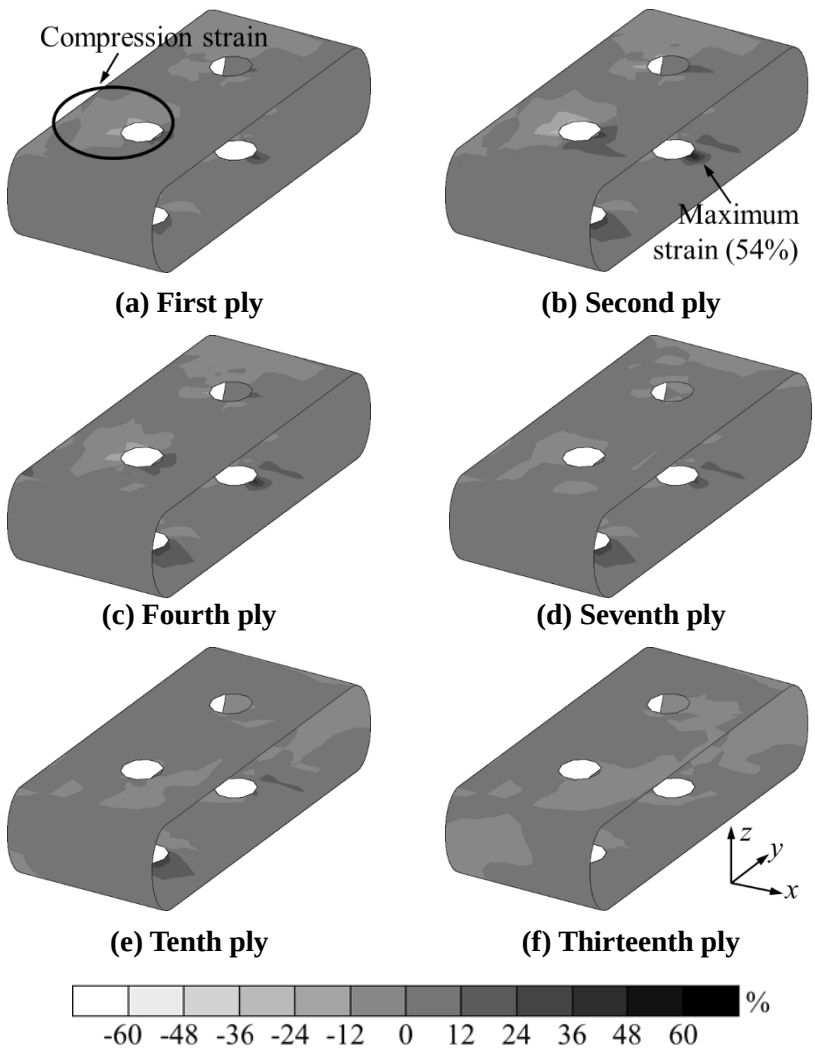

(a) First ply **(b) Second ply**

(c) Fourth ply **(d) Seventh ply**

(e) Tenth ply **(f) Thirteenth ply**

Fig. 3.24 Longitudinal strain margin distribution on the blade root

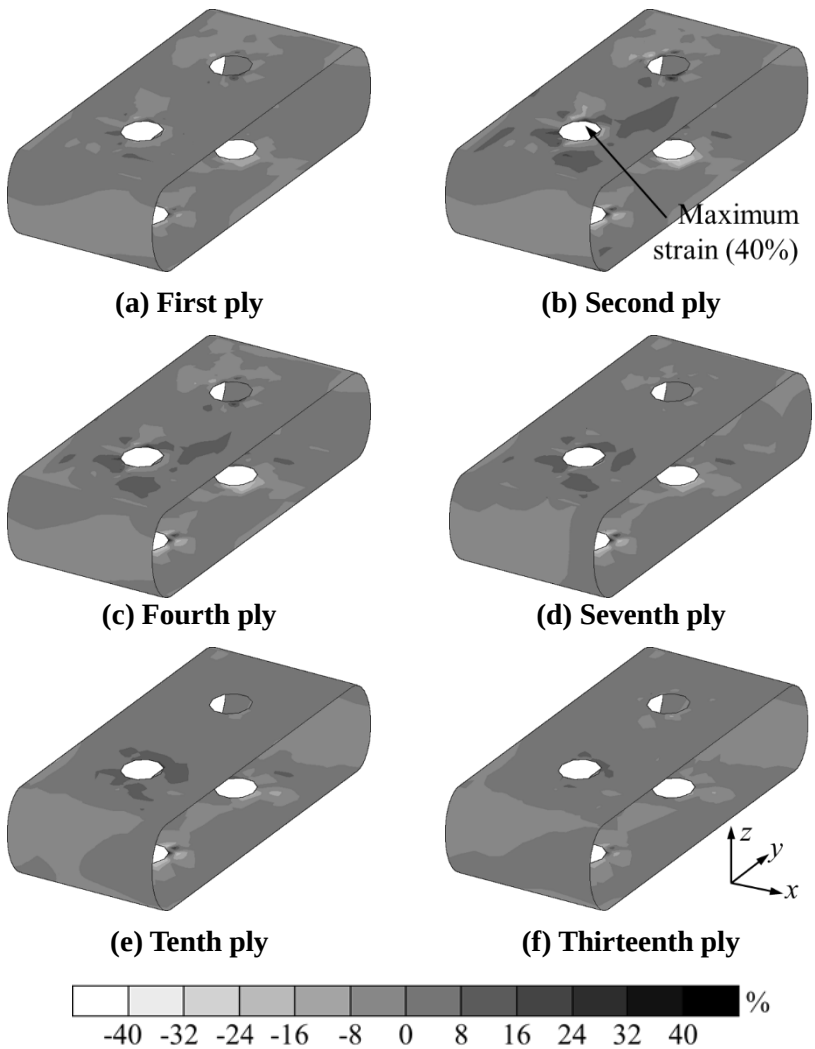

(a) First ply **(b) Second ply**

(c) Fourth ply **(d) Seventh ply**

(e) Tenth ply **(f) Thirteenth ply**

Fig. 3.25 Transverse strain margin distribution on the blade root

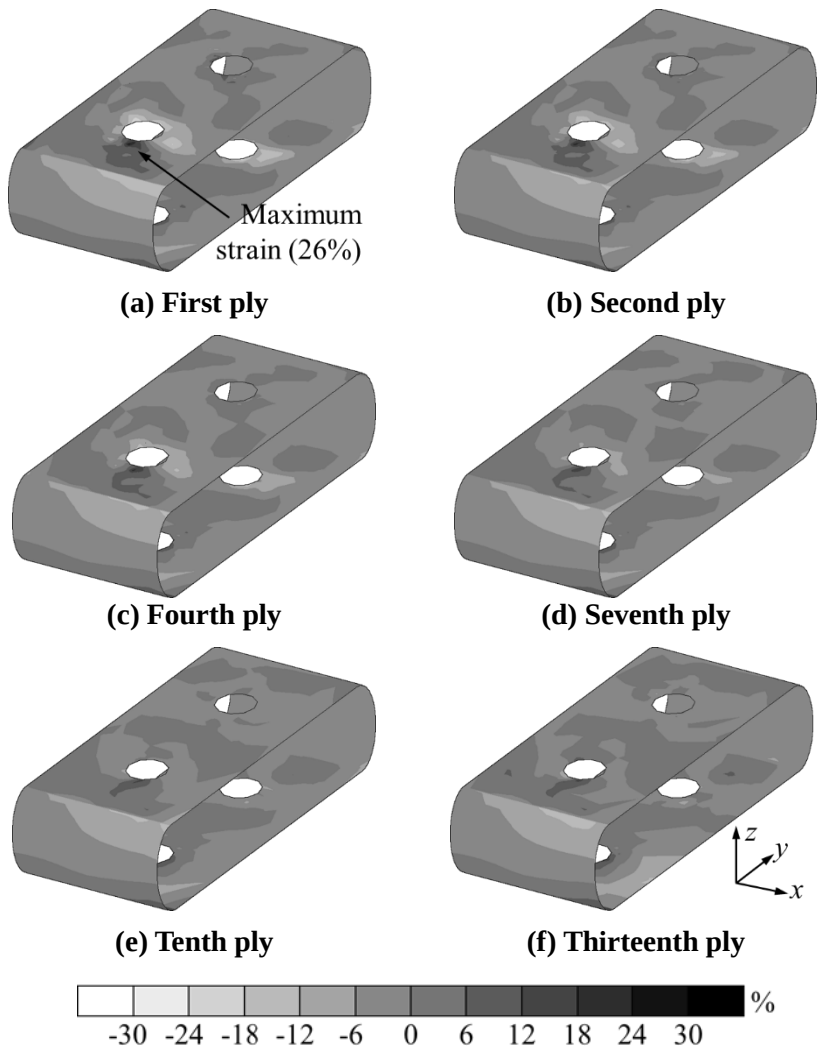

(a) First ply **(b) Second ply**

(c) Fourth ply **(d) Seventh ply**

(e) Tenth ply **(f) Thirteenth ply**

Fig. 3.26 Shear strain margin distribution on the blade root

The strain margins on the blade transition region are shown in Figs. 3.27-3.29. The maximum strain margin value reveals the longitudinal strain as shown in Fig. 3.27, which is 21% out of the allowable strain in the fourth ply. As shown in Figs. 3.28 and 3.29, the maximum strain in the transverse and shear direction are 13% and 16% out of the allowable stress, respectively.

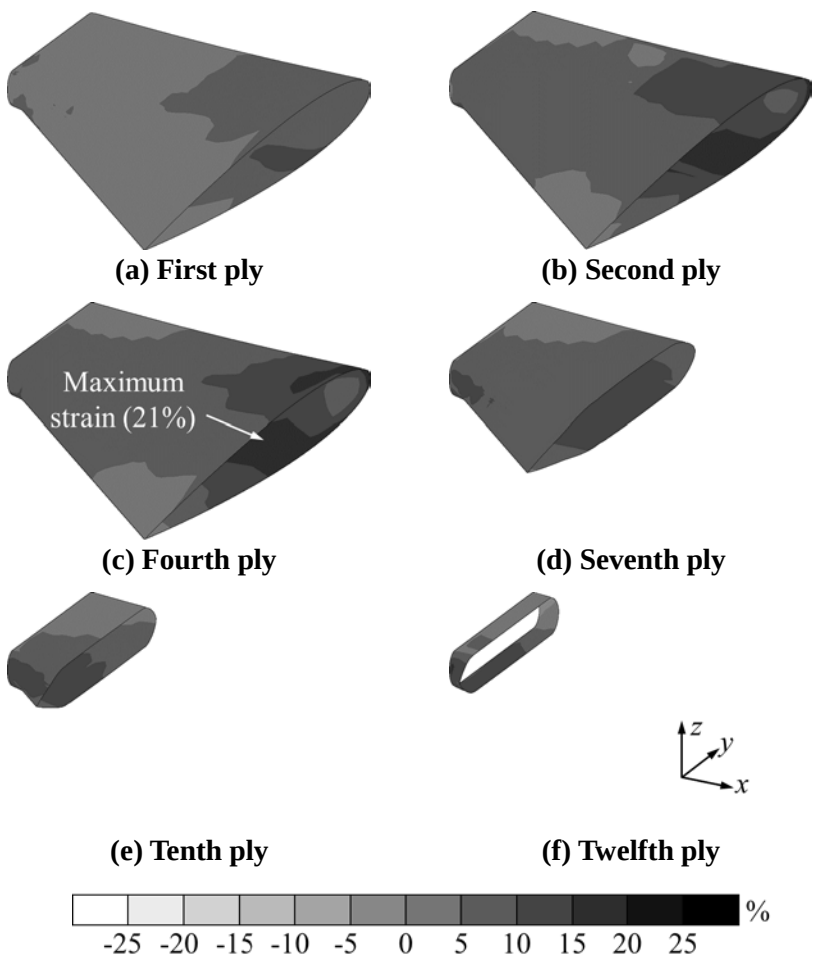

(a) First ply **(b) Second ply**

(c) Fourth ply **(d) Seventh ply**

(e) Tenth ply **(f) Twelfth ply**

Fig. 3.27 Longitudinal strain margin distribution on the blade transition

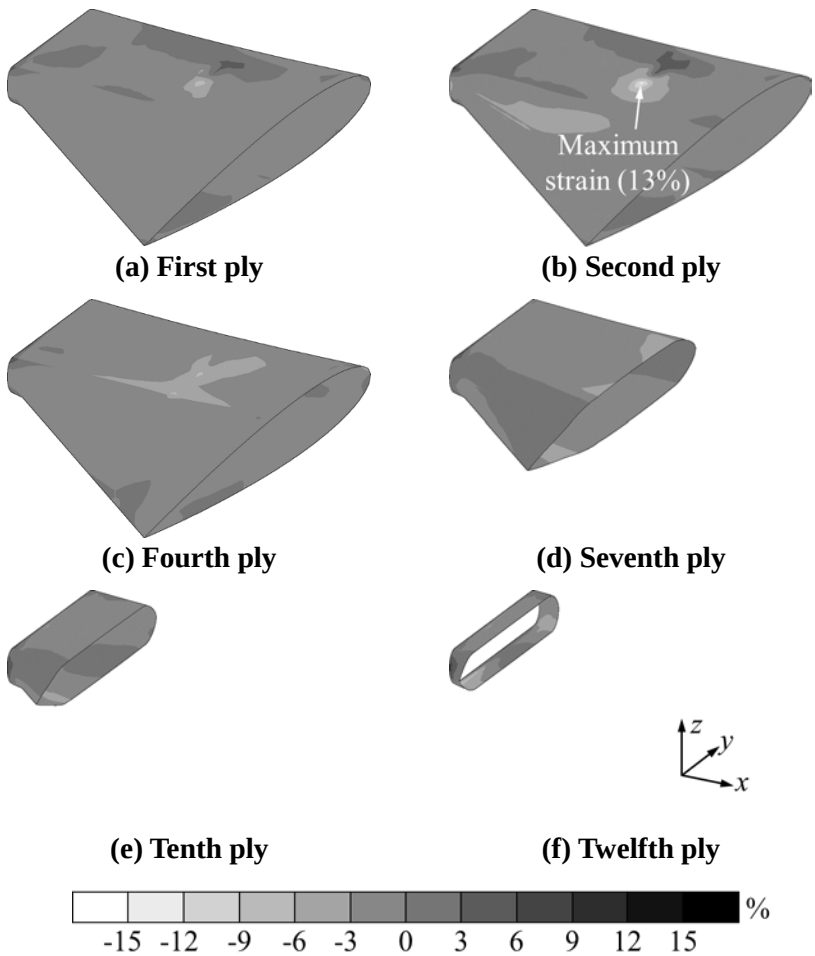

(a) First ply **(b) Second ply**

(c) Fourth ply **(d) Seventh ply**

(e) Tenth ply **(f) Twelfth ply**

Fig. 3.28 Transverse strain margin distribution on the blade transition

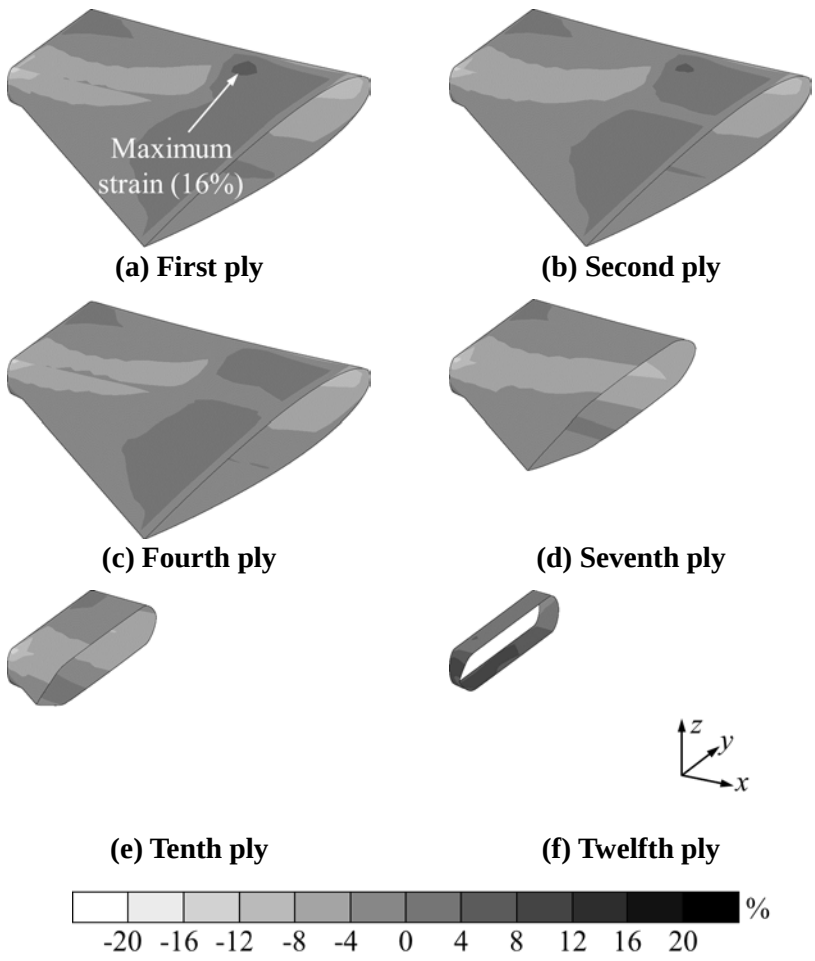

(a) First ply **(b) Second ply**

(c) Fourth ply **(d) Seventh ply**

(e) Tenth ply **(f) Twelfth ply**

Fig. 3.29 Shear strain margin distribution on the blade transition

Figure 3.30-3.32 show the strain margin distribution of the upper blade skin and Fig. 3.33-3.35 show those of the lower blade skin. As can be seen in Fig. 3.30, the maximum strain at the upper blade skin is 39% out of the allowable strain, which is found in the first ply and coincides with the point where the hinge mount is connected to the blade skin. This result can be seen in detail in the magnified part of Fig. 3.30(a). It can be seen that the tensile and compression strain are generated on the root and tip side with respect to the connecting point, respectively. This is caused by the centrifugal load acting on the hinge mount, which may be another evidence indicating that the present analytical results provides an accurate prediction. In the transverse direction of the upper blade skin, the maximum strain is the 20% out of the allowable transverse strain, and the maximum strain in the shear direction is 28% out of its allowable strain. The maximum strain of the lower blade skin occurs in the transverse direction as shown in Fig. 3.34. This 72% out of the allowable strain, which is the maximum value among all the strains within the blade skin. Also the maximum strain occurs at the location where the lower blade skin and guide are connected. The maximum strain in the longitudinal and shear directions are also observed at the location where the blade skin and guide are combined. These values are 35% and 39% out of the allowable strain, respectively, as shown in Figs. 3.33 and 3.35.

As a results of examining the stress distribution in the three-dimensional elements and the strain distribution in the two-dimensional elements, all the

stresses or strain are within the allowable limits. The external aerodynamic loads of the worst loading condition, the centrifugal load, and particular contact conditions are used in the present analysis. In addition, the stress or strain distribution results are predicted accurately. Therefore, it can be concluded that the present SNUF blade is free from the structural failure due to the static loading conditions. However, there still exist additional requirements for verification on the fatigue life.

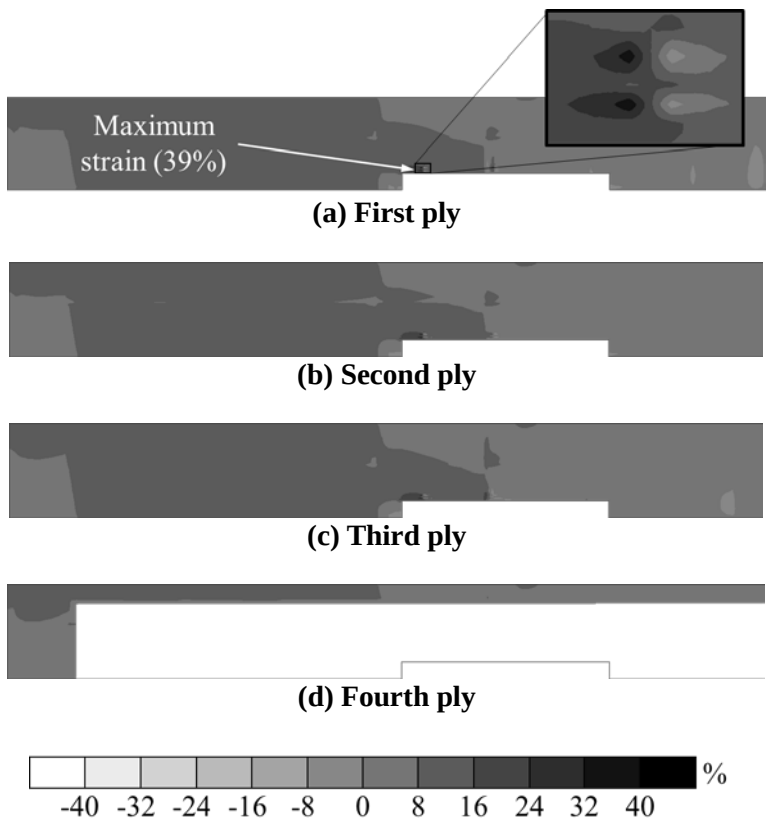

Fig. 3.30 Longitudinal strain margin distribution on the upper blade skin

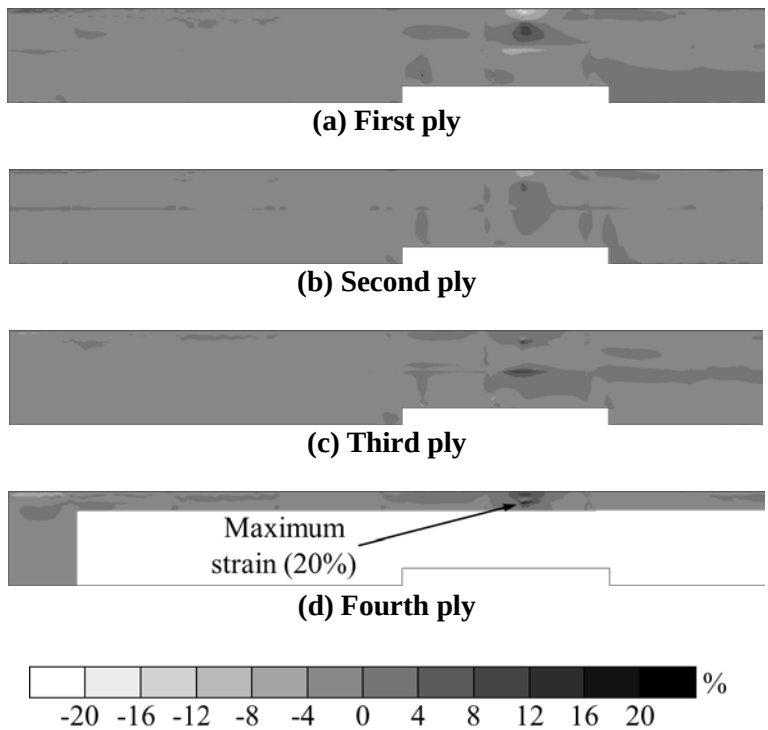

(a) First ply

(b) Second ply

(c) Third ply

(d) Fourth ply

Fig. 3.31 Transverse strain margin distribution on the upper blade skin

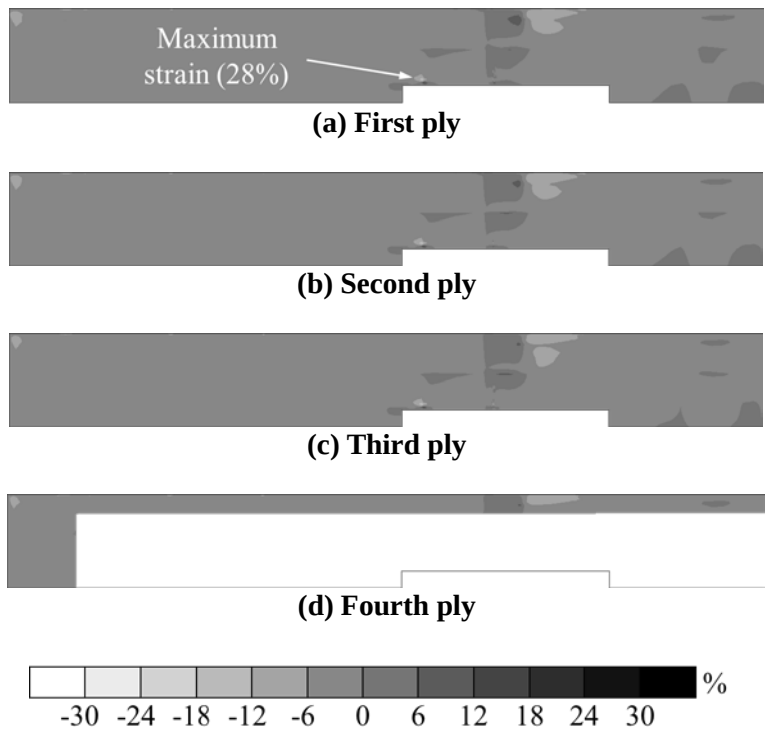

Fig. 3.32 Shear strain margin distribution on the upper blade skin

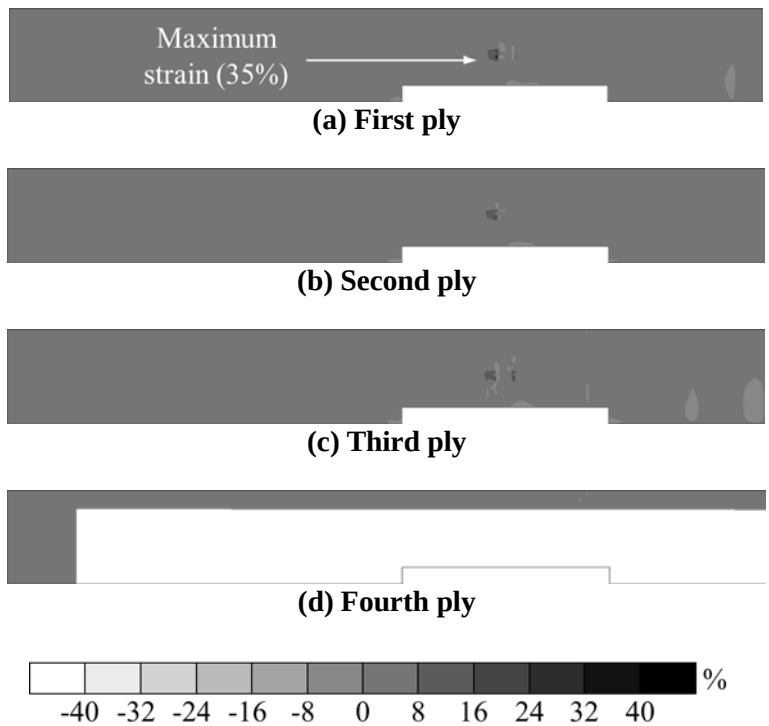

Fig. 3.33 Longitudinal strain margin distribution on the lower blade skin

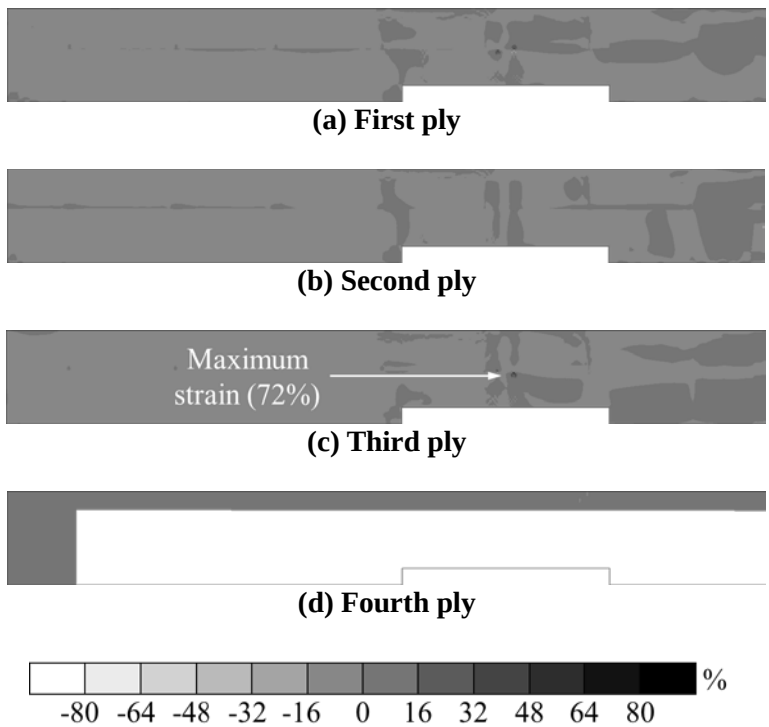

(a) First ply

(b) Second ply

(c) Third ply

(d) Fourth ply

Fig. 3.34 Transverse strain margin distribution on the lower blade skin

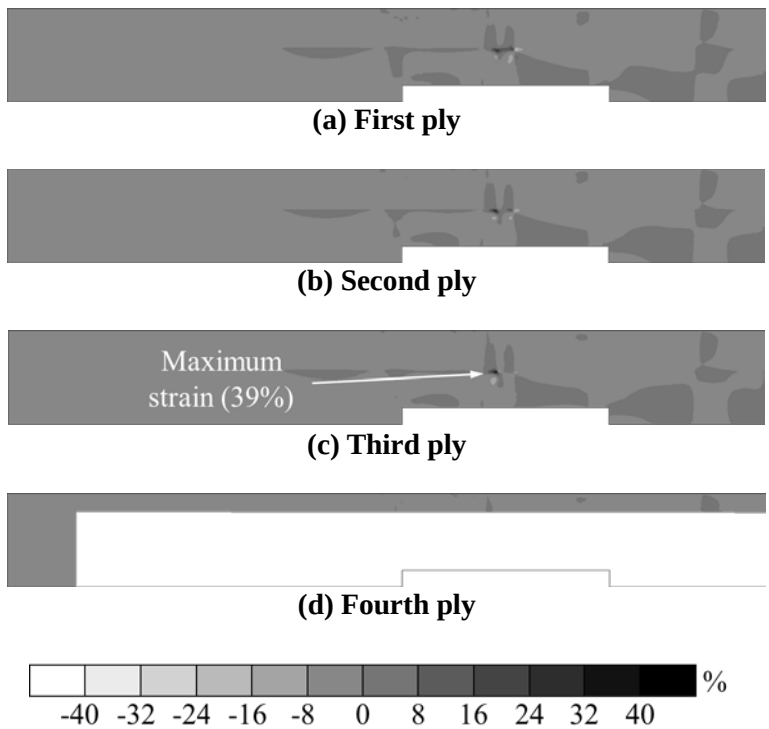

(a) First ply

(b) Second ply

(c) Third ply

(d) Fourth ply

Fig. 3.35 Shear strain margin distribution on the lower blade skin

Chpater 4

Static Bench and Endurance Experiments on the Present Flap-driving Components

The present SNUF blade is designed using the optimization procedure introduced in Chapter 2 and evaluated with respect to its structural integrity as presented in Chapter 3. In this chapter, the flap-driving components of the present SNUF will be fabricated and its flap deflection will be measured. In the design process of the flap-driving mechanism, the external aerodynamic loads expected to act on the flap is estimated. However, due to the rotation of the blade, an excessive centrifugal load will be generated on the flap-driving components. This centrifugal load may cause the friction among the flap-driving components and degrade flap deflection. Therefore, it is necessary to measure the flap deflection of the present flap-driving components by going through the experiments. The measurement of the flap deflection will be conducted by the following two methods. First, a bench experiment will be carried out without external aerodynamic and centrifugal loading condition. Second, an endurance experiment will be performed considering the centrifugal load and operation duration. By these two experiments, it will be determined whether the present flap-driving components satisfy the aimed flap deflection

and whether there exists a restriction in operability when the flap-driving components are driven during the required operation duration.

4.1 Fabrication of the Flap-driving Components

4.1.1 Guide Component for the Stoke Conservation

In the design process of the flap-driving components, difficulties are caused by the centrifugal loads and need to be taken into account in advance. Consideration is given to the piezoelectric actuator occupying the largest weight in the flap-driving components. In order for the stroke generated by the actuator to be transferred to the flap without any loss, the actuator rod and the push rod need to be aligned in a straight line. However, the piezoelectric actuator with weight of 190 g is exerted by the centrifugal load of approximately 4,000 N, which may induce significant displacement of the actuator itself and the actuator rod. Figure 4.1(a) illustrates such issue that may occur on the actuator and the actuator rod in a rotating condition. Therefore, as shown in Fig. 4.1(b), a guide is incorporated in the flap-driving components of the present SNUF for restraining the transverse displacement of the actuator rod.

In order to find the displacement of the flap-driving components under either presence or absence of the guide, the three-dimensional finite element model of

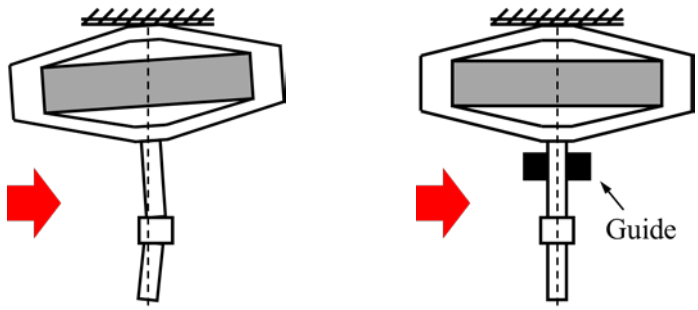

(a) Without a guide **(b) With a guide**

Fig. 4.1 Exertion of the centrifugal loads on the actuator

Table 4.1 SNUF components used in the guide analysis

Number used in Table 3.2	Component	Material
12	Actuator housing	Stainless steel
13	Piezo stack	Piezoelectric material
14	Actuator rod	SUJ2
15	Guide	Stainless steel
16	Bracket	SCM440C
18	Push rod	SCM440C

the present SNUF is simplified and static structural analyses are performed by using MSC.NASTRAN. In these analyses, only six components among the flap-driving components are considered, as summarized in Table 4.1. In Case A, the centrifugal load is applied to the components excluding the guide. The contact/glue table for Case A is summarized in Table 4.2. The case containing the guide is titled as Case B and its contact/glue table is summarized in Table 4.3. The static structural analysis results are shown in Figs. 4.2 and 4.3. As can be seen in Fig. 4.2, in the absence of the guide, the maximum 4.96 mm

Table 4.2 Contact table in Case A

No. in Table 3.2	12	13	14	16	18
12		G	G		
13	G				
14	G			G	
16			G		G
18				G	

Table 4.3 Contact table in Case B

No. in Table 3.2	12	13	14	15	16	18
12		G	G			
13	G					
14	G			C	G	
15			C			
16			G			G
18					G	

displacement occurs in the flap-driving components. On the other hand, as shown in Fig. 4.3, the maximum displacement in the guide is 0.29 mm, and this result indicates that the actuator rod and the push rod are aligned in a straight line.

By adding the guide, it is found that the actuator rod and the push rod are aligned well and the stroke of the actuator can be transmitted without loss. However, as shown in the analysis results of Chapter 3, there is a large stress induced between the guide and the actuator rod. This large stress can increase

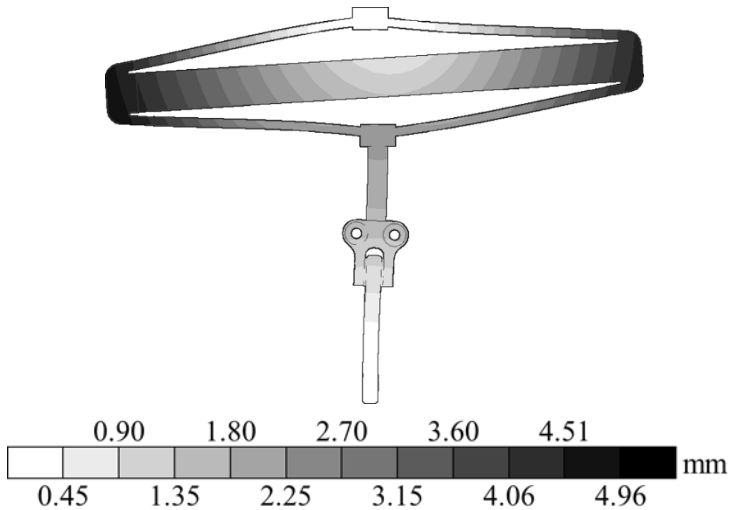

Fig. 4.2 Deflection result for Case A

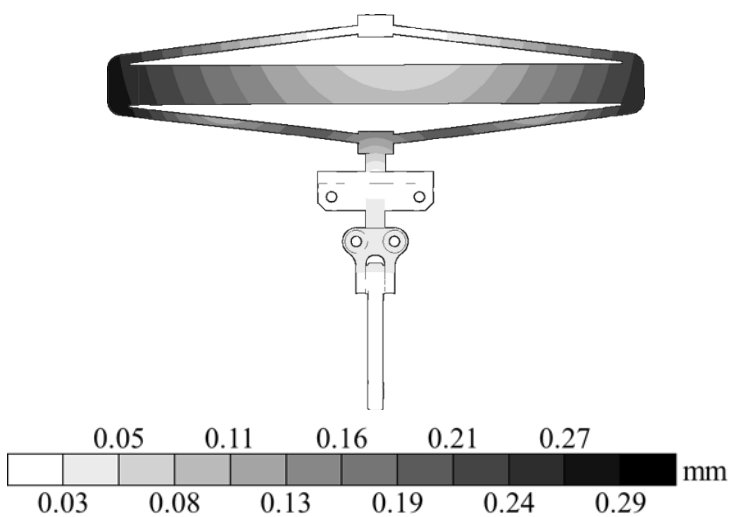

Fig. 4.3 Deflection result for Case B

friction, and the friction between the guide and the actuator rod may induce the degradation in the flap deflection. Therefore, a linear bushing will be mounted in the guide when the flap-driving components are fabricated. The structure of

the linear busing is shown in Fig. 4.4. In the linear busing, since the actuator rod and the load ball are in point contact, a frictional resistance is hardly generated.

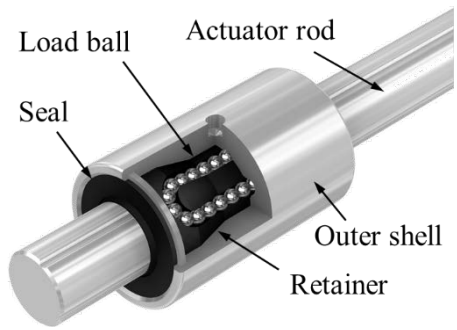

Fig. 4.4 Detailed drawing of the linear bushing

4.1.2 Thrust Bearing for the Flap Deflection

The centrifugal loads generated in the trailing-edge flap may also cause the degradation of the flap deflection. As shown in Fig. 2.17, there are three hinges connected to the trailing-edge flap. When the trailing-edge flap drifts in the radial direction of the blade due to the centrifugal load, the frictional forces between the hinge and the flap will increase. This increase of the frictional force adversely will affect not only the flap deflection but also the service life of the flap-driving components. The trailing-edge flap weighs 10 g and is mounted at 75% radial location of the 1.5 m-span SNUF blade. Since the rotational speed of the present SNUF is 1,300 RPM, the centrifugal load acting on the flap is

approximately 200 N. Thus, a device capable of ensuring the operability of the hinge even under such harsh loading condition is required.

Thus adding bearings along the flap rotation axis is considered. In the full scale blades, bearings can be added easily, but miniature bearings will be suitable for the small scale blade. Among the various types, a thrust bearing is selected considering its superior load carrying capability in the axial as well as radial direction. In Ref. 166, addition of the thrust bearing considerably improved the flap deflection amplitude especially at high rotational speed. In one of the previous designs of SNUF [133], there was a 1.5 mm diameter hinge pin in the trailing-edge flap. Therefore, the miniature thrust bearing F2-6 which had a static load rating of 83 N and a dynamic load raring of 117 N was selected. However, in the present SNUF flap-driving components, the trailing-edge flap is rotated by three hinges without a hinge pin. Since the diameter of the present hinge shaft is 3 mm, a thrust bearing larger than F2-6 can be implemented. The characteristics of various thrust bearings are summarized in Table 4.4. Considering the larger magnitude of centrifugal loads, the maximum constraint force acting on the flap support needs to be smaller than the load rating of the thrust bearing. Among the thrust bearing listed in Table 4.4, only F3-8M has load ratings greater than 200 N, the centrifugal load acting on the present trailing-edge flap. Hence, it is concluded that the thrust bearing F3-8M will be suitable for SNUF blade. Because of the manufacturing complexities, one thrust bearing is decided to be added at the middle hinge (Fig. 3.15).

Table 4.4 Properties of the various thrust bearings

Product	Bore diameter	Outer diameter	Height	Dynamic load rating	Static load rating
F2-6	2 mm	6 mm	3 mm	117 N	83 N
F2X-7	2.5 mm	7 mm	3.5 mm	156 N	117 N
F3-8	3 mm	8 mm	3.5 mm	166 N	137 N
F3-8M	3 mm	8 mm	3.5 mm	993 N	590 N

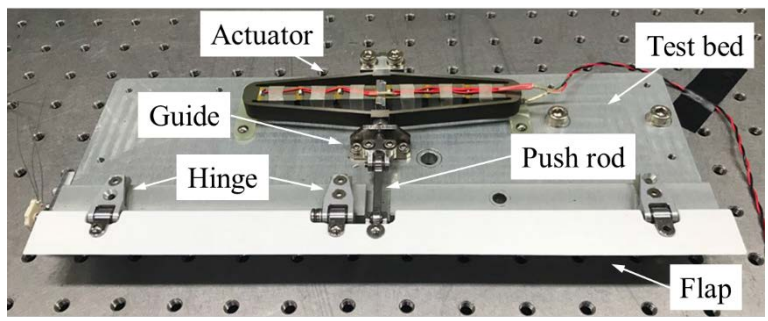

Fig. 4.5 Fabricated flap-driving components

4.1.3 Prototype Flap-driving Components Fabrication

The prototype flap-driving components are fabricated based on the present design. Figure 4.5 shows the fabricated flap-driving components. A test bed for the static bench experiment is also fabricated. F3-8M thrust bearings are fitted between the middle hinge and the trailing-edge flap, as shown in Fig. 4.6. It is also possible to adjust the moment arm of the trailing-edge flap by adding washers to the flap horn (Fig. 4.7). The static bench experiment and endurance experiment are conducted using this fabricated flap-driving components. In the

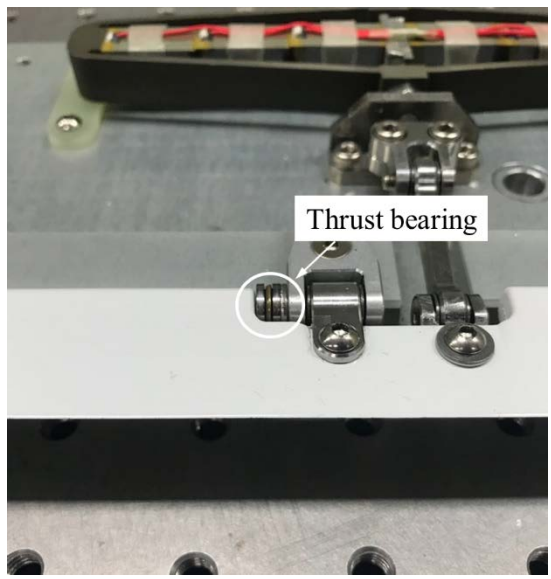

Fig. 4.6 Thrust bearing mounted between the hinge and flap

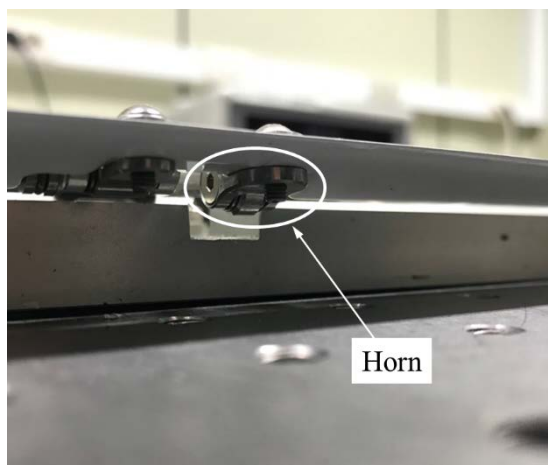

Fig. 4.7 Flap horn component for adjustment of the moment arm

static bench experiment, external loads are not applied to the flap-driving components, and only the centrifugal load acting on the trailing-edge flap is simulated in the endurance experiment. Since the centrifugal load on the piezoelectric actuator itself is not included in this experiment, the guide

component except the linear bushing is fabricated for the prototype flap-driving components.

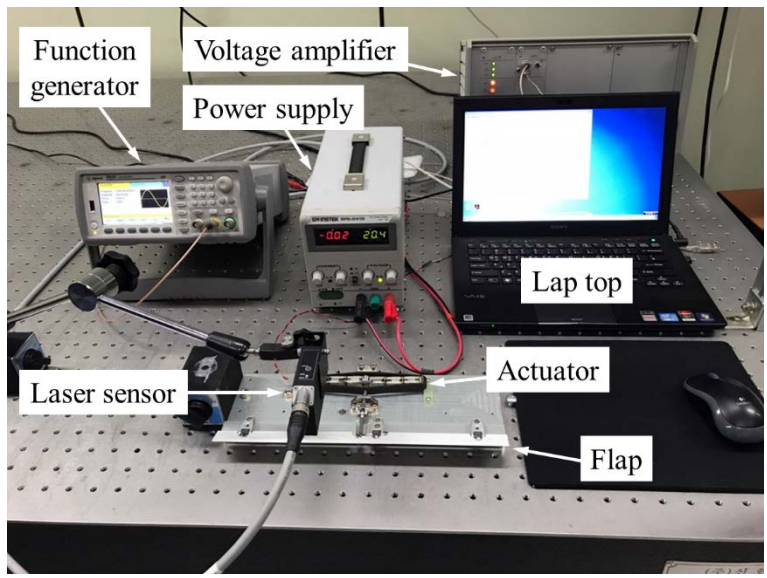

Fig. 4.8 Experimental set-up for SNUF flap-driving components

4.2 Static Bench Experiment

4.2.1 Experimental Setup for Bench Test

The static bench-top experiment is done initially to validate the flap-driving mechanism and check the flap deflection before moving on to endurance experiment. The aim is to achieve a flap deflection of $\pm 4°$ of larger, since the performance of the actuator may deteriorate under the influence of the external

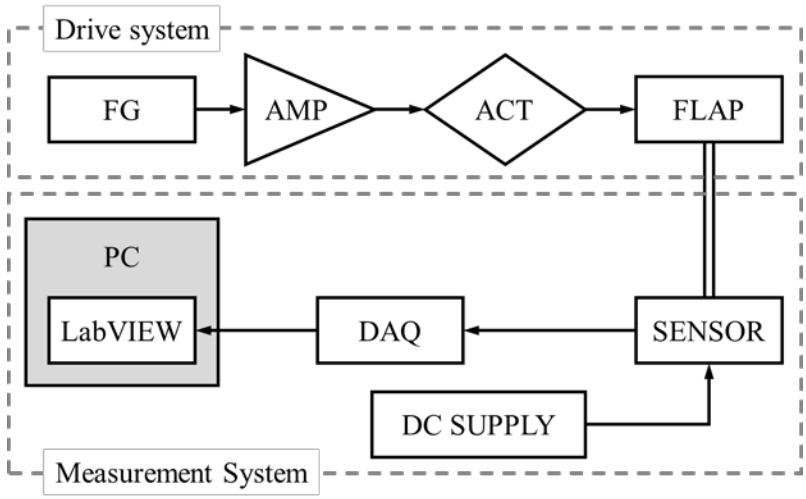

FG: Function Generator
PC: Personal Computer
DAQ: Data Acquisition S/W
AMP: Voltage Amplifier
ACT: Piezoelectric Actuator

Fig. 4.9 Block diagram of the experimental set-up

loads such as aerodynamic or centrifugal. The experimental setup (Fig. 4.8) required for conducting the bench experiment is explained in the block diagram as illustrated in Fig. 4.9. It can be broadly classified into following two categories:

i) Drive system

ii) Measurement system

4.2.1.1 Drive System

The drive system is comprised of the components required to drive the piezoelectric actuator indicated in Fig. 4.9. A function generator is required to supply the necessary AC signal at the appropriate frequency to the amplifier. The amplified signal drives the APA 1000L actuator. Agilent 33522A stand-alone arbitrary waveform generator is selected and used. It has a 16-bit 250 MS/s (mega samples per second) arbitrary waveform capability. The maximum driving frequencies of the piezoelectric actuator are dependent on the characteristics of the amplifier. Therefore, an experimental set-up is established including the amplifier which is capable of driving up to required frequencies. In more detail, the maximum input frequency is estimated as

$$f_{\max} = \frac{I_{\text{peak}}}{\pi C_{\text{load}} \Delta V} \tag{4.1}$$

where $f_{\max}$ is the maximum actuation frequency, I_{peak} is the peak amplifier source sink current, C_{load} is the piezoelectric actuator capacitance, and ΔV is the peak to peak drive voltage.

The nominal rotational angular frequency of the SNUF blade is 21.66 Hz. In order to simulate 5/rev actuation condition, the actuation frequency of 108.32 Hz will need to be applied. Table 4.5 summarizes the properties of several amplifiers and the maximum operating frequency results. Thus, the CEDRAT

Table 4.5 Comparison of the amplifiers possibly used

Company	CEDRAT	TREK	NF
Product	LA75C	PZD 2000A	HAS 4052
I_{max}, A	2.4	0.2	2.0
C_{load}, μF		40.0	
ΔV		150	
f_{max}, Hz	127.32	10.61	106.10

amplifier LA75C which is characterized by a continuous maximum current 2.4 A is selected. Considering a peak-to-peak voltage of 150 V and with the capacitance of the APA1000L actuator at 40 μF, the maximum frequency is 127.32 Hz. The LA75C amplifier has an amplification factor of 20.

4.2.1.2 Measurement System

The measurement system capable of measuring high frequency movements in the flap is required. It consists mainly the sensor and the supporting hardware shown in Fig. 4.9. The supporting hardware is required for power-supply and to collect the signal from the sensor. The Micro-Epsilon optoNCDT 1402 type laser displacement sensor is selected for the flap deflection measurement. It has an adjustable mearing rate up to 1.5 kHz. Among the various ranges, the type 1402-100 with 100 mm measuring range is chosen and mainly used for flap deflection measurements as shown in Fig. 4.10. The height and width of the gray triangle part of Fig. 4.10 can be expressed by the following equation.

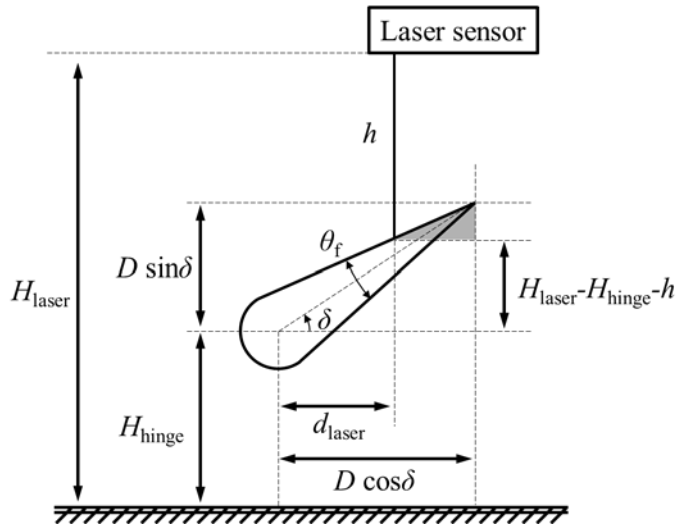

Fig. 4.10 Flap deflection measurement

$$D\cos\delta - d_{\text{laser}} \tag{4.2}$$

$$D\sin\delta - \left(H_{\text{laser}} - H_{\text{hinge}} - h\right) \tag{4.3}$$

where D is the length of the flap, δ is the flap deflection angle, d_{laser} is the horizontal distance between the hinged location and laser measurement location, H_{laser} is the height of the laser displacement sensor, H_{hinge} is the height of the hinged location and h is the measured value by the laser displacement sensor. Therefore, the slope of the gray triangles in Fig 4.10 can be expressed as Eq. (4.4).

$$\frac{D\sin\delta - \left(H_{\text{laser}} - H_{\text{hinge}} - h\right)}{D\cos\delta - d_{\text{laser}}} = \tan\left(\delta - \frac{\theta_f}{2}\right) \tag{4.4}$$

where θ_f is the angle of flap edge. Since the values except h and δ are all constants, the displacement measured by the laser displacement sensor can be converted to the deflection angle of the flap by using Eq. (4.4).

GW INSTEK SPS 2415 is used to supply DC power for the laser displacement sensor. The sensor analog output signal (1-5 V) is transmitted to NI USB-6281 through a cable PC 1402-3/U. NI USB-6281 DAQ is capable of 16 analog inputs at 625 kS/s and the data acquisition is handled using LabVIEW software.

4.2.2 Static Bench Experiment Results

The static bench experiment is an initial step for validating the present flap-driving mechanism before testing in the actual load like centrifugal. The SNUF blade is a four-bladed rotor system, and it requires 3, 4 and 5/rev to alleviate the vibratory loads in an open-loop fashion. The static bench experiment results of the present flap-driving components are found to be much larger than the flap deflection target, ±4° for all actuation condition as shown in Fig. 4.11. The specific flap deflections are summarized in Table 4.6. The maximum flap deflections of ±10.4°, ±17.5° and ±11.0° are achieved at 3, 4 and 5/rev actuation, respectively.

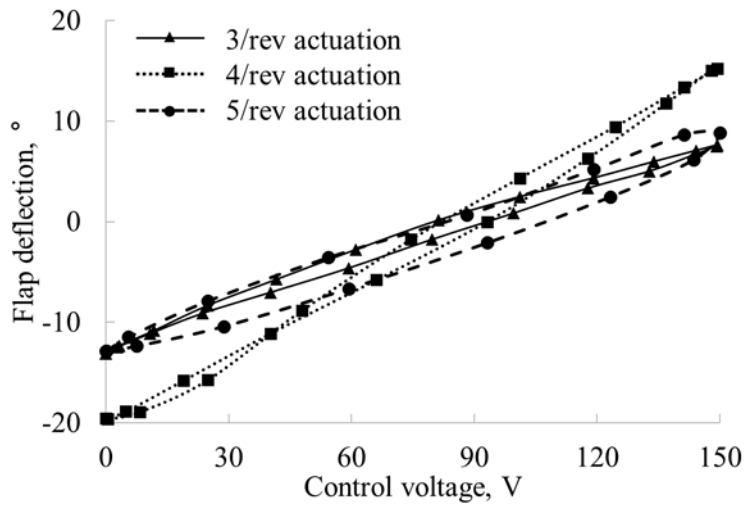

Fig. 4.11 Deflection angle measurement with dynamic voltage input, 150 $V_{peak\text{-}peak}$

Table 4.6 Flap deflection results of the present static bench experiment

Flap deflection	3/rev	4/rev	5/rev
Minimum	-13.1°	-19.7°	-12.9°
Maximum	+7.6°	+15.3°	+9.1°
Peak to peak	±10.4	±17.5	±11.0

4.3 Endurance Experiment

In order to investigate whether the fabricated flap-driving components are capable of producing the expected flap deflection under the operating condition, the endurance experiment is come up with in order to take into account the following two aspects:

- The flap deflection under the centrifugal loading condition

- Durability of the flap-driving components which consists of various bearings and hinges

4.3.1 Endurance Experiment Set-up including Centrifugal Loading

There is a concern that the flap deflection may degrade due to the centrifugal loads on the flap in the rotating condition of the blade. Therefore, as shown in Fig. 4.12, an experiment considering the centrifugal loads acting on the flap is come up with. The test bed equipped with the flap-driving components is fixed to the vibration isolation table, and the dummy weight is suspended on the flap. In this setup, the dummy weight is connected to the five holes in the flap by the fishing wire so that the virtual centrifugal loading may be distributed on the flap. Moreover, long fishing wires and a jig are used to maintain the loads acting on the flap to be as horizontal as possible.

When the flap-driving components are mounted on the blade and operated, fatigue accumulates on the components, such as hinges and bearings, due to the centrifugal load, and the flap deflection may be degraded. Therefore, the centrifugal load experiment shown in Fig. 4.12 is required and carried out during the target operation duration, one hour. The conditions of the endurance experiment are summarized in Table 4.7.

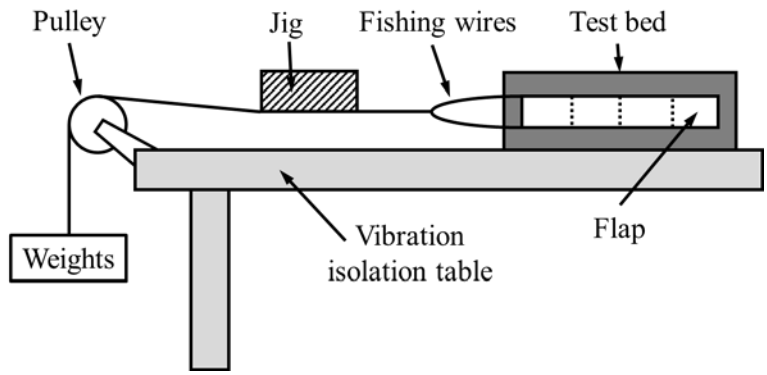

Fig. 4.12 Schematic of the centrifugal loading condition

Table 4.7 Flap deflection results of the present static bench experiment

Condition	Value
Dummy weights hanging on the flap	20 kg
Operation duration	3,600 sec (1 hour)

In this endurance experiment, instead of the piezoelectric actuator APA1000L, a screw ball type electric cylinder and a servo motor are implemented to produce the same stroke of the actuator. CASM-32-BS screw ball type electric cylinder transfers the rotational motion to the rectilinear motion by its screw. Thus the motions and the torque of M36N-4E servo motor are converted into rectilinear motions and loads with minimum loss. Figure 4.13 shows a test bed equipped with the electric cylinder and servo motor. In order to control the servo equipment, 332CPR encoder is installed and motor control is performed using NI DAQ. The endurance experiment is conducted at a frequency of 10 Hz, considering the bandwidth of the servo motor. In this

experiment, as shown in Fig. 4.14, two laser displacement sensors are employed. Sensor A measures the flap deflection, and Sensor B measures the flap drift displacement in the direction of the centrifugal loads.

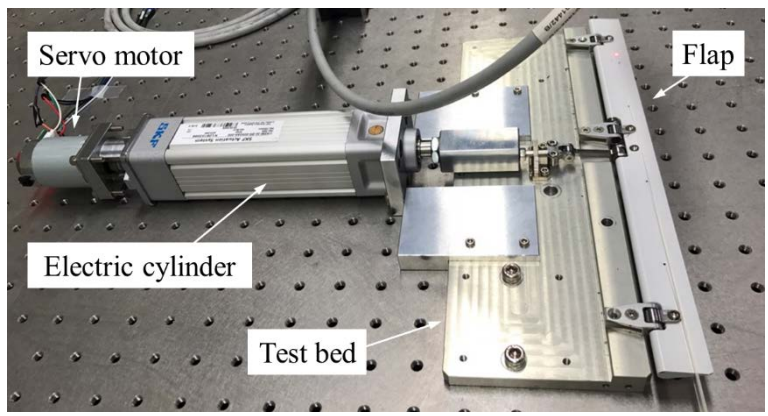

Fig. 4.13 Test bed with the ball screw type electric cylinder and the servo motor

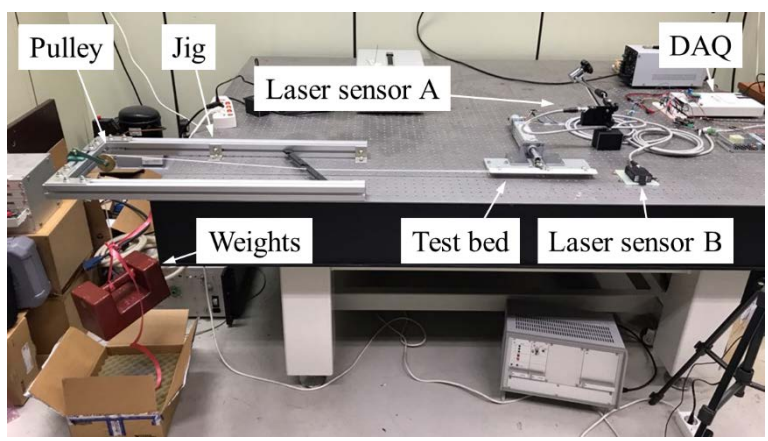

Fig. 4.14 Endurance experiment set-up

4.3.2 Flap Deflection Measurement Results

The endurance experiment is conducted for 3,600 seconds. Figure 4.15 shows the flap deflection measured by the laser displacement sensor A. It is observed that the flap deflection at the initial stage (59 ~ 60 sec) and the final stage (3599 ~ 3600 sec) show similar trends. Figure 4.16 shows the results of FFT to analyze the measured flap deflection in the frequency domain. As shown in Fig. 4.15, the flap deflection reaches -8° to +10°, exceeding the target value of ±4°, even under the centrifugal load of 20 kg acting on the flap. This result implies that the thrust bearing operates properly. The flap deflections are maintained throughout the entire actuation, and its amplitudes are observed to remain constant during one hour operation. As a result of FFT analysis of the flap deflection, the largest values are found at the operating frequency of 10 Hz in both initial and final periods, and the magnitudes are also similar.

In addition, the results of the flap drift displacement measurements in the centrifugal direction and the FFT results of these values are shown in Figs. 4.17 and 4.18, respectively. The maximum flap drift value is 0.016 mm, which indicates that the effect of centrifugal loading on the flap drift displacement is insignificant. According to the FFT results of the flap drift measurements, only values corresponding to N times the operating frequency (10 Hz) are obtained. It is verified that the amplitude and the frequency of the flap deflection of the present flap-driving components are maintained during the operation duration

(3,600 sec) under the expected centrifugal loading condition.

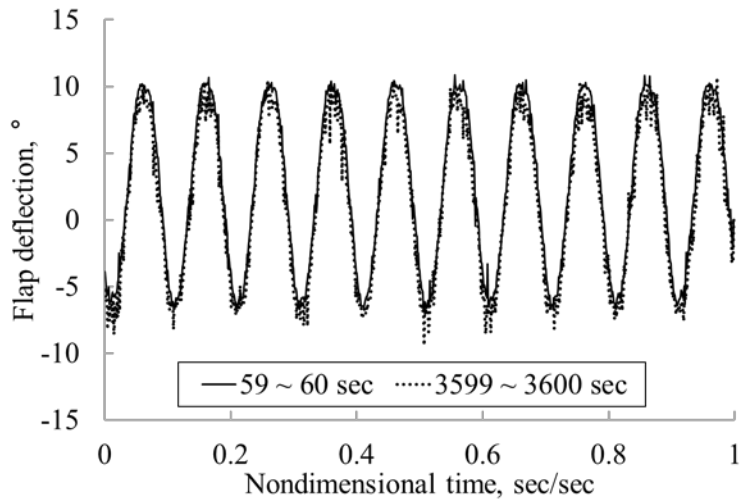

Fig. 4.15 Flap deflection measurement

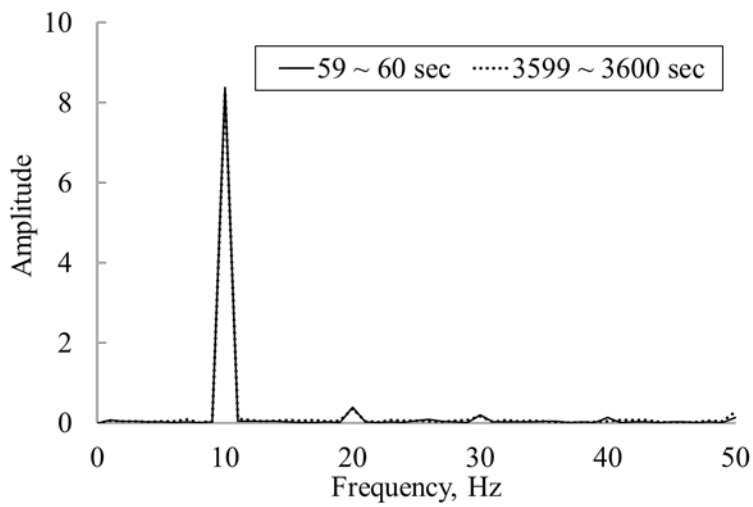

Fig. 4.16 FFT results of the flap deflection

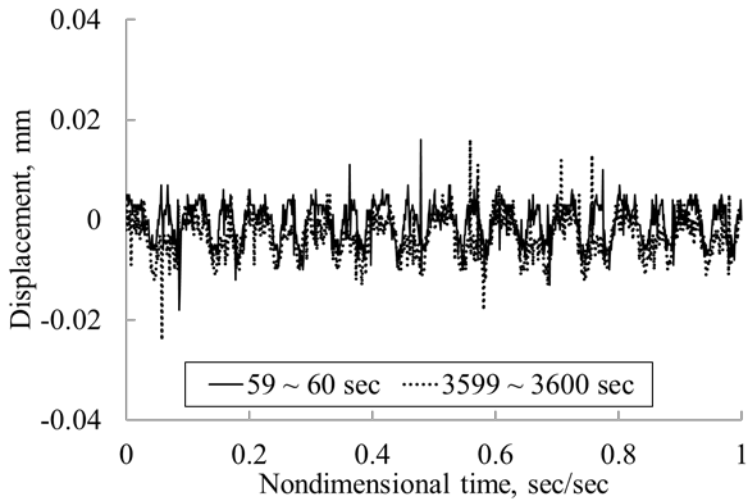

Fig. 4.17 Flap drift measurement

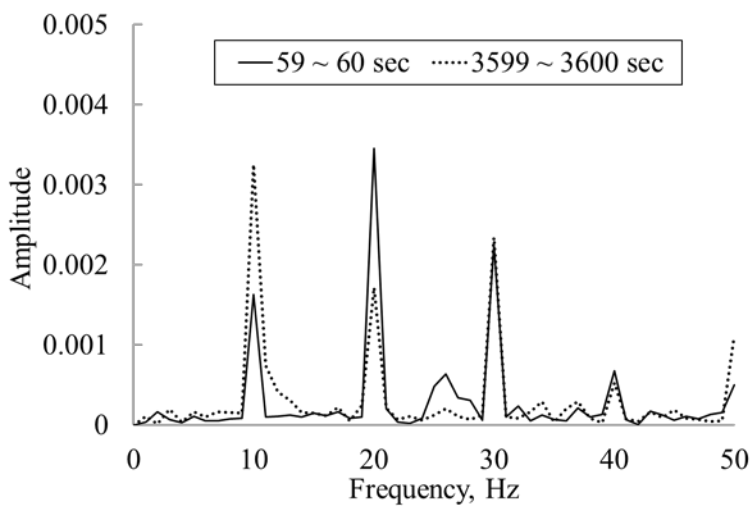

Fig. 4.18 FFT results of the flap drift

Chpater 5

Active Flap Closed-loop Controller for Vibration Reduction in Forward Flight

The four-active bladed rotor system based on the present SNUF blade design is modeled as the multibody structure and analyzed in the open-loop control manner for the forward flight condition as described in Section 2.4.5. In this chapter, the closed-loop controller of the present SNUF rotor system in the forward flight condition is established. System identification is conducted to obtain the plant transfer function needed for the controller design. Then, the results from system identification are utilized to design the closed-loop controller for the hub shear vibratory load reduction.

5.1 System Identification of the SNUF rotor system in Forward Flight

The behavior of a nonlinear system can be complicated, yet some nonlinear systems can be linearized in small regions near equilibrium. Thus, the

extraction of a linear time invariant (LTI) approximation of the rotor system is an essential step toward carrying out the active flap control. The first step in the extraction of the LTI representation is to obtain a linear time periodic (LTP) representation by linearizing the nonlinear representation about a periodic equilibrium. Subsequently, the LTI representation is extracted from the LTP representation. Various methods, such as Lyapunov-Floquet transformation method, Hill's method, time-lifting and frequency-lifting methods [167] have been investigated in the literature for casting a LTP into LTI form. In this dissertation, a method is adopted which results in multi-component harmonic transfer function [168].

5.1.1 Linear time periodic system [168]

It is not straightforward to characterize a linear time periodic system than to do a LTI system. In LTP systems, the coefficients of the differential equations that describe the dynamics are time-varying and periodic. Those system may be modeled in a state-space form as shown in Eq. (5.1).

$$\begin{aligned} \dot{x}(t) &= A(t)x(t) + B(t)u(t) \\ y(t) &= C(t)x(t) + D(t)u(t) \end{aligned} \tag{5.1}$$

The matrices $A(t)$, $B(t)$, $C(t)$ and $D(t)$ are in general periodic, with period T. Therefore, those matrices can be expressed as Eq. (5.2) for any integer N, and

similarly for *B*, *C* and *D*.

$$A(t+NT)=A(t) \tag{5.2}$$

Since the system matrices in Eq. (5.2) are all *T*-periodic, those can be represented by an infinite Fourier series with pumping frequency $\omega_p=2\pi/T$. For the system matrix $A(t)$, it is expressed as Eq. (5.3).

$$A(t)=\sum_{n=-\infty}^{\infty} A_n e^{j\omega_p nt} \tag{5.3}$$

The matrices $B(t)$, $C(t)$ and $D(t)$ can be similarly decomposed. In addition, the state and output vector also can be expanded since they are both exponentially modulated periodic (EMP) signals. Substituting these expansions into Eq. (5.1) and applying the principle of harmonic balance as explained in Ref. 168, the harmonic state space representation is obtained as Eq. (5.4).

$$\begin{aligned} s\mathcal{X} &= (\mathcal{A}-\mathcal{N})\mathcal{X}+\mathcal{B}\mathcal{U} \\ Y &= \mathcal{C}\mathcal{X}+\mathcal{D}\mathcal{U} \end{aligned} \tag{5.4}$$

The doubly infinite vectors representing the harmonics of the state, control and output signals are written as Eq. (5.5).

$$\begin{aligned}\mathcal{X}^T &:= \begin{bmatrix}\cdots & x_{-2}^T & x_{-1}^T & x_0^T & x_1^T & x_2^T & \cdots\end{bmatrix} \\ \mathcal{U}^T &:= \begin{bmatrix}\cdots & u_{-2}^T & u_{-1}^T & u_0^T & u_1^T & u_2^T & \cdots\end{bmatrix} \\ \mathcal{Y}^T &:= \begin{bmatrix}\cdots & y_{-2}^T & y_{-1}^T & y_0^T & y_1^T & y_2^T & \cdots\end{bmatrix}\end{aligned} \tag{5.5}$$

And the doubly infinite input modulation matrix is defined as Eq. (5.6).

$$\mathcal{N} := \text{blockdiag}\left\{ jn\omega_p I \right\} \tag{5.6}$$

The input modulation matrix modulates the input frequency to different harmonic frequencies. Detailed on the derivations can be found in Ref. 168.

The T-periodic dynamics matrix, $A(t)$, is expressed in terms of its complex Fourier coefficients, A_n, as a doubly infinite block Toeplitz matrix is expressed as Eq. (5.7) with a similar definition for $B(t)$, $C(t)$ and $D(t)$.

$$\mathcal{A} = \begin{bmatrix}\ddots & \vdots & \vdots & \vdots & \\ \cdots & A_0 & A_{-1} & A_{-2} & \cdots \\ \cdots & A_1 & A_0 & A_{-1} & \cdots \\ \cdots & A_2 & A_1 & A_0 & \cdots \\ & \vdots & \vdots & \vdots & \ddots\end{bmatrix} \tag{5.7}$$

This collection of doubly infinite matrices is called the harmonic state space (HSS) model of the system given in Eq. (5.1). However, it is useful to determine an explicit input-output functional relationship between the Fourier coefficients

of the harmonics of the input, and those of the output. This relationship is represented by a harmonic function, $G(s)$, which is also an infinite dimensional matrix of Fourier coefficients, satisfying Eq. (5.8).

$$\mathcal{Y} = G\mathcal{U} \tag{5.8}$$

Based on Eq. (5.4), G can be computed as Eq. (5.9).

$$G = \mathcal{C}\left[sI - \left(\mathcal{A} - \mathcal{N}\right)\right]^{-1}\mathcal{B} + \mathcal{D} \tag{5.9}$$

5.1.2 Input Data Requirements

As mentioned in Ref. 168, sinusoids are used for determining the transfer function. More specifically, chirp signals are implemented to obtain the system response over a specific range of frequencies. In the LTP system, it is important to take the chirp phases into consideration as well. Unlike the LTI system, the dynamic response of the LTP system is dependent on the system phase at the time of input application, in addition to the input frequency content. Therefore, it is imperative to ensure that during data collection, the test signals are applied with appropriate phases relative to the system period.

In Ref. 168, it was pointed out that great care needed to be taken in applying the input signals at appropriate time intervals relative to the system period. For

a rotor system, it should also be noted that the system period is not the period of the rotor, it is the blade passage period. Therefore, for a helicopter rotor composed of N_b blades, and the rotational period T, the period T_p of the rotor system is T/N_b. Thus, the output frequencies of the input signal at frequency ω, are shifted by positive and negative multiples of the blade passage frequency ω_p, which is defined as Eq. (5.10).

$$\omega_p = \frac{2\pi}{T_c} = \frac{2\pi N_b}{T} \tag{5.10}$$

In this system identification, the linear up-chirp signal is embedded. Therefore, the instantaneous frequency $f(t)$ varies exactly linearly with time as expressed in Eq. (5.11).

$$f(t) = f_0 + kt \tag{5.11}$$

f_0 is the starting frequency, and k is the rate of frequency change called the chirpiness which is stated in Eq. (5.12).

$$k = \frac{f_1 - f_0}{T_c} \tag{5.12}$$

f_1 is the final frequency and T_c is the time which takes to sweep from f_0 to f_1.

0.5/rev and 10/rev frequencies are selected for f_0 and f_1, respectively, since such range is found to have important frequency content for the present SNUF rotor system. The corresponding time-domain function for the phase of signal is the integral of the frequency function, since one expects the phase to grow like Eq. (5.13).

$$\phi(t+\Delta t) \simeq \phi(t) + 2\pi f(t)\Delta t \tag{5.13}$$

The derivative of the phase is the angular frequency is written as Eq. (5.14).

$$\phi'(t) = 2\pi f(t) \tag{5.14}$$

For the linear chirp, this results in Eq. (5.15).

$$\begin{aligned} \phi(t) &= 2\pi \int_0^t f(\tau)\, d\tau \\ &= 2\pi \int_0^t (f_0 + k\tau)\, d\tau \\ &= 2\pi \left(f_0 t + \frac{k}{2} t^2 \right) \end{aligned} \tag{5.15}$$

Thus it is also called quadratic-phase signal. The corresponding time-domain function for a sinusoidal linear chirp is the sine of the phase in radians as expressed in Eq. (5.16).

$$x(t) = \sin\left[2\pi\left(f_0 t + \frac{k}{2}t^2\right)\right] \tag{5.16}$$

The chirp is generated using the unwrapped azimuth angle measurements. The relation between rotor rotational speed Ω (rad/s) and azimuth angle ψ (rad) is defined as Eq. (5.17) where time t is in seconds.

$$\psi = \Omega t \tag{5.17}$$

A pseudo-time $\hat{t}$ is generated based on this relation, and uniformly distributed phase of N chirps over 2π rad can be produced by considering the number of the chirps that has already been generated, n_c, and shifting the time vector accordingly. Now a pseudo-time is expressed as Eq. (5.18).

$$\hat{t} = \left[\psi + \left\{2\pi - \mathrm{mod}\left(\frac{2\pi n_c}{N}, 2\pi\right)\right\}\right]\frac{1}{\Omega} \tag{5.18}$$

The constructed chirp signal $\mathbf{U}_c$ with flap deflection amplitude $d_{\max}$ can be represented as Eq. (5.19).

$$\mathbf{U}_c = d_{\max}\sin\left[2\pi\left(f_0\hat{t} + \frac{k}{2}\hat{t}^2\right)\right] \tag{5.19}$$

Using the algorithm established, a flap deflection chirp input signal is

constructed with the deflection amplitude 1° and nine chirp phase angle over 2π rad for the present SNUF rotor system identification. According to the definition of IBC mode, each blade has the different input signal for actuation with 'blade phase' as described in Section 2.3.1. That is, when the actuation signal of the blade 1 for a particular chirp phase is generated, the signals of the other blades are additionally constructed with respect to the blade phase. Considering this behavior of each flap, the chirp input signal can be written as Eq. (5.20) where *k* is the blade number.

$$\mathbf{U}_c = d_{\max} \sin\left[2\pi \left\{ f_0 \left(\hat{t} + \frac{k-1}{4f\left(\hat{t}\right)} \right) + \frac{k}{2} \left(\hat{t} + \frac{k-1}{4f\left(\hat{t}\right)} \right)^2 \right\} \right] \tag{5.20}$$

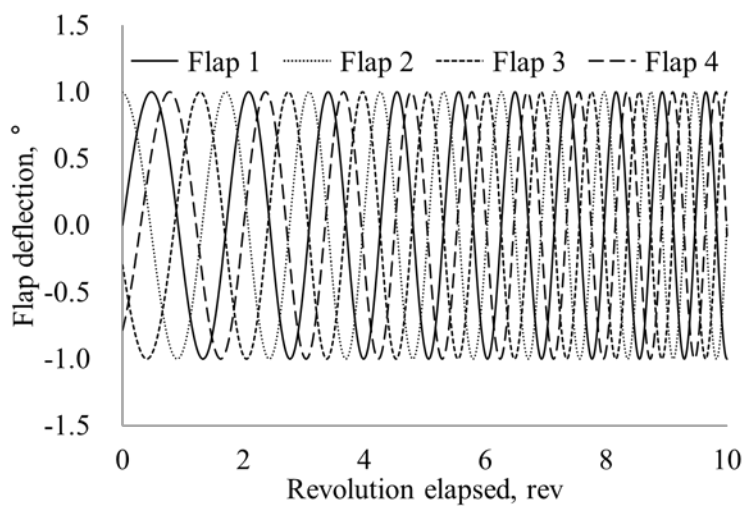

Fig. 5.1 Flap deflection chirp signals for each trailing-edge flap

Figure 5.1 the shows chirp signals corresponding to each blade with a

specific phase angle. In Fig. 5.1 the chirp signal generated for each different trailing-edge flap is overlapped with one another along the azimuthal location. It can be clearly seen that the phase angle for each flap signal is uniformly separated. Therefore, the chirp signal for trailing-edge flap with considering IBC mode is established.

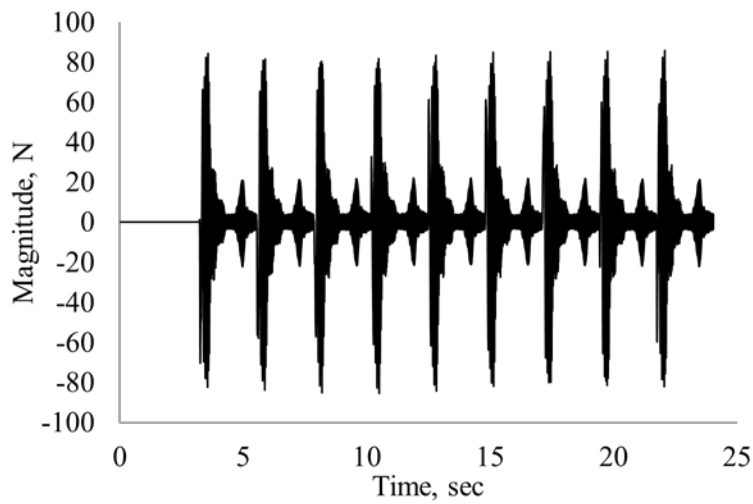

Fig. 5.2 Time history of hub vertical shear loads from which the baseline loads are subtracted

5.1.3 System Identification Result of the SNUF Rotor System

Using the constructed input signal, the response of the ATR system at the forward flight condition which is considered in Chapter 2 are obtained by the multibody dynamic analysis. The time history of the present SNUF rotor hub vertical shear loads from which the baseline loads are subtracted are shown in Fig. 5.2 from the time-domain forward flight simulation results with μ=0.3 and

α_s=-6°. The system identification scheme described in Ref. 168 is now implemented with the weighting factor α amounting to 10^5, and five harmonic transfer function (G_{-2}, G_{-1}, G_0, G_{+1}, G_{+2}) are estimated in this process. Results of the estimated transfer functions are shown in Fig. 5.3, and G_0 is observed to have significantly larger amplitude compared with the others.

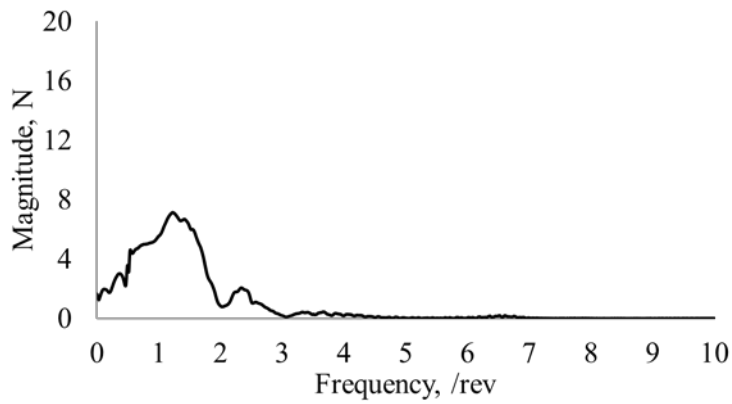

(a) G_{-2}

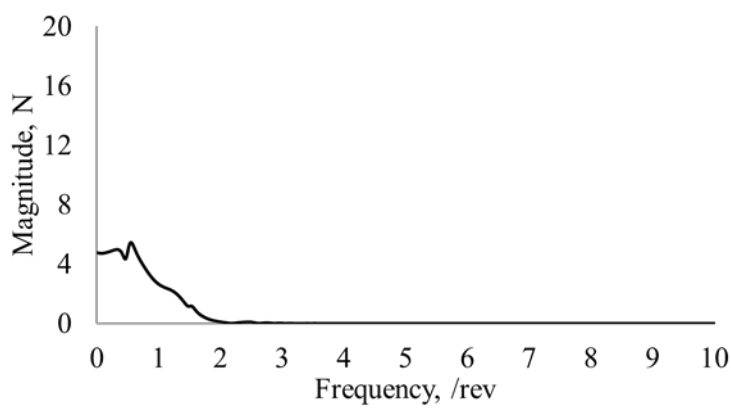

(b) G_{-1}

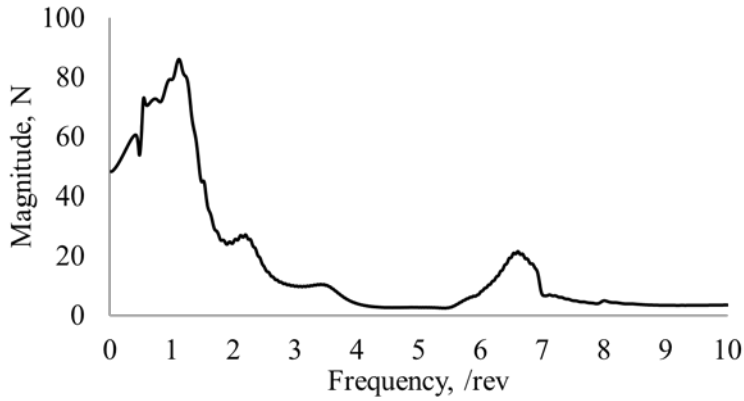

(c) G_0

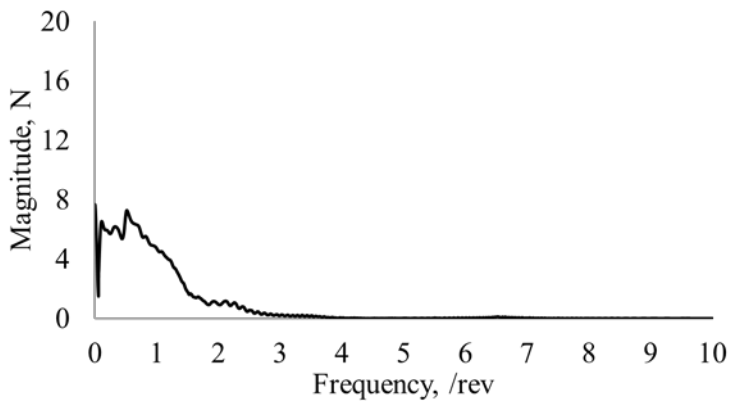

(d) G_{+1}

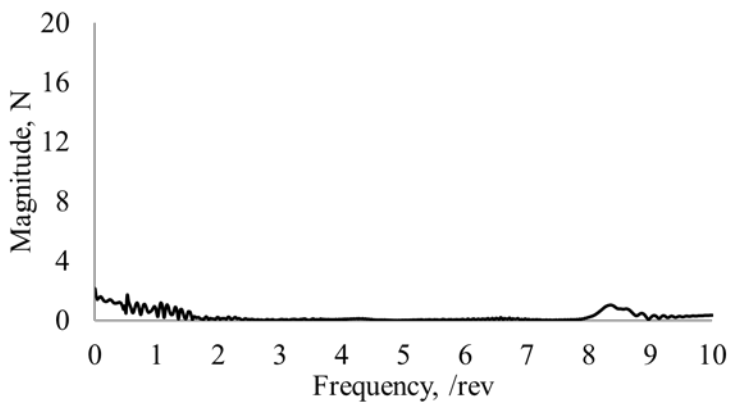

(e) G_{+2}

Fig. 5.3 Five harmonic transfer functions estimated for hub vertical shear load

This leads to the possibility that the response of the SNUF rotor system may be described only by G_0 components, just like in a linear time invariant system. The remnant component from the original response after subtracting the one described by G_0 is shown in Fig. 5.4. As it is compared with the original response in Fig 5.3, it is reduced by further than 1/4 in its amplitude. This implies that the energy contained in the remnant component becomes less than 1/16 of that in the original response since the energy is proportional to the square of the amplitude. It is therefore concluded that approximately 93% of the SNUF rotor system response can be described by G_0 alone. Based on this simplification to the LTI representation, a closed-loop controller can be designed.

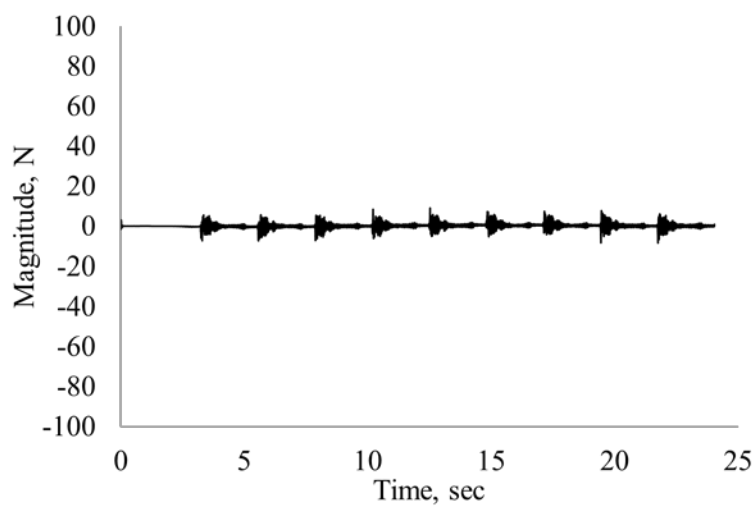

Fig. 5.4 Component remaining from the original response after subtracting the one represented by G_0

5.2 Closed-loop Controller Design

The vast majority of helicopter vibration reduction studies [28, 34, 44, 46, 60, 76 and 83] to date have employed control strategies based on the frequency domain formulations of the control problem. The periodic nature of the blade response in a forward flight is used to transfer the control problem from the time to the frequency domain. The time domain is described by a set of differential equations with periodic coefficients, and the frequency domain is governed by a set of algebraic equations with constant coefficient. However, since the periodic assumption is only valid under a steady state condition, the control solution obtained is only applicable toward the reduction of the vibration level experienced in the steady flight.

The HHC algorithm has been extensively used for active controls of vibration in rotorcraft [23-37]. The primary reasons for its wide acceptance are its relative simplicity, effectiveness, and robustness. A schematic of the HHC is shown in Fig. 5.5. While knowledge of the disturbance frequencies simplifies the rotorcraft problem, other complications arise from the fact that the helicopter dynamics around a trim condition are linear time periodic (LTP) and not linear time invariant (LTI). Such complications are avoided by enforcing simplifying assumptions.

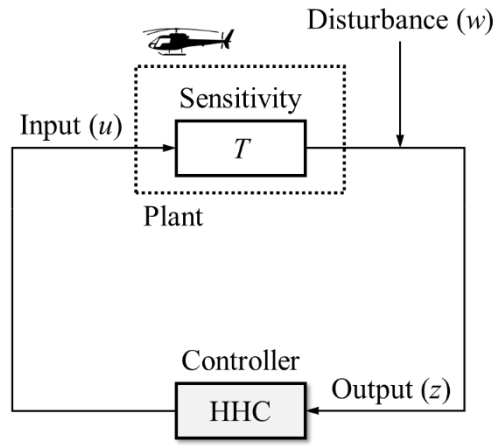

Fig. 5.5 Schematic of the higher harmonic control architecture implemented on a helicopter

5.2.1 Discrete-time HHC Algorithm

As conceived in Refs. 28, 35 and 64, HHC is a discrete-time algorithm based on the assumption that the helicopter can be represented by a linear, quasi-steady frequency domain representation relating the output *z* to control input *u*. Such linear representation can be identified using the Kalman filter method. Here, *z* is a vector of the harmonic sine and cosine amplitudes of the vibratory loads, and *u* is a vector of the harmonic sine and cosine amplitudes of the flap deflection. The output vector at the *i*-th time step is given by Eq. (5.21).

$$z_i = z_0 + T\left(u_i - u_0\right) \tag{5.21}$$

The sensitivity matrix *T* represents a linear approximation of the hub vibratory

load response to the flap control angle and is given by Eq. (5.22).

$$T = \frac{\partial z}{\partial u} \tag{5.22}$$

Equation (5.22) is referred to as the global representation of the response. Note that this representation depends on the assumption of the linearity and that the sensitivity T is invariant and known completely either by an identification procedure or direct measurement.

The controller is based on the minimization of a general quadratic cost function as expressed in Eq. (5.23).

$$J\left(z_i, u_i\right) = z_i^T Q_z z_i + u_i^T R u_i \tag{5.23}$$

Q_z is the weighting on the vibration output and R is the weighting on the control input. The optimal control input is determined from the requirement as Eq. (5.24).

$$\frac{\partial J\left(z_i, u_i\right)}{\partial u_i} = 0 \tag{5.24}$$

Equation (5.24) yields an explicit relation for the optimal control law $u_{i,\text{opt}}$, given by Eq. (5.25) which minimizes the cost function.

$$u_{i,\text{opt}} = -\left(T^T Q_z T + R\right)^{-1}\left(T^T Q_z\right)\left(z_0 - Tu_0\right) \tag{5.25}$$

This is the classical HHC algorithm that yield an explicit relation for the optimal control input.

5.2.2 HHC Algorithm Implementation for Vibration Reduction

The discrete-time HHC algorithm for vibratory load reduction is implemented on the present four-bladed SNUF rotor. The algorithm is based on a linear, quasi-static, frequency domain representation of the helicopter response to control inputs. In this case, the flap deflection of the *k*-th blade can be expressed as a sum of harmonic signals with frequencies that are integral multiples of the rotor frequency. The final expression of the relevant deflection is given as Eq. (5.26).

$$\delta\left(\Psi_k\right) = \sum_{N=2}^{5}\left\{\delta_{Nc}\cos\left(N\Psi_k\right) + \delta_{Ns}\sin\left(N\Psi_k\right)\right\} \tag{5.26}$$

To ensure that all four blades behave in the same track, it is assumed that each trailing-edge flap on each blade be executed in the same motion, but be shifted in phase by an angle designated to implement the IBC mode. Thus the control input for vibration reduction using the present controller is represented by the vector containing the cosine and sine amplitudes of the various *N*/rev

input harmonics as expressed in Eq. (5.27).

$$u_k = \begin{bmatrix} \delta_{2c} & \delta_{2s} & \cdots & \delta_{5c} & \delta_{5s} \end{bmatrix}^T \tag{5.27}$$

For hub vibratory load reduction, the output vector z_i consists of N_b/rev vibratory hub shear loads and moments, given in Eq. (5.28),

$$z = \begin{bmatrix} F_{HX} & F_{HY} & F_{HZ} & M_{HX} & M_{HY} \end{bmatrix}^T \tag{5.28}$$

F_{HX}, F_{HY} and F_{HZ} is the N_b/rev hub shear, and M_{HX} and M_{HY} is N_b/rev hub moments. The weighting matrix Q_z in Eq. (5.23) is a diagonal matrix. For vibration control, it consists of five weights corresponding to the three vibratory shear loads and the two vibratory hub moments.

5.2.3 Continuous-time HHC algorithm

Hall and Wereley [169] reformulated the original discrete-time HHC algorithm in a continuous-time framework as illustrated in Fig. 5.6. The HHC algorithm is represented as a continuous-time controller that employs an oscillator to extract the vibration frequency of interest. The matrix T represents a quasi-steady, linear time-invariant relation between the sine and cosine components of the input and the output. Hall and Wereley [169] proved that the

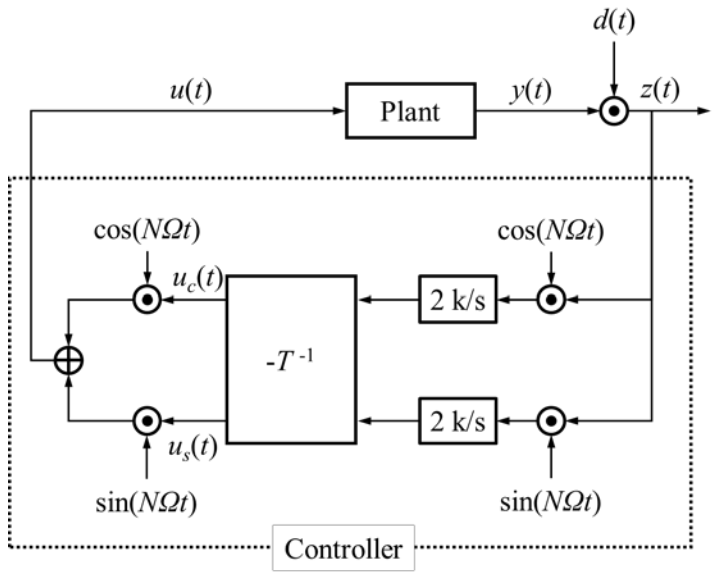

Fig. 5.6 Continuous-time higher harmonic control architecture [169]

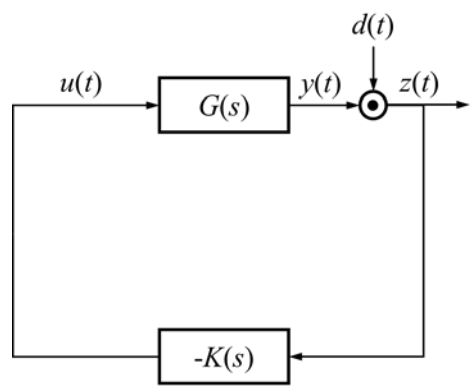

Fig. 5.7 Block diagram of the classical disturbance rejection representation

control system shown in Fig. 5.6 is equivalent to the classical control system shown in Fig. 5.7. The control input is expressed in the Laplace domain as Eq. (5.29)

$$u(s) = -K(s)z(s) \tag{5.29}$$

where

$$K(s) = \frac{2k(as + bN\Omega)}{s^2 + (N\Omega)^2} \tag{5.30}$$

$$a = \frac{\mathrm{Re}\{G(jN\Omega)\}}{|G(jN\Omega)|^2} \tag{5.31}$$

$$b = -\frac{\mathrm{Im}\{G(jN\Omega)\}}{|G(jN\Omega)|^2} \tag{5.32}$$

The linear relation between the control inputs and the rotor loads is represented by the transfer function $G(s)$, and $K(s)$ is the continuous-time controller using frequency selective filter. The primary advantage of using the continuous-time HHC (CTHHC) is that it enables use of the classical control techniques to evaluate performance and stability. In this dissertation, CTHHC approach is embedded for on-blade vibration control by the trailing-edge flap in the multibody dynamic simulation of the present SNUF rotor system.

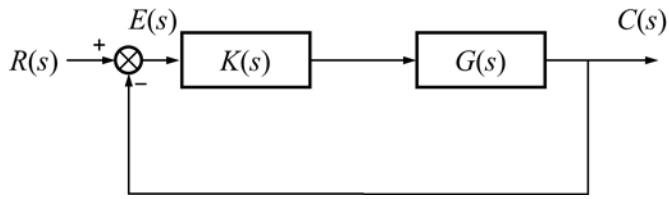

Fig. 5.8 Block diagram of the standard cascade compensation and unity feedback system

5.3 Implementation of the Closed-loop Controller

5.3.1 Stability Evaluation of the Closed-loop System

Before implementing the controller, the stability of the closed-loop system should be evaluated in order to examine whether it is an appropriate controller. For this purpose, the closed-loop transfer function is investigated in the frequency domain. The block diagram shown in Fig. 5.8 is the standard cascade compensation and the unity feedback system. The error signal $E(s)$ is given Eq. (5.33).

$$E(s) = R(s) - C(s) \tag{5.33}$$

$R(s)$ is the reference input and $C(s)$ is the output. The plant transfer function $G(s)$ and the compensator transfer function are determined from the preceding section. The block diagram illustrated in Fig. 5.8 represents the following Eqs. (5.34) and (5.35).

$$C(s) = G(s)K(s)E(s) \tag{5.34}$$

$$\begin{aligned} E(s) &= R(s) - C(s) \\ &= R(s) - G(s)K(s)E(s) \end{aligned} \tag{5.35}$$

Therefore, Eqs. (5.34) and (5.35) can be expressed as Eqs. (5.36) and (5.37).

$$\frac{E(s)}{R(s)} = \frac{1}{1+G(s)K(s)} := S_c(s) \tag{5.36}$$

$$\frac{C(s)}{R(s)} = \frac{G(s)K(s)}{1+G(s)K(s)} := G_c(s) \tag{5.37}$$

$S_c(s)$ is the sensitivity function and $G_c(s)$ is the closed-loop system transfer function.

Bode plot of the closed-loop transfer function and the sensitivity is estimated as shown in Fig. 5.9. In order to evaluate the stability of the present closed-loop control system, the gain and phase margin are estimated. The amount by which the gain can be increased before instability is called the gain margin, and is indicated as GM in Fig. 5.9. The gain margin may be determined from Bode plot as well, as also shown in Fig. 5.9, by noting the value of the gain where the phase crosses -180°. This value is one measure of how adjacent the closed-loop system is to instability: a small gain margin (close to unity) indicates the system is close to instability. The present controller has a sufficient gain margin of -38 dB.

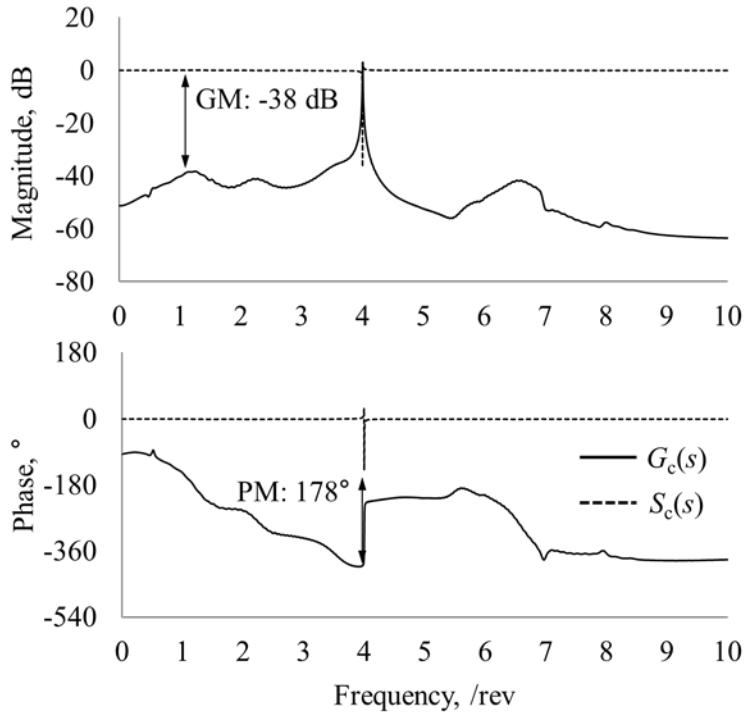

Fig. 5.9 Bode plot of the closed-loop transfer function and sensitivity

Another important quantity is the phase margin, also show in Fig 5.9 (denoted PM). The phase margin specifies how much the phase at the crossover frequency (where the magnitude is 1) differs from -180°. If the phase equals -180° at crossover, the system is on the verge of instability. Thus, the phase margin is another measure of how close the system is to instability. The phase margin of the present controller is found to be 178°. Therefore, it is considered that the present closed-loop control system has an adequate stability. In addition, the magnitude of the sensitivity function at 4/rev frequency has the minimum peak value of -37 dB which implies that the present closed-loop controller has the adequate control authority to reduce the 4/rev hub vibratory loads.

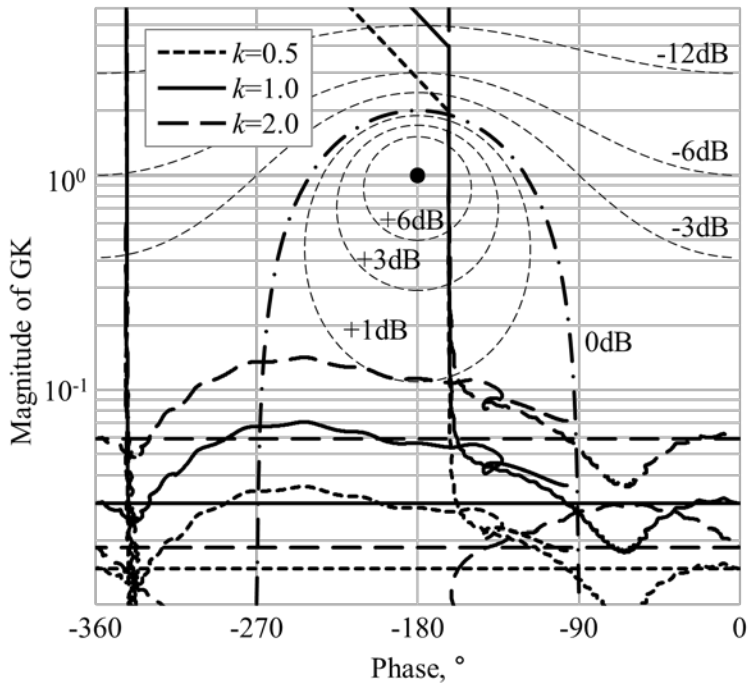

Fig. 5.10 Nichols plot of the loop transfer functions according to the control gain *k*=0.5, 1.0 and 2.0

Nichols plot of the loop transfer function is introduced to examine the present controller stability in a different way. A Nichols plot contains the same information as a Bode plot. The difference is that instead of plotting the gain and phase separately as a function of frequency, in Nichols plot, the gain is plotted against the phase and the frequency information is not displayed explicitly. In order to investigate variation of the present system stability according to the change of the *k* shown in Eq. (5.30), *k* is varied to 0.5, 1.0 and 2.0. Those results are plotted in Fig. 5.10. The stability of the system is ensured since there are no encirclements of the critical point (unity magnitude at 180°

of phase). This point is shown by the circle in Fig 5.10. Contours of the constant disturbance rejection, given by Eq. (5.38) are also presented on Nichols plot.

$$\frac{y}{d} = \frac{1}{1+GK} \tag{5.38}$$

The closed contours around the critical point represent levels of vibration amplification. The alternated long and short dash line, U-shaped contour is the 0 dB boundary, where no vibration rejection or amplification is achieved. The open contours above the critical point represent levels of vibration reduction. The dB values listed next to each contour indicate how much either amplification or rejection is caused at the frequency where the loop transfer function intersects the contour.

By using Nichols plot, the gain and phase margins are easily identified by measuring the proximity of the contour to the critical point when the phase equals 180° of the gain equals unity, respectively. The gain and phase margin for each control gain is summarized in Table 5.1. In principle, all those level of stability margins are regarded as enough for a general feedback compensator. When the gain of the controller is increased, there appears a chance of instability since it induces the gain margin to be diminished. For example, if the gain increases extremely to 18.0, the gain margin is only 0.13 dB, as shown in Fig.5.11. Therefore, it is considered that the stability of the present controller is sufficient when applying a moderate control gain value.

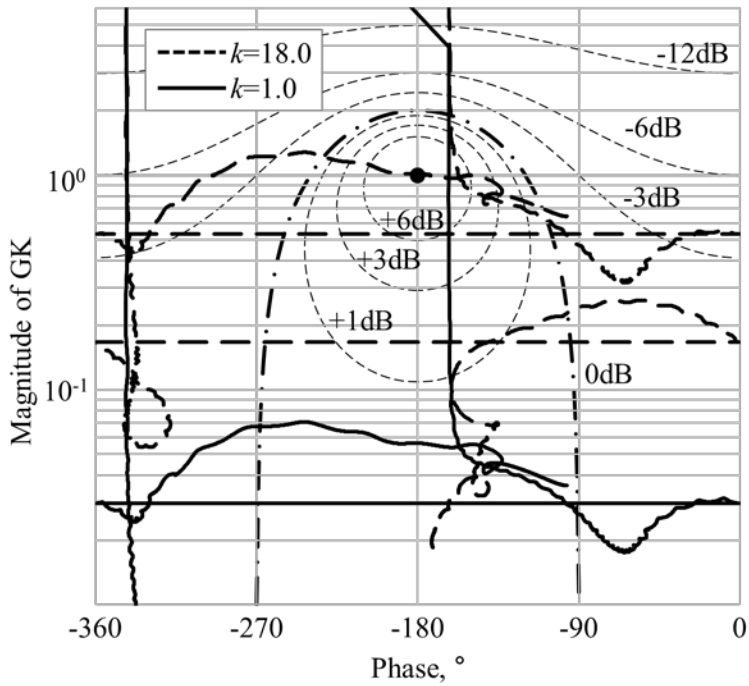

Fig. 5.11 Nichols plot of the loop transfer functions with the control gain *k*=1.0 and 18.0

5.3.2 Numerical Simulation of the Closed-loop Controller

In DYMORE, a linear control law is the one embedded and implements a generic linear control law of the following form as expressed in Eqs. (5.39) and (5.40).

$$\dot{x} = Ax + B\left(y - \hat{y}\right) \tag{5.39}$$

$$u = Cx + D\left(y - \hat{y}\right) \tag{5.40}$$

x is an array of the controller internal states, y is the measured value, such as the hub vertical shear load in this analysis, $\hat{y}$ is the specified target value of y, and u is an output value of the controller, i.e., the flap deflection in this analysis. The control law, Eq. (5.39), is discretized as Eq. (5.41) using the central difference scheme.

$$\frac{x_f - x_i}{t_f - t_i} = A\frac{x_f + x_i}{2} + B\left(\frac{y_f + y_i}{2} - \hat{y}\right) \tag{5.41}$$

The subscripts i and f denote quantities computed at the initial and final times of the time step, respectively. The final value of the control law internal states now becomes Eq. (5.42).

$$x_f = \left(\frac{I}{t_f - t_i} - \frac{A}{2}\right)^{-1}\left\{\left(\frac{I}{t_f - t_i} + \frac{A}{2}\right)x_i + B\left(\frac{y_f + y_i}{2} - \hat{y}\right)\right\} \tag{5.42}$$

The final output of the control law from Eq. (5.40) then follows as Eq. (5.43).

$$u_f = Cx_f + D\left(y_f - \hat{y}\right) \tag{5.43}$$

The state-space of the present controller in Eq. (5.30) involves three state variables, meaning that x becomes a 3×1 array.

By applying the matrix representation expressed in Eqs. (5.39) and (5.40)

into DYMORE linear controller module, the time domain analyses are executed in order to verify the performance of the closed-loop controller. The controller is engaged with a different magnitude of its gain constant discretely adjusted at 0.5, 1.0 and 2.0. In order to establish the steady-state equilibrium, these analyses are conducted with 10-second period for each gain constant. The result time history of the hub vertical shear load is presented in Fig. 5.12. As one can see, the vibratory load without control is significantly reduced by the implementation of the controller. As control gain in the controller varies, different response behavior are derived. By increasing the control gain, it is observed that it takes longer to attain the steady-state equilibrium.

5.4 Flap-driving Mechanism Representation

The piezoelectric actuator, APA 1000L, features a linear characteristic for small amount of input voltage. If the flap-driving mechanism is represented by a single *n*-th order equation, it is easy to represent it in transfer function form. The flap-driving mechanism is mathematically represented by the mechanical properties of *m*, *c* and *k* and the electrical property of capacitance, as shown in Eq. (5.44).

$$G_{\text{Act}} = \frac{k}{(\tau s + 1)} \frac{1}{\left(ms^2 + cs + k\right)} \tag{5.44}$$

The parameters of the transfer function are estimated with the experiment results of the flap-driving components. It is possible to estimate the linear transfer function from the small input and the small deflection response of the flap-driving system. In order to identify the flap-driving system, the frequency response sweep experiment is conducted. Figure 5.13 shows the input and output responses of the present flap-driving mechanism under 3/rev actuation.

The present flap-driving system can be represented as the piece-wise LTI using the response near 3/rev frequency. This LTI representation of the flap-driving system will be implemented to perform the precise control of the flap deflection in forward flight experiment, and expected to guarantee the performance of the CTHHC method.

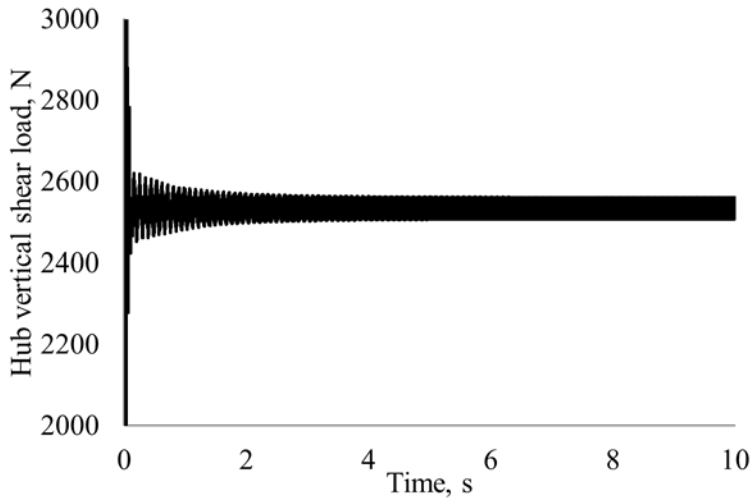

(a) Baseline (No control)

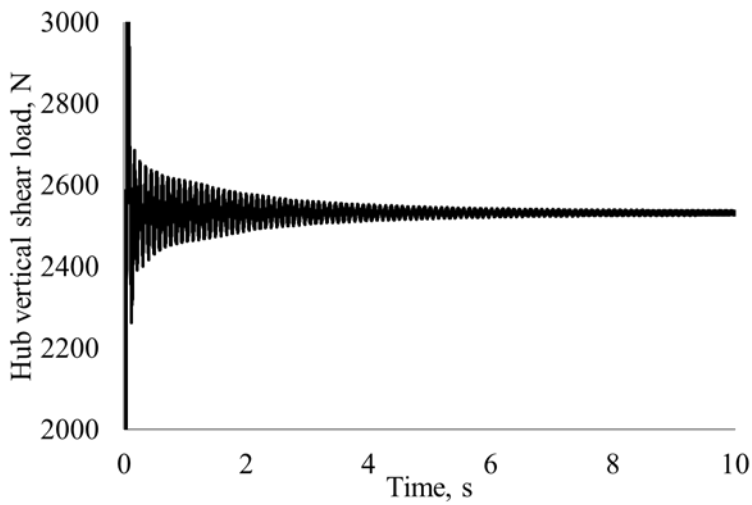

(b) Control with gain 0.5

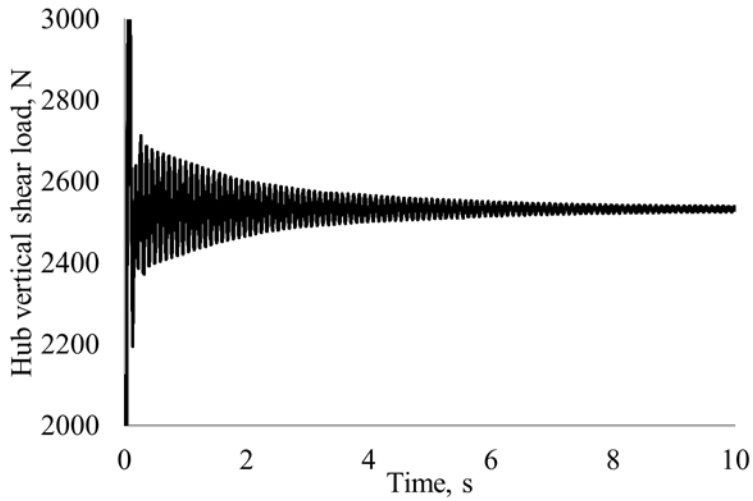

(c) Control with gain 1.0

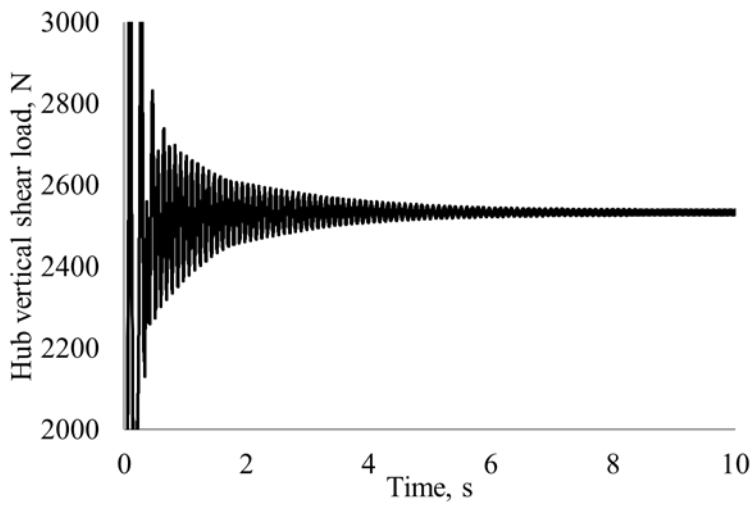

(d) Control with gain 2.0

Fig. 5.12 Hub vertical shear loads for μ = 0.3, α_s = -6° and C_T/σ = 0.060 without and with the closed-loop controller

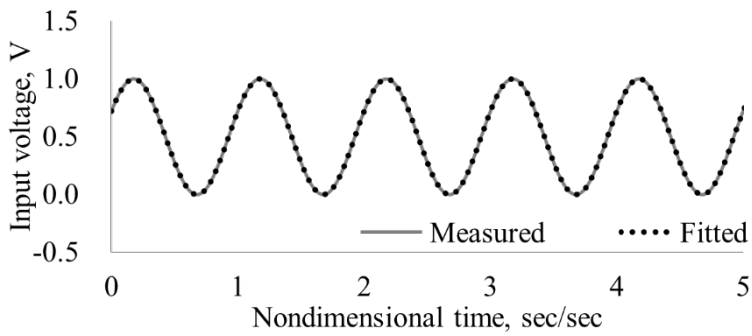

(a) Voltage input response

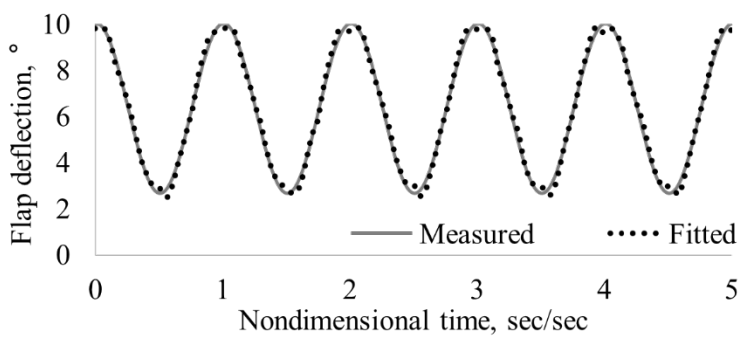

(b) Flap deflection response

Fig. 5.13 Input and output responses of the flap-driving mechanism at 65.0 Hz (3/rev)

Chpater 6

Conclusion

6.1 Summary

In this dissertation, the design of the active vibration reduction blade using the trailing-edge flap is improved, and the structural integrity of the present design and the vibration reduction performance of the trailing-edge flap are estimated further. The present design improvement process is conducted in the following two phases: blade planform and cross-sectional design. The structural integrity is evaluated by the three-dimensional finite element analysis including rotating and contact situation. The vibration reduction capability simulation of the trailing-edge flap is performed by the following two methods: open-loop control with the control phase sweep and closed-loop control.

In order to improve the previous SNUF blade, the multidisciplinary design of the flap-driving mechanism is performed. The flap hinge moment is predicted by CFD analysis, and the relevant driving mechanism is designed considering the result. To understand the influence of the location and dimension of the trailing-edge flap, the SNUF blade is modeled with regard to multibody dynamics, and the vibratory load reduction capability according to the selected flap parameters is estimated. In addition, the sectional design

optimization framework using the genetic algorithm is established. In such process the first torsional frequency is limited to smaller than 3/rev to enhance the vibratory load reduction capability by the trailing-edge flap. The sectional optimization is performed with the objective function of reducing the blade weight, thereby optimization of the SNUF blade design is accomplished.

The present SNUF blade design is modeled with regard to multibody dynamics and its vibratory load reduction capability is verified. The trim analysis is performed preliminarily to derive trimmed pitch angle and baselines of the vibratory loads are obtained. The open-loop control analysis is carried out by phase sweeps at 3, 4 and 5/rev flap actuation frequencies. It is observed that the vibratory load reduction capability of the present SNUF is improved further than that by the previous design.

The structural integrity of the present SNUF blade is evaluated by various methods. The strain recovery analysis in the blade section is implemented in the design optimization framework. In addition, the in-plane stress occurring at the blade root – hub connection region is considered. Also, the three-dimensional finite element analysis is performed with applying the rotation and contact condition. It is concluded that the structural integrity of the present SNUF blade design is sufficient.

A prototype of the present flap-driving component is fabricated and its flap deflection is measured. A steel guide and thrust bearing are included in the flap-driving component to minimize degradation of the flap deflection due to the

large centrifugal loads expected to occur during the blade rotation. In the static bench experiment without external loads, the flap deflection exceeds the target value. An endurance experiment is conducted to verify the performance and durability of the flap-driving components under the virtual centrifugal loading condition. As a result, it is found that the present flap-driving components is capable of generating the flap deflection larger than the aimed value during the required operation duration.

Finally, a closed-loop controller is designed to reduce the hub vibratory loads under the forward flight condition. In order to estimate the transfer function between the flap deflection and the hub vibratory load, the system identification of the multibody dynamics model is performed. The closed-loop controller is designed based on the system identification results and the continuous-time HHC algorithm. A preliminary stability check of the designed compensator is conducted, and demonstrated numerically by implementing it in the multibody dynamics analysis. The present controller shows a satisfactory vibratory load reduction capability.

6.2 Contribution of the Present Work

The major contribution of the present dissertation can be summarized as follows:

- Using the flap-driving mechanism that achieves the desired flap deflection angle under significant aerodynamic loads condition is proposed. . In this process, the external aerodynamic loads from the prediction results of the transient CFD analysis is implemented. In the most of the previous researches, performance of the flap-driving mechanisms was verified by experiments directly. On the contrary, using the present method, it is found to be possible to predict the flap deflection of the flap-driving mechanism by estimating accurately the characteristics of the actuator and the aerodynamic loads acting on the trailing-edge flap.

- Most of the previous active flap blades were designed by utilizing the existing helicopter rotor blade shape and properties. In several studies where new blades were designed by optimization, dimensions of the trailing-edge flap and lay-up configuration of the blade section were not extensively considered. In this dissertation, vibration reduction capability of the active flap blade is investigated in terms of the dimension and location of the trailing-edge flap. In addition, the cross-sectional optimization framework based on the genetic algorithm is introduced considering variety of design variables.

- Various methods are proposed to evaluate the structural integrity of the present SNUF blade design. Three-dimensional static structural analysis is

performed including the details of the flap-driving components. In this process, various contact conditions are considered to simulate practical loading conditions, and external aerodynamic/centrifugal loads due to the rotation of the blade are included.

- Performance of the present flap-driving mechanism under the centrifugal loading condition is experimentally verified. The centrifugal load acting on the trailing-edge flap is simulated by using the dummy weights. Under those loading conditions, the flap deflection of the present flap-driving components is measured. In addition, these experiments are performed during the aimed operation duration. By such endurance experiment, the performance and durability of the present flap-driving components are ascertained.

The hub vibratory load reduction capability of the present active flap rotor under forward flight condition is investigated analytically using both open-loop and closed-loop control. In the open-loop control, hub vibratory load reduction analyses with various actuation frequencies and phases are conducted. In addition, the closed-loop controller based on the transfer function of the multibody dynamics is obtained analytically. And its stability and vibration reduction capability is demonstrated.

6.3 Future Works

In addition to the present dissertation, there are a few future items to research as follows:

- Tensile experiments will be conducted on the sample sections to verify the strength for the present composite blade layup. Two sample sections will be fabricated, namely, the root section and the special section. During the experiments, a pure tensile load will be applied to simulate the centrifugal load which will be the most dominant loading on the blade.

- Once the tensile experiment is successfully conducted, preparations for the hover experiment will begin. The purpose of the hover experiment will be experimentally determine the structural integrity and operability of the present SNUF blade and flap-driving components. First, the hover experiment with single active blade and three passive blades will be performed on KARI's whirl tower. The static balancing will be done in order to make sure the total mass on the all blades used in the hover experiment will be balanced. Then, while rotating the SNUF rotor system, the strain of the blade and the deflection of the trailing-edge flap will be monitored at several collective pitch control input.

KARI whirl tower does not provide the cyclic pitch control and is installed outside a wind tunnel. In order to carry out the experiment to reduce the hub vibratory load by the active trailing-edge flap in the forward flight condition, a whirl tower which is installed in a wind tunnel and capable of collective and cyclic pitch control will be required.

Reference

[1] Veca, A. C., *Vibration Effects on Helicopter Reliability and Maintainability*, Sikorsky Aircraft Division, No. SER-611567, 1973.

[2] Heffernan, R., Precetti, D. and Johnson, W. *Vibration Analysis of the SA349/2 Helicopter*, NASA Technical Report, TM-102794, 1991.

[3] Johnson, W., *Recent Developments in the Dynamics of Advanced Rotor System*, NASA Technical Report, TM-86669, 1985.

[4] Reichert, G. "Helicopter Vibration Control: A survey," *Vertica*, Vol. 5, No. 1, 1981, pp. 1-20.

[5] Breitbach, E. and Büter, A. "The main Sources of Helicopter Vibration and Noise Emissions and Adaptive Concepts to reduce them," *Journal of Structural Control*, Vol. 3, No. 1-2, 1996, pp. 21-32.

[6] Gerstenberger, W., "The Rotary Round Table: Practical Aspects of Vibration Control," *Journal of the American Helicopter Society*, Vol. 2, No. 3, 1957, pp. 3-4.

[7] Hamounda, N. H. and Pierce, G. A., "Helicopter Vibration Suppression Using Simple Pendulum Absorbers on the Rotor Blades," *Journal of the American Helicopter Society*, Vol. 29, No. 3, 1984, pp. 19-29.

[8] Kottapalli, S., "Sources of Helicopter Rotor Hub Inplane Shears," *Proceedings of 34th AIAA/ASME/ASCE/AHS/ASC Structures, Structural Dynamics and Materials Conference*, La Jolla, CA, April 19-22, 1993.

[9] Schuett, E., "Application of Passive Rotor Isolation for Alleviation of Rotor Induced Vibration," *Journal of the American Helicopter Society*, Vol. 14, No. 2, 1969, pp. 34-48.

[10] Viswanathan, S. P. and Myers, A. W., "Reduction of Helicopter Vibration through Control of Hub-Impedance," *Journal of the American Helicopter Society*, Vol. 25, No. 4, 1980, pp. 3-12.

[11] Braun, D., "Development of Antiresonant Force Isolators for Helicopter Vibration Reduction," *Journal of the American Helicopter Society*, Vol. 27, No. 4, 1982, pp. 37-44.

[12] Freidmann, P. P. and Shanthakumaran, P., "Optimum Design of Rotor Blades for Vibration Reduction in Forward Flight," *Journal of the American Helicopter Society*, Vol. 29, No. 4, 1984, pp. 70-80.

[13] Davis, M. W. and Weller, W. H., "Application of Design Optimization Techniques to Rotor Dynamics Problems," *Proceedings of the 42nd American Helicopter Society Annual Forum,* Washington D.C., June 2-4, 1986.

[14] Lim, J. W., *Aeroelastic Optimization of a Helicopter Rotor*, Ph.D. thesis, University of Maryland, 1988.

[15] Lim, J. W. and Chopra, I., "Aeroelastic Optimization of a Helicopter Rotor Blade," *Journal of the American Helicopter Society*, Vol. 34, No. 3, 1989, pp. 52-62.

[16] Freidmann, P. P. and Shanthakumaran, P., "Helicopter Vibration

Reduction Using Structural Optimization with Aeroelastic/Multidisciplinary Constraints - A Survey," *Journal of Aircraft*, Vol. 28, No. 1, 1991, pp. 8-21.

[17] Young, D. K. and Tarzanin, F. J., "Structural Optimization and Mach Scale Test Validation of a Low Vibration Rotor," *Journal of the American Helicopter Society*, Vol. 38, No. 3, 1993, pp. 83-92.

[18] Ganguli, R. and Chopra, I., "Aeroelastic Optimization of an Advanced Geometry Composite Helicopter Rotor," *Proceedings of the 51st American Helicopter Society Annual Forum*, Fort Worth, TX, May 9-11, 1995.

[19] Yuan, K. A. and Friedmann, P. P., "Structural Optimization for Vibration Reduction of Composite Helicopter Rotor Blades with Advanced Geometry Tips Subject to Multidisciplinary Constraints," *Proceedings of the 51st American Helicopter Society Annual Forum*, Fort Worth, TX, May 9-11, 1995.

[20] Tarzanin, F. J., Young, D. K., and Panda, B., "Advanced Aeroelastic Optimization Applied to an Improved Performance, Low Vibration Rotor," *Proceedings of the 55th American Helicopter Society Annual Forum*, Montréal, Canada, May 25-27, 1999.

[21] Bao, J., Chopra, I., Bernhard, A. P. F., and Nagaraj, V. T., "Design and Hover Test of Low Vibration Mach Scale Rotor with Twisted Composite Tailored Blades," *Proceedings of 44th AIAA/ASME/ASCE/AHS/ASC*

Structures, Structural Dynamics and Materials Conference, Norfolk, VA, April 7-10, 2003.

[22] Chiu, T. and Friedman, P. P., "ACSR System for Vibration Suppression in Coupled Helicopter Rotor/Flexible Fuselage Model," *Proceedings of the 37th AIAA/ASME/ASCE/AHS/ASC Structures, Structural Dynamics and Materials Conference*, Salt Lake City, UT, April 15-17, 1996, pp. 1972-1990.

[23] Yen, J. G., "Higher Harmonic Control for Helicopters with Two-Bladed and Four-Bladed Rotors," *Journal of Aircraft*, Vol. 18, No. 12, 1981, pp. 1064-1069.

[24] Nygren, K. and Scharge, D., "Fixed-Gain versus Adaptive Higher Harmonic Control Simulation," *Journal of the American Helicopter Society*, Vol. 34, No. 3, 1989, pp. 51-58.

[25] Nguyen, K. and Chopra, I., "Application of Higher Harmonic Control to Rotors Operating at High Speed and Thrust," *Journal of the American Helicopter Society*, Vol. 35, No. 3, 1990, pp. 78-89.

[26] Robinson, L. H. and Friedmann, P. P., "A Study of Fundamental Issues in Higher Harmonic Control Using Aeroelastic Simulation," *Journal of the American Helicopter Society*, Vol. 36, No. 2, 1991, pp. 32-43.

[27] Nguyen, K. and Chopra, I., "Effects of Higher Harmonic Control on Rotor Performance and Control Loads," *Journal of Aircraft*, Vol. 29, No. 3, 1992, pp. 336-342.

[28] McHugh, F. J. and Shaw, J., "Helicopter Vibration Reduction with Higher Harmonic Blade Pitch," *Journal of the American Helicopter Society*, Vol. 23, No. 4, 1978, pp. 26-35.

[29] Shaw, J. and Albion, N., "Active Control of the Helicopter Rotor for Vibration Reduction," *Journal of the American Helicopter Society*, Vol. 26, No. 3, 1981, pp. 32-39.

[30] Hammond, C. E., "Wind Tunnel Results Showing Rotor Vibratory Loads Reduction Using Higher Harmonic Blade Pitch," *Journal of the American Helicopter Society*, Vol. 28, No. 1, 1983, pp. 10-15.

[31] Shaw, J., Albion, N., Hanker, E., and Teal, R., "Higher Harmonic Control: Wind Tunnel Demonstration of Fully Effective Vibratory Hub Force Suppression," *Journal of the American Helicopter Society*, Vol. 34, No. 1, 1989, pp. 14-25.

[32] Kottapalli, S., Swanson, S., Lemasurier, P., and Wang, P., "Full-Scale Higher Harmonic Control Research to Reduce Hub Loads and Noise," *Proceedings of the 49th American Helicopter Society Annual Forum*, St. Louis, Missouri, April 19-21, 1993.

[33] Kube, R., "New Aspects of Higher Harmonic Control on a Four-Bladed Hingeless Model Rotor," *Journal of the American Helicopter Society*, Vol. 37, No. 3, 1992, pp. 61-68.

[34] Brooks, T. F. and Booth, E. R., "The Effects of Higher Harmonic Control on Blade- Vortex Interaction Noise and Vibration," *Journal of the*

American Helicopter Society, Vol. 38, No. 1, 1993, pp. 45-55.

[35] Wood, E. R., Powers, R. W., Cline, J. H., and Hammond, C. E., "On Developing and Flight Testing a Higher Harmonic Control System," *Journal of the American Helicopter Society*, Vol. 30, No. 1, 1985, pp. 3-20.

[36] Miao, W. Kottapalli, S. B. R. and Frye, H. M., "Flight Demonstration of Higher Harmonic Control (HHC) on S-76," *Proceedings of the 42nd American Helicopter Society Annual Forum*, Washington D.C., June 2-4, 1986.

[37] Walsh, D. M., *Flight Test of an Open Loop Higher Harmonic Control System on an S-76A Helicopter*, Master's thesis, Florida Atlantic University, 1986.

[38] Ham, N. D., "A Simple System for Helicopter Individual-Blade-Control Using Modal Decomposition," *Vertica*, Vol. 4, No. 1, 1980, pp. 23-28.

[39] Guinn, K. F., "Individual Blade Control Independent of Swashplate," *Journal of the American Helicopter Society*, Vol. 27, No. 3, 1982, pp. 25-31.

[40] Ham, N. D., "Helicopter Individual-Blade-Control and its Applications," *Proceedings of the 9th European Rotorcraft Forum*, Stresa, Italy, September 13-15, 1983.

[41] Ham, N. D., "Helicopter Individual-Blade-Control: Promising Technology for the Future Helicopter," *Proceedings of the 21st European*

Rotorcraft Forum, Stain-Petersburg, Russia, August 30-September 1, 1995.

[42] Jacklin, S. A., Leyland, J. A., and Blaas, A., "Full Scale Wind Tunnel Investigation of a Helicopter Individual Blade Control System," *Proceedings of the 44th AIAA/ASME/ASCE/AHS/ASC Structures, Structural Dynamics and Materials Conference*, Lajolla, CA, April 19-22, 1993.

[43] Jacklin, S. A., Nguyen, K., Blaas, A., and Richter, P., "Full-Scale Wind Tunnel test of a Helicopter Individual Blade Control System," *Proceedings of the 50th American Helicopter Society Annual Forum*, Washington, D.C., May 11-13, 1994.

[44] Jacklin, S., Nguyen, K., Richter, P., and Blaas, A., "Reduction in Helicopter BVI Noise, Vibration, and Power Consumption through Individual Blade Control," *Proceedings of the 51st American Helicopter Society Annual Forum*, FortWorth, TX, May 9-11, 1995.

[45] Schimke, D., Arnold, U. T. P., and Kube, R., "Individual Root Control Demonstration Evaluation of Recent Flight Tests," *Proceedings of the 54th American Helicopter Society Annual Forum*, Washington, D.C., May 20-22, 1998.

[46] Kube, R., Van der Wall, B. G., Schultz, K. J., and Splettstoesser, W. R., "IBC Effects on BVI Noise and Vibrations -A Combined Numerical and Experimental Investigation," *Proceedings of the 55th American*

Helicopter Society Annual Forum, Montrëal, Canada, May 25-27, 1999.

[47] Jacklin, S., Haber, A., de Simone, G., Norman, T., Kitaplioglu, C., and Shinoda, P., "Full-Scale Wind Tunnel Test of an Individual Blade Control System for a UH-60 Helicopter," *Proceedings of the 58th American Helicopter Society Annual Forum*, Montrëal, Canada, June 11-13, 2002.

[48] Kunze, O., Arnold, U. T. P., and Waaske, S., "Development and Design of an Individual Blade Control System for the Sikorsky CH-53G Helicopter," *Proceedings of the 55th American Helicopter Society Annual Forum*, Montrëal, Canada, May 25-27, 1999.

[49] Arnold, U. T. P. and Strecker, G., "Certification, Ground and Flight-Testing of an Experimental IBC System for the CH-53G Helicopter," *Proceedings of the 58th American Helicopter Society Annual Forum*, Montréal, Canada, June 11-13, 2002.

[50] Kessler, C., Fuerst, D., and Arnold, U. T. P., "Open Loop Flight Test Results and Closed Loop Status of the IBC System on the CH-53G Helicopter," *Proceedings of the 59th American Helicopter Society Annual Forum*, Phoenix, AZ, May 2003.

[51] Arnold, U. T. P., "Recent IBC Flight Test Results from the CH-53G Helicopter," *Proceedings of the 29th European Rotorcraft Forum*, Friedrichshafen, Germany, September 16-18, 2003.

[52] Fuerst, D., Hausburg, A., and Neuheuser, T., "Experimental Verification of an Electro-Mechanical-Actuator for a Swashplateless Primary and

Individual Helicopter Blade Control System," *Proceedings of the 64th American Helicopter Society Annual Forum*, Montrëal, Canada, April 29 -May 1, 2008.

[53] Chen, P. C., *Development of a Smart Rotor with Induced-Strain Actuation of Blade Twist*, Ph.D. thesis, University of Maryland, 1996.

[54] Chen, P. C. and Chopra, I., "Hover Testing of Smart Rotor with Induced Strain Actuation of Blade Twist," *AIAA Journal*, Vol. 35, No. 1, 1997, pp. 6-16.

[55] Derham, R., Weems, D., Mathew, M. B., and Bussom, R., "The Design Evolution of an Active Materials Rotor," *Proceedings of the 57th American Helicopter Society Annual Forum*, Washington, D.C., May 9-11, 2001.

[56] Cesnik, C. E. S., Shin, S., Wilkie, W. K., Wilbur, M. L., and Mirick, P. H., "Modeling, Design, and Testing of the NASA/ARMY/MIT Active Twist Rotor Prototype Blade," *Proceedings of the 55th American Helicopter Society Annual Forum*, Montréal, Canada, May 25-27, 1999.

[57] Shin, S. and Cesnik, C. E. S., "Helicopter Vibration Reduction in Forward Flight using Blade Integral Twist Control," *Proceedings of 43rd AIAA/ASME/ASCE/AHS/ASC Structures, Structural Dynamics and Materials Conference*, Denver, CO, April 22-25, 2002.

[58] Shin, S. and Cesnik, C. E. S., "Helicopter Performance and Vibration Enhancement by Twist-Actuated Blades," *Proceedings of 44th*

AIAA/ASME/ASCE/AHS/ASC Structures, Structural Dynamics and Materials Conference, Norfolk, VA, April 7-10, 2003.

[59] Bernhard, A. P. F. and Wong, J., "Wind-Tunnel Evaluation of a Sikorsky Active Rotor controller Implemented on the NASA/ARMY/MIT Active Twist Rotor," *Journal of the American Helicopter Society*, Vol. 50, No. 1, 2005, pp. 65-81.

[60] Shin, S., Cesnik, C. E. S., and Hall, S. R., "Closed-Loop Control Test of the NASA/Army/MIT Active Twist Rotor for Vibration Reduction," *Journal of the American Helicopter Society*, Vol. 50, No. 2, 2005, pp. 178-194.

[61] Wei, F. and Gallagher, F., "Servo-Flap Rotor Performance Flight Testing and Data Identification," *Proceedings of the 57th American Helicopter Society Annual Forum*, Washington, D.C., May 9-11, 2001.

[62] Rocconella, B. andWei, F., "Wind Tunnel Model Testing of the Improved KMAX Servo-Flap Blade Section," *Proceedings of the 57th American Helicopter Society Annual Forum*, Washington, D.C., May 9-11, 2001.

[63] McCloud, J. L. and Weisbrich, A. L., "Wind Tunnel Test Results of a Full Scale Multicyclic Controllable Twist Rotor," *Proceedings of the 34th American Helicopter Society Annual Forum*, Washington, D.C., May 15-17, 1978.

[64] McCloud, J. L., "An Analytical Study of a Multicyclic Controllable Twist Rotor," *Proceedings of the 31st American Helicopter Society Annual*

Forum, Washington, D.C., May 15-17, 1975.

[65] Millot, T. A. and Friedmann, P. P., "Vibration Reduction in Helicopter Rotors Using an Active Control Surface located on the Blade," *Proceedings of 33rd AIAA/ASME/ASCE/AHS/ASC Structures, Structural Dynamics and Materials Conference*, Dallas, TX, April 13-15, 1992.

[66] Milgram, J. H. and Chopra, I., "Helicopter Vibration Reduction with Trailing Edge Flaps," *Proceedings of 36th AIAA/ASME/ASCE/AHS/ASC Structures, Structural Dynamics and Materials Conference*, New Orleans, LA, April 10-12 1995.

[67] Straub, F. K. and Hassan, A. A., "Aeromechanic Considerations in the Design of a Rotor with Smart Material actuated Trailing Edge Flaps," *Proceedings of the 52nd American Helicopter Society Annual Forum*, Washington, D.C., June 4-6, 1996.

[68] Milgram, J. and Chopra, I., "A Parametric Design Study for Actively Controlled Trailing Edge Flaps," *Journal of the American Helicopter Society*, Vol. 43, No. 2, 1998, pp. 110-115.

[69] Straub, F. K. and Charles, B. D., "Aeroelastic Analysis of Rotors with Trailing Edge Flaps Using Comprehensive Codes," *Journal of the American Helicopter Society*, Vol. 46, No. 3, 2001, pp. 192-199.

[70] Shen, J. and Chopra, I., "Aeroelastic Stability of Trailing Edge Flap Helicopter Rotors," *Journal of the American Helicopter Society*, Vol. 48, No. 4, 2003, pp. 236-243.

[71] Zhang, J., Smith, E., and Wang, K., "Active-Passive Hybrid Optimization of Rotor Blades with Trailing Edge Flaps," *Journal of the American Helicopter Society*, Vol. 49, No. 1, 2004, pp. 54-65.

[72] Patt, D., Liu, L., and Freidmann, P. P., "Rotorcraft Vibration Reduction and Noise Prediction Using a Unified Aeroelastic Response Simulation," *Journal of the American Helicopter Society*, Vol. 50, No. 1, 2005, pp. 95-106.

[73] Liu, L., Freidmann, P. P., Kim, I., and Bernstein, D., "Rotor Performance Enhancement and Vibration Reduction in Presence of Dynamic Stall Using Actively Controlled Flaps," *Journal of the American Helicopter Society*, Vol. 53, No. 4, 2008, pp. 338-350.

[74] Dawson, S. and Straub, F. K., "Design, Validation, and Testing of a Model Rotor with Tip Mounted Active Flaps," *Proceedings of the 50th American Helicopter Society Annual Forum*, Washington, D.C., May 11-13, 1994.

[75] Dawson, S. and Straub, F. K., "Wind Tunnel Test of an Active Flap Rotor: BVI Noise and Vibration Reduction," *Proceedings of the 51st American Helicopter Society Annual Forum*, Fort Worth, TX, May 9-11, 1995.

[76] Straub, F. K., "Active Flap Control for Vibration Reduction and Performance Improvement," *Proceedings of the 51st American Helicopter Society Annual Forum*, Fort Worth, TX, May 9-11, 1995.

[77] Straub, F. K., "Whirl Tower Test of the SMART Active Flap Rotor,"

Proceedings of the AHS Fourth Decennial Specialists' Conference on Aeromechanics, San Francisco, CA, January 21-23, 2004.

[78] Bernhard, A. P. F., O'Neill, J., Kohlhepp, F., Welsh, W., and Lorber, P., "Active Rotor Control (ARC) of a Mach-Scale Trailing Edge Flap Rotor," *Proceedings of the 57th American Helicopter Society Annual Forum*, Washington, D.C., May 9-11, 2001.

[79] Samak, D., Chopra, I., "A Feasibility Study to Build a Smart Rotor: Trailing Edge Flap Actuation," *Proceedings of the 1993 North American Conference on Smart Structures and Materials*, Vol. 1917, Albuquerque, NM, 1993.

[80] Chopra, I., "Development of a Smart Rotor," *Proceedings of the 19th European Rotorcraft Forum*, Cernobbio, Italy, September 14-16, 1993.

[81] Ben-Zeev, O., Chopra, I., "Advances in the Development of an Intelligent Helicopter Rotor Employing Smart Trailing-Edge Flaps," *Smart Materials and Structures*, Vol. 5, No. 1, 1996, pp. 11–25.

[82] Walz, C., and Chopra, I., "Design and Testing of a Helicopter Rotor Model with Smart Trailing Edge Flaps," *Proceedings of the 35th Structures, Structural Dynamics and Material Conference*, Adaptive Structures Forum, Hilton Head, SC, 1994.

[83] Koratkar, N. and Chopra, I., "Analysis and Testing of Mach Scaled Rotor Model with Piezoelectric Bender Actuated Trailing-edge Flaps for Helicopter Vibration Control," *Proceedings of the 40th Structures,*

Structural Dynamics, and Materials Conference and Exhibit, St. Louis, MO, April 12-15, 1999.

[84] Koratkar, N. *Smart Helicopter Rotor with Piezoelectric Bender Actuated Trailing-Edge Flaps*, Ph.D. thesis, University of Maryland, 2000.

[85] Koratkar, N. and Chopra, I., "Wind Tunnel Testing of a Mach-scaled Rotor Model with Trailing-edge Flaps," *Smart Materials and Structures*, Vol. 10, No. 1, 2001, pp. 1–14.

[86] Spencer, B. and I. Chopra "Design and Testing of a Helicopter Trailing Edge Flap with Piezoelectric Stack Actuators," *Proceedings of the 1996 Symposium on Smart Structures and Materials*, Vol. 2717, San Diego, CA, 1996.

[87] Chandra, R., & Chopra, I. "Actuation of Trailing Edge Flap in a Wing Model Using Piezostack Device," *Journal of intelligent material systems and structures*, Vol. 9, No. 10, 1998, pp. 847-853.

[88] Lee. T., *High Displacement Piezoelectric Trailing-Edge Flap Mechanism for Helicopter Rotors*, Ph.D. thesis, University of Maryland, 1999.

[89] Lee. T. and Chopra, I., "Design Issues of a High-Stroke, On-Blade Piezostack Actuator for a Helicopter Rotor with Trailing-Edge Flaps," *Journal of Intelligent Material Systems and Structures* Vol. 11, No. 5, 2000, p.328-342.

[90] Lee. T. and Chopra, I., "Design of Piezostack-driven Trailing-edge Flap Actuator for Helicopter Rotors," *Smart Materials and Structures*, Vol. 10,

No. 1, 2001, pp. 15.

[91] Lee. T. and Chopra, I., "Design of Bidirectional Piezoelectric Actuator for Blade Trailing-Edge Flap," *Proceedings of the SPIE's 8th Annual International Symposium on Smart Structures and Materials*, Vol. 4327, Newport Beach, CA, March 4-8, 2001.

[92] Spangler, R. L., *Piezoelectric Actuators for Helicopter Rotor Control*, Master's thesis, Massachusetts Institute of Technology, 1989.

[93] Spangler, R. L. and Hall, S. R., "Piezoelectric Actuators for Helicopter Rotor Control," *Proceedings of 31st AIAA/ASME/ASCE/AHS/ASC Structures, Structural Dynamics and Materials Conference*, Long Beach, CA, April 2-4, 1990.

[94] Hall, S. R. and Spangler, R. L., *Piezoelectric Helicopter Blade Flap Actuator*, U.S. Patent, No. 5,244,826, 1993.

[95] Hall, S. R. and Spangler, R. L., "Development of a Piezoelectric Servoflap for Helicopter Rotor Control," *Journal of Smart Materials and Structures*, Vol. 5, No. 1, 1996, pp. 26-34.

[96] Hall, S. R. and Prechtl, E., "Development of a Piezoelectric Servoflap for Helicopter Rotor Control," *Smart Materials and Structures*, Vol. 5, No. 1, 1996, pp. 26-34.

[97] Prechtl, E. *Design and Implementation of a Piezoelectric Servo-Flap Actuation System for Helicopter Rotor Individual Blade Control*, Ph.D. thesis, Massachusetts Institute of Technology, 2000.

[98] Hall, S. R. and Prechtl, E., “Preliminary Testing of a Mach-Scaled Active Rotor Blade with a Trailing Edge Servo-Flap,” *Proceedings of the 1999 Symposium on Smart Structures and Materials*, Newport Beach, CA, June 9, 1999.

[99] Hall, S., Tzianetopoulou, T., Straub, F. and Ngo, H., “Design and Testing of a Double X-Frame Piezoelectric Actuator,” *Proceedings of the SPIE's 7th Annual International Symposium on Smart Structures and Materials*, Newport Beach, CA, June 22, 2000.

[100] Dawson, S. and Straub, F., “Design, Validation and Test of A Model Rotor with Tip Mounted Active Flaps,” *Proceedings of the 50th American Helicopter Society Annual Forum*, Washington, D.C., May 11-13, 1994.

[101] Straub, F., “A Feasibility Study of Using Smart Materials for Rotor Control,” *Proceedings of the 49th American Helicopter Society Annual Forum*, St. Louis, Missouri, April 19-21, 1993

[102] Straub, F. and Merkley, D., “Design of a Smart Material Actuator for Rotor Control,” *Proceedings of the Smart Structures and Materials '95*, San Diego, CA, May 8, 1995.

[103] Straub, F., Ealey, M. and Schetky, L., “Application of Smart Materials to Helicopter Rotor Active Control,” *Proceedings of the Smart Structures and Materials '97*, San Diego, CA, May 23, 1997.

[104] Straub, F., Ngo, H., Anand, V. and Domzalski, D., “Development of a Piezoelectric Actuator for Trailing Edge Flap Control of Full Scale Rotor

Blades," *Smart Materials and Structures*, Vol. 10, No. 1, 2001, pp.25-34.

[105] Straub, F., Kennedy, D., Stemple, A., Anand, V. and Birchette T., "Development and Whirl Tower Test of the SMART Active Flap Rotor," *Proceedings of the Smart Structures and Materials*, San Diego, CA, July 29, 2004.

[106] Straub, F., Kennedy, D., Domzalski, D., Hassan, A., Ngo, H., Anand, V. and Birchette, T. "Smart Material-Actuated Rotor Technology-SMART," *Journal of Intelligent Material Systems and Structures*, Vol. 15, No. 4, 2004, pp. 249-260.

[107] Straub, F., Anand, V. R., Birchette, T. and Lau, B. H., "SMART Rotor Development and Wind Tunnel Test," *Proceedings of the 35th European Rotorcraft Forum*, Hamburg, Germany, September 22-25, 2009.

[108] Fulton, M. and Ormiston, R., "Hover Testing of a Small-Scale Rotor with On-Blade Elevons," *Proceedings of the 53rd American Helicopter Society Annual Forum*, Virginia Beach, VA, April 29 - May 1, 1997.

[109] Fulton, M. and Ormiston, R., "Small-Scale Rotor Experiments with On-Blade Elevons to Reduce Blade Vibratory Loads in Forward Flight," *Proceedings of the 53rd American Helicopter Society Annual Forum*, Washington, D.C., May 20-22, 1998.

[110] Clement, J., Brei, D., Moskalik, A. and Barrett, R., "Bench-Top Characterization of an Active Rotor Blade Flap System Incorporating C-Block Actuators," *Proceedings of 39th AIAA/ASME/ASCE/AHS/ASC*

Structures, Structural Dynamics and Materials Conference, Long Beach, CA, April 20-23, 1998.

[111] Clement, J., Brei, D. and Barrett, R., "Wind Tunnel Testing of a High Authority Airspeed Insensitive Rotor Blade Flap," *Proceedings of 39th AIAA/ASME/ASCE/AHS/ASC Structures, Structural Dynamics and Materials Conference*, St. Louis, MO, April 12-15, 1999.

[112] Hongu, T., Sato, M. and Yamakawa, E., "Elementary studies of Active Flap Control with Smart Material Actuators," *Proceedings of the 12th European Rotorcraft Forum*, Stresa, Garmisch-Partenkirchen, Germany, September 22-25, 1986.

[113] Hasegawa, Y., Katayama, N., Kobiki, N., Nakasato, E., Yamakawa, E. and Okawa, H., "Experimental and Analytical Results of Whirl Tower Test of ATIC Full Scale Rotor System," *Proceedings of the 57th American Helicopter Society Annual Forum*, Washington, D.C., May 9-11, 2001.

[114] Enenkl, B., Klöppel, B., Preißler, D. and Jänker, P., "Full Scale Rotor with Piezoelectric Actuated Blade Flaps," *Proceedings of the 28th European Rotorcraft Forum*, Bristol, UK, September 17-20, 2002.

[115] Dieterich, O., Enenkl, B. and Roth, D., "Trailing Edge Flap for Active Rotor Control Aeroelastic Characteristics of the ADASYS Rotor System," *Proceedings of the 62nd American Helicopter Society Annual Forum*, Phoenix, AZ, May 9-11, 2006.

[116] Roth, D., Enenkl, B. and Dietrich O., "Active Rotor Control by Flaps for Vibration Reduction - Full Scale Demonstrator and First Flight Results," *Proceedings of the 32nd European Rotorcraft Forum*, Maastricht, Netherlands, September 12-14, 2006.

[117] Centolanza, L., Smith, E. and Munsky, B., "Induced-shear piezoelectric actuators for rotor blade trailing edge flaps," *Smart Materials and Structures*, Vol.11, No. 1, 2002, pp. 24-35.

[118] Szefi, J., Mockensturm, E., Smith, E., Wang, K., Rehrig, P. and Centolanza, L., "Development of a Novel High Authority Piezoelectric Actuator for Rotor Blades with Trailing Edge Flaps," *Proceedings of the 62nd American Helicopter Society Annual Forum*, Phoenix, AZ, May 9-11, 2006.

[119] Mercier des Rochettes, H. and Leconte, P., "Experimental Assessment of an Active Flap Device," *Proceedings of the 58th American Helicopter Society Annual Forum*, Montreal, Canada, June 11-13, 2002.

[120] Delrieux, Y., Le Pape, A., Leconte, P., Crozier, P., Gimonet, B. and Mercier des Rochettes, H., "Wind-Tunnel Assessment of the Concept of Active Flaps on a Helicopter Rotor Model," *Proceedings of the 63rd American Helicopter Society Annual Forum*, Virginia Beach, VA, May 1-3, 2007.

[121] Noboru, K. Saito, S., Fukami, T. and Komura, T., "Design and Performance Evaluation of Full Scale On-board Active Flap System,"

Proceedings of the 63rd American Helicopter Society Annual Forum, Virginia Beach, VA, May 1-3, 2007

[122] Noboru, K. and Saito, S., "Performance Evaluation of Full Scale On-board Active Flap System in Transonic Wind Tunnel," *Proceedings of the 64th American Helicopter Society Annual Forum*, Montreal, Canada, April 29 -May 1, 2008.

[123] Saito, S., Kobiki, N. and Tanabe, Y., "Application of an Active Device for Helicopter Noise Reduction in JAXA," *Fluid Dynamics Research*, Vol. 42, No. 1, 2010, p. 24.

[124] Fulton, M., Gold, N., Nielsen, G., Mansur, M., Tischler, M. and Domzalski, D., "Development and Hover Testing of the Active Elevon Rotor," *Proceedings of the 68th American Helicopter Society Annual Forum*, Fort Worth, TX, May 1-3, 2012.

[125] Jung, K. H., Kim, D. H., Song, G. W., Kim, S. H. and Lee, J. D., "Ground Test of Rotor Blades with Active Trailing Edge Flap for Noise Reduction," *Proceedings of the 2008 KSAS Fall Conference*, Jeju, Korea, November 20-21, 2008, pp. 196-1993

[126] Joo, J., et al., *Development of the Next Generation Helicopter Rotor System (IV)*, Final report, Korea Evaluation Institute of Industrial Technology, Project No. 1410053417, 2005.

[127] Crozier, P., Leconte, P., Delrieux, Y., Gimonet, B., Le pape, A. and des Rochettes, H. M., "Wind-Tunnel Test of a Helicopter Rotor with Active

Flaps," *Proceedings of the 32th European Rotorcraft Forum*, Maastricht, Netherlands, September 12-14, 2006.

[128] Kumar, D., *Design and Analysis of Composite Rotor Blades for Active/Passive Vibration Reduction*, Ph.D. Thesis, University of Michigan, 2013.

[129] Jain, R. and Yeo, H., "Effects of Torsion Frequencies on Rotor Performance and Structural Loads with Trailing Edge Flap," *Smart Materials and Structures*, Vol, 21, No. 8, 2012, pp. 1–11.

[130] Lee, J. H., Kwak, J. S., Son, K. T. and Shin, S. J., "Development of an SNU Intelligent Rotor Blade with an Active Trailing-edge Flap," *Proceedings of the 66th American Helicopter Society Annual Forum*, Phoenix, AZ, May 11-13, 2010.

[131] Lee, J. H. and Shin, S. J., "Structural Integrity Design for an Active Helicopter Rotor Blade with Piezoelectric Flap Actuators," *Proceedings of the SPIE Smart Structures and Materials + Nondestructive Evaluation and Health Monitoring*, San Diego, CA, March 6-10, 2011.

[132] Natarajan, B., Eun, W. J. and Shin, S. J., "Structural Design and Flap Actuation Mechanism Validation of an Active Trailing-edge Flap Blade," *Proceedings of the 1st Asian/Australian Rotorcraft Forum*, Busan, Korea, February 13-15, 2012.

[133] Natarajan, B., Eun, W. J., Lee, J. H. and Shin, S. J., "Structural Design of an Active Trailing-Edge Flap Blade for Helicopter Vibration Control,"

Proceedings of the 53rd AIAA/ASME/ASCE/AHS/ASC Structures, Structural Dynamics and Materials Conference, Honolulu, HI, April 23-26, 2012.

[134] Lee, J. H., Natarajan, B., Eun, W. J., Viswamurthy S. R., Park, J. S., Kim, T. S. and Shin, S. J., "Structural and Mechanism Design of an Active Trailing edge Flap Blade," *Journal of Mechanical Science and Technology*, Vol. 29, No. 9, 2013, pp.2605-2617.

[135] Kang, J. P., Eun, W. J., Lim, J. H., Visconti, U. and Shin, S. J., "Design Improvements of Smart Active Trailing-edge Flap for Rotating Test," *Proceedings of the 56th AIAA/ASME/ASCE/AHS/ASC Structures, Structural Dynamics and Materials Conference*, Kissimmee, FL, January 5-9, 2015.

[136] Visconti, U., Kang, J. P., Lim, J. H., Sim, J. S. and Shin. S. J., "Transient Flow Analysis and Static Bench Measurements for an Active Trailing-Edge Flap," *Proceedings of the 57th AIAA/ASME/ASCE/AHS/ASC Structures, Structural Dynamics and Materials Conference*, San Diego, CA, Jan 4-8, 2016.

[137] Visconti, U., Eun W. J., Sim J. S., Lee S. W. and Shin S. J., "Design Improvements and Flap Deflection Evaluations with Considering Centrifugal Load on Active Trailing Edge Flap," *Aircraft Engineering and Aerospace Technology*, Accepted, 2017.

[138] Eun, W. J., Sim, J. S., Lee, S. W. and Shin, S. J., "Advancement of the

SNUF Blade Design through Flap Configuration Parametric Study and Optimization Framework," *Proceedings of the 73rd American Helicopter Society Annual Forum*, Fort Worth, TX, USA, May 8-11, 2017.

[139] Eun, W. J., Sim, J. S., Lee, S. W. and Shin, S. J., "Further Improvements in the SNUF Blade Design by Numerical Design Optimization Framework," *ASCE's Journal of Aerospace Engineering*, Vol. 31, No. 1, 2018.

[140] Cesnik, C. E. S., Mok, J. W., Parikh, A. S., and Shin, S. J., "Optimization Design Framework for Integrally Twisted Helicopter Blades," *Proceedings of the 45th AIAA/ASME/ASCE/AHS/ASC Structures, Structural Dynamics and Materials Conference*, Palm Springs, CA, April 19-22, 2004.

[141] Kim, S. B., Kim, D. G., Kim, D. M., Choi, H. J. and Kim E. J., "Structure Characteristics of Tail Rotor Whirl Test Facility," *Proceedings of the 2008 KSAS Fall Conference*, Jeju, Korea, November 20-21, 2008, pp. 371-374.

[142] Song, K. W., Kim, J. H., Kim, D. G. and Lee. W., "An Experimental Study of Aeroelastic Stability of Hingeless Hub System with Metal and Composite Hub Flexure," *Journal of the Korean Society for Aeronautical and Space Sciences*, Vol. 33, No. 2, 2005, pp. 98-105.

[143] Glauert, H., *Theoretical Relationship for an Aerofoil with Hinged Flap*, British ARC, R & M No. 1095, 1927.

[144] Anonymous, *ANSYS Fluent v.17.0 User Guide*, Ansys Inc., 2016.

[145] Bauchau, O. A., Bottasso, C. L. and Nikishkov, Y. G., "Modeling Rotorcraft Dynamics with Finite Element Multibody Procedure," *Mathematical and Computer Modeling*, Vol. 33, No. 10-11, 2001, pp. 1113-1137.

[146] Bauchau, O. A., *Dymore User's Manual*, Georgia Institute of Technology, 2006.

[147] Peters, D. A. and He, C. J., "Finite State Induced Flow Models. II: Three-dimensional Rotor Disk," *Journal of Aircraft*, Vol. 32, No. 2, 1995, pp. 323-333.

[148] Anonymous, *MATLAB: User's Guide*, MathWorks Inc., 2017

[149] Halland, J. H., *Adaptation in Natural and Artificial Systems: An Introductory Analysis with Applications to Biology, Control, and Artificial Intelligence*, First MIT Press edition, The MIT Press, Cambridge, Massachusetts, London, England, 1992.

[150] Mitchell, M., *An Introduction to Genetic Algorithms*, The MIT Press, Cambridge, Massachusetts, London, England, 1998.

[151] Hirstakeva, M., and Shrestha, D., "Solving the 0-1 Knapsack Problem with Genetic Algorithms," *Proceedings of the 37th Midwest Instruction and Computing Symposium*, Morris, MN, April 16-17, 2004.

[152] Jiang, F. and Yu, W., *ANSYS-VABS Graphic User Interface (GUI) Release Alpha-V-1: Document for Developers*, Purdue University, 2015.

[153] Hodges, D. H., Atilgan, A. R., Cesnik, C. E. S. and Fulton, M. V., "On a Simplified Strain Energy Function for Geometrically Nonlinear Behaviour of Anisotropic Beam," *Composite Engineering*, Vol. 2, No. 5-7, 1992, pp. 513-526.

[154] Yu. W., Hodges, D. H., Volovoi, V. V. and Cesnik, C. E. S., "On Timoshenko-Like Modeling of Initially Curved and Twisted Composite Beams," *International Journal of Solids and Structures*, Vol. 39, No. 19, 2002, pp. 5101-5121.

[155] Yu. W., Volovoi, V. V., Hodges, D. H. and Hong, X., "Validation of the Variational Asymptotic Beam Sectional Analysis," *AIAA Journal*, Vol. 40, No. 10, 2002, pp. 2105-2113.

[156] Yu. W. and Hodges, D. H., "Elasticity Solutions versus Asymptotic Sectional Analysis of Homogeneous, Isotropic, Prismatic Beams," *Journal of Applied Mechanics*, Vol. 71, No. 1, 2004, pp. 15-23.

[157] Yu. W. and Hodges, D. H., "Generalized Timoshenko Theory of the Variational Asymptotic Beam Sectional Analysis," *Journal of the American Helicopter Society*, Vol. 50, No. 1, 2005, pp. 46-55.

[158] Berdichevsky, V. L., "Variational-Asymptotic Method of Constructing a Theory of Shells," *Journal of Applied Mathematics and Mechanics*, Vol, 43, No. 4, 1979, pp. 664-687.

[159] Johnson, W., *CAMRAD II Manual*, Vol. 1-9, Johnson Aeronautics, Palo Alto, California, 2005.

[160] Icten, B. M. and Sayman, O., "Failure Analysis of Pin-loaded Aluminum-glass-epoxy Sandwich Composite Plates," *Composite Science and Technology*, Vol. 63, No. 5, 2003, pp. 727-737.

[161] Zhou, Y., Fei, Q. and Tao, J., "Profile Design of Loaded Pin in Composite Single Lap Joints: From Circular to Non-circular," *Results in Physics*, Vol. 6, 2016, pp. 471-480.

[162] Zhou, Y. and Ishikawa, T., "Bearing Strength and Failure Behavior of Bolted Composite Joints (Part I: Experimental Investigation)," *Composite Science and Technology*, Vol, 65, No. 7-8, 2005, pp. 1022-1031.

[163] Catalanotti G. and Camanho P. P., "A Semi-analytical Method to Predict Net-tension Failure of Mechanically Fastened Joints in Composite Laminates," *Composite Science and Technology*, Vol. 76, 2013, pp. 69-76.

[164] Ataş, A, Mohamed G. F. and Soutis C., "Modeling Delamination Onset and Growth in Pin Loaded Composite Laminates," *Composite Science and Technology*, Vol. 72, No. 10, 2012, pp. 1096-1101.

[165] Anonymous, *MSC Nastran 2014 Nonlinear User's Guide (SOL 400)*, MSC. Software Corporation, 2014.

[166] Koratkar, N. A. and Chopra, I., "Design, Fabrication and Testing of a Mach Scaled Rotor Model with Trailing-edge Flaps," *Proceedings of the 55th American Helicopter Society Annual Forum*, Montréal, Canada,

May 25-27, 1999.

[167] Colaneri, P., Celi, R. and Bittanti, S., “Constant-coefficient Representations of Periodic Coefficient Discrete Linear Systems,” *Proceedings of the AHS 4th Decennial Specialists Conference on Aeromechanics, San Francisco*, California, January 21-23, 2004.

[168] Siddiqi, A. and Hall, S. R., *Identification of the harmonic transfer functions of a helicopter rotor*, Master's thesis, Massachusetts Institute of Technology, 2001.

[169] Hall, S. R. and Wereley, N. M., “Performance of Higher Harmonic Control Algorithm for Helicopter Vibration Reduction,” *Journal of Guidance, Control and Dynamics*, Vol. 16, No. 4, 1993, pp. 193-197.

국문초록

회전익기 진동 저감을 위한 능동 뒷전 플랩 블레이드의 설계 최적화 및 구동 시험

은원종

서울대학교 대학원

기계항공공학부

본 논문에서는 뒷전 플랩을 장착한 마하 스케일 축소 블레이드(SNUF)의 개선이 수행되었다. 플랩 구동 메커니즘은 압전 작동기의 특성과 플랩에 작용하는 외부 공기력을 고려하여 개선되었다. 허브 진동 하중 저감 성능을 높이기 위하여 블레이드 설계 최적화가 수행되었다. 첫째로, 플랩의 크기 및 위치가 진동 하중 저감에 미치는 영향을 확인하기 위하여 다물체 구조 동역학 해석이 수행되었다. 다음으로 블레이드 단면 설계를 개선하기 위하여

수치적인 최적화 기법이 적용되었다. 유전자 알고리즘을 사용한 단면 최적화 프레임워크를 정립하고, 이를 통하여 1 차 비틀림 주파수가 낮고 무게가 가벼운 블레이드가 설계되었다. 블레이드의 구조적 강건성은 다양한 방면에서 평가되었다. 단면 변형률 회복 해석을 수행하고, 블레이드 뿌리 부근에서의 면내 응력이 예측되었다. 추가적으로 허브, 블레이드 및 구체적인 플랩 구동부를 모두 포함하고, 외부 공기력, 원심력 및 구성품들 간의 구체적인 접촉 조건을 고려한 3 차원 정적 구조 해석이 수행되었다. 이러한 플랩 구동부의 시제품을 제작하고, 외부 공기력 및 원심력이 없는 정적 벤치 시험을 통하여 플랩 변위가 측정되었다. 또한 무게추를 이용하여 플랩에 가상의 원심력을 가하고, 이를 목표 운용 시간 동안 작동하는 내구성 시험 또한 수행되었다. 끝으로, SNUF 로터의 시스템 식별을 거쳐 연속 시간 고차 조화 제어 (CTHHC)가 가능한 제어기가 설계되었다. 이 제어기의 안정성 및 진동 하중 저감 성능이 수치적으로 입증되었다.

주제어: 허브 진동 하중 저감, 능동 뒷전 플랩, 블레이드 설계 최적화, 내구성 시험, 페루프 제어

학번: 2012-20686